Structure and Properties of Supercapacitor and Lithium-Ion Battery Electrodes: The Role of Material, Electrolyte, Binder and Additives

Dissertation

zur Erlangung des Grades

des Doktors der Naturwissenschaften

der Naturwissenschaftlich-Technischen Fakultät

der Universität des Saarlandes

von

Nicolas Jäckel

Saarbrücken

2018

Tag des Kolloquiums:	08.06.2018
Dekan:	Prof. Dr. G. Kickelbick
Berichterstatter:	Prof. Dr. V. Presser
	Prof. Dr. E. Arzt
	Prof. Dr. Y. Gogotsi
Vorsitz:	Prof. Dr. G. Kickelbick
Akad. Mitarbeiter:	Dr.-Ing. F. Aubertin

Imagination is more important than knowledge,
because knowledge is limited.

Albert Einstein

Dedicated to my family

TABLE OF CONTENTS

ACKNOWLEDGEMENTS

I met a lot of great people during my time as PhD student in the Energy Materials group at the INM Leibniz Institute for New Materials and all the internships and visits around the world.

First, I would like to thank my supervisor Prof. Dr. Volker Presser for giving me the opportunity to work in his group on a German-Israeli Foundation (GIF) founded project. It was a fruitful and scientifically intense period of my life with many helpful discussions, controversies, and outstanding achievements. I had the great honor to visit 12 conferences on 4 different continents during my time as PhD student. There was no wrong daytime/nighttime and no email too long to find the best solution for any kind of problem. Second, I was delighted to work with Prof. Dr. Eduard Arzt as my scientific advisor and as head of the institute.

The friendly and helpful atmosphere at the whole institute is based on the daily actions of all the people you get in contact. I thank everyone for the wonderful time and special thanks to Dr. Mesut Aslan, Dr. Daniel Weingarth, Dr. Marco Zeiger, Dr. Ingrid Grobelsek, Dr. Slawomir Porada, Dr. Soumyadip Choudhury, Anna Schreiber, Simon Fleischmann, Benjamin Krüner, Juhan Lee, Pattarachai Srimuk, Aura Tolosa, Marius Rodner, Hwirim Shim, Jeon Jeongwook, Sethuraman Sathyamoorthi, and Mathias Widmaier. This thesis at this time would not exist without your great support and motivation.

I would like to thank the INM workshop, especially Herbert Beermann and Werner Schneider, for the support in all technical and electrical questions and the fast process of custom made cells.

Further, I want to thank Prof. Dr. Doron Aurbach and Prof. Dr. Mikhael Levi and their team at Bar-Ilan University for the great atmosphere and the enjoyable discussions, not only during my internships. Special thanks to Netanel Shpigel, Vadim Dargel, and Sergey Sigalov for helping me in the lab and with explanations about the mysteries of EQCM-D.

I had the opportunity to work with Prof. Dr. Yury Gogotsi and his team at Drexel University. It was a nice time there with instructive debates about MXene and Co. Special thanks to Dr. Katherine van Aken, Dr. Babak Anasori, Mohamed Alhabeb, and Muhammed Boota for providing material and support.

During my internship at CSIR in Pretoria, I had the pleasure to work with Prof. Dr. Kenneth Ozoemena and his team. It was a short but informatory stay with the chance of meeting great people. Special thanks to Dr. Katlego Makgopa, Dr. Mkhulu Mathe, Dr. Kumar Raju, Funeka Nkosi, and Annabelle Davis. Moreover, I want to thank the CREATe network for funding and all network members.

The new insights gained with SAXS were impossible without the fantastic work of Prof. Dr. Oscar Paris, Dr. Christian Prehal, and Christian Koczwara. Thank you for the outstanding collaboration and the always nice time when I visited Leoben.

Our collaborators from the Philipps-Universität Marburg, namely Prof. Dr. Bernhard Roling and Steffen Emge, helped me to understand the mechanisms of ion electrosorption in nanopores. Thank you for the fruitful work together and the successful publication.

The numerous discussions on conferences and meetings throughout the whole time has broadly widened my horizons and I'm grateful for everyone who shared his/her thoughts with me.

A very special thank you to Amanda Bellafatto and Jemma Rowlandson for correcting my thesis and to Fabian Eckel and Christopher Thurn for help with the graphs.

The support of my family during every part of my life and especially during my time as PhD student was the anchor for me in all circumstances. Thank you very much for everything.

ABSTRACT

Key parts of an electrochemical energy storage device are the active material, the electrolyte, the binder, and the conductive additives. This dissertation investigates the role of such individual components on the device's overall performance and how they interact with each other to influence the device's ability to store energy and longevity.

Three aspects of the performance of electric double-layer capacitors are investigated: (1) The role of the conductive additives on performance and longevity, where 5 wt% admixture shows the best capability. (2) The role of the active material and the electrolyte with an increased capacitance when the pore width matches the ion size. (3) The volumetric expansion of carbon electrodes during charging is depending on the size ratio of the ions and the pore width.

Further, an asymmetry in charging mechanism is found for two-dimensional metal carbides, MXenes, in ionic liquids. The charging mechanism is based on cation (de-)intercalation. The role of binder properties on the performance of battery electrodes was investigated with intercalation-induced volumetric changes of the active material. Moreover, the multi-length scale approach using different in situ measurement techniques reveals a promising way to understand mechanisms in electrochemical energy storage devices. The combination of dilatometry with quartz-crystal microbalance, X-ray diffraction or small-angle X-ray scattering shed light on potential-induced structural changes in the systems.

ZUSAMMENFASSUNG

Vier wichtige Bestandteile einer elektrochemischen Energiespeicherzelle sind aktives Material, Elektrolyt, Binder und Leitruß. In dieser Dissertation wird der Einfluss dieser Bestandteile untereinander und auf die elektrochemischen Eigenschaften untersucht.

Drei Themenkomplexe werden in Bezug auf elektrische Doppelschichtkondensatoren untersucht: (1) Die Rolle von leitfähigen Additiven auf Leistung und Langlebigkeit, wobei eine 5 %-ige Beimischung die beste Leistung zeigt. (2) Die Rolle des aktiven Materials und des Elektrolyten mit einer erhöhten Kapazität, wenn die Porenbreite mit der Ionengröße übereinstimmt. (3) Die volumetrische Ausdehnung von Kohlenstoffelektroden während des Ladens hängt von dem Größenverhältnis der Ionen und der Porenweite ab.

Es wurde eine Asymmetrie im Lademechanismus bei zweidimensionalen Metallkarbiden, MXenen, in ionischen Flüssigkeiten gemessen. Der Lademechanismus basiert auf Kationeninterkalation. Für ein Batteriesystem mit interkalationsbedingter Volumenänderung des aktiven Materials wurde der Einfluss vom Binder auf die Leistung untersucht. Darüber hinaus zeigt der Multi-Längenskalen-Ansatz mit verschiedenen in-situ-Messmethoden eine vielversprechende Möglichkeit um Mechanismen in elektrochemischen Energiespeichern zu verstehen. Die Kombination von Dilatometrie mit entweder Quarzkristall-Mikrowaage, Röntgenbeugung oder Kleinwinkel-Röntgenstreuung konnte ladungs-induzierte Strukturänderungen im System zeigen.

ABBREVIATIONS

Wh	watt-hour
mAh	milliamp-hour
q	charge
C	capacity/capacitance
U	potential/voltage
i	electrical current
R	resistance
A	surface area
E	energy density
η	efficiency
μ_{Ch}	chemical potential
σ	surface charge
σ_m	cross-section area
ρ	density
μ	kinetic viscosity
δ_n	penetration depth
λ	wavelength
k	wave vector
Q	scattering vector
I	intensity
f	frequency
df	shift in frequency
W	dissipation
dW	change in dissipation
p/p_0	relative pressure
n	number
n_m	adsorption capacity of a monolayer
Ψ	coverage value
C_{BET}	specific heat of condensation
L	Avogadro constant
E_g	thermodynamic stability window
d	distance of the atomic planes

EDLC	electric double-layer capacitor
SC	supercapacitor
LIB	lithium-ion battery
AC	activated carbon
IHP	inner Helmholtz plane
OHP	outer Helmholtz plane
(RT)IL	(room temperature) ionic liquid
EMIM	1-ethyl-3-methylimmidazolium
TFSI	bis(trifluoromethylsulfonyl)imide
TEA	tetraethylammonium
BF_4	tetrafluoroborate
ACN	acetonitrile
PC	propylene carbonate
CV	cyclic voltammograms
GCPL	galvanostatic cycling with potential limitation
LFP	lithium iron phosphate
LMO	lithium manganese oxide
LTO	lithium titanate
HOMO	highest occupied molecular orbital
LUMO	lowest unoccupied molecular orbital
SSA	specific surface area
PSD	pore size distribution
DFT	density functional theory
WE	working electrode
CE	counter electrode
(Q)RE	(quasi-) reference electrode
eD	electrochemical dilatometer
PVdF	polyvinylidene fluoride
PTFE	polytetrafluoroethylene
NaCMC	sodium carboxymethyl cellulose
EQCM	electrical quartz-crystal microbalance
EQCM-D	electrical quartz-crystal microbalance with dissipation monitoring

1. MOTIVATION

The urban society of the 21st century is used to a constant power supply in their homes and offices. In today's factories and manufacturing facilities, the highly intertwined production processes are only possible with a stable and interruption-free electrical grid. The economic deficit due to the interruption of an assembly line, for example in car manufacturing companies, is remarkable. To fulfill the continuous demand for energy, an extremely stable electrical grid and a controlled power system must be achieved. [1] Nowadays, the main sources to generate electrical power (secondary source) are fossil fuels such as oil, gas, or coal (primary sources; **Fig. 1A**). The burning of these materials is responsible for a constant generation of electrical energy. Yet, the exhaust of carbon-dioxide causes harm to the environment in the form of the global climate change and contributes to the 'greenhouse effect' and is the main contributor to the global warming. [2, 3] With the development of the global economy and the consequences of climate change, sustainable growth is only possible by a transition to renewable energy production with green technologies like wind power and solar energy (**Fig. 1B**). [4]

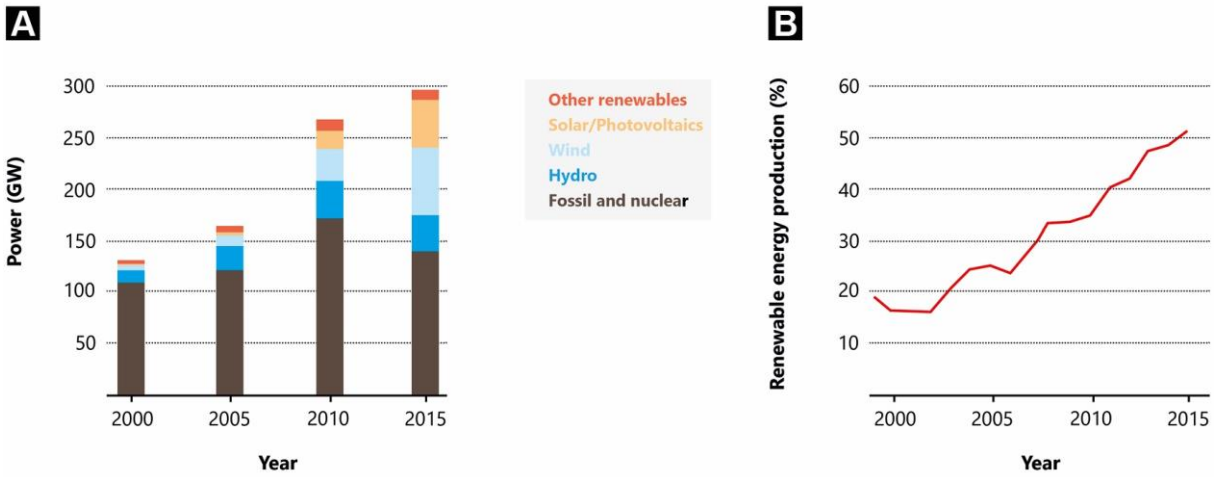

Figure 1. (A) Growth of global economy results in larger amount of energy consumption. (B) The share of renewables in global capacity addition reached over 50 % in 2015 (based on data from Ref. [4]).

Part of the energy transition to renewable resources includes the production of electrical energy with sustainable methods including wind, water and photovoltaic power generation. These resources cannot provide constant energy production because the sun rises and sets every day and the wind pattern and intensities vary. The differences in demand and supply of power from sustainable sources necessitate energy storage if there is an excess amount of energy to fill the gaps when the demand is higher than the production. Therefore, energy storage research is at the focal point of current research activities. [5, 6]

In general, energy can be stored, among others, by physical, chemical, thermal or mechanical methods (**Fig. 2A**). [7, 8] Regarding feasibility and availability, electrochemical energy storage has advantages, such as high efficiency with high volumetric and gravimetric storage density. [9, 10] Many governments, international entities, and companies across the globe have initiated research programs to investigate new and better energy storage. [4] The use of a specific type of storage device is mostly determined by the demand for energy density and maximum volume. The required capacity for certain applications differs from a smart device like a mobile phone, which needs only several watt-hours (Wh), to a (hybrid) electrical vehicle (HEV) with up to 5000 Wh to ensure a customer-requested range (**Fig. 2B**). [11] However, the high energy density can lead to exothermal reactions and generate enough heat for a fire in case of misusage, fatigue, damage or faulty workmanship. [12]

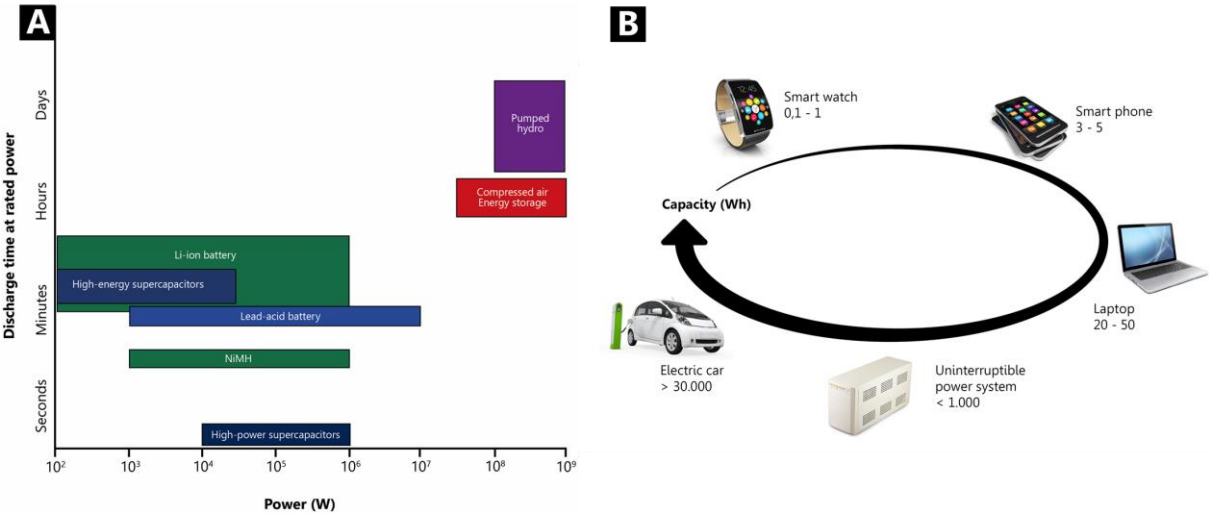

Figure 2. (A) Comparison of different types of energy storage systems and their most promising use (based on data from Ref. [8]). (B) Use of energy storage systems with different required capacity (based on data from Ref. [11]).

For example, a practical implementation of supercapacitors has already been performed by the Rhein-Neckar-Verkehrsverband (RNV, Germany). The RNV created trams powered by supercapacitor arrays located on the tram roof. [13] In the motor racing cars of Formula One, the use of a kinetical energy recovery system (KERS) is allowed. Those systems usually contain a supercapacitor-based energy storage, because they can offer up to 10 kW/kg specific power and the systems must last at least five races. [14]

2. INTRODUCTION

Electrochemical energy storage devices are part of our daily lives. Those devices qualify as a direct way to store and deliver electric energy via faradaic or non-faradaic charge mechanisms. [15] Among those, rechargeable systems like batteries are preferred. Nowadays, most investigations focus on Li-ion batteries (LIBs). [10] Commonly, LIBs are composed of a transition metal intercalation compound as the cathode and a graphitic anode. The chemical nature of the cathodic and anodic reactions, which can use the full bulk volume of the material, result in an excellent energy density of LIBs. [16] However, their performance deteriorates over time with usually only 1000 charge and discharge cycles, due to the chemical energy storage mechanisms which are nor fully reversible. [17] Supercapacitors (SCs), in contrast to LIBs, are physical energy storage devices with a large cycle life of more than 10^5 cycles but lack about a factor of 10 in specific energy (**Fig. 3**). Usually, SCs are built with two porous carbons and use only physical adsorption of ions on the carbon surface as the energy storage mechanism.

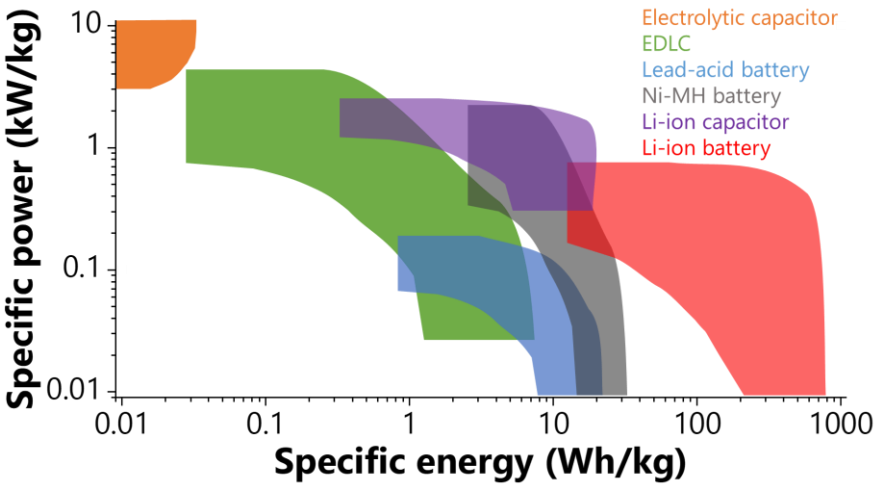

Figure 3. Ragone plot to compare power performance and specific energy of several different energy storage systems (based on data from Ref. [15, 18, 19 , 20]).

The performance of an energy storage system is conveniently plotted in a Ragone plot to compare different storage systems. [21, 22] Usually, the energy is plotted versus the power (**Fig. 3**). A rechargeable battery provides a high energy density but a slow charging and discharging rate and is therefore plotted on the lower right-hand side of the plot. An electric double-layer capacitor (EDLC, or supercapacitor) has a better power output with a much lower energy density and can be found on the upper right-hand side of the Ragone plot. However, such a plot lacks in information about longevity and efficiency. Yet, in general, supercapacitors are very efficient with almost 100% efficiency in laboratory conditions. [23]
This thesis aims to monitor and understand the charging processes and mechanisms of LIBs and SCs and the interactions of all components in these devices. Additionally, the influence of ion size on the

capacitance of SCs is investigated. Finally, the last part of this thesis focuses on a multi-length and multi-apparatus characterization of LIBs and SCs.

2.1 Supercapacitor

The commonly used name supercapacitor, based on the patent of D. L. Boos from Standard Oil Company [24] and licensed to Nippon Electric Company [25], or ultracapacitor, named by the Pinnacle Research Institute, describes an electrochemical double-layer capacitor (EDLC). [26] The terms 'super' or 'ultra' are related to the high capacitance of EDLCs as compared to conventional capacitors (**Fig. 3**). By definition of B. E. Conway [27], a supercapacitor is an electrochemical device where ions of an electrolyte adsorb on the surface of an electrode. If there is no electron transfer between the ions and the electrode, the device is called an EDLC. In the case of a Faradaic reaction, which is an exchange of electrons between the liquid phase (electrolyte) and the solid phase (electrode), it is called a pseudocapacitor according to the definition of D. C. Grahame. [28] The term pseudo is used due to the rectangular shape of the cyclic voltammogram (CV), as seen for an EDLC, but with the presence of electrolyte-electrode charge transfer. The use of the term supercapacitor to describe the physical storage system in an EDLC and the mixed physical-chemical energy storage system in a pseudocapacitor can be confusing. Therefore, the introduction is split into a general description of EDLCs (*Ch. 2.1.1*) and a description of the possible charging mechanisms of pseudocapacitors (*Ch. 2.1.2*).

2.1.1 Electric double-layer capacitors

Electric double-layer capacitors (EDLCs) are physical energy storage devices where the ions reversibly adsorb on a charged surface. Energy is stored via ion electrosorption in the electric double-layer (EDL), where the charge (Q) is stored according to the capacity (C) of the electrode and the applied potential (U) (*Eq. 1*)

$$Q = C \cdot U \tag{1}$$

The electrically charged interface must provide a high surface area (A) in contact with an electrolyte to ensure a high surface charge (σ), which is balanced by the electrosorbed ions in the EDL (*Eq. 2*)

$$Q = \int \sigma \, dA \tag{2}$$

The nature of the EDL was first described by Helmholtz in the 19th century. [29] His simple model failed to account for ion distribution in the bulk, ion-ion interactions, and heat of solvation. These factors are considered by D. C. Grahame in his model from 1947 (**Fig. 4**). [30] The model describes two characteristic

layers: the Stern layer containing the inner Helmholtz plane (IHP), the outer Helmholtz plane (OHP), and the diffuse layer. The Stern layer contains only ions with the opposite charge, defined as counter-ions, electrosorbed on the electrode surface. The solvation shell hinders a direct attachment to the surface and the potential in the IHP is equal to the electrode potential. The second part of the Stern layer, which is the OHP, contains the charged ions and most of the potential is counterbalanced in this plane. The remaining charge is balanced in the diffuse layer, which contains weakly bound counter-ions and co-ions (ions with the same charge as the electrode).

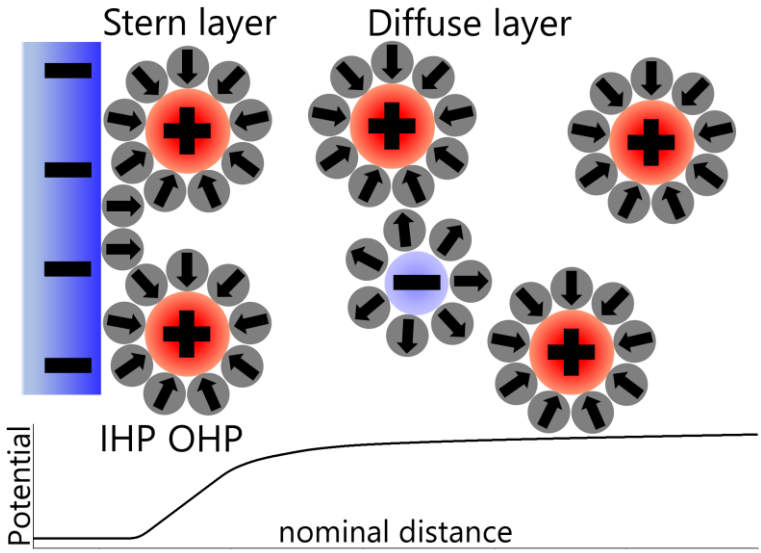

Figure 4. Schematic drawing of the electrosorption of ions in a polar solvent on a planar, negatively charged electrode for an EDLC.

The two main active parts of the EDLC cell are the electrolyte and the electrode material. The active material is commonly activated carbon due to high abundance, low cost, and controllable porosity. [31] These carbons must have a well-developed porosity and pore size distribution, because the electrochemical performance of EDLCs is highly dependent on the electrode material and the pore structure. [23, 32, 33]

The electrolyte, which connects the two electrodes, can be aqueous, organic, or a room temperature ionic liquid (RTIL, or here shortly called IL). [34] RTILs are defined as ILs which are liquid at temperatures above 60 °C and from now on all used ionic liquids in this thesis are RTILs. [35] According to the different electrochemical stability window the maximum operational cell voltage (V) and energy (E) are determined via *Eq. 3* and simplified to *Eq. 4*

$$E = \int_0^{Q_{tot}} V dQ \tag{3}$$

$$E = \frac{1}{2} C \cdot V^2 \tag{4}$$

RTILs are a special case due to the abundance of solvation with an organic or aqueous liquid. The bare ionic content results in strong ion-ion interactions. [36, 37] These molten salts (RTILs) are liquid at room

temperature and ambient pressure because it is the thermodynamically favorable state. [38] In contrast, aqueous electrolytes contain a dissolved salt, where each different type of ion has a distinct solvation shell, and the final size of the ion does not directly depend on the bare ion radius. [39] For example, the fully solvated Li^+ ion has a diameter of 0.482 nm (bare Li^+ 0.138 nm), solvated Na^+ has a diameter of 0.436 nm (bare Na^+ 0.204 nm), and solvated Cs^+ is 0.438 nm (bare Cs^+ 0.170 nm). [39] In organic electrolytes the bare ion size and fully solvated ion size are also different [40], but the solvation energy is usually lower compared to water. [41, 42] A lower solvation energy means it is easier to strip-off solvent molecules. Consequently, matching of pore width to the bare ion size is more important than the solvated ion size. [33] The third group of electrolytes, ionic liquids, are of interest because some of them have a large electrochemical potential window, which can be advantageous since the energy is determined by the potential squared (*Eq. 4*). [43] However, due to the much lower ion mobility in ILs the higher energy is correlated with a lower rate capability, especially for electrodes with small pores in the range of the ion size or slightly smaller. [34]

The highest capacitance for a symmetrical EDLC is published with 180 F/g or 80 F/cm^3 for an activated carbon (approx. 2000 m^2/g SSA) in 1-ethyl-3-methylimmidazolium bis(trifluoromethylsulfonyl)imide (EMIM-TFSI). [44] A direct comparison between tetraethylammonium tetrafluoroborate (TEA-BF_4) in acetonitrile with EMIM-BF_4 (both electrolytes containing the same anion) and AC shows a higher capacitance for the IL, even at the same applied potential of ±1 V vs. carbon. [33] In general, an optimized performance requires careful matching of the electrode properties to the ions in the electrolyte. A more detailed discussion about the correlation between pore width and ions in the electrolyte can be found in *Ch. 4.2 and 4.3*.

When moving from single electrode measurements to the device level, some things must be considered because the electrochemical measurements of a single electrode and the measurement of an electrical device (full cell) are different. In a device there are two electrodes: a cathode (positively charged) with the capacitance (C_C) and an anode (negatively charged) with C_A, interconnected via a serial connection. The total capacitance (C_{tot}) can, therefore, be calculated as *Eq. 5*

$$\frac{1}{C_{tot}} = \frac{1}{C_C} + \frac{1}{C_A} \tag{5}$$

When measuring in a symmetrical full cell mode, the calculated capacitance must be multiplied by a factor of 4 to get the single electrode capacitance, since two electrodes with the same mass are measured and the total capacitance is C/2 according to *Eq. 5* for C_C is equal to C_A. This assumes a symmetrical charge on both electrodes.

2.1.2 Pseudocapacitors

Pseudocapacitors gain capacity from electrosorption of ions on the electrode surface and surface redox reactions or ion intercalation. Therefore, the energy storage mechanism is based on mixed physical and chemical processes. Regarding the D. C. Grahame model for pseudocapacitive systems (**Fig. 5**) the IHP

also contains charged ions now. [30] This contrasts with EDLCs possible because the chemical charge, which is a specific adsorption of ions directly on the electrode surface, leads to higher surface charges. The energy storage capability exceeds the values of bare EDLCs '*since the excess capacity which arises from the reversible electro-reduction of an ion is not a characteristic of the electrical double layer, it will be termed a "pseudo-capacity" to distinguish it from the other kinds of capacity.*' [28] Regard that the chemical energy storage via electron transfer is added to the physical EDL mechanism.

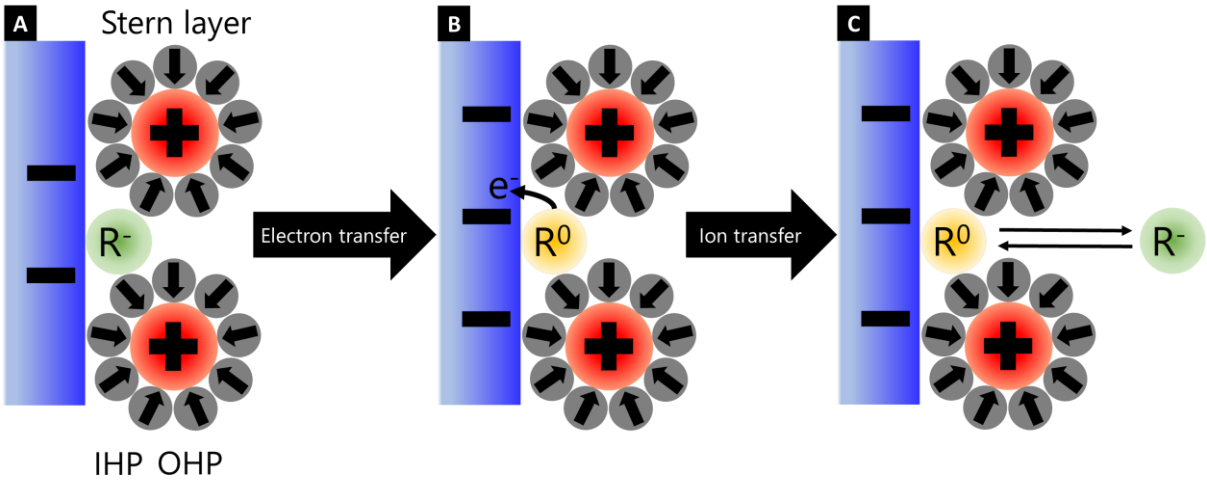

Figure 5. Schematic drawing of the reactions in the Stern layer in the case of pseudocapacitive energy storage.

According to the chemical nomenclature, ions can be oxidized or reduced on the electrode surface by the Faradaic electron transfer. A reduced ion (R^-) gets close to the electrode surface (**Fig. 5A**) and gives an electron (e^-) to the electrode (**Fig. 5B**). The ion after oxidation (R^0) leaves the electrode surface (**Fig. 5C**) to allow another R^- to adsorb on the surface to proceed the process again.

Typical pseudocapacitive materials with surface redox charge mechanism include conducting polymers [45], for example, polyaniline (PANI) [46], poly(3,4-ethylenedioxythiophene) (PEDOT) [47], polystyrene sulfonate (PSS). [48] The pseudocapacitance can also arise from ion intercalation into metal oxides, for example, manganese dioxide [49] and ruthenium dioxide. [50] Intercalation is explained in detail in *Ch. 2.2* but in the special case of a nanoscopic layered metal oxide electrode the pseudocapacitive behavior of a battery material is possible. [51, 52]

Pseudocapacitance arises when the surface charge (σ) required for electrosorption is a continuous function of the potential (U) and the reduction of an oxidized species occurs on the solid phase (ions) within the electrochemical stability window of the electrolyte. The Faradaic charge transfer leads to an increased total charge (Q_{tot}) and, according to *Eq. 3*, to a higher total energy. The derivative (dQ/dU) describes a capacitance with a Faradaic charge transfer contribution, which leads to the rectangular shaped CV. [53] This behavior differs from a battery where the potential does not depend on the state of charge. As described in the Nernst equation, the electrode potential is constant and independent of

the extent of the reaction. [54] The difficulties of quantification between EDL capacitance and intercalation pseudocapacitance are explained in *Ch. 2.3.4*.

Some of the most important parameters for pseudocapacitive devices are rate handling and reversibility. Yet, the physical energy storage in the electric double-layer is combined with a chemical amount of Faradaic charge transfer-based energy storage. The EDLCs with fully reversible adsorption and desorption usually have a high reversibility of almost 100 %. By contrast, the reversibility of chemical reactions is distinctly reduced (typical batteries have about 60-80 % reversibility, more details in *Ch. 2.2* and *Ch. 2.3.4*). [55, 56]

2.2 Lithium-ion Batteries

A Li-ion battery (LIB) is a chemical energy storage device. The intercalation of ions into a bulk material based on the work of Armand et al. was the start of a highly successful technique, which is now used in almost every portable device for its energy storage system. [57] This so-called rocking chair battery was further improved by Goodenough et al. [58], Lazzari and Scrosati [59] and finally patented by Yoshino et al. [60] for the currently used LIB systems. The intercalation and removal of Li^+-ions into the cathode material, usually a transition metal oxide (i.e., lithium cobalt oxide $LiCoO_2$, lithium iron phosphate $LiFeO_4$, or lithium manganese oxide $LiMn_2O_4$) occurs at a specific potential in a reversible reaction. These materials can be clustered into the three possible structure classes: layered materials (i.e., $LiCoO_2$, $LiTiS_2$), spinel structured materials (i.e., $LiMn_2O_4$), or olivine structured materials (i.e., $LiFePO_4$, $LiMnPO_4$). [61, 62] For anodes hard carbon (i.e., artificial graphite or mesophase carbon microbeads (MCMB)) are predominantly used. [62, 63] The advantage of LIBs is the high energy density with more than 100 Wh/kg, which is over ten times higher than EDLCs with typical less than 10 Wh/kg. [15] The drawback for LIBs is a much lower power performance (**Fig. 3**). [9, 15] The difference in energy and power is related to the physically stored ions on the surface of EDLCs, in contrast to chemically intercalated ions into the bulk of the electrodes for LIBs.

In general, the physical transfer of ions from the liquid phase of the electrolyte into the solid phase of the electrode material corresponds to the efficiency of charge transfer and intercalation. The reactions on the anode at the charging step (*Eq. 6*) and the discharging step (*Eq. 7*) are

Charging $$M_A + xLi^+ + xe^- \leftrightarrow Li_xM_A \quad (6)$$

Discharging $$xLi \leftrightarrow xLi^+ + xe^- \quad (7)$$

with the anode material (M_A), the lithium ions (Li^+), the electrons (e^-), the lithium (Li), and number of involved species (x). The Li^+ can reversibly intercalate into M_A. On the cathode, the following reactions occur on the charging (*Eq. 8*) and discharging (*Eq. 9*) step:

Charging $$LiM_C \leftrightarrow Li_{1-x}M_C + xLi^+ + xe^-$$ (8)

Discharging $$Li_{1-x}M_C + xLi^+ + xe^- \leftrightarrow LiM_C$$ (9)

with the cathode material (M_C), which is a lithium deficit oxide. The redox-potential (μ) of the electrode material for Li-ion intercalation in anode materials and Li-ion deintercalation from cathode materials determines the total cell voltage. However, this potential must be within the electrochemical stability window of the used electrolyte.

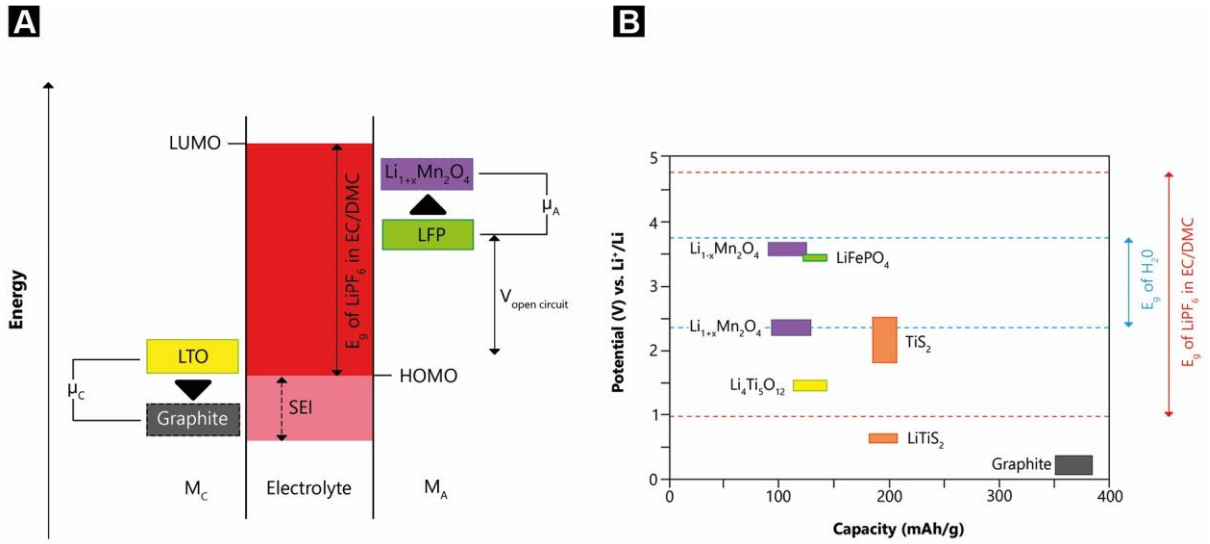

Figure 6 (A) Energy diagram of a battery. μ_C and μ_A are the chemical potentials for the cathode (M_C) and anode (M_A), respectively. (B) Redox potentials of several typical LIB electrode materials in relation to the electrochemical stability window (E_g) of 1 M $LiPF_6$ in EC/DMC (1:1) (red) and water (H_2O, blue). (based on data from Ref. [64])

The most commonly used electrolyte is one molar lithium fluorophosphate (1 M $LiPF_6$) in a one-to-one mixture of ethylene carbonate and dimethyl carbonate (EC/DMC). This electrolyte has a stability window of 1.0-4.8 V vs. Li^+/Li (**Fig. 6A**). A unique property of this electrolyte is the ability to form a solid electrolyte interface (SEI). This layer contains a complex and highly discussed decomposition product of the solvents but can let Li-ions diffuse through the layer. [65, 66] The SEI formation is possible if the chemical potential of the cathode is lower than the highest occupied molecular orbital of the electrolyte (μ_C < HOMO) or if the chemical potential of the anode is higher than the lowest unoccupied molecular orbital of the electrolyte (μ_A > LUMO). [64] The SEI is a protection layer to prevent the total decomposition of the electrolyte and, at the same time, it makes it possible to reach potentials for the onset of lithium intercalation, for example, into graphite (**Fig. 6A**). A detailed discussion of SEI is out of scope for this thesis because it is a very complex and a highly discussed topic in the LIB research community. [66-68]

For example, a cell containing Lithium iron phosphate ($LiFePO_4$, LFP) as cathode and Lithium titanate ($Li_4Ti_5O_{12}$, LTO) as an anode will have a potential of 1.8 V since the intercalation in LTO takes place at 1.6 V vs. Li^+/Li (*Eq. 10*) and the deintercalation from LFP occurs at 3.4 V vs. Li^+/Li (*Eq. 11*, **Fig. 7**).

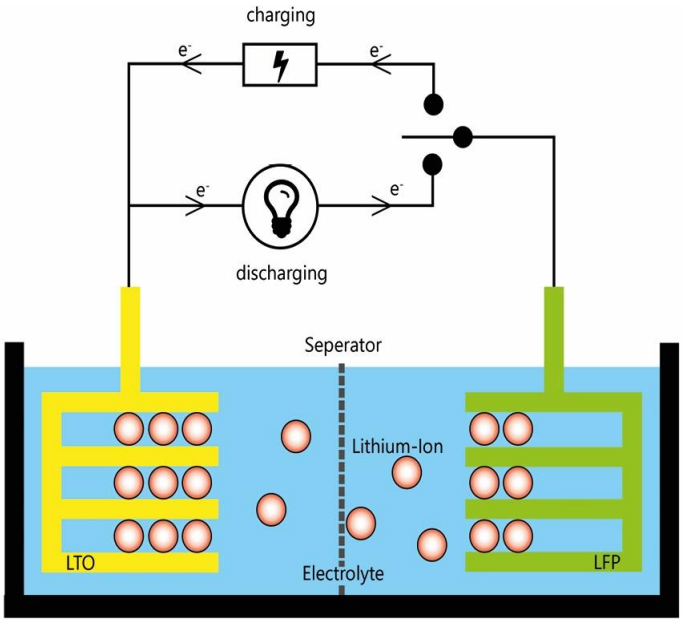

Figure 7. Scheme of the current and ion fluxes, during charging and discharging, in a LIB. (based on data from Ref. [69])

The chemical reactions which occur during charging and discharging are

$$Li_4Ti_5O_{12} + 3Li^+ + 3e^- \leftrightarrow Li_7Ti_5O_{12} \quad (10)$$

$$LiFePO_4 \leftrightarrow FePO_4 + Li^+ + e^- \quad (11)$$

The maximum battery potential window is in general determined by the electrolyte, and the redox-potentials of the active materials must be within this potential window. In aqueous electrolytes, the thermodynamic stability window (E_g) is 1.23 V, which translates to a potential of approximately 2.4-3.7 V vs. Li^+/Li (**Fig. 6B**).

Several performance parameters characterize the intercalation of electrode materials and the most important are: Charge storage ability, intercalation potential, rate handling, and Coulombic efficiency. In general, the charge storage capability is measured in milliamp hours (mAh), which is equal to the ability of lithium uptake in a reversible way. Classical intercalation materials have theoretical storage capacities of several hundred mAh per gram, for example, graphite: 372 mAh/g, LFP: 170 mAh/g, LTO: 175 mAh/g (**Fig. 6B**). [61, 70, 71] The values for materials which form alloys or with conversion reactions are usually much higher, e.g., lithium silicon alloys: 4200 mAh/g for $Si_{21}Li_5$, or lithium sulfur alloys: 1672 mAh/g for Li_2S [72, 73] However, conversion reactions suffer from a variety of chemical side reactions and a large volumetric change, which are difficult to control. This can create stress inside the bulk, which may result in crack formation and the loss of electrical contact. This will lead to a poor cycling stability. [61, 74, 75]

2.3 Measurement techniques

In the following chapter, the measurement techniques, which are of importance for this thesis, will be introduced. A general introduction to each technique is given in each experimental part of the paper, so

here the focus will be on a more fundamental description of the techniques and related models. Furthermore, the use of custom-made in situ cells for a deeper understanding of charging mechanisms and related properties is outlined.

2.3.1 Gas sorption analysis

The specific surface area (SSA) and pore size distribution (PSD) of porous and non-porous materials can be measured using gas sorption analysis. It is a useful and well-established tool for the characterization of hard solids, porous solids, foams, and powders. [76] An isotherm over a certain pressure range is measured according to the adsorbent (the sample) and adsorbate (the used gas) of interest. Typical conditions for highly porous materials are nitrogen (N_2) sorption at 77 K (temperature of liquid nitrogen) in the pressure range of 10^{-7}-1 relative pressure (p/p_0), carbon dioxide (CO_2) adsorption at 273 K in the relative pressure range 10^{-4}-10^{-2} p/p_0, and argon (Ar) sorption at 87 K in the relative pressure range of 10^{-5}-1 p/p_0. [77] Argon is advantageous over CO_2 and N_2 due to the absence of a quadrupole moment. CO_2 sorption measurements can be used to gain fast and precise information about pores in the range of 0.4-1 nm since the measurements are at 273 K where a fast diffusion of gas molecules drastically decreases the time to reach equilibration. [76, 78] The calculation of the specific surface area based on the covered cross-section area (σ_m) of a measured amount of adsorbate can lead to inaccurate values if molecules adsorb in different orientation according to the energetic minimum between the quadrupole moment of the adsorbate and the surface atoms of the adsorbent. Further, from a practical point of view, argon has the advantage of faster measurements because no high vacuum is needed, and the diffusion is faster due to the higher measurement temperature. This is especially relevant in comparison to nitrogen sorption measurements, which have very long equilibration times, especially at the lowest pressures. [79] A too short equilibrium time can lead to an incorrect quantification of adsorption uptakes at a certain pressure, which will ultimately lead to incorrect SSA and PSD values. [80] Further, Ar measurements can also be done at the temperature of liquid nitrogen (77 K) but this temperature is below the triple point and the specific adsorption of Ar molecules is highly depending on the surface chemistry. [76]

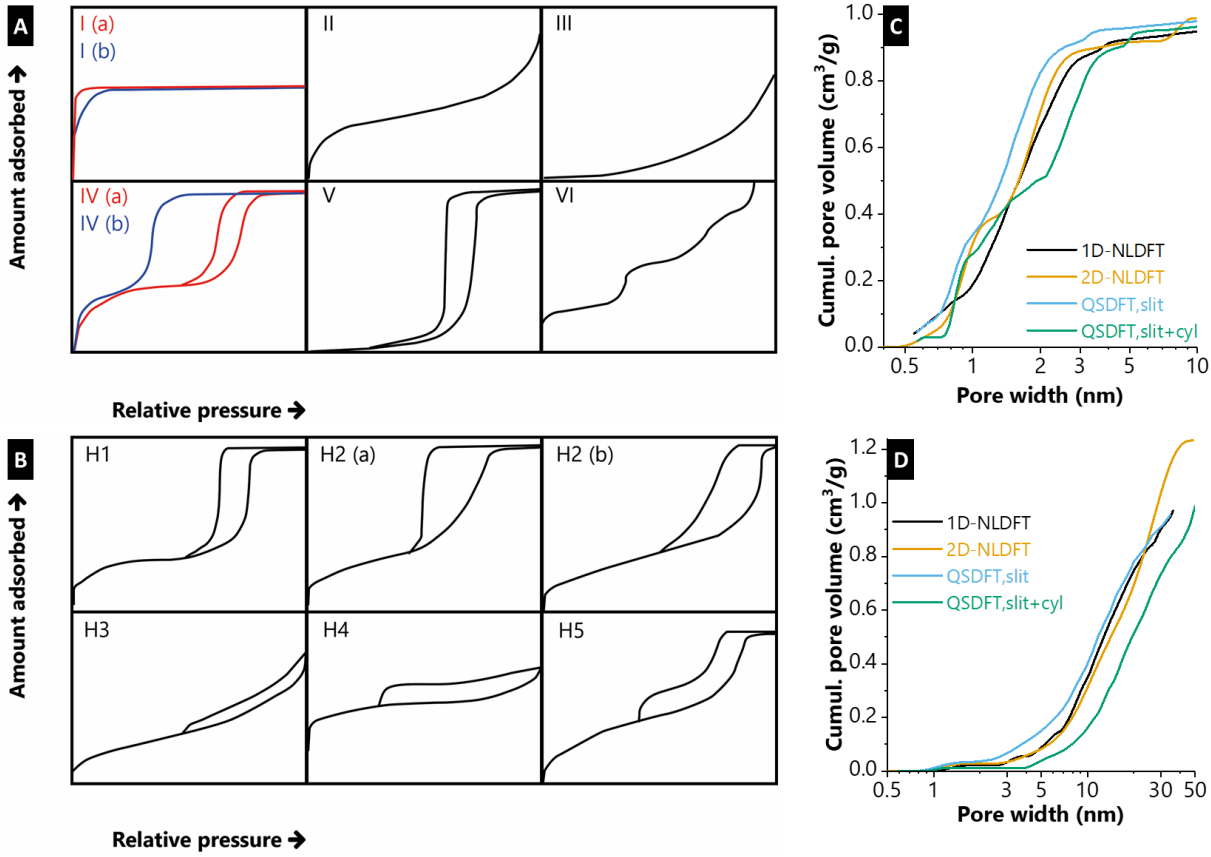

Figure 8. Classification of (A) isotherms and (B) types of hysteresis according to the IUPAC declaration (based on data from Ref. [76]). Deconvoluted data with different kernels from (C) an activated carbon as microporous material and (D) onion-like carbon as mesoporous material with little amount of micropores

The recorded isotherm can be firstly categorized into six major groups with two sub-groups, according to the volume of pores in a certain size range and the interaction between the gas and solid. The IUPAC committee lists three categories of pores: micropores (pore width <2 nm), mesopores (pore width 2-50 nm), and macropores (pore width >50 nm). [76] From this we can describe with the shape of an isotherm and the major pore sizes as follows (**Fig. 8A**): Type I isotherms result from an exclusively microporous material with either pores >1 nm in type I(a) or pores smaller than 2.5 nm in type I(b). Mesoporous materials with a major of pores smaller than 4 nm exhibit a type IV(a) isotherm. If the pores are more cylindrical and the diameter is larger than 4 nm the resulting isotherm will be type IV(b) or type V, where the latter has a weaker gas-solid interaction. Non-porous or macroporous materials can have a type II or type III isotherm. Type III has a weaker interaction between the adsorbent and adsorbate, and no full monolayer evolves. Therefore, the point B describing a fully evolved monolayer adsorption, which occurs in Type II isotherms, is not visible in the isotherm. The last type of isotherm (type VI) shows a layer-by-layer adsorption on the surface and at each step in the curve, a full monolayer of adsorbate is evolved.

Further information about the pore size and shape can be gained by examination of the hysteresis between the adsorption and desorption branch. The appearance of a hysteresis at higher pressure ranges is related to capillary condensation in narrow pores in the micro- and mesopore range. The metastability of the adsorbed multilayer of gas atoms in cylindrical pores leads to a delayed condensation. In more complex geometries the effect of bottle-neck pores, which have a small diameter at the pore entrance (i.e., 5-6 nm for nitrogen sorption isotherms) and a much larger pore diameter in the middle of the pore, will lead to cavitation (a spontaneous growth of a gas bubble in the condensed fluid inside the larger pore volume). [76] The International Union of Pure and Applied Chemistry (IUPAC) further identifies five major shapes of hysteresis, described in the following (**Fig. 8B**): Type H1 is typical for mesoporous materials with a narrow pore size distribution and uniform pore geometry. The narrow loop results from delayed condensation on adsorption. Type H2 have a distinct and steep desorption branch, which can result from either pore blocking in a certain range of pore necks (more likely type H2(b)) or cavitation-induced evaporation (more likely type H2(a)). Type H3 evolves for type II isotherms or if the macropores are not completely filled during adsorption. In this thesis, many samples show type H4 hysteresis which is typical for micro-mesoporous carbons, where the flat line in the relative pressure range of 0.5-0.7 is associated with the filling of micropores. The shape of hysteresis type H5 is exotic. It is associated with both open and partially blocked mesopores. It is obvious, that for H3, H4, and H5 the sharp decrease in adsorbed gas results from the breakdown of the metastable capillary effects. In all cases, the desorption branch must overlap with the adsorption branch in the pressure range below 0.4 p/p_0 to ensure a correct measurement.

The primary mathematical approach utilized in calculating the specific surface area (SSA) from an isotherm is the BET-SSA, according to the theory of Brunauer, Emmett, and Teller. [81] This theory describes the relation of a general number of adsorbed molecules (n) divided by the adsorption capacity of a monolayer (n_m) (Langmuir isotherm [82]) as *Eq. 12*

$$\Psi = \frac{n}{n_m} = \frac{C_{BET}}{(1-\frac{p}{p_0})(1+(C-1)\frac{p}{p_0})} \tag{12}$$

with the coverage value (Ψ) and the specific heat of condensation of the adsorbate on the adsorbent (C_{BET}). The linear form of *Eq. 12* can be written as *Eq. 13*

$$\frac{\frac{p}{p_0}}{n(1-\frac{p}{p_0})} = \frac{1}{C_{BET}\cdot\ n_m} + \frac{C_{BET}-1}{C_{BET}\cdot n_m}\cdot\frac{p}{p_0} \tag{13}$$

The linear relation between left and right side of the equation is drawn in the BET plot for p/p_0 values about 0.05-0.3. According to the BET theory, the parameter C_{BET} is exponentially related to the monolayer adsorption energy and should be in the range of approximately 2-150. [76]

The BET specific surface area (A_{BET}) can be calculated according to *Eq. 14*

$$A_{BET} = \frac{n_m \cdot L \cdot \sigma_m}{m} \tag{14}$$

with the Avogadro constant (L) and the mass of the adsorbent (m).

Applicability of the BET theory fails if the material is mainly microporous since independent monolayer growth is not possible if the pores are too narrow. In such cases, the calculated BET-SSA will be higher than the actual SSA. Therefore, other data treatment must be performed and density functional theory (DFT) is one such promising method. [83] The first approach using a one-dimensional non-local DFT (1D-NLDFT) [84] with the assumption of flat, slit-like graphene walls contained some mathematical artifacts. The zero pore volume at a pore size of 1 nm is the most prominent one. [77] Further addition of parameters into the DFT kernel lead to the most popular and accurate programs, either, quenched-solid DFT (QSDFT) with a roughness parameter for the slit-like pore model, [85] or a hybrid QSDFT model where pores smaller than 2 nm are assumed to be slit-like and wider pores are assumed to be cylindrical. [86] Another way to improve the kernel was done using two-dimensional NLDFT (2D-NLDFT), which considers surface energetical heterogeneity and geometrical corrugation. [87] A direct comparison of those models is shown for an activated carbon with mostly micropores (**Fig. 8C**) and an onion-like carbon with mostly mesopores (**Fig. 8D**). All the kernels show some specific steep increases in a certain pore range or no pore volume in relation to certain pore size range. I assume the amount and loading of artifacts is lowest for the 2D-NLDFT and QSDFT slit kernels, and that these curves exhibit the most accurate PSD. [88] The latter kernels contain most of the parameters implemented in the code, so the interactions between gas-solid, liquid-solid and gas-liquid, as well as the non-ideal carbon surface, are considered. However, the influence of surface functional groups, surface defects and non-carbon content on the adsorption of N_2 and CO_2 is still not quantifiable. Therefore, SSA measurements must be always considered as a method to gain information with an error bar of approximately 10 % and further characterization, for example with electron microscopy, elemental analysis, or X-ray diffraction must be done.

2.3.2 X-ray diffraction

X-ray diffraction (XRD) is a powerful tool to gain information about the structure of a material on the atomic level. The technique is based on the interaction between a monochromatic X-ray source and a solid sample, which was first described by Max von Laue in 1913. [89]

Diffraction of incoming light with the wavelength (λ) on any ordered structure leads to a peak in the diffractogram according to the Bragg-equation [90] (*Eq. 15*)

$$n\lambda = 2d \cdot \sin(\Theta) \tag{15}$$

with the distance of the atomic planes (d) and the angle (Θ) of the incoming light (**Fig. 9A**). The theory is only valid for full elastic scattering of incoming light with matter since Θ and λ of incoming and outgoing waves must be the same and no energy of the incoming wave is transferred to the sample. This is a major difference of scattering effects (*Ch. 2.3.3*), where an interaction of waves and matter is wanted and quantified.

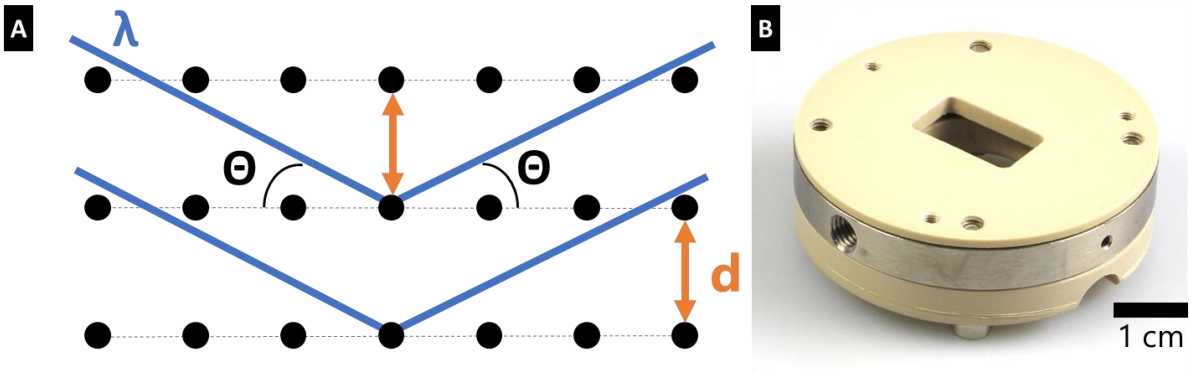

Figure 9. (A) Scheme of the Bragg reflection and (B) picture of the custom-built in situ test cell.

The focus of using XRD in this thesis was to introduce the in situ investigation of ion movement between the layer of two-dimensional (2D) materials (MXenes [91]) with the interlayer distance d, also known as d-spacing. *In situ* describes the simultaneously measured current signal and the changes in XRD signal in a custom-built test cell (**Fig. 9B**). Since the incoming X-rays are copper K-alpha waves with an energy of 8.04 keV, corresponding to λ=0.15405 nm, the resolution of the d-spacing is quite high. Typically, in crystallography, the three vectors **a**, **b**, and **c** describe an orthogonal room of a unit cell, which translates for 2D materials to the in-plane atomic distances a and b and the inter-plane atomic distance c. The distance c and the d-spacing are equivalent in this specific case. In the resulting diffractogram, the two main parameters are the peak position, which corresponds to the interlayer distance and the peak width, which gives information about the distribution of the distances. [92, 93] In the case of Ti_3C_2-MXenes, the complex assembly of the in situ XRD cell with the PEEK body, glass fiber separator, platinum current collector, and polymer cover make a further processing of the diffractogram, like Rietveld refinement [94], highly error-prone.

2.3.3 Small-angle X-ray scattering

The interaction of matter with an incoming wave of light can be fully elastic, and the resulting diffractogram can be described as in the previous chapter or, in the case of inelastic interaction, it can be described with a different theory. Depending on the amount of transferred energy from the incoming wave to the solid matter, the residual energy of the scattered wave will be changed, which is documented in the scattering pattern. [95] X-ray scattering is firstly described by G. P. Thomson [96] and later on

explained by A. H. Compton [97] with the photoelectrical effect. This is where the incoming photon removes a bound electron of an atom into the vacuum, and fluorescence radiation occurs due to relaxation of electrons from a higher shell (higher energy level of bound electrons).

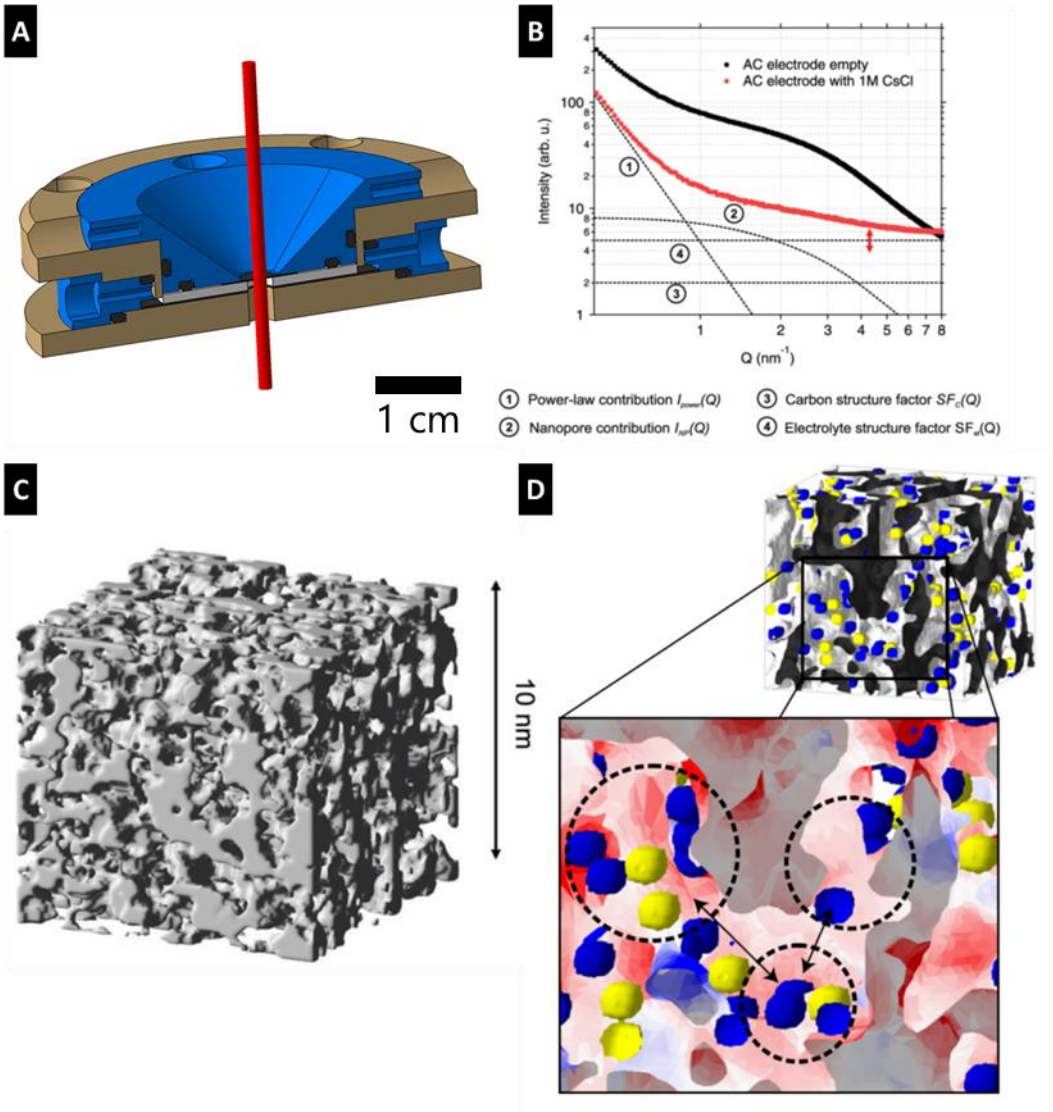

Figure 10. (A) The custom-built in situ SAXS cell in section with the beam going through the working electrode. (B) The SAXS intensity according to Q for an activated carbon (AC) electrode in an empty state (black line) and filled with an aqueous electrolyte (red line). (C) 3d real space pore structure of an activated carbon and (D) results from Monte-Carlo calculations with cations (blue) and anions (yellow), which are visualized for -0.6 V. The local electrode charge density is visualized in the zoomed views, whereas red indicates high negative surface charge density, which is generally found close to cations. In contrast, a positive electrode charge is visualized in blue (induced by cations). The white areas indicate regions with zero electric field. (B+C reproduced from Ref. [98] with permission from the PCCP Owner Societies, D reproduced from Ref. [99] with permission from Nature Publishing Group)

Like XRD (previous chapter), the scattering of incoming light with the wavelength (λ) and a wave vector (k) will be recorded according to the angle (Θ) (for small-angle X-ray scattering typically >10°) with the scattering vector (Q). The scattering vector is defined as the difference between scattered wave vector and incoming wave vector $Q = k_2 - k_1$. The data for small-angle X-ray scattering (SAXS) is usually

plotted as intensity (I) versus Q and any ordering above a characteristic length of 1 nm (like ordered mesopores in carbon) will lead to Bragg reflections and a peak in the plot. [100] When using a synchrotron radiation source with great intensity SAXS curves can be measured within seconds, and kinetical effects or in situ measurements with activated carbon and electrolytes are possible. [98, 99, 101] Using our custom-built in situ SAXS cell (**Fig. 10A**) we can correlate the SAXS signal with electrochemical tests, e.g., the influence of an applied voltage on the electrosorption of ions in nanopores. [99] The SAXS curve contains a vast amount of information, and the contribution of 4 main factors can be separated according to the dashed lines in the graph (**Fig. 10B**). These are (1) the power-law contribution (I_{power}) at smallest Q values, which results from scattering contribution of the activated carbon (AC) particles, [102] (2) the contribution of nanopores (I_{NP}) at intermediate Q values, which is the actual contribution of the smallest pores of AC, (3) the constant influence of the carbon structure (I_C) [103], and (4) the slightly changing influence of the electrolyte structure (I_{el}), which is a function of the applied voltage and based on ion adsorption close to the surface. [98] The changes in I_{el} are marked with the red arrow in the graph. Please note that both structure factors are independent of Q. The total intensity (I_{tot}) is the sum of each contribution factor (*Eq. 16)*

$$I_{tot} = I_{power} + I_{NP} + I_C + I_{el} \quad (16)$$

The combination of the SAXS signal of a dry carbon electrode and a Gaussian random fields simulation calculated a 3d real space pore structure with a size of 15x15x15 nm^3 possible (**Fig. 10C**). [98, 99] The application of Monte-Carlo simulations on a system with the 3d pore structure, water as a solvent, and cations/anions, allow us to understand and quantify ion movement in nanopores at applied potentials (**Fig. 10D**). [99] In general, the question about the behavior of finite sized ions in nanoconfinement, meaning (sub-)nanometer pores was not fully understand. [104] Further, the influence of the hydration shell, or more general the solvation shell, around the ions on the electrosorption in small pores was poorly understood. [105-107] Calculations about the solvation energy and amount of solvation molecules around ions in bulk were done but the influence of narrow pores, sometimes smaller than the fully solvated ion, on the degree of solvation was not fully described. The quantification of ion confinement and degree of desolvation can be summarized in three major aspects: First, counter ions show a preferred movement into sites with a high degree of confinement and this can be explained solely by electrostatic interactions. Second, cations prefer to electrosorb on sites with a higher degree of confinement due to better electrical screening. Third, the degree of desolvation is a function of the average pore size, wherein the amount of desolvation decreases for an increasing pore size. Moreover, the desolvation occurs for less than one percent of the hydration shell. Though, a decrease in solvation was measurable for systems where it would not be necessary because the ions could stay fully solvated in wider pores. This can be explained by the better screening if ions enter a higher confinement, even if the fully solvated ion would be too large to enter the confined space. The energy loss by a partial strip-

off of hydration shell is smaller than the gained electrical screening energy. [99] The established supercapacitor sandbox can be used to predict the performance of certain porous structures in EDLCs.

2.3.4 Basic electrochemical characterization methods

The cornerstone of quantitative electrochemical measurements is a stable and reliable measurement cell with good reproducibility. Precise electrochemical measurements require an elaborate cell design, which can drastically increase the reproducibility of the measurements. Our cell design is a custom-built spring-loaded system with a constant load of 10 N. [108] Further parts are titanium pistons (diameter 1.2 cm), a polyether ether ketone (PEEK) body and brass lids to close the cell (**Fig. 11**). The RE can be mounted via a titanium screw in the cavity very close to the other electrodes. We often use activated carbon as a quasi-reference electrode (QRE) since it is easy to handle and confirmed as a stable quasi-reference electrode for organic electrolytes [109] and ionic liquids. [110] We further showed the stability of treated activated carbon QREs in lithium-containing electrolytes [111] and neutral aqueous electrolytes.[112] One important but often overseen part is the current collector, which must provide a good electrical connection between the titanium piston and the electrode. [113-115] In this thesis it is always a carbon-coated aluminum foil used for all non-aqueous measurements and a platinum disc for aqueous cells to ensure a good comparability between the experiments. However, we found a drastic increase in power performance when sputtering a very thin aluminum layer directly on the electrode due to the highly intertwined structure of aluminum and carbon which drastically decreases the interfacial resistance. [113] With a robust cell design, the focus can now be on the measurement. The field of electrochemistry is a subset of the field of physical chemistry. The driving force for any reaction is the minimization of the Gibbs free energy, which means participating substances must end up at the same chemical potential (μ) (**Fig. 6**). In a Faradaic reaction, an exchange of electrons will occur until the Gibbs free energy reaches the local minimum. An applied voltage will lead to a controlled change in chemical potential and the resulting electron transfer continues until the reaction is completed. The initial potential of an electrode (Φ_{single}) in contact with an electrolyte is determined by the Nernst equation (*Eq. 17*) [54]

$$\Phi_{single} = E_0 + \frac{RT}{zF} \cdot \ln\left(\frac{c_{Ox}}{c_{Red}}\right) \tag{17}$$

with the standard electrode potential (E_0), gas constant (R), absolute temperature (T), number of involved electrons (z), Faraday constant (F), and concentration of oxidized (c_{Ox}) and reduced (c_{Red}) species, respectively, determine the potential. This process happens at each interface of the working electrode (WE) and counter electrode (CE) which is in contact with the electrolyte until a stable potential is reached. The same process occurs at the reference electrode (RE). However, because this electrode is currentless, the potential is stable and gives a constant value over the whole measurement, which is used as a reference potential. The total equilibrium voltage between two electrodes (either between WE and RE in

a three-electrode measurement or between WE and CE in a full cell with two electrodes) is determined by the difference in the single potentials after an equilibration of the chemical potentials. By applying a voltage, the system gets shifted from the equilibrium state into higher or lower potentials, and some reactions will occur. For example, tis can be the intercalation of Li-ions into graphite, the exertion of Li-ions from LFP, or another reaction like conversion, which is not in the focus of this thesis.

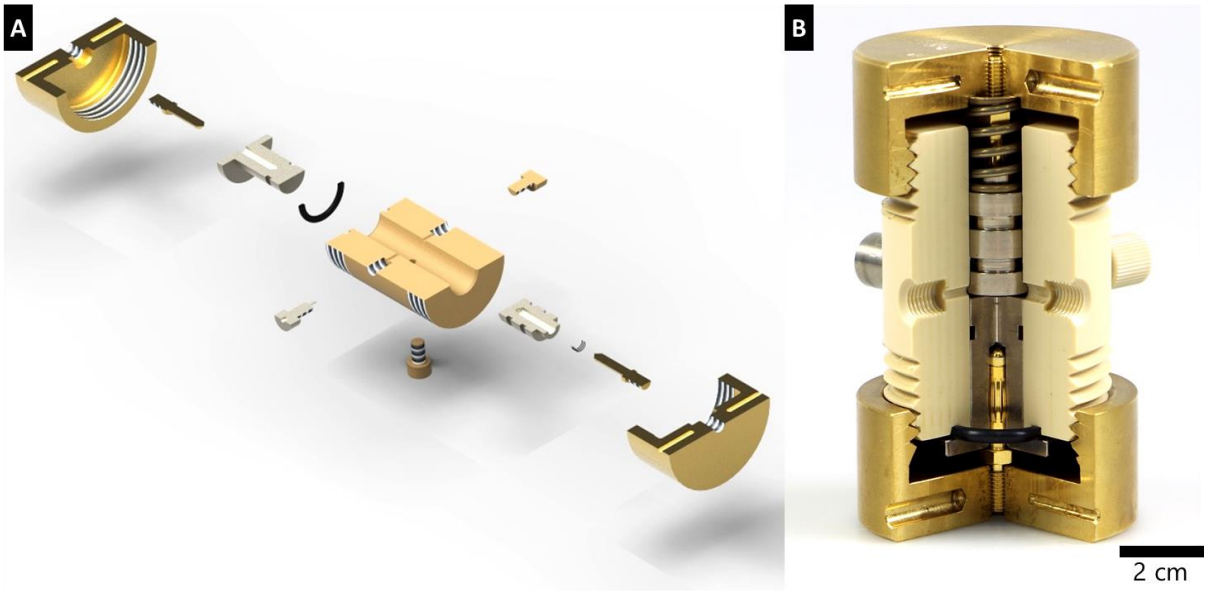

Figure 11. (A) Exploded drawing and (B) a picture of the cut-open custom-built electrochemical test cell.

The cell is carefully assembled and placed in a climate chamber at a constant temperature (room temperature, 25±1 °C), and measurements begin after an appropriate equilibration time (approximately 1 h). A standard characterization is performed with cyclic voltammetry (CV) and galvanostatic measurements. The reactions take place at a certain potential in a cyclic voltammogram (CV), where the potential is linearly changed with the time, one will see some distinct peaks when testing a battery since the plot is current over potential/voltage. This is in strong contrast to a CV of a capacitor, where current is in the ideal case independent of the applied voltage (dQ/dU=const.) within the stability window of the electrolyte. The independence from the voltage results from electrosorption and absence of electron transfer between electrode and electrolyte. Those easy to distinguish mechanisms are blurred when the electrode architecture gets more complex with, for example, nanometer-sized battery materials, which show rectangular-shaped CVs (**Fig. 12**). [116] The possible mechanisms can be pseudocapacitance with Faradaic charge transfer but rectangular-shaped CVs [51] or reversible hydrogen sorption in nanopores. [117] Further, the use of a new class of materials with two-dimensional characteristics can show pseudocapacitive intercalation. [91] Yet, also the electrolyte can have a contribution on the charging mechanism by the use of redox-active electrolytes. [118] All these factors make a direct determination based on the shape of CV impossible and further characterization is needed. The material's behavior and interaction with the electrolyte must be investigated separately.

Another standard electrochemical characterization technique is the galvanostatic measurement with potential limitation (GCPL). Here, in contrast to CVs, the applied current (i_{GCPL}) is constant and the potential is measured over time. The advantage of this method is that it makes quantification of charge transfer at a certain load possible because the applied current is manually set. The current values are either normalized to electrode mass (meaning amperes per gram) or in time with the C-rate, where 1C means the charging or discharging duration is one hour.

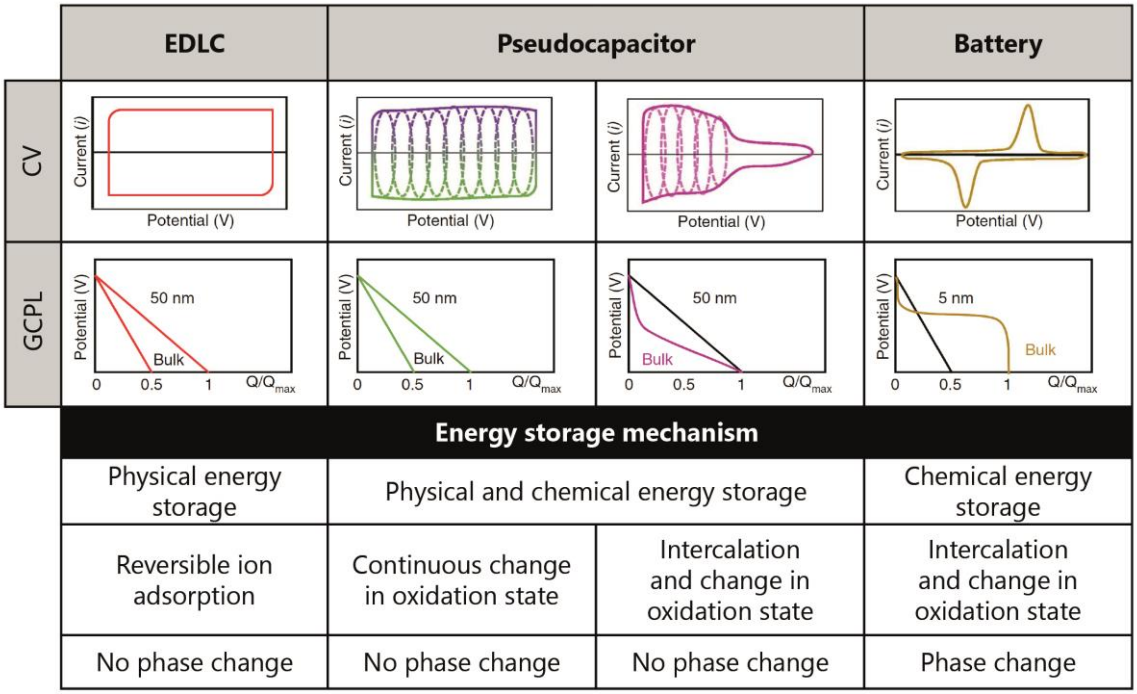

Energy storage mechanism			
Physical energy storage	Physical and chemical energy storage		Chemical energy storage
Reversible ion adsorption	Continuous change in oxidation state	Intercalation and change in oxidation state	Intercalation and change in oxidation state
No phase change	No phase change	No phase change	Phase change

Figure 12. Comparison of possible charge storage mechanisms and the resulting CVs and GCPL curves (adapted from Ref. [119]).

With the GCPL, the internal resistance of the system can be investigated by an iR-drop (U_{iR}) at the beginning of the voltage profile. According to Ohm's law $U_{iR} = R_{ESR} \cdot i_{GCPL}$ the electrical series resistance (R_{ESR}) can be measured. A typical plot for those measurements in the supercapacitor field is the voltage profile over time to show the straight (dis-)charging lines. In the battery field, one commonly plots voltage versus charge, where the voltage profile indicates the Coulombic and energy efficiency. The Coulombic efficiency (η_C) is the quotient of charge from discharge (Q_{dis}) divided by the charge invested for charging (Q_{ch}) ($\eta_C = {}^{Q_{dis}}/_{Q_{ch}}$), and the energy efficiency (η_E) is the same quotient but for the invested energies ($\eta_E = {}^{E_{dis}}/_{E_{ch}}$). The specific energy is in this case calculated by *Eq. 18*

$$E_{sp} = \frac{i_{GCPL}}{m} \int_{t_0}^{t_{end}} U(Q)dt \tag{18}$$

with the mass (m) and the integral over the voltage profile U(Q) over the time from start (t_0) until end (t_{end}). Mind that U is a function of Q. For an ideal supercapacitor the Coulombic efficiency must be one because the charge storage mechanism is fully reversible. However, η_E will not reach this value but due

to losses based on several effects, for example, the R_{ESR}. The ion redistribution and leakage current of SCs further diminishes the total efficiency. [56] Moreover, each activated carbon will have a certain non-carbon content like adsorbed water in the pores and functional groups. Those impurities can catalyze electrolyte decomposition (see *Ch. 4.1*) and are therefore unwanted in non-aqueous electrolytes. [120-123] The decomposition will lead to a reduced efficiency because the chemical reactions during degradation are irreversible. The first cycle effects, which occur during the first contact between electrodes and electrolyte as well as during the first applied potential are in this thesis always insignificant due to a proper conditioning. Further, usually the third or fifth cycle after conditioning was used for published data.

In general, a system with very high efficiency will also have a promising longevity and therefore the calculation of efficiency is a fast technique to roughly extrapolate the lifespan of a SC. [56] Highly optimized and laboratory scale supercapacitors can yield values for η_C of 97-99 %. [23]

2.3.5 In situ electrochemical dilatometry

In general, a dilatometer is a device which measures strain (i.e., linear volumetric changes). The specification of an in situ electrochemical dilatometer (eD) is the combination of an electrochemical cell connected to a dilatometer. The history of eD starts in 1977 with a paper by Métrot et al. [124] where the changes in thickness were measured for a pyrographite electrode in contact with boron trifluoride in ethoxyethane. [124] The focus at the beginning was on the intercalation behavior of a certain species into graphite and the resulting dilatation. The poor resolution of the first used apparatus was improved by Biberacher et al. [125] with an estimated resolution of 25 nm. Later, this system was also used for the intercalation of Li-ions into industrially produced graphite. [126] The apparatus was further improved at the Paul Scherrer Institute in the Group of Rüdiger Kötz by Hahn et al. [127] and is now commercially available from the company EL-CELL. The system provides a non-contact setup, where the WE is connected to a moveable plunger and via a membrane to the height transducer, which applies a constant load on the WE (**Fig. 13**). The WE is placed between the glass T-frit and the spacer disc (**Fig. 13B**). This setup allows the measurement of a variety of electrode materials and electrolytes since the cell can be sealed inside a glove box. This simplifies the use of materials/electrolytes that require handling in a certain atmosphere, e.g., oxygen free for lithium or water free for organic electrolytes and ionic liquids. Those cells can now be measured in a climate chamber outside of the glove box.

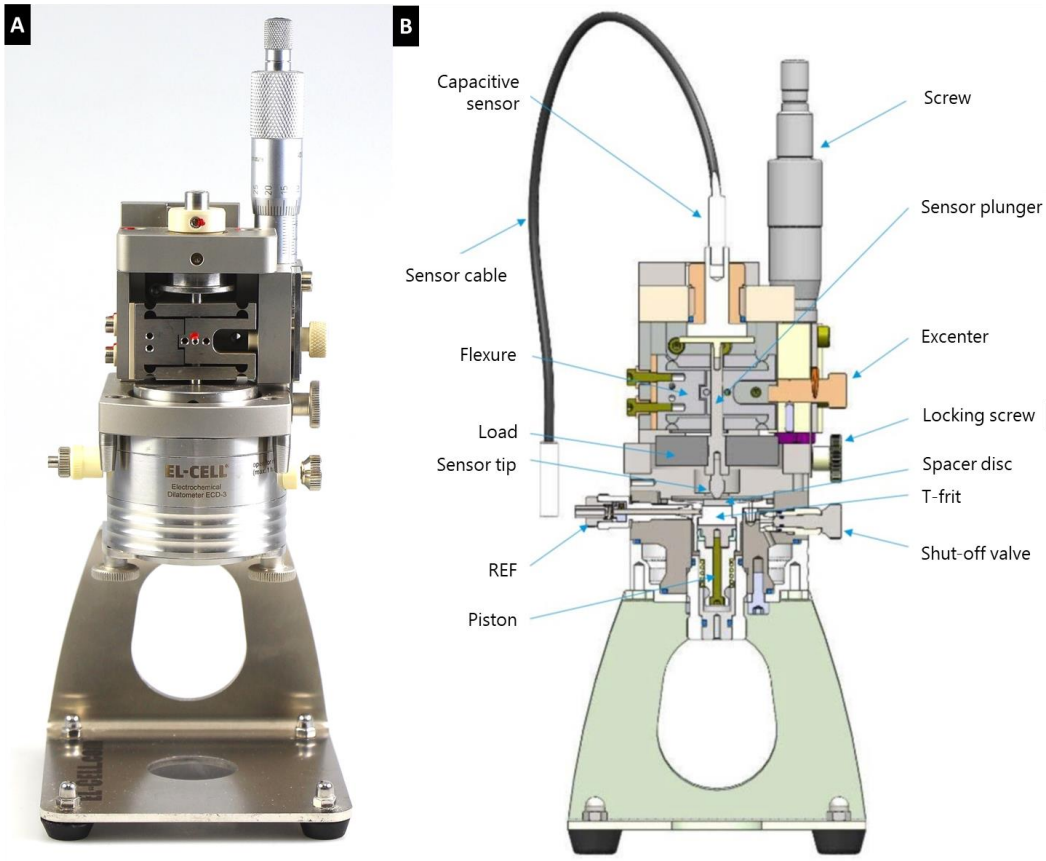

Figure 13. (A) Picture of the in situ electrochemical dilatometry system ECD-3nano from EL-CELL. (B) Schematic drawing of the main components of the dilatometer (with permission of EL-CELL, Germany).

The expansion for an intercalation type of energy storage can be several percent, for example, for Li-ions into graphite with full intercalation (ideally until LiC_6 is reached) about 10 % [128], for $LiFePO_4$ to $Li_{1-x}FePO_4$ about 6.5 % (for x=0.98) in correlation to the phase change from olivine to orthorhombic structure. [129] As an example, lithium manganese oxide ($LiMn_2O_4$, LMO) particles were drop-casted with 10 mass% conductive additive and 10 mass% polyvinylidenfluorid (PVdF) on a platinum disc as a current collector and placed as WE in the dilatometer. The LMO is usually used as a cathode in a LIB because of the high (de-)lithiation potentials (**Fig. 6B**). However, the LMO structure and phases are still a major concern according to lithium content and unit cell construction. A common accepted model describes three major phases, depending on the loading of lithium, which are first almost fully delithiated $Li_{1-x}Mn_2O_4$ (with $x < 0.98$) rutile structure, second $LiMn_2O_4$ with spinel structure, whereas the lithiation occurs at 3.6 V vs. Li/Li^+, and third a lithium rich $Li_2Mn_2O_4$ spinel structure which forms at potentials below 2.5 V vs. Li/Li^+. [131, 132] During the delithiation, the $LiMn_2O_4$ spinel structure changes to $Li_{1-x}Mn_2O_4$ rutile structure with a theoretical compaction of up to 6.5 %. [133, 134] Instead, the formation of a lithium-rich $Li_2Mn_2O_4$ phase leads to a further increase in volume by 6 % compared to $LiMn_2O_4$. [135] Yet, this expansion is not isotropic since the c-direction expands approximately 16 % more than the a-direction, what is a Jahn-Teller distortion. [132-136] The thin electrode, which was used in the dilatometer, with 2.1 mg total mass and 51 µm thickness shows three distinctive peaks in the CV for

anodic and cathodic scan at a scan rate of 1 mV/s, which are typical for battery materials and correspond to Nernstian behavior (*Ch. 2.2*, **Fig. 14A**). The corresponding height change, normalized to strain by dividing the displacement with the initial thickness and set to zero at 0 V vs. Ag/Ag^+, follows the peaks of the CV, where the slope in strain is highest for the largest current. Applying a positive potential leads to the extraction of lithium and the compaction of the structure, which is in this case 0.8 % decrease in strain at +0.8 V vs. Ag/Ag^+. For negative potentials, the lithium-rich phase occurs after the peak occurs in CV at -0.5 V vs. Ag/Ag^+ with an increase in strain of 0.7 %. The total volumetric change for the composite electrode is significantly less compared to the theoretical values, but this is due to many parameters like void volume, reorganization of particles due to plastic deformation of the binder, or non-complete lithium insertion and extraction. [32, 137]

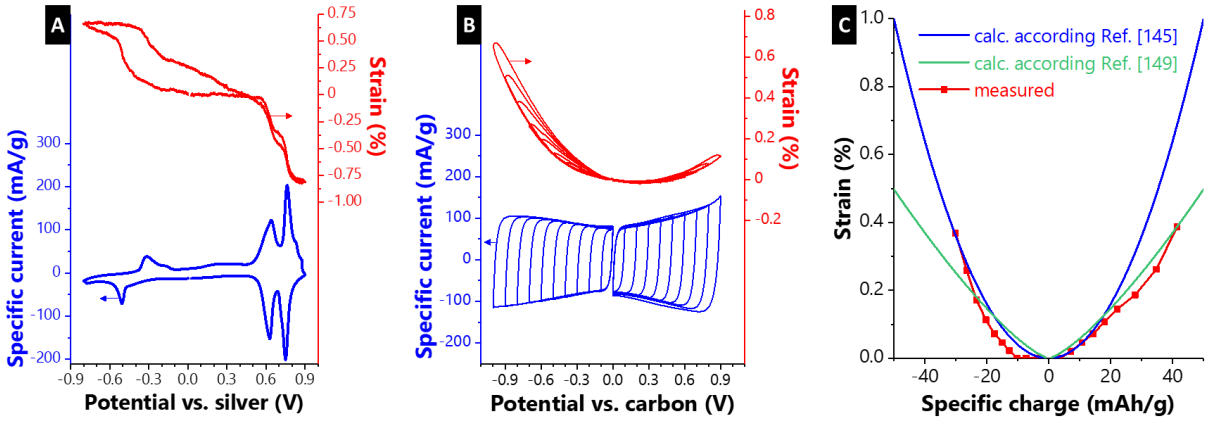

Figure 14. Cyclic voltammogram (blue) and simultaneously recorded strain signal (red) for (A) a lithium manganese oxide electrode (LIB electrode) in an aqueous lithium sulfate electrolyte, and (B) for an activated carbon electrode (EDLC electrode) in an organic electrolyte. (C) The EDLC electrode was quantitatively investigated with charge versus strain and compared to simulations.

The next example is an organic EDLC with activated carbon as electrode material (**Fig. 14B**). In an ill-considered approximation, no macroscopic change in volume for an electric double-layer capacitor would be expected since the energy storage is based on charge separation on the electrode-electrolyte interface. The standard electrode material is porous carbon with a high surface area and pores in the subnanometer to mesopore range. [34] However, the pressure necessary to place an ion into a subnanometer pore can reach several hundred megapascals. This causes a volumetric change of the whole electrode, even if the Young's modulus of carbon (graphite) is in the range of gigapascal. [138, 139] One can expect that not the elastic stretching of the C-C bonds is the reason for the expansion. The simulation of the pressure values, which is based on a constant-voltage grand-canonical ensemble with hard spheres as ions, a dielectric constant, a pair of hard electrode planes, constant surface charge, and a Coulombic energy term between the ions, may contain mathematical artifacts due to those simplifications. [139, 140] However, the electrostatic energy based on Coulombic interaction in combination with thermodynamic terms, which are based on surface charge density, ion density and the pore size reveal the influence of those parameters on the pressure needed to create an electric double-

layer in narrow pores at an applied voltage. [140] The results of these simulations show a decrease in pressure for higher dielectric constants since the electrostatic force is better shielded in those cases and the repulsion force of ions with the same charge is decreasing and buffered by the electrolyte. Further, an increased pressure is related to the ion size and pore size, whereas the maximum increase was calculated for pore sizes in the range of the ion size. However, for all calculations the pressure was increased after applying a voltage. [139] Those simple calculations reveal the importance of ion size, pore size, and applied voltage on the macroscopic behavior of the electrode material. A macroscopic change in volume will happen when the internal pressure in the micropores increases above the stress level that the material can handle without a change in strain.

Regarding graphitic carbon there are three charge-induced volumetric changes possible: First, the intercalation, as described earlier, with an increase in the c-axis and a volumetric change of approx. 10 %. [128] Second, the change in the intralayer C-C bond length based on quantum-mechanical effects due to electron or hole injection with approx. 1.5 % change in volume. [141] Third, the reduced surface tension leads to an expansion of the electrode material with a linear correlation between surface charge and strain. [142] This effect has been measured, but the macroscopic volume changes below 0.05 % show an almost negligible effect. [143] A direct comparison between intercalation and the electrosorption-induced strain shows a large expansion (>5 %) for ion intercalation at potentials far from the point-of-zero charge (pzc) and a less pronounced expansion (<3 %) for electrosorption, but the expansion begins already at low applied potentials. [127] In EDLCs there is a two-phase interaction between the porous carbon electrode and the ions inside the electrolyte. The finite-sized ion together with possible solvent molecules is attracted into nanoconfinement to compensate the surface charge.

Usually the expansion for EDLCs at negative potentials is larger compared to positive potentials, even at the same charge. [144] This non-symmetrical behavior is shown for many types of carbons and electrolytes. [32, 40, 100, 144-147] Possible explanations for this asymmetry can be based on two main factors. Firstly, the different size of ions in the double-layer, where often cations are larger than anions, what results in greater pressure for larger ions in the same pore size. [139] Secondly, the change in C-C bond length according to quantum-mechanical effects causes a contraction of up to 1.5 % for hole injection (positive charging) and up to 1.5 % expansion for electron injection (negative charging). [141] Yet, several other competing mechanisms like electrowetting, ion desolvation, and steric effects, which are functions of the state of charge and are further influenced by the amount of functional groups, make a precise prediction of carbon swelling impossible at present. [32, 40, 105, 148] As an example, activated carbon (type YP80-F) bound with 5 mass% polytetrafluoroethylene (PTFE) was measured in an organic electrolyte (one molar tetraethylammonium tetrafluoroborate in acetonitrile, 1 M TEA-BF_4/ACN) (**Fig. 14B**). The predominately rectangular shape of the CV confirms a near ideal double-layer behavior during charging and discharging, whereas the quantum capacitance at higher/lower potentials leads to

the butterfly-shaped CV. [108] The asymmetric expansion with an increase in strain of 0.75 % at -1 V vs. carbon and 0.15 % at +0.9 V vs. carbon does not directly correspond to the very symmetric CV. However, considering the different size of cation (TEA^+ with 0.67 nm diameter) and anion (BF_4^- with 0.45 nm diameter) and the aforementioned possible effects, the total strain signal is a sum of many parameters. [33] Earlier publications predicted, for example, a $\frac{dl}{l_0} \propto \sigma^2$ [138, 140, 145] dependency of expansion $\left(\frac{dl}{l_0}\right)$ and surface charge (σ) or, based on calculations according to the Donnan model, a dependency of $\frac{dl}{l_0} \propto \sigma^{4/3}$. [149] The measured strain in comparison to the model prediction shows no direct overlapping between the different simulation results and the measured points (**Fig. 14C**). Summarizing, the swelling of carbon when applying a potential is depending on many different parameters and a precise prediction is not currently possible.

2.3.6 Electrochemical quartz-crystal microbalance

The quartz-crystal microbalance (QCM) is a tool for measuring small masses with the shift of the resonance frequency (f) of a quartz crystal. The linear correlation between a rigidly attached mass (m) on the quartz-crystal and the change in frequency (df) was formulated by G. Sauerbrey [150] in 1959 according to *Eq. 19*

$$df = k \cdot m \tag{19}$$

with the characteristic coupling constant (k), which only depends on the type of the quartz-crystal and natural constants. This correlation is valid in vacuum or air. For application in a liquid, i.e., water, the generated shear wave from the crystal surface towards the liquid needs to be considered. The relation between df and the density (ρ) and the kinetic viscosity (μ) can be drawn as (*Eq. 20*)

$$df = k \cdot \sqrt{\frac{\rho_L \mu_L}{\rho_Q \mu_Q}} \tag{20}$$

with the density of the liquid (ρ_L) and the crystal (ρ_Q) as well as the viscosity of liquid (μ_L) and crystal (μ_Q). [151] The first in situ electrochemical measurement with a QCM (so-called EQCM) was published in 1969 to monitor the electrodeposition of metals. [152] This method was investigated by many groups and the influence of an applied voltage on a material deposited on the quartz crystal has a dominant role. [153-155] Applying knowledge of the mass of ions and solvents on the raw EQCM data improved understanding of ion fluxes in supercapacitors [156-161], batteries [162, 163] and 2d materials. [164]
Further investigation opened the next step in applying EQCM to probe viscoelasticity. This was possible by considering the dissipation of the signal and is established as EQCM-D (EQCM with dissipation monitoring). By using this technique, the excitation of the quartz-crystal stops immediately and the decay of the signal is investigated. [165, 166] The dissipation factor, which is the exponential decay of

the amplitude, contains information about viscoelasticity, slipping of active material on the surface, and more. [166, 167]

The understanding of interfacial phenomenon and the correlation with the impact on the EQCM-D signal helped us to develop a new approach; the use of overtones in the quartz-crystal resonance together with a model fit to the shape of peak and dissipation made hydrodynamic spectroscopy possible. [168, 169] With this approach the penetration of a shear wave with a certain wave length was correlated to the battery performance. The frequency is connected to the penetration depth (δ_n) of the shear wave, according to *Eq. 21*

$$\delta_n = \sqrt{\frac{\eta}{\pi n f_0 \rho}} \tag{21}$$

with η and ρ of the electrolyte, the odd overtone numbers from 3 to 13 (n), and the fundamental resonance frequency (f_0). [168]

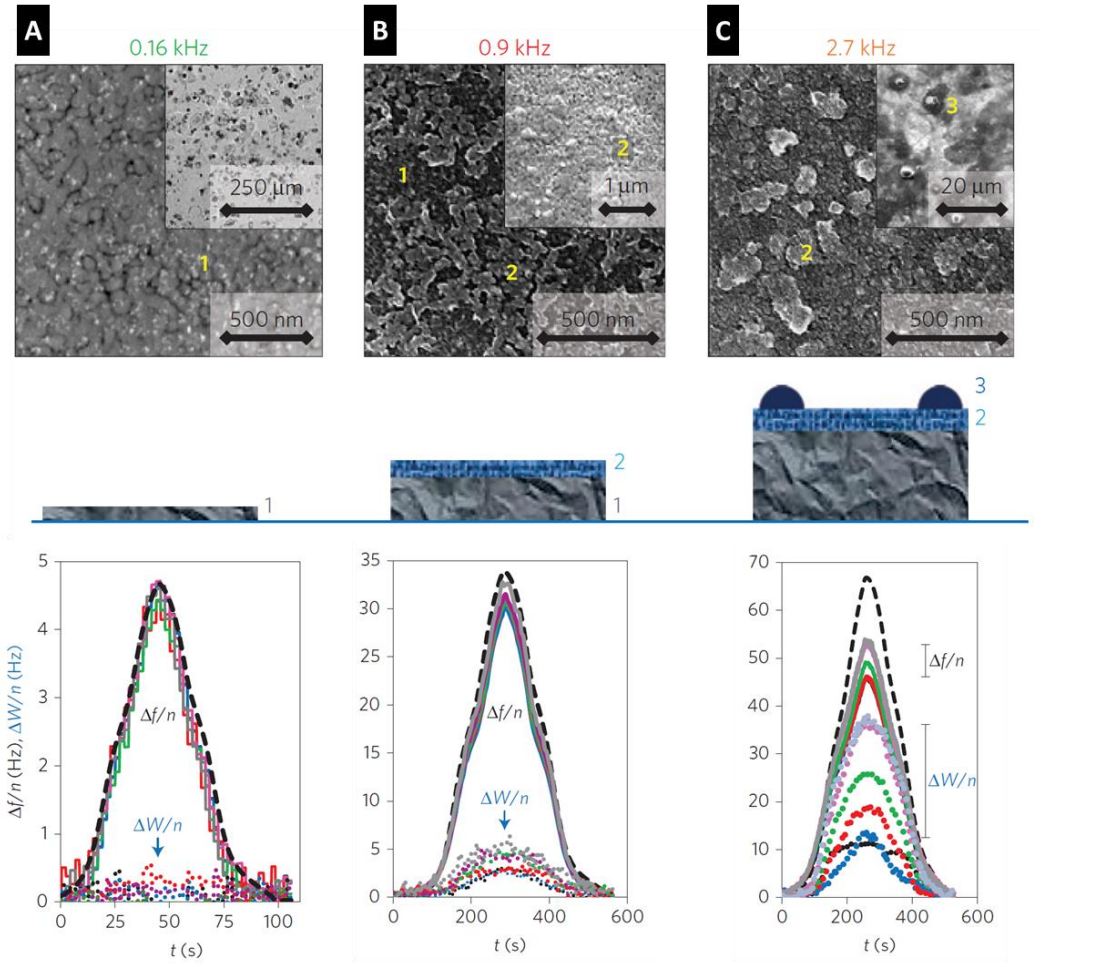

Figure 15. Three stages of loading of an EQCM with (A) a dense layer of active material, which is only gravimetric active and has no change in dW, (B) onset of hydrodynamic activity for higher loadings with a still fully electrochemical active electrode, and (C) creation of secondary structures, which are no longer electrochemical active (dead mass), with huge impact on the dissipation signal and dependency of the overtone number (reproduced from Ref. [168] with permission from Nature Publishing Group)

The hydrodynamic model is based on a combined mathematical approach with Darcy's law [170] and a special solution of the Navier-Stokes equation. [171] In general, the fitting parameters are the average thickness of the hydrodynamic active porous layer (h), the characteristic permeability length (ξ) which is linked to the porosity of the electrode layer, the crystal surface coverage (q), the average radius of the semi-spherical non-porous aggregates (r, secondary structure, see 3 in **Fig. 15C**), and the density. [168, 169]

The changes of resonance frequency (df(n)) and resonance width (dW(n)) as functions of the overtone number made a non-gravimetric measurement of the electrode behavior possible (**Fig. 15**): We conducted EQCM measurements with binder-free LMO particles attached via air-brushing on the gold-coated quartz-crystal. The measurements start with fully lithiated LMO and during one cycle with constant sweep rate the LMO is delithiated and fully lithiated again at the end (df=0). A calculated frequency shift according to the measured charge, meaning Li-ion extraction and insertion, is plotted with dashed black lines. Very thin layers with free space between the particles result in an exclusive gravimetric signal df and no measurable change in dissipation dW (**Fig. 15A**, 0.16kHz is indicating the change in resonance frequency after spray coating the LMO particles on the gold-coated crystal). For higher loadings, as soon as a dense layer of active material covers the surface the dissipation signal dW changes over time, which is the onset of a possible hydrodynamic spectroscopy measurement. Since the hydrodynamic layer is still quite small, the dissipation signal remains independent of n (**Fig. 15B**). Going to even thicker coatings will lead to the creation of dead mass, which is not electrochemically active. This shows the frequency shift which is for all n smaller than the expected shift (dashed black line). However, the dW signal is now highly dependent on n, and hydrodynamic spectroscopy can be applied (**Fig. 15C**). The dependency of the dW signal on n is related to the penetration depth of the shear wave trough the porous electrode. For low overtones, δ_n is large, and water in pores smaller than δ_n is trapped. The higher overtones have smaller δ_n values and for those dW is different since the water is no longer trapped but hydrodynamic active.

This new spectroscopy tool helped us to understand in situ the dependency of electrochemical behavior of battery materials on mechanical stability. [172] A further development was the implementation of surface acoustic waves and their influence on the mechanical rigidity of the attachment between active material and crystal surface to the model. [173] Using LFP as an intercalation-active material with either small particles (average size 300 nm) or larger particles in an aqueous electrolyte and a soft (sodium carboxymethylcellulose, NaCMC) or a rigid (polyvinylidene fluoride, PVdF) binder, the influence of particle size and binder rigidity was investigated, showing: (1) Small LFP particles in a rigid binder matrix (PVdF) yield exclusive hydrodynamic interaction; no measurable energy dissipation detected. (2) Small LFP particles in a soft binder matrix (NaCMC) shows viscoelastic effects, and shear storage and loss moduli can be fitted. It is also possible to get information about the effective electrode thickness, which

is important since NaCMC swells when getting in contact with water. [169] (3) Large particles slide over the surface, even with the rigid PVdF binder. [173] These results help to understand the ageing mechanisms based on binder properties of a composite battery electrode and led us to the combination of the new EQCM-D approach and eD (see *Ch. 4.6*). [137]

3. SCOPE

This dissertation is focused on the influence of structure and design of batteries and supercapacitors, which are electrochemical energy storage devices. In the first part, the electric double-layer capacitor devices are investigated with studies about the role of conductive additives (*Ch. 4.1*), the influence of pore size and ion size on the capacity (*Ch. 4.2+4.3*), the understanding of ion electrosorption in carbon nanopores (*Ch. 4.4*), and the influence of micropores on the volumetric expansion of carbon electrodes during cycling (*Ch. 4.5*) (**Fig. 16**).

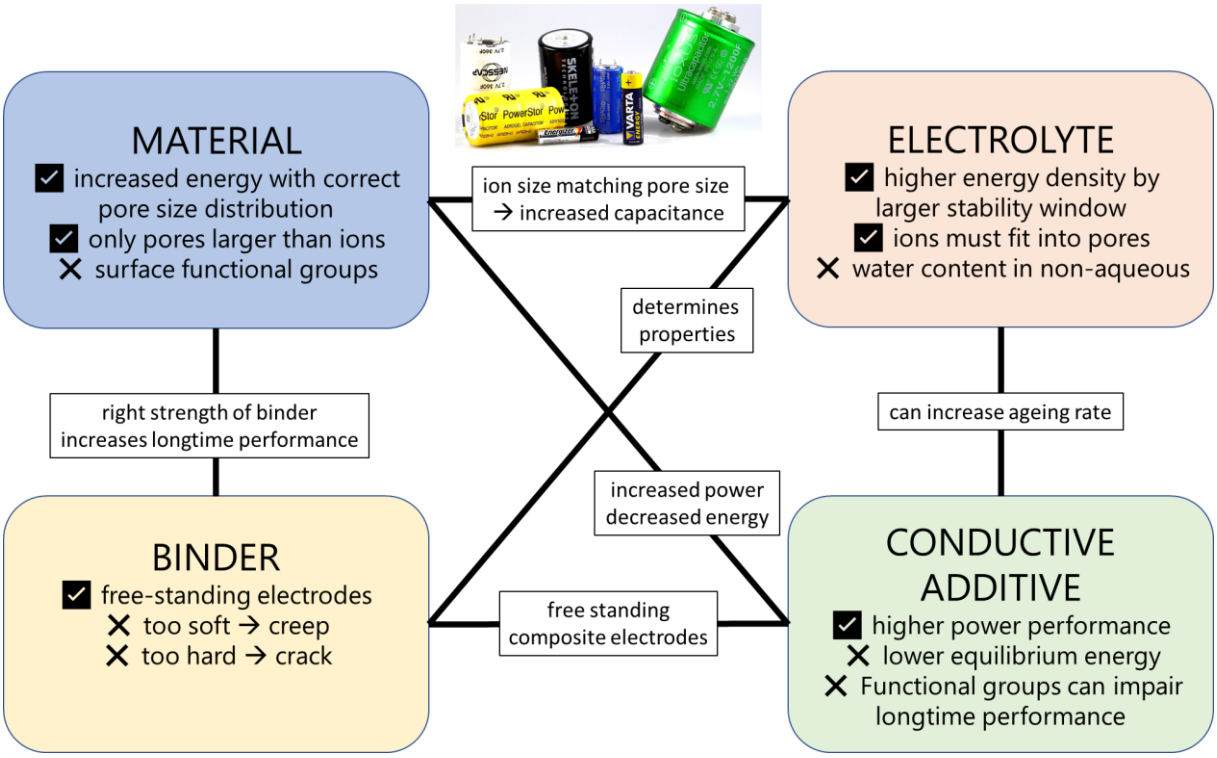

Figure 16. Influence of material, electrolyte, binder, and conductive additive on an electrochemical energy storage device and the conjunction between the parts on the performance of the device.

The performance of an EDLC attributes to three main factors: (1) The energy storage capacitance, which is measured in F/g or F/cm^3 with gravimetric and volumetric normalization respectively. [174] (2) The rate handling or power performance describes the ability of the system to be (dis-)charged with higher loads and the capacitance retention is measured versus the specific current/load. [175] (3) The long-time stability, which is measured either with cycling by charging and discharging at a specific load (often 1 A/g) through the whole potential window or voltage floating, where the potential is held at the maximum potential window for a certain time. The latter is a faster technique for EDLCs to gain information about ageing since the system is held at the maximum potential at which degradation reactions of the electrolyte or/and electrode material are most likely to occur. [176]

EDLCs often contain activated carbon (AC) with a high surface area as the active material. This ACs are highly activated, but the electrical conductivity is low in comparison to highly graphitized carbons like

carbon black. However, carbon black or other highly conductive carbons are still bad conductors in comparison to metals. Further, most highly carbon blacks suffer from a low specific surface area (SSA). Hence, the use of high conductive and low SSA carbons as conductive additive in the AC particles matrix is the best compromise for high energy density and good rate capability. [177-181] In this study (*Ch. 4.1*), we investigated two different ACs with either a micro or a micro-mesoporous pore size distribution and four conductive additive materials, all produced in industry. The addition of conductive additives at low rates decreases the capacitance due to the low SSA of the additive. However, an increase of 20% in capacitance can be achieved when using an optimized amount of conductive additives (between 2.5-5 mass%). [177, 179, 181] Regarding the long-time stability in our study, any conductive additive should be avoided. The performance for almost all kinds of additive in the AC electrodes was reduced, in the worst case more than 10 % less capacitance retention after 100 h floating compared to the bare AC electrodes. The explanation for the inferior long-time stability of mixed carbon electrodes is based on acidic and basic surface functional groups. Especially at the contact area of different surface groups the generation of water might be possible and water in general is highly critical for the stability of the electrolyte at an applied voltage. [120-123]

In the next chapter (*Ch. 4.2*), the focus is the maximization of energy storage capacity with non-aqueous electrolytes and the influence of pore size dispersity on the capacitance. The scientific controversy about the correlation between pore size and SSA normalized capacitance (F/m^2) with either the concept of an increase in capacitance if the pore size decreases [182] or the concept of a constant capacitance and an independency of the pore size [183] was the motivation for this work. In the first part a detailed discussion about the deconvolution of gas sorption data into pore size distributions (PSDs) and specific surface area (SSA) was done (see also *Ch. 2.3.1*). Both concepts could be reproduced with one single data set, depending on the normalization. An increase in capacitance was calculated when using the BET-SSA and a constant capacitance was calculated using the DFT-SSA. Both concepts only seemingly contradict each other; instead, the dispute is overcome when combining carbon dioxide adsorption data for micropores smaller than 1 nm with the PSD generated from nitrogen sorption for pores between 1-30 nm and considering the whole PSD, not an average value. Further, a pore size incremental analysis made the identification of specific ranges of pore widths for maximized energy storage possible. [33] These core results are presented in a Viewpoint publication (*Ch. 4.3*). [23] A comprehensive understanding of the correlation of pore size and capacitance is found when properly measuring the pore size distribution, considering the accessibility of finite ions into pores, and mark the pore size dispersity when using average values. [23] Finally, the surface-normalized capacitance is increasing when most of the pores are in the range of the bare ion size when the system is equilibrated at slow rates.

Until now, the research was focused on the measurement of carbon electrodes in different electrolytes with standard electrochemical test routines and the explanation of phenomena based on detailed

characterization of the materials. The following chapters are based on in situ measurements, where electrochemical cells were engineered to simultaneously measure structural changes during an electrochemical measurement. According to the type of measurement, a specific characteristic length scale is investigated, for example, the structural changes with XRD in a typical probing range of 0.05-50 nm or dilatometry (eD) with 20 nm-10 µm (**Fig. 17**). The combination of techniques with different length scales allows to quantify and understand the influence of microscopic changes in the macroscopic behavior.

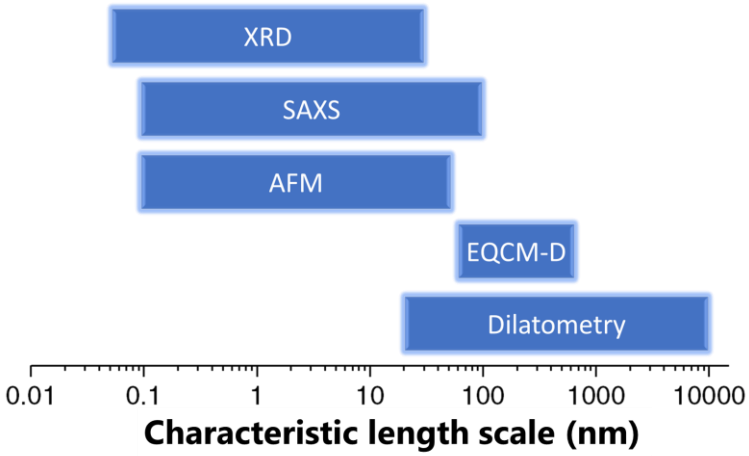

Figure 17. Different in situ measurement techniques and their characteristic length scale.

The first study with this approach is a combination of EQCM and eD to understand the mechanisms of electrosorption of ionic liquids in carbon nanopores (*Ch. 4.4*). [32] Combining both in situ methods, the correlation of the charging behavior on particle level (EQCM) and electrode level (eD) was possible. The study revealed the discriminative behavior of large ions over smaller ions at an applied voltage where more smaller ions are exchanged by fewer larger ions. Depending on the size ratio an increased surface charge can lead to a macroscopic volume increase or decrease. Moreover, at higher potentials, the electrosorption changes to a preferred adsorption of ions with the opposite charge than the surface charge due to depletion of ions with the same charge sign. Yet, a crowding of pores with ions of the same charge is breaking the electrical neutrality of the electrolyte because of the Coulombic repulsion of same charges ions. However, the break of Coulombic ordering of ionic liquids in nanopores was also confirmed by other publications. [184-186] Further, the interaction between micropore wall and IL ion is strong enough to change the coordination of the ions, as drawn in *Ch. 4.4*. [187-189] A similar behavior was found with different techniques for a solvent-containing organic electrolyte. [190, 191]

In the next chapter, we combine in situ SAXS with eD to understand the importance of micropores on the macroscopic swelling of carbons in an aqueous electrolyte (*Ch. 4.5*). After a successful introduction of in situ SAXS for tracking ion movement in highly diluted aqueous electrolytes [101] and for concentrated aqueous electrolytes in a supercapacitor system [98, 99] in activated carbons, the measurements were focused on ordered mesoporous carbons. [100] We used a hierarchical carbon with

ordered mesopores between the struts and a tunable amount of micropores inside the struts. Combining in situ SAXS with eD, we tracked the expansion and shrinkage on the nanometer scale of the electrode with the shift of the (10) peak in the SAXS signal and on the macroscopic scale with the displacement in eD. The measurements revealed an increased expansion and a more pronounced asymmetry in expansion with higher micropore volume. [192]

At this point of the thesis the investigation of a new class of layered materials, which is called MXenes, was done. [91, 193] Those pseudocapacitive materials are measured in ionic liquids. MXenes are based on ternary carbides in the MAX phase, where M is an early transition metal, A is an A-group element like aluminum, silicon, or tin, and X stands for carbide, nitrogen, or carbonitride. [194] The selective etching of A with a strong acid, usually hydrofluoric acid, results in a two-dimensional material with highly decorated surfaces and slight van-der Waals interaction between the layers. [195] This binder-free, free-standing, two-dimensional material with very high conductivity is an ideal specimen to correlate expansion on the structural level measured with XRD with bulk expansion measured with eD. [196] To avoid any influence of solvation we used two different ILs. The spontaneous wetting of MXenes with IL can be explained by the vast amount of negative surface functional groups on the surface of MXene and it has been proved that surface functional groups enhance the wetting with IL. [189] Those generate a driving force for ions to move between the layers. [93, 197-200] Mostly cations are inserted and extracted, depending on the applied potential. [93, 199, 200] This charging mechanism was recently confirmed by a molecular dynamics simulation using EMIM-TFSI as electrolyte. [201] Further, the enhanced MXene performance after cation intercalation was also confirmed in an aqueous electrolyte. [202]

In the last chapter, a commercial battery material is used with different binders in an aqueous electrolyte (*Ch. 4.7*). [137] After investigating the influence of conductive additives (*Ch. 4.1*), the role of the electrolyte and the material on the capacitance (*Ch. 4.2-4.5*), and the structural changes of MXenes after contact with an IL (*Ch. 4.6*), now the influence of binder on an intercalation material is focused. With the combination of eD and EQCM-D, the changes of the bulk electrode (eD) can be combined with knowledge from the particle size level (EQCM-D) for a stiff binder (PVdF) and a soft binder (NaCMC). The use of a battery material enhances the stress inside a composite matrix with a polymeric binder since the active material has an increase of about 6 vol% during lithiation. Furthermore, the first longtime eD measurement over several hundred cycles shows a direct influence of the binder properties on the ageing.

4. PAPER AND RESULTS

The following paper are part of this cumulative dissertation:

4.1 Performance Evaluation of Conductive Additives for Activated Carbon Supercapacitors in Organic Electrolyte

4.2 Anomalous or Regular Capacitance? The Influence of Pore Size Dispersity on Double-layer Formation

4.3 Increase in Capacitance by Subnanometer Pores in Carbon

4.4 Quantitative Information about Electrosorption of Ionic Liquids in Carbon Nanopores from Electrochemical Dilatometry and Quartz Crystal Microbalance Measurements

4.5 In Situ Measurement of Electrosorption-Induced Deformation Reveals the Importance of Micropores in Hierarchical Carbons

4.6 Electrochemical in Situ Tracking of Volumetric Changes in Two-Dimensional Metal Carbides (MXenes) in Ionic Liquids

4.7 In Situ Multi-Length Scale Approach to Understand the Mechanics of Soft and Rigid Binder in Composite Lithium Ion Battery Electrodes

4.1 Performance Evaluation of Conductive Additives for Activated Carbon Supercapacitors in Organic Electrolyte

N. Jäckel [a,b], D. Weingarth [a], A. Schreiber [a], B. Krüner [a,b], M. Zeiger [a,b], A. Tolosa [a,b], M. Aslan [a]

V. Presser [a,b]

[a] INM—Leibniz Institute for New Materials, Campus D2 2, 66123 Saarbrücken, Germany

[b] Department of Materials Science and Engineering, Saarland University, Campus D2 2, 66123 Saarbrücken, Germany

published in Electrochimica Acta. 2016. 191: p. 284-298

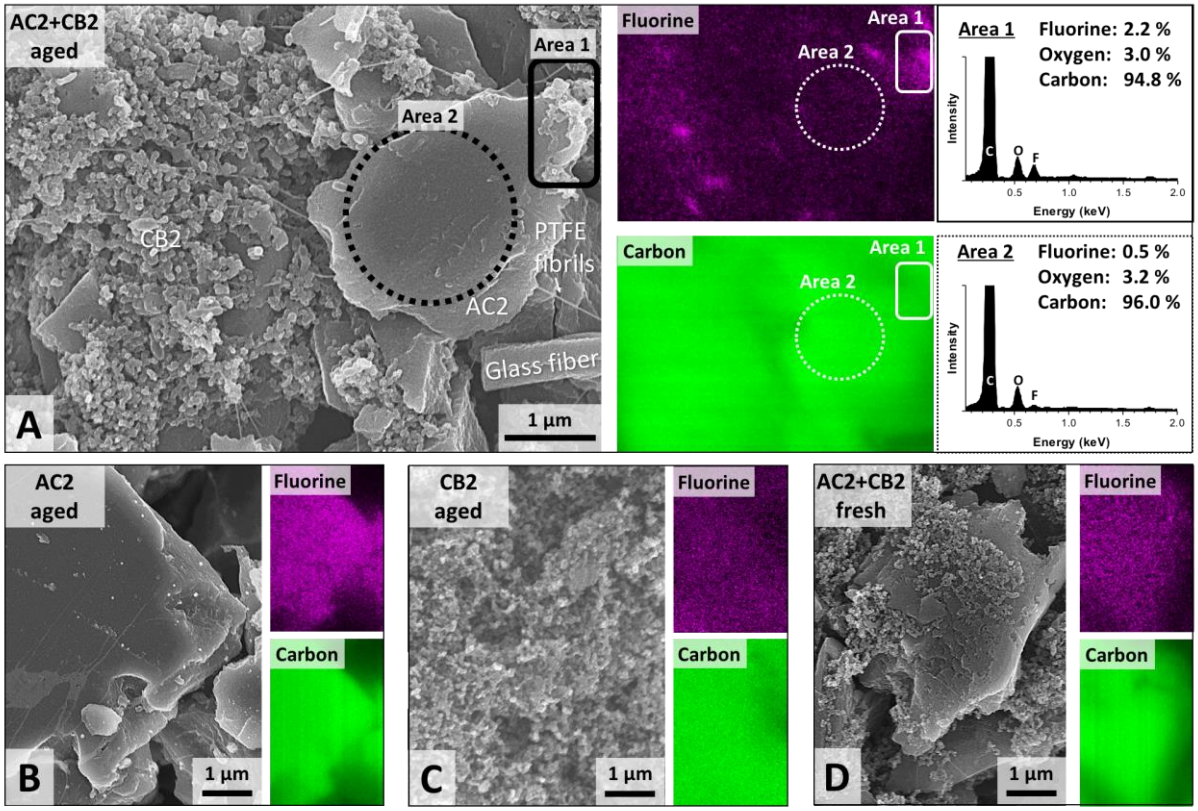

Own contribution:

Data generation 50 %

Data analysis 90 %

Interpretation 90 %

Writing 75 %

Electrochimica Acta 191 (2016) 284–298

Contents lists available at ScienceDirect

Electrochimica Acta

journal homepage: www.elsevier.com/locate/electacta

Performance evaluation of conductive additives for activated carbon supercapacitors in organic electrolyte

N. Jäckel[a,b,1], D. Weingarth[a], A. Schreiber[a], B. Krüner[a,b], M. Zeiger[a,b], A. Tolosa[a,b], M. Aslan[a], V. Presser[a,b,*]

[a] INM—Leibniz Institute for New Materials, Campus D2 2, 66123 Saarbrücken, Germany
[b] Department of Materials Science and Engineering, Saarland University, Campus D2 2, 66123 Saarbrücken, Germany

ARTICLE INFO

Article history:
Received 2 July 2015
Received in revised form 21 November 2015
Accepted 10 January 2016
Available online 16 January 2016

Keywords:
supercapacitor
conductive additive
activated carbon
rate capability
performance evaluation
long-time stability

ABSTRACT

In this study, we investigate two different activated carbons and four conductive additive materials, all produced in industrial scale from commercial suppliers. The two activated carbons differed in porosity: one with a narrow microporous pore size distribution, the other showed a broader micro-mesoporous pore structure. Electrochemical benchmarking was done in one molar tetraethylammonium tetrafluoroborate in acetonitrile. Comprehensive structural, chemical, and electrical characterization was carried out by varied techniques. This way, we correlate the electrochemical performance with composite electrode properties, such as surface area, pore volume, electrical conductivity, and mass loading for different admixtures of conductive additives to activated carbon. The electrochemical rate handling (from 0.1 A g^{-1} to 10 A g^{-1}) and long-time stability testing via voltage floating (100 h at 2.7 V cell voltage) show the influence of functional surface groups on carbon materials and the role of percolation of additive particles.

1. Introduction

Electrical double-layer capacitors (EDLCs, also known as supercapacitors or ultracapacitors) are energy storage devices with high efficiency and long lifetime durability [1–3]. Today, EDLCs are used in electric vehicles, energy recuperation modules, systems for uninterrupted power supply, or fast recharging energy modules for high-power applications [4]. In EDLCs, energy storage is accomplished via ion electrosorption in the electrical double-layer (EDL) at the electrically charged interface of high surface area carbon electrodes with an electrolyte, being typically aqueous or organic solvent based [5]. Supercapacitors excel in high power handling and longevity, but they show only a moderate energy density compared to lithium-ion batteries [6,7]. The electrochemical performance of supercapacitors is related to the pore structure and high values are obtained for high surface area materials, such as activated carbon (AC) [3,8,9]. In particular, carbons for supercapacitor application must show a well-developed porosity and pore size distribution, which have to be optimized for a certain electrolyte system with matching the ion size and pore size [10–14].

Supercapacitor electrodes require mechanical binding of carbon particles [9,15]. This is commonly accomplished by using polymeric binders. Dependent on the polymer, typically 5-15 mass % are needed to obtain film electrodes with sufficient mechanical integrity [4]. To overcome the intrinsically low electrical conductivity of such film electrodes, conductive additives like carbon black (CB) with a specific surface area (SSA) of typically below 100 $m^2 g^{-1}$ and average primary particle sizes of about or less than 50 nm are added [16,17]. There are also carbon additives with a high surface area, for example, some CBs show a SSA of ca. 1500 $m^2 g^{-1}$ while preserving a nanoscopic size of below 50 nm [4]. In addition to CB, also other materials have been explored as conductive additive, such as carbon nanotubes, graphite nanoparticles, or carbon onions [16–22]. Typically, the literature reports an optimum amount of conductive additive at around 5 mass% [16,19,20]. When we consider that most carbon powders with a high intrinsic electrical conductivity, especially those used as conductive additives, have a much smaller SSA compared to typical AC, we see that mixing results in a lower total surface area of the electrode and a lower equilibrium capacitance [18]. However, to enhance the power handling ability, admixing of conductive additives still is a very practical approach.

* Corresponding author.
E-mail address: volker.presser@leibniz-inm.de (V. Presser).
[1] ISE member.

http://dx.doi.org/10.1016/j.electacta.2016.01.065
0013-4686/

As shown previously, the admixture of conductive additives to an AC particle matrix does not always improve the electrochemical performance [18]. Especially at a low specific current, the decrease in total SSA by adding a low surface material to AC leads to a drop in gravimetric capacitance. Nevertheless, the electrical conductivity can be increased with an improved capacitance retention at high loads. Especially small additive particles with low tendency of forming aggregates are preferred because of the facile dispersibility and resulting distribution homogeneity within a composite electrode (i.e. lowering the percolation threshold) [17]. The optimal amount of conductive additive also depends on the target application and the electrolyte system. For example, in 1 M TEA-BF_4/ACN (TEA-BF_4 = tetraethylammonium tetrafluoroborate; ACN = acetonitrile), the optimum amount of additive was found to be 5 mass%, whereas in 1 M TEA-BF_4/PC (PC = propylene carbonate) the best performance was reached at 2.5 mass% admixture of conductive additives like high and low SSA carbon black and carbon onions [18].

Developing an improved supercapacitor with high power handling cannot be accomplished without addressing device lifespan. Typically, supercapacitors are assume to last over hundreds of thousands of charge and discharge cycles [2]. The actual lifespan strongly depends on the operation mode and temperature [13,23]. Device lifetime also concerns the selection of a suitable cell voltage window in which stable performance is possible [24]. Even when only operating within the electrochemical stability window, carbon electrodes will age over time [23]. In particular, the performance stability is challenged by electrochemical degradation of surface functional groups on the carbon surface, which can react with the electrolyte and decomposition products may cause pore blocking [25]. A suitable way of accelerated aging testing is voltage floating, which is in case of EDLC more adequate to reveal limitations to the cell operation compared to voltage cycling [23]. During floating testing, gas evolution can take place resulting from the decomposition of the electrolyte [24,26]. Compared to many AC materials, higher ordered materials such as CB tend to have a lower concentration of surface groups and a

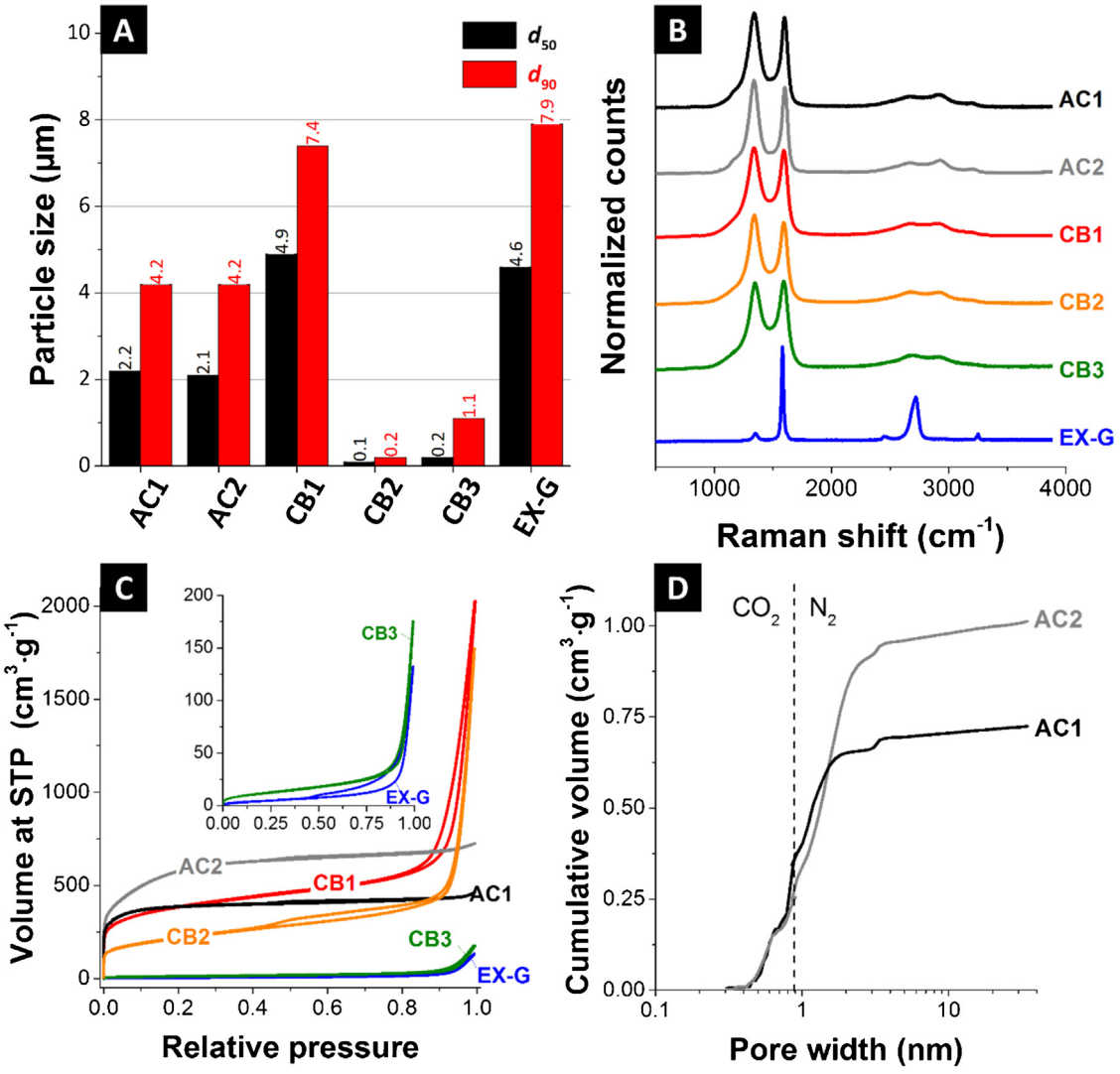

Fig. 1. (A) Particle size distribution of the used carbon materials, derived by centrifugal sedimentation analyses. (B) Raman pattern with increasing degree of ordering from upper to lower pattern. (C) Nitrogen sorption isotherms of the materials without binder (inset: zoom on CB3 and EX-G only; the inset has the same units on the axes as the main graph). (D) Pore volume distribution of the two activated carbons. Below 1 nm, the data is derived by carbon dioxide sorption measurements and above 1 nm from nitrogen sorption data.

higher affinity to yield better long-term stability [23,25]. Yet, the role of surface functionalities on the performance stability in composite film electrodes (i.e., AC plus conductive additive plus polymer binder) remains poorly understood.

This study provides a comprehensive comparison of four different conductive additives used for two kinds of activated carbon electrodes. Electrodes with up to 10 mass% of conductive additive were investigated by structural measurements like transmission electron microscopy (TEM), elemental analysis (EDX), streaming potential, and gas sorption analysis. The electrochemical performance was measured via rate capability in galvanostatic mode. Long-time stability tests were carried out over 100 h of voltage floating at 2.7 V.

2. Experimental description

2.1. Electrode materials and preparation

Two commercial steam-activated coconut-derived activated carbon powders (AC) were used, namely type YP-50F and YP-80F (Kuraray Chemicals Co., Japan), called AC1 and AC2, respectively. Different commercial conductive additives were used: high surface area carbon black BP2000 (Cabot, USA; called CB1), medium SSA carbon black Ensaco350 (CB2) and low surface area carbon black Super C65 (CB3). The latter two were provided by Imerys Graphite & Carbon, Switzerland. Another additive was an experimental expanded graphite (EX-G). The conductive additives were added to AC at an amount of 2.5 mass%, 5 mass%, and 10 mass% ("100%" with respect to the total carbon mass without binder).

For electrode preparation, a uniform distribution of AC and additive components was obtained by mixing the materials as an ethanolic slurry. For this, 1 g of carbon powder (i.e., activated carbon plus conductive additive) was dispersed in 20 mL ethanol. The slurry was sonicated for 15 min and then heated to 90 °C while stirring to evaporate the ethanol until the slurry became paste-like consistency. 5 mass% of dissolved polytetrafluoroethylene (PTFE, 60 mass% solution in water from Sigma Aldrich, USA) were added as binder (for electrodes only composed of conductive additive materials: 10 mass% PTFE). The resulting material was rolled with a rolling machine (MTI HR01, MTI Corp., USA) to a 200 ± 20 μm thick free standing film electrode and finally dried at 120 °C at 2 kPa for 24 h before use.

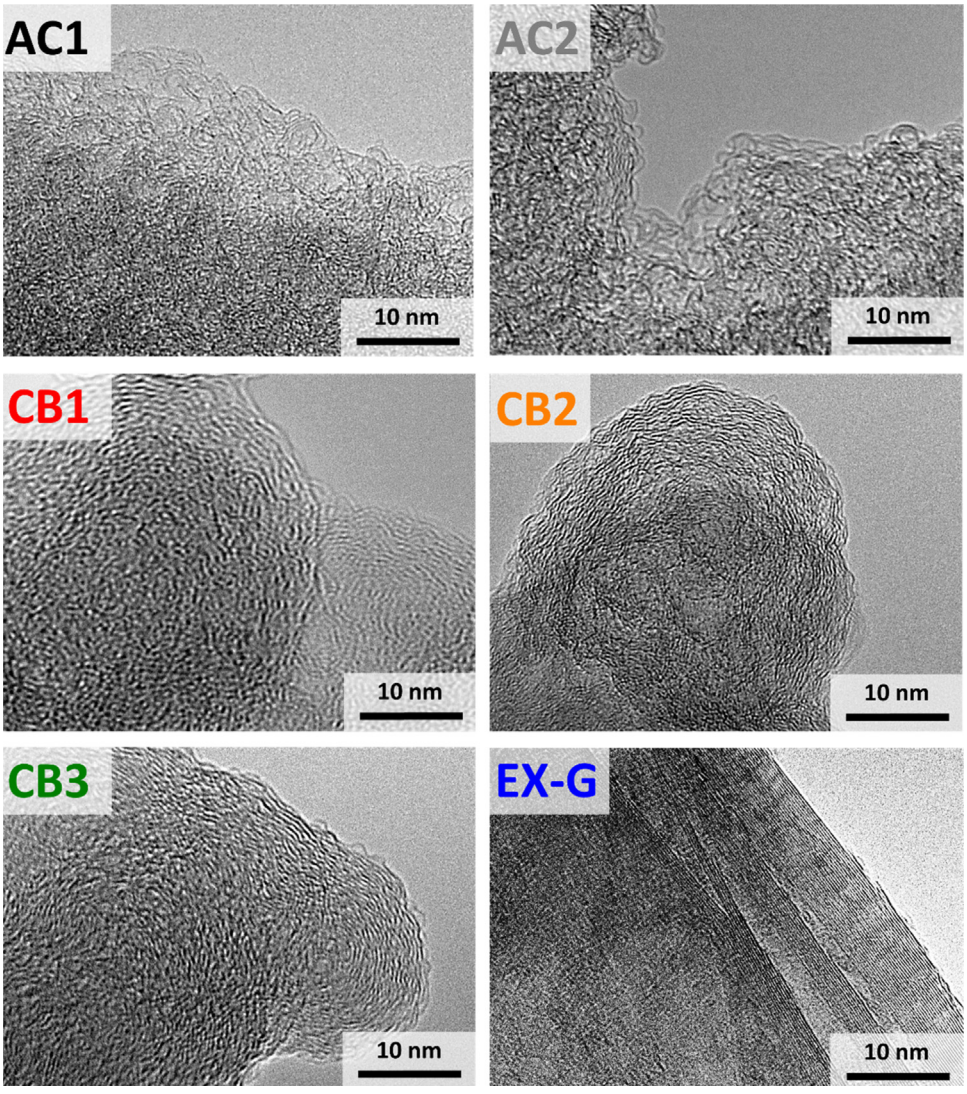

Fig. 2. TEM micrographs of the materials used in this study.

2.2. Cell preparation, electrical, and electrochemical measurements

Sheet resistance measurements were made with a custom-built spring-loaded four-point probe with blunt gold contacts (tip diameter: 1.5 mm, tip distance: 3 mm). For electrochemical testing, we employed a custom-built polyether ether ketone (PEEK) cell with spring loaded titanium pistons as a three electrode system described elsewhere [27]. Electrode discs (same mass and material for the working- and counter electrode) with 12 mm diameter and 200 ± 20 μm thickness were punched out of the free standing film electrode (total mass of carbon in a symmetrical cell was 20 ± 5 mg) and separated by a glass-fiber separator (GF/A from Whatman, USA) and placed on a carbon-coated aluminum foil current collector (type Zflo 2653 from Coveris Advanced Coatings, USA) [28,29]. The assembled cells were dried at 120 °C for 12 h at 2 kPa in an inert gas glove box (MBraun Labmaster 130, O_2 and $H_2O < 1$ ppm) and, after cooling to room temperature, vacuum-filled with 1 M tetraethylammonium tetrafluoroborate (TEA-BF_4) in electrochemical grade acetonitrile (ACN) purchased from BASF, Germany (i.e., water content <20 ppm).

Electrochemical measurements were carried out using a potentiostat/galvanostat VSP300 from Bio-Logic, France, with cyclic voltammetry (CV) and galvanostatic cycling with potential limitation (GCPL). CVs were recorded in full cell mode at 10 mV s^{-1} in the potential range from 0-2.5 V cell voltage. In GCPL mode, the specific current was increased in several steps from 0.1 A g^{-1} to 10 A g^{-1} with 10 s resting period between charging/discharging to access information on the IR-drop.

The gravimetric capacitance during discharging was calculated via Eq. (1):

$$C_{sp} = 4 \cdot \frac{\left(\int_{t_0}^{t_{end}} Idt\right)}{U} \cdot \frac{1}{m} \quad (1)$$

with specific capacitance C_{sp}, time t (t_0: starting time of discharge, t_{end}: end of discharging time), IR-drop corrected cell voltage U, and total mass of the electrodes m (i.e., considering carbon and the binder). For every type of electrode composition, four electrodes were prepared and these two cells were tested individually to calculate mean values. Long-time stability tests were made after rate capability test in galvanostatic mode at 2.7 V cell voltage for 100 h with measuring capacitive retention every 10 h at 1 A g^{-1} with cell potential 0-2.5 V.

2.3. Porosity analysis

Nitrogen gas sorption measurements were carried out with an Autosorb iQ system (Quantachrome, USA) at the temperature of liquid nitrogen (-196 °C) after outgasing (at 150 °C for 10 h for electrode samples and at 300 °C for 24 h for powder samples) at about 10^2 Pa. The relative pressure range was varied from $5\,10^{-7}$ to 1.0 in 68 steps. The specific surface area (SSA) was calculated with the ASiQwin-software using the Brunauer–Emmett–Teller (BET) equation [30] in the linear relative pressure range 0.01-0.2. We also calculated the SSA and pore size distribution (PSD) via quenched-solid density functional theory (QSDFT) with a slit model and pore size between 0.56 and 37.5 nm [31]. Values for the total pore volume correspond to $p/p_0 = 0.95$. Carbon dioxide gas sorption measurements were carried out at 0 °C in the relative pressure range from $1{\cdot}10^{-4}$ to $1{\cdot}10^{-2}$ in 40 steps. SSA and PSD values were calculated for pore sizes between 0.3 and 1 nm with the ASiQwin software using nonlocal density functional theory (NLDFT) for CO_2 sorption [32,33].

2.4. Effective density and particle size distribution analysis

The particle size distribution of carbon powders was measured using centrifugal sedimentation analysis (LUMiSizer from LUM GmbH, Germany). In a typical measurement, the powder was dispersed in ethanol (0.25 mg mL^{-1}), sonicated for 30 min, and measured at 200-4000 rpm. A dispersion in ethanol was chosen for comparability with the situation during actual electrode preparation (which involved ethanolic suspensions). The starting transmission for all samples was 25-60%. The d_{90} and d_{50} values denote the particle size in the cumulative particle size distribution encompassing 90 vol% and 50 vol%, respectively.

For measurements of the effective electrode density, an as-prepared 5×5 cm^2 sized film electrode was post-compacted with 1 kN cm^{-2} to ensure a constant compaction level and analyzed gravimetrically. The thickness after compaction was measured at four points with a micrometer caliper (Digi-Met from Helios-Preisser, Germany).

2.5. Structural characterization

Samples for transmission electron microscopy (TEM) were dispersed and sonicated in ethanol and placed on a copper grid with a thin lacey carbon film (Gatan Inc., USA). TEM images were recorded with a JEOL 2100F system at 200 kV in vacuum. EDX spectra of carbon powders were measured with a Thermo Fisher Scientific system placed in a JSM-7500F from JEOL, Japan. Carbon powder samples were placed on a conductive carbon tape and spectra were recorded at 50 different positions for each sample with 10 kV acceleration voltage. The composition of the composite electrodes was measured by energy dispersive X-ray spectroscopy (EDX) mapping using a X-Max-150 detector from Oxford Instruments attached to the SEM chamber. Using an accelerating voltage of 5 kV and an emission current of 10 μA, the mapping was measured and the average of 3 values were calculated. The aged (positive) electrodes were several times washed in neat acetonitrile to remove the salt from the electrolyte inside the glovebox. Afterwards they were dried in vacuum and put into the SEM chamber.

Raman spectra of the raw materials were recorded with a Renishaw inVia Raman system using an Nd-YAG laser (532 nm) with 0.2 mW power at the sample's surface. The spectral resolution of ca. 1.2 cm^{-1} corresponds to a grating with 2400 lines mm^{-1} and

Table 1
Raman data fitted with two Lorentzian peaks, one for the D-band and one for the G-band.

Material	D-mode position (cm^{-1})	G-mode position (cm^{-1})	FWHM D-mode (cm^{-1})	FWHM G-mode (cm^{-1})	Integral I_D/I_G ratio
AC1	1338	1596	140	65	2.2
AC2	1337	1599	161	76	2.1
CB1	1339	1589	212	100	2.1
CB2	1341	1589	145	78	2.0
CB3	1350	1588	173	89	1.8
EX-G	1350	1581	20	45	0.1

Table 2
Specific surface area of used powder materials. BET-SSA and QSDFT-SSA, pore volume and average pore size.

Material	BET SSA ($m^2 g^{-1}$)	QSDFT SSA ($m^2 g^{-1}$)	Pore volume ($cm^3 g^{-1}$)	Average pore size (nm)
AC1	1681	1560	0.78	0.9
AC2	2347	1756	1.15	1.6
CB1	1389	1272	1.92	19
CB2	770	715	0.77	14
CB3	65	56	0.15	27
EX-G	20	21	0.10	46

Table 3
Chemical analysis via EDX shows the different amount of carbon and oxygen in powder samples.

Material	Carbon (atom%)	Oxygen (atom%)
AC1	97.4 ± 0.5	2.4 ± 0.5
AC2	97.8 ± 0.5	2.0 ± 0.5
CB1	98.1 ± 0.1	1.3 ± 0.1
CB2	97.9 ± 0.1	1.9 ± 0.1
CB3	98.9 ± 0.1	0.9 ± 0.1
EX-G	98.8 ± 0.6	1.0 ± 0.5

the spot size on the sample was in the focal plane ca. 2 μm (numeric aperture = 0.9). The acquisition time was 30 s and 50 accumulations were recorded. Peak analysis and peak fitting were performed assuming one Lorentzian peak for each the D-mode and the G-mode.

Streaming potential measurements were made in a Mütek PCD (BTG Eclépens, Switzerland) with 100 mg carbon powder dissolved in 30 mL DI water. Suspensions were first sonicated for 10 min, followed by a homogenization step of 48 h on a moving table. Prior to the experiment, the starting pH value was set to 9.5 with aqueous 50 mM NaOH solution, which was corrected after another 10 h homogenization on a moving table. For each measurement 20 mL suspension was titrated to an end pH value of 3 by using 50 mM HCl.

3. Results and discussion

3.1. Structure, porosity, and chemistry of the powder materials

Particle size analysis of the carbon materials is a first important characterization method. We chose two common commercial-grade steam-activated coconut-derived carbons with anisomeric shape [18] and typical agglomerate size of several micrometers ($d_{50} \approx 2$ μm, $d_{90} \approx 4$ μm; Fig. 1). This is a typical value for AC materials used for supercapacitor electrodes [34]. The high SSA carbon black CB1 showed aggregates and particle clusters in the range of 1-10 μm ($d_{50} = 4.9$ μm, $d_{90} = 7.4$ μm), whereas these values are in contrast to the much smaller primary particle size in the range of 20-50 nm seen in the TEM images (Fig. 2). CB2 shows no cluster formation ($d_{50} = 0.1$ μm, $d_{90} = 0.2$ μm) and CB3 forms much smaller clusters below 1 μm ($d_{50} = 0.2$ μm, $d_{90} = 1.1$ μm) even if the primary particle size is about 100 nm, according to TEM (Fig. 2). The flake size of EX-G is in the micrometer range ($d_{50} = 4.6$ μm, $d_{90} = 7.9$ μm).

The materials also differ in the degree of carbon ordering, as evident from Raman analysis (Fig. 1B) and TEM micrographs (Fig. 2). Raman spectra are characterized by the D-mode between 1337 and 1350 cm^{-1} and the G-mode between 1581 and 1599 cm^{-1}. The G-mode is related to the bond stretching of sp^2-hybridized carbon atoms in rings and chains according to the zone center E_{2g} mode [35]. The double-resonant D-mode, or "disordered" mode, arises due to the breathing of six-fold rings, but is only Raman active in the presence of defects, such as related to curvature, edges, heteroatoms, or vacancies [36]. The graphite flakes (EX-G) demonstrate the Raman spectrum of nearly ideal graphite with a G-mode at 1581 cm^{-1}, sharp peaks, and a very small D-mode, resulting in an integral intensity ratio I_D/I_G of 0.1 (Table 1). The G-mode position varies between 1588 and 1589 cm^{-1} for the different carbon blacks used in this study (CB1-CB3). Compared to ideal graphite, this value is slightly shifted to larger values, but still lower compared to nanocrystalline graphite at ~1600 cm^{-1} [37]. This indicates the existence of nanocrystalline domains in the material combined with an amorphous carbon phase. The presence of an amorphous carbon phase is supported by the broad transition between the D- and G-mode, leading to a broad signal at ~1520 cm^{-1}. The existence of nanocrystalline carbon is demonstrated by the large I_D/I_G areal intensity ratios with similar values between 1.8 for CB3 and 2.1 for CB1 [37]. TEM shows small parts with a nanocrystalline nature for CB2 and CB3, whereas CB1 is mostly characterized by disordered carbon and only few crystalline areas (Fig. 2). The Raman spectra for the two activated carbons (AC1 and AC2) present a similar I_D/I_G ratio of 2.1 and 2.2, indicative for nanocrystalline carbon [37]. The nanocrystalline nature of the materials is also shown by TEM, with small crystalline parts connected by disordered carbon, which is in agreement with literature [38].

Using Raman spectroscopy and TEM, we can assign the highest degree of carbon ordering to EX-G [35]. Among the carbon blacks, CB1 presents the lowest degree of carbon ordering with distinct bond-length variation and distortion. Both AC materials show a distinct nanocrystalline nature indicated by a G-mode slightly smaller than 1600 cm^{-1} (nanocrystalline carbon), but smaller FWHMs of the G-mode than CB. Thus, both activated carbons present a higher degree of carbon ordering than the carbon blacks but lower than exfoliated graphite (EX-G).

The nitrogen sorption isotherms show a characteristic type I(a) shape for AC1 and type I(b) for AC2, which is related to microporous materials with pores smaller than 1 nm or 2.5 nm, respectively [39], with BET-SSA of 1681 $m^2 g^{-1}$ (QSDFT-SSA 1560 $m^2 g^{-1}$) for AC1 powder and a larger surface area for AC2 with BET-SSA of 2347 $m^2 g^{-1}$ (QSDFT-SSA 1756 $m^2 g^{-1}$). CB1 and CB2 display a mixture of type I(b) isotherm, related to the internal microporosity, and type IV(b) isotherm (mesopores) with a slight H4 hysteresis indicative of a predominantly microporous and mesoporous material and QSDFT-SSA of 1272 $m^2 g^{-1}$ and 715 $m^2 g^{-1}$, respectively (Fig. 1C) [39]. The isotherms of CB3 and EX-G are characteristic for non-porous carbons with very low SSA of less than 100 $m^2 g^{-1}$ (Fig. 1C and Table 2) with a type II shape and a H3 hysteresis. The very high nitrogen adsorption of CB1 with a specific pore volume of 1.92 $cm^3 g^{-1}$ is related to its high internal porosity and the large

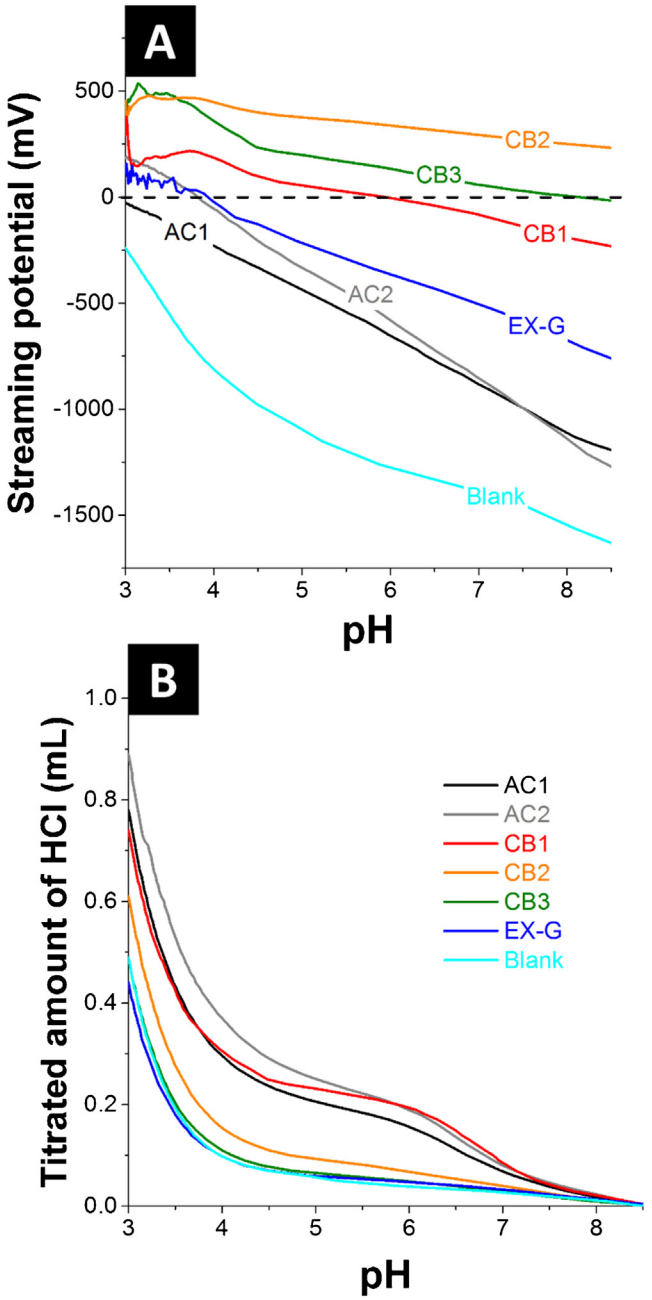

Fig. 3. (A) Streaming potential of all used carbons in pH range from 9.5 to 3 with isoelectric point at potential zero and (B) amount of needed HCl solution to set the pH value.

amount of interparticle voids due to the primary particle size of about 50 nm, as shown by TEM (Fig. 2). The same effect can be seen for CB2. The primarily microporous AC samples show the same amount of (ultra) micropores, as seen from CO_2 sorption data (Fig. 1D), but AC2 has much more micro-mesopores in the range of 1.5-5 nm in contrast to AC1. As shown in Table 2, this is a result of the higher total SSA and a much higher pore volume (1.15 $cm^3 g^{-1}$) of AC2 (1756 $m^2 g^{-1}$ QSDFT-SSA) versus AC1 (1560 $m^2 g^{-1}$ QSDFT-SSA, 0.78 $cm^3 g^{-1}$).

EDX measurements confirm the presence of oxygen, as seen from the data shown in Table 3. Two groups of materials are distinct with respect to oxygen content, namely very pure carbons like CB3 and EX-G with more than 98 atom% carbon, and the other samples with higher amount of oxygen. Oxygen in carbon materials is mainly resulting from the oxygen containing surface groups. The nature of the latter can be investigated by streaming potential measurements. One can see a high amount of acidic groups (carboxylic, lactonic, and phenolic) on AC1, AC2, and EX-G, indicated by the negative potential in the measured pH range from 8.5 to 3 and an isoelectric point below 4 (Fig. 3A and B). These acidic groups are protonated at low pH values (pH 3-5) and loose a proton by increasing the pH to neutral and basic regimes, resulting in a negative surface charge of the carbon [40]. The data for CB1 show the smallest variation in potential values ranging from +250 mV to -250 mV in the measured pH range and an isoelectrical point at neutral pH 6 (Fig. 3A). The high SSA carbons AC1, AC2, and CB1 have also the highest HCl uptake to decrease the pH value from 8.5 to 3 in contrast to the low SSA carbons CB3 and EX-G, which are very close to the uptake of the blank probe (Fig. 3B). The total amount of surface groups seems to be related to the total SSA of the material (Table 2) [41]. The streaming potentials of CB2 and CB3 have an isoelectrical point at pH 8.5 or higher and the values gradually increase to about 500 mV at pH 3 (Fig. 3A). The positive streaming potential in the acidic range ($pH < 7$) is indicative for alkali groups like carbonyl groups and these groups accept another proton in acidic regime. The settle point at ~pH 6 in Fig. 3B is related to the neutralization of NaOH with HCl.

3.2. Density, electrical conductivity, and pore size analysis of electrodes

The effective film electrode density was determined for 5 mass% PTFE-bound electrodes after compaction (Fig. 4A and C). Without any conductive additive, the density of free standing AC electrodes differs greatly: 629 ± 4 mg cm^{-3} for AC1 and 439 ± 7 mg cm^{-3} for AC2. The major difference in density is related to the much higher pore volume of AC2 in contrast to AC1 (Table 2). The electrode density remains constant when admixing CB3 or EX-G to AC1 in the range of 624-639 mg cm^{-3} (Fig. 1A). For admixture of CB1, the electrode film density decreases by 5-10% to values of 569-601 mg cm^{-3} since CB1 forms big agglomerates and the filling of void volume does not occur. The electrode density increases in case of CB2 to 710 mg cm^{-3} for 10 mass% CB2 in AC1 (Fig. 4A). This increase might be related to a unique fitting of CB2 particles in AC1 interparticle voids, supported by the absence of agglomerate formation in ethanol by centrifugation analysis (Fig. 1A); by this virtue, CB2 can effectively fill the void volume between the AC particles in contrast to all other additive particles. For AC2 and any admixture of conductive additives, the electrode density remains fairly constant with values from 425 mg cm^{-3} to 447 mg cm^{-3} (Fig. 4C).

The electrical sheet resistance (Fig. 4B and D) can be significantly improved when admixing a conductive additive to AC film electrodes (AC1: $11.4 \pm 1\ \Omega$ cm, AC2: $9.0 \pm 0.5\ \Omega$ cm). Compared to AC electrode films, electrodes composed only of the conductive additive (with 10 mass% PTFE) show a much lower electrical resistance of 0.3–0.9 Ω cm (Fig. 4B and D, 100%). All conductive additives show a comparable trend of reduced resistance with increased loading with conductive additive. For quite all additives, there is a drop in sheet resistance of 25-35% with 2.5 mass% additive content. This can be explained by high intrinsic conductivity of the additives and by a larger number of particle-particle-contacts, resulting in a higher carbon-carbon contact area. Especially, CB2 admixture to AC1 at 2.5 mass% additive content strongly reduces the sheet resistance from $11.4 \pm 1\ \Omega$ cm (constituent AC1) to $3.1 \pm 0.3\ \Omega$ cm with a 5%

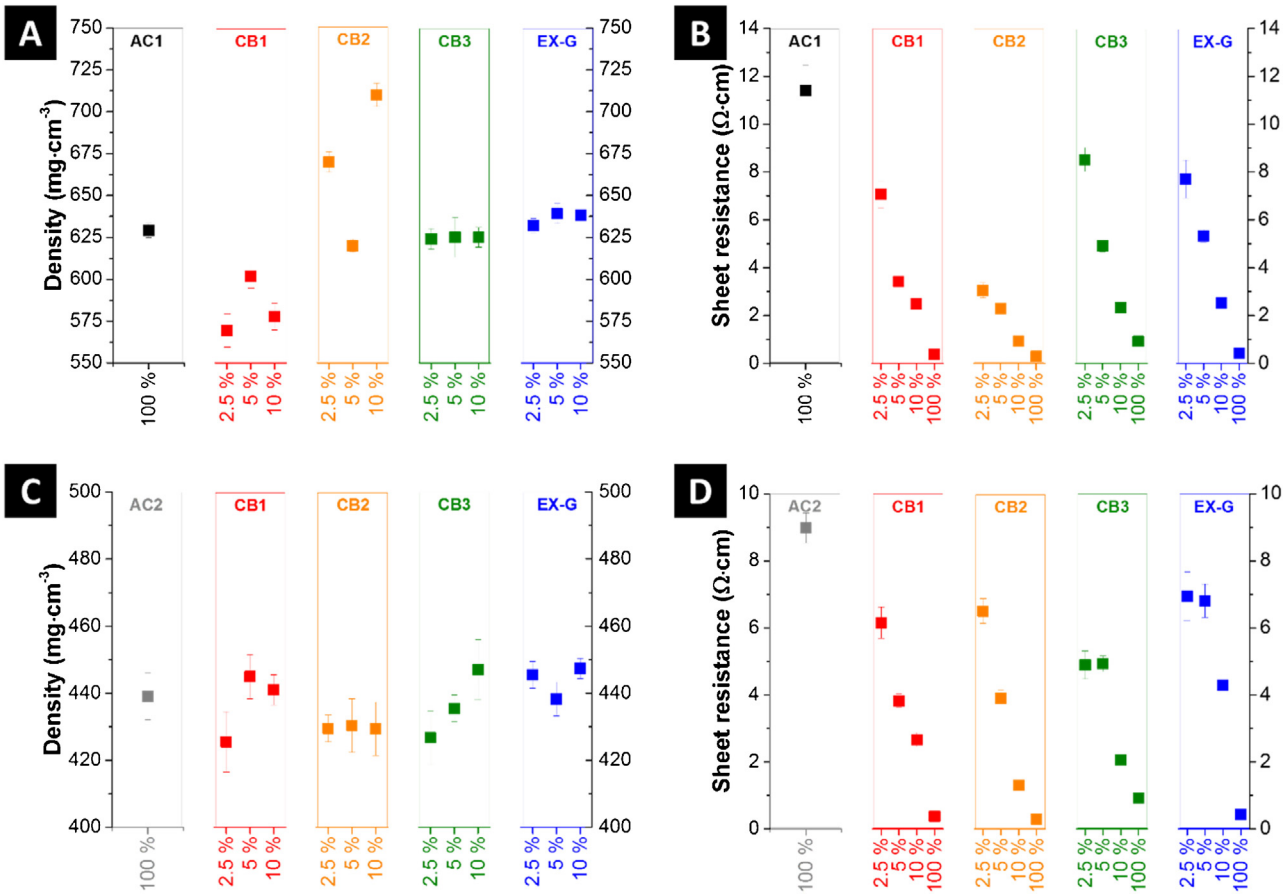

Fig. 4. Density of PTFE-bound composite electrodes with conductive additive admixture in (A) AC1 matrix and (C) AC2 matrix. Sheet resistance of the used composite electrodes with (B) AC2 and (D) AC1. The amount of additive admixture is displayed with the numbers on the *x*-axis. "100%" for AC1 and AC2 refers to the sample with constituent activated carbon (i.e., no conductive additive).

Table 4
Specific surface area of electrodes (BET-SSA and QSDFT-SSA), pore volume and average pore size of all used materials and composites. All values in percent are related to mass-percent. The average pore size denotes the volume-weighed pore size average.

Material	BET SSA ($m^2 g^{-1}$)	QSDFT SSA ($m^2 g^{-1}$)	Pore volume ($cm^3 g^{-1}$)	Average pore size (nm)
AC1 + 5% PTFE	1481	1320	0.67	0.8
AC1 + 2.5% CB1 + 5% PTFE	1392	1302	0.64	1.6
AC1 + 5.0% CB1 + 5% PTFE	1422	1357	0.69	1.0
AC1 + 10% CB1 + 5% PTFE	1403	1357	0.74	1.2
AC1 + 2.5% CB2 + 5% PTFE	1374	1321	0.61	0.9
AC1 + 5.0% CB2 + 5% PTFE	1342	1308	0.64	1.0
AC1 + 10% CB2 + 5% PTFE	1100	1085	0.53	1.0
AC1 + 2.5% CB3 + 5% PTFE	1432	1281	0.71	0.9
AC1 + 5.0% CB3 + 5% PTFE	1355	1356	0.64	0.9
AC1 + 10% CB3 + 5% PTFE	1287	1260	0.61	0.9
AC1 + 2.5% EX-G + 5% PTFE	1445	1317	0.68	0.9
AC1 + 5.0% EX-G + 5% PTFE	1408	1298	0.65	0.9
AC1 + 10% EX-G + 5% PTFE	1277	1300	0.62	0.9
AC2 + 5% PTFE	2105	1672	1.01	1.6
AC2 + 2.5% CB1 + 5% PTFE	1864	1496	0.90	1.6
AC2 + 5.0% CB1 + 5% PTFE	1940	1522	0.98	1.8
AC2 + 10% CB1 + 5% PTFE	1987	1587	1.00	2.0
AC2 + 2.5% CB2 + 5% PTFE	1948	1565	0.98	1.4
AC2 + 5.0% CB2 + 5% PTFE	1912	1496	0.96	1.4
AC2 + 10% CB2 + 5% PTFE	1881	1531	0.94	1.4
AC2 + 2.5% CB3 + 5% PTFE	1962	1506	1.03	1.4
AC2 + 5.0% CB3 + 5% PTFE	1924	1493	1.01	1.4
AC2 + 10% CB3 + 5% PTFE	1773	1363	0.94	1.5
AC2 + 2.5% EX-G + 5% PTFE	1808	1435	0.88	1.3
AC2 + 5.0% EX-G + 5% PTFE	1803	1429	0.91	1.3
AC2 + 10% EX-G + 5% PTFE	1606	1253	0.79	1.4

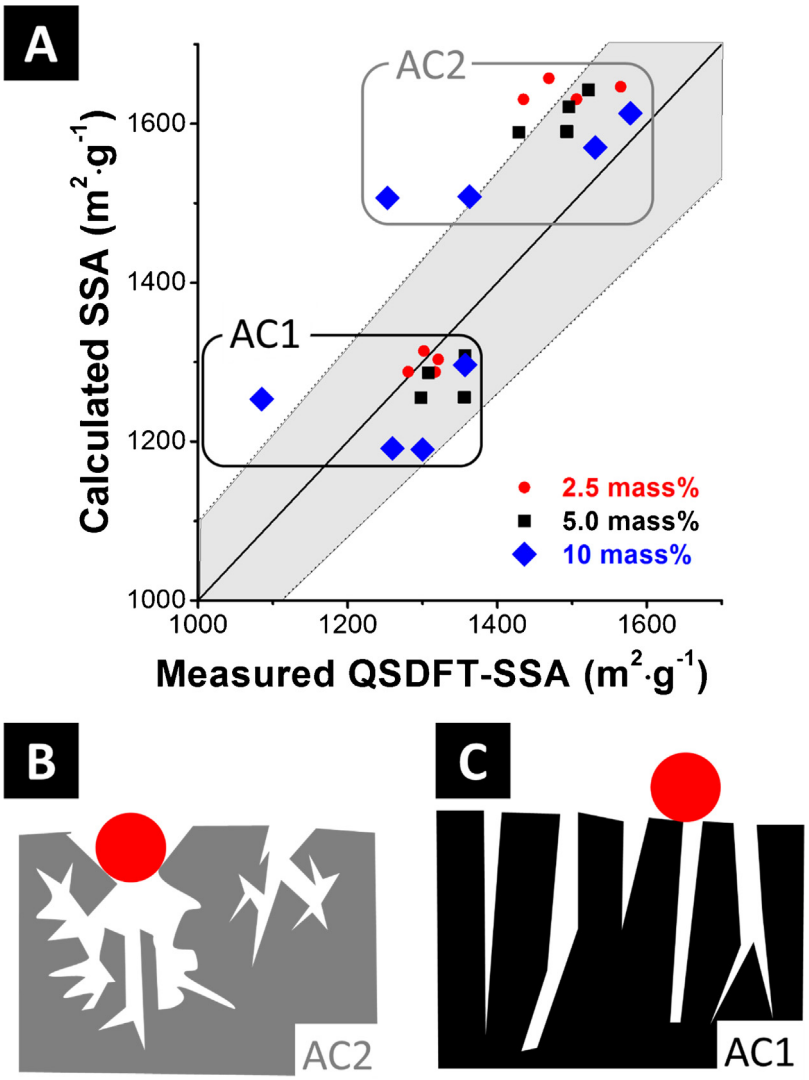

Fig. 5. (A) Parity plot of all composite electrodes with measured QSDFT-SSA versus calculated SSA, which is linear addition of constituent SSA measurements. (B) Scheme of the hierarchical pore size distribution of AC2 with an additive particle blocking the entrance to smaller pores. (C) Scheme of the slit-like pores of AC1, whereas the pore blocking does not diminish the total SSA of the composite.

increase in electrode density. This supports the statement with a unique fitting of CB2 within the AC1 particle matrix. The percolation of additive particles in AC seems to depend strongly on the structure of particle shape and interparticle voids of AC and the agglomerate size of the used additive.

The presence of polymer binder in composite electrodes impacts on the ion-accessible surface area and pore volume [42]. The QSDFT-SSA values are significantly lower for film electrodes containing 5 mass% PTFE compared to the QSDFT-SSA of the powders without binder with a decrease of 5-18% (Tables 2 and 4). This effect is caused by pore blocking [43], but also the mere presence of binder, which basically is dead mass with a surface area of less than 5 $m^2 \cdot g^{-1}$ (see Ref [42]). Roughly, we can attribute a 5% decrease in QSDFT-SSA just due to the presence of 5 mass% of polymer binder without additionally considering pore blocking.

The pore blocking effect by PTFE and the influence of conductive additive particles on the total SSA of the electrodes was calculated by assuming a mechanical rule-of-mixture (Fig. 5). This enables us to plot calculated values for an ideal mechanical mixture via linear addition of constituent carbon electrodes calculated values (e.g., 0.95·AC1-SSA + 0.05·CB1-SSA = calculated value of AC1 + 5% CB1) versus the experimentally measured SSA of the electrodes for different amounts of conductive additive admixture (data also provided in Table 4). As seen from Fig. 5, most of the values fall within a ±10% error margin (grey box) compared to the ideal case (parity line = solid line) what is an average error supposed on nitrogen sorption derived data. The outliers are all related to AC with admixture of EX-G. The inhomogeneous distribution is related to the large flake size (Fig. 1A) and the low amount of tested electrode film (approx. 10 mg) as well as the very different SSA of AC and EX-G can explain the larger difference between calculated value and measured sample. Nevertheless, in case of AC1 many points remain below the parity line (measured SSA is larger than calculated SSA) in contrast to the points of AC2 which are mostly above the parity line (measured SSA is smaller than calculated SSA). A smaller measured SSA than calculated can be explained with pore blocking. For AC2 with a wider pore size distribution and

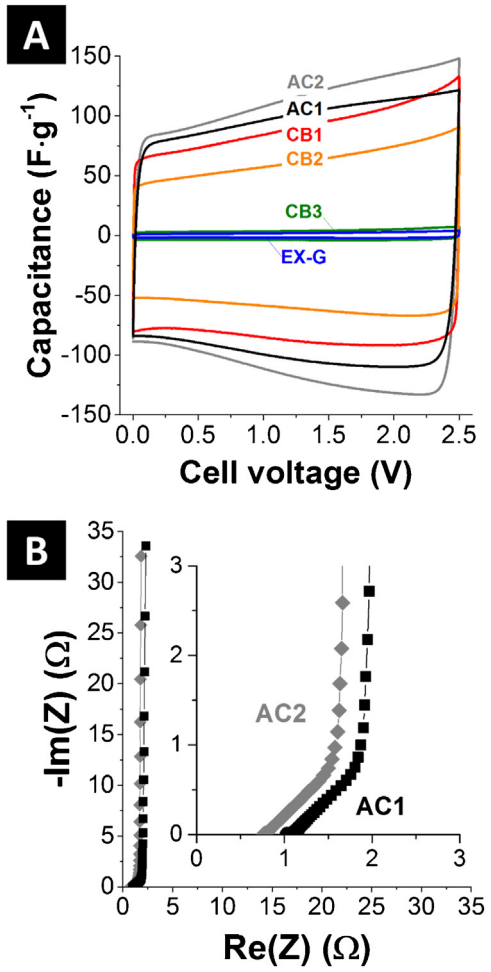

Fig. 6. (A) CVs of constituent carbon electrodes at 10 mV s^{-1} in 1 M TEA-BF_4/ACN. (B) Nyquist plot of electrical impedance spectroscopy with two activated carbon electrodes in 1 M TEA-BF_4/ACN. Inset shows the enlarged plot at low resistance.

more hierarchical pores the additive particles can block the entrance to several smaller pores and a lot of surface of the AC particle is no longer available (Fig. 5B). Since AC1 has only long, uniform and slit-like pores the pore blocking also occurs but there is only a very small amount of SSA blocked by the additive particle and the total SSA of the composite electrode is not diminished (Fig. 5C).

3.3. Electrochemical behavior and rate capability

Cyclic voltammetry (CV) in symmetrical full cells was carried out first on all constituents, without mixing AC and conductive additives. The measured CVs show all a rectangular shape at low scan rates (10 mV s^{-1}) in 1 M TEA-BF_4/ACN (Fig. 6A). Both AC materials yield a more pronounced resistive behavior compared to electrodes only composed of conductive additive, as seen by the presence of a resistive knee in the CVs. The characteristic increase in current at higher voltage, resulting in the so-called "butterfly" shape and an increase in differential capacitance, is a result of the increase in density of states (DOS) [27,44,45]. The electrical impedance spectra show a similar behavior of both ACs, whereas the slightly higher degree of carbon ordering of AC2 (I_D/I_G ratio = 2.1) results in a lower electrical series resistance (ESR) [2] compared to AC1. In addition, both ACs show roughly the same EDR (equivalent distributed resistance) [2]. which is particularly characteristic in predominately microporous carbon materials where electrolyte ion penetration becomes a limiting factor [22]. As shown in Fig. 1D, the (ultra) micropore structure is equal for both ACs and this results in equal EDR values. Moreover, both curves end up at the same resistance what is related to an equal thickness of electrodes (Fig. 6B).

As a next step, we investigated the electrochemical performance when admixing discrete amounts of conductive additive (i.e., 2.5, 5.0, and 10 mass%) to both AC materials. Four different conductive additive are added to the two activated carbons (Fig. 7). The rate capability was evaluated by GCPL from 0.1 A g^{-1} to 10 A g^{-1} and the performances at these two specific currents are shown in Fig. 7. The data shows that AC1 and AC2 exhibit a clear trend at low specific current of 0.1 A g^{-1}: adding any amount of any of the investigated conductive additives causes a decrease in specific capacitance (Fig. 7A and C). This is related to the effective reduction in total pore volume of the film electrodes when mixing high surface area AC with conductive additives having a lower porosity. When only using activated carbon, the film electrodes yield at lowest specific current a specific capacitance of 104 F g^{-1} (AC1) or 112 F g^{-1} (AC2), in agreement with the higher surface area of the latter. The general trend is that higher amounts of admixture reduce the specific capacitance even further whereas the decrease in specific capacitance is more significant for AC2 compared to AC1.

The situation changes at a high specific current of 10 A g^{-1} (Fig. 7B and D). As a baseline, AC1 without any additive yields a specific capacitance of 71 F g^{-1} and AC2 of 81 F g^{-1}. The lower relative loss in capacitance compared to the low specific current performance for AC2 (i.e., -32%,) is related to the lower sheet resistance conductivity (9.0 Ω cm) in comparison with AC1 (71 F g^{-1}; i.e., −28%, 11.4 Ω cm, I_D/I_G = 2.2). In contrast, composite electrodes containing additives can deliver up to 87 F g^{-1} in case of 2.5% CB2 admixture (Fig. 7B).

From these data, two general conclusions can be drawn: (1) A capacitance drop of 4–10% at 0.1 A g^{-1} appears by comparison of constituent AC electrode with conductive additive composite electrodes (Fig. 7A and C) and (2) the smallest capacitance loss for composite electrodes occurs only with certain admixture of conductive additive at high loads. Thus, conductive additives are only useful at high specific currents (Fig. 7B and D). This fact has also been shown for onion-like carbon (OLC) or graphene-based additives [18,46].

The equilibration time until the final state of ion (re) distribution within the pore network of micrometer-sized AC particles pores is rather long at low specific current [47]; this process is much faster in nanometer-sized porous carbons [48] or non-porous [49] nanoparticles where double-layer formation occurs only on the outer surface. For better comparability, the specific capacitance of either AC1 or AC2 at either 0.1 A g^{-1} or 10 A g^{-1} has been set to zero in Fig. 8 and only the deviation ΔC in% of the constituent AC electrode performance is shown. This way, it is easier to see if adding a conductive additive increases or decreases the specific capacitance. When comparing the performance of just AC1 or AC2 with electrodes containing conductive additive admixtures, one can see a decrease of 2-17% of the specific capacitance at 0.1 A g^{-1} (Fig. 8A and C). Especially for AC2 we see a particularly strong decrease about 5-17% of the electrochemical performance when adding any conductive additive (Fig. 8C) which is related to the pore blocking phenomenon as described in Fig. 5. At high specific currents (10 A g^{-1}), the situation is more complex and while some additives at some admixture contents still decrease the performance, there are several important exceptions. For example, there is an increase in capacitive retention of more than 20% for the system AC1 + 2.5 mass% CB2

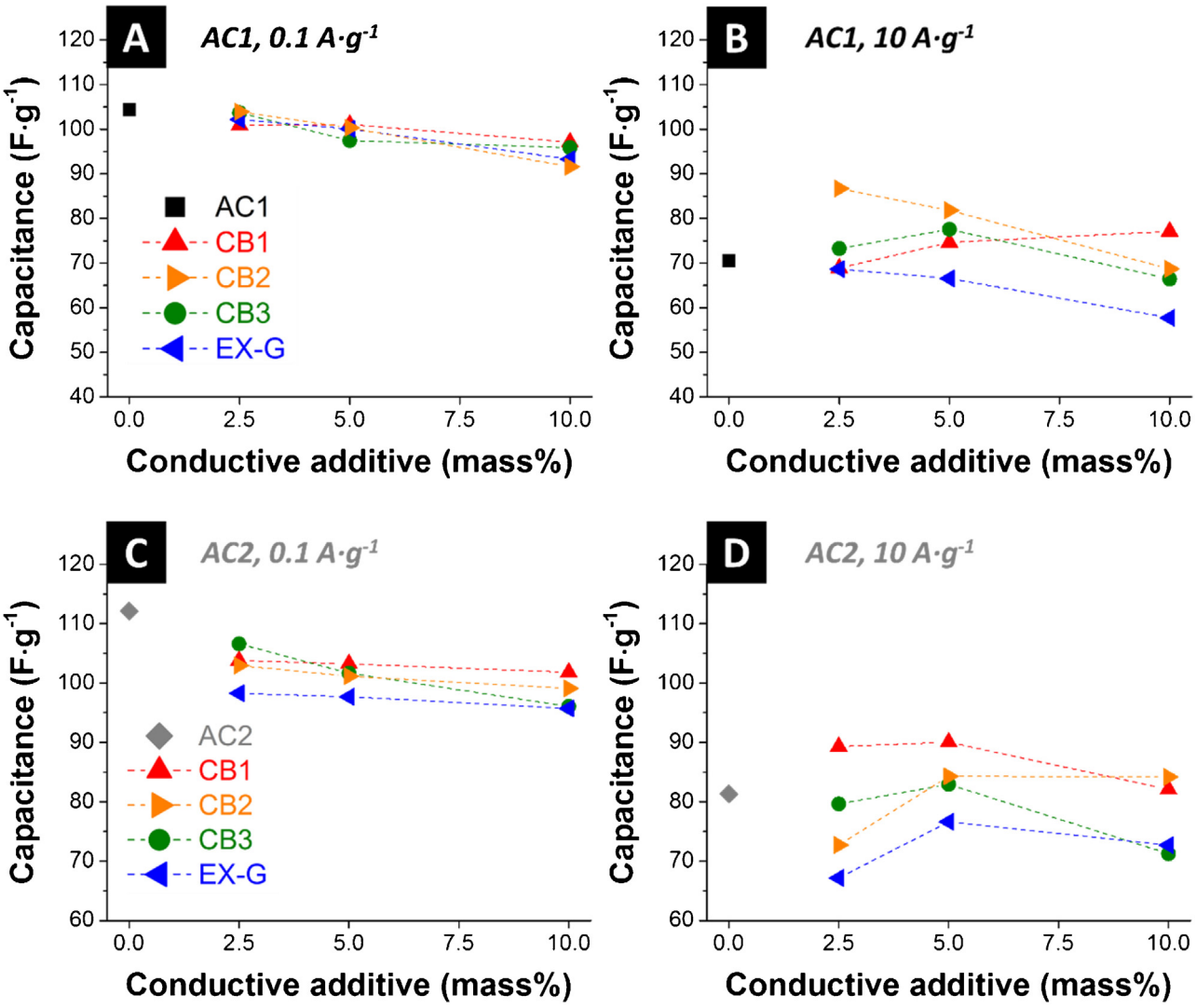

Fig. 7. Rate capability measurements of all composite electrodes with (A and C) a low rate of 0.1 A g^{-1} and (B and D) with a high rate of 10 A g^{-1}. The *x*-axis shows the amount of used conductive additive in the AC matrix of (A and B) AC1 and (B and D) AC2. "0%" is related to constituent AC electrode. The color and symbol chart given in panel A and C also relate for panel B and D, respectively.

(Fig. 8B), whereas the maximum enhancement of AC2 is 11% with the mixture AC2 + 5 mass%CB1.

The different effects of the conductive additives can be rationalized by considering the influence of agglomerate size (Fig. 1A) and the effective percolation level within the AC particle matrix. Furthermore, the intrinsic behavior of each carbon material, like SSA (Table 2), density, and surface functional groups, has to be taken into account. For example, when mixing AC1 and CB1, we see a continuous improvement of the electrochemical performance with higher additive content related to the high SSA of CB1 (powder: 1272 $m^2 g^{-1}$) and its high electrical conductivity (Fig. 4B). For this system, there is only a minor loss in total SSA of the electrode (Table 4) and it can be assumed that the highly conductive particles form a percolated network at a concentration of around 5 mass% in AC1. For CB2 with moderate SSA (powder: 715 $m^2 g^{-1}$) we see a continuous decrease in electrode capacitance when increasing the amount of additive to more than 2.5 mass% in AC1 (Fig. 8B). This effect is due to the small agglomerate size (d_{90} = 0.2 μm), resulting in a homogenous distribution of CB2 even at a very low amount (i.e., the percolation threshold is reached at low concentration of CB2). In case of CB3, a maximum capacitive enhancement is seen when admixing 5 mass% either to AC1 (+7.1 F g^{-1} at 10 A g^{-1},Fig. 8B) or AC2 (+1.6 F g^{-1} at 10 A g^{-1}, Fig. 8D). A homogeneous distribution of all used CB particles in-between AC grains reduces the overall contact resistance effectively (Fig. 4B and D). Any further increase of the amount of conductive additive particles beyond 5 mass% decreases the total electrode SSA and leads to a decreased overall supercapacitor performance, while the electrical conductivity of the composite electrode still improves.

In contrast to CB, admixing graphite flakes never yielded any improvement in the electrochemical performance. We explain this effect by the very large particle size of EX-G and its very low SSA. It can be assumed that the two-dimensional in-plane conductivity of EX-G cannot decrease the interparticle resistance as effectively as a three-dimensional network of highly conductive graphitic shells of carbon blacks. Seemingly, the carbon-carbon contact area can be effectively increased by using spherical carbon additives with a small aggregate size to ensure a homogeneous distribution in the AC particle matrix.

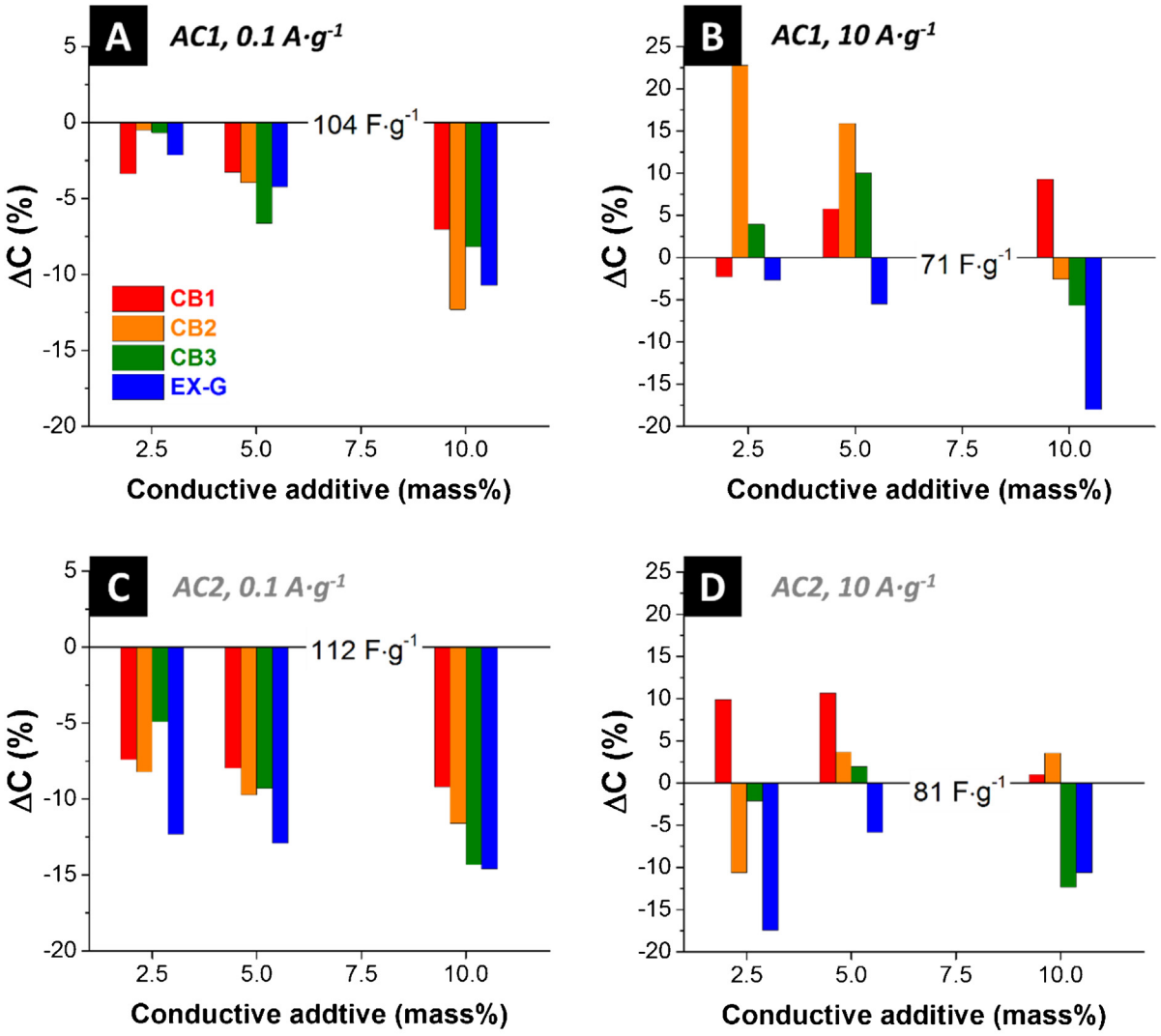

Fig. 8. Gain (positive values) or loss (negative values) of specific capacitance for conductive additive composite electrodes in comparison to performance of constituent AC electrodes (A and C) at a low rate of 0.1 A g^{-1} and (B and D) at a high rate of 10 A g^{-1}. The black line (and the value) marks the performance of a constituent AC full cell. The color code in panel (A) relates to all panels.

3.4. Long-time performance testing by voltage floating

Long-time performance evaluation was carried out at 2.7 V in a symmetrical full cell for 100 h. Voltage floating enables demanding benchmarking and is commonly employed in industry [23]. This method yields stable performance over long floating time when subjecting AC electrodes to a cell voltage of 2.75 V in 1 M TEA-BF_4/ACN with less than 30 ppm of water [24]. Floating test has proven as more demanding test compared to cycling in the same voltage window because the floating test delivers clear results in less time [23]. First, we investigated the performance stability for AC1 and admixtures to AC1. In Fig. 9, we see a decrease in capacitance of 6.2% for AC1 after 100 h. Admixing any amount of any of the studied additives decreased the performance stability over time; yet, the performance stability of any of the conductive additives constituently was very high yielding a decrease in capacitance below 5% after 100 h of voltage floating. The only exception: admixing CB2 to AC1 (Fig. 9B) slightly increases the floating performance stability (+2% for 2.5 mass% CB2 in AC1), but any further increase of CB2 amount also decreases the performance as described before. Adding CB3 to AC1 (Fig. 9C), the capacitive retention after 100 h is always below that of either only AC1 or only CB3. The data also show that different amounts of CB3 admixture barely influence the performance and the same effect can be seen when adding EX-G (Fig. 9D).

Next, we investigated the same set of conductive additive admixtures and their influence on the long-time stability of AC2-based electrodes. The results are very similar to the data set of AC1 (Fig. 10). However, the performance of constituent AC2 (89% retention after 100 h floating test) is lower than for AC1 (94% after 100 h). Especially the admixture of CB2 into AC2 matrix decreases the long-time stability tremendously: already after 10 h of voltage

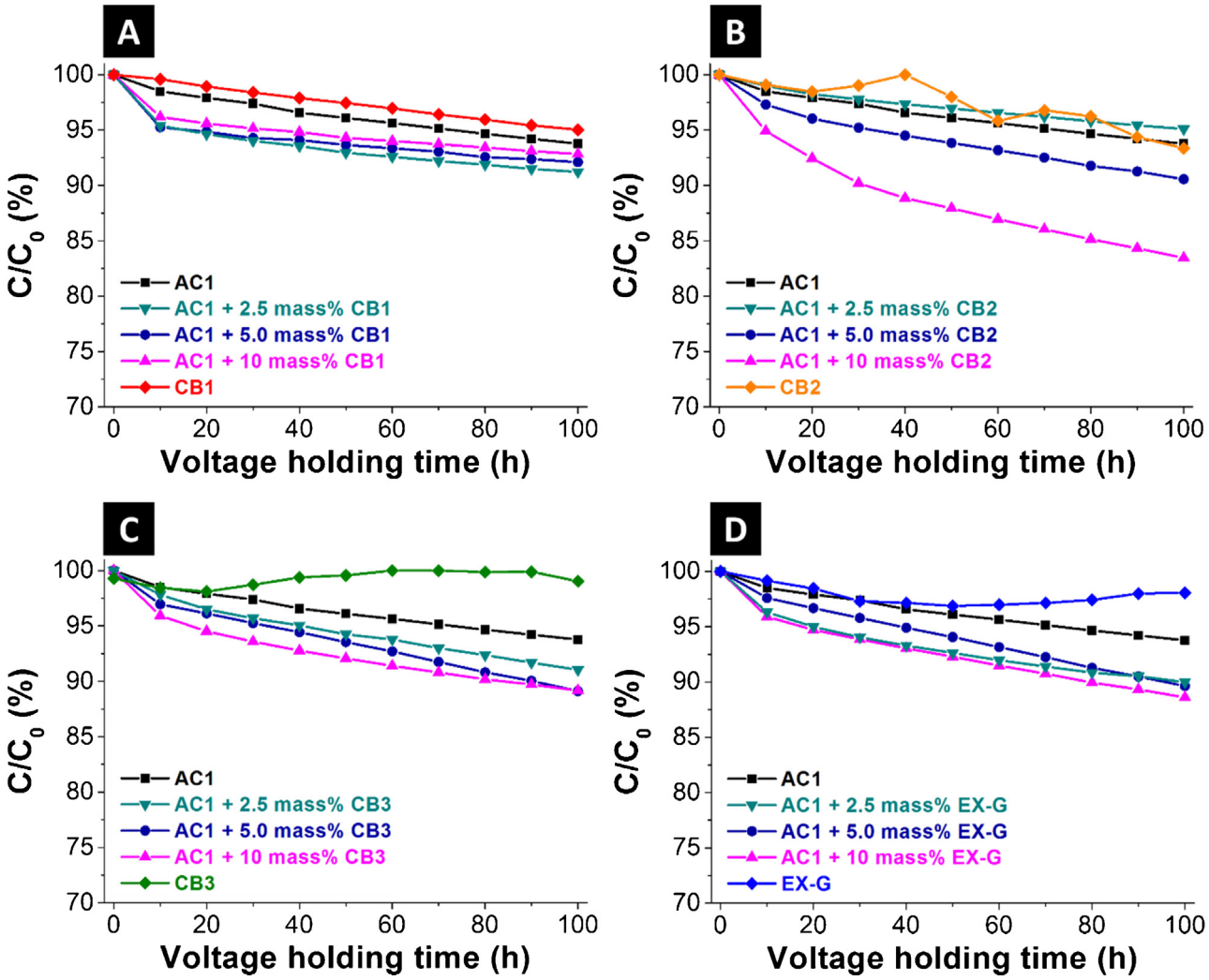

Fig. 9. Long-time floating stability testing at 2.7 V for AC1 with (A) admixture of CB1, (B) admixture of CB2, (C) admixture of CB3, and (D) admixture of EX-G. The amount of additive is 0 mass% (i.e., pure AC1), 2.5 mass%, 5 mass%, or 10 mass%.

floating, the retention drops to 80% C/C_0 when adding 10 mass% CB2.

The decrease in longevity of AC electrodes when using a composite electrode containing activated carbon and conductive additive is surprising, especially when considering the excellent stability for either just AC or just the conductive additives. The exact mechanism of this behavior remains unclear at the moment. A possible mechanism explaining the decrease in long-time performance for composite electrodes may relate to the combined presence of acidic and alkaline surface groups. The highly acidic surface groups, for example of AC1 (Fig. 3A), may react with the mostly alkaline groups of CB2 at an elevated potential of 2.7 V during voltage floating. This leads to an exchange of protons and the possible production of free water molecules, especially at the contact area of both types of carbon, with a deteriorating effect on the stability of acetonitrile near the electrode surface [50].

With the limited detectability of degradation products by post mortem analysis in the electrolyte itself, we investigated chemical changes of the aged electrodes by EDX to gain further insights (Fig. 11). Electrochemical decomposition of TEA-BF_4/ACN forms (fluoro) acetic acid, as well as acetamide, depending on the concentration of free water in the electrolyte, and free water is generated by condensation of amino-carbonyl compounds. Moreover, the corrosion (i.e., hydrolysis) of the BF_4 ion produces free fluorine atoms which like to react with protons to produce HF and this is further accelerating the decomposition of the electrolyte [51]. These processes severely affect the long-time stability, as shown by Cericola et al. [52]. For our system, we cannot identify these degradation products via the boron signal considering the very strong signal intensity of carbon. Thus, we can use for aged and thoroughly ACN rinsed electrodes the fluorine signal coming from F trapped at the surface from reactions and decomposition of the BF_4 [51]. The fresh composite electrode after contact with electrolyte (AC2 + 10 mass% CB2 + 5 mass% PTFE) showed a constant and omnipresent fluorine signal across the scanned area related to the PTFE binder. In fact, we did not find any significant increase in the measured fluorine signal even when mapping the ultrathin PTFE fibrils seen in the SEM micrographs, whereas the aged positive electrode shows certain regions with much higher

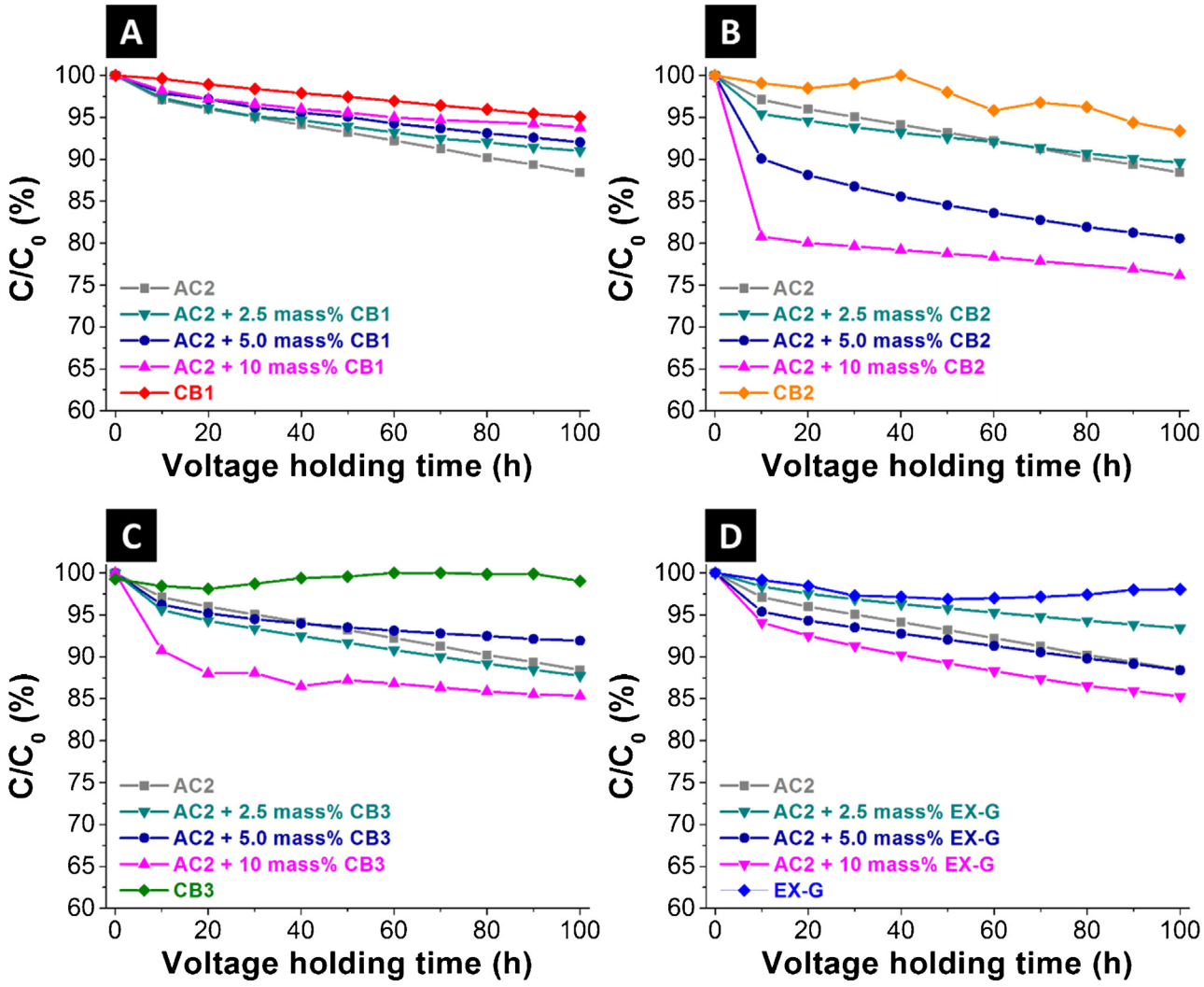

Fig. 10. Long-time floating stability testing at 2.7 V for AC2 with (A) admixture of CB1, (B) admixture of CB2, (C) admixture of CB3, and (D) admixture of EX-G. The amount of additive is 0 mass% (i.e., pure AC2), 2.5 mass%, 5 mass%, or 10 mass%.

fluorine signal. Some slight variations in the total signal strength only occurred in relation to the particle shape and morphology. However, reproducibly and significantly at contact between CB2 and AC2, we found an increase of fluorine (Fig. 11A) which was absent for the non-aged mixture (Fig. 11D). We assume this is related to the decomposition of the electrolyte at the interface between activated carbon and conductive additive where the exchange of protons is possible at elevated potential. The trace water may, accordingly, act as a catalyst for the decomposition of the electrolyte.

The implication of a decreased electrochemical performance longevity when adding conductivity certain conductive additive is of high importance for industrial applications and needs to be considered accordingly.

4. Conclusions

We present a comprehensive study of two activated carbons and four conductive additives with structural, chemical, and electrochemical measurements. The conductive additives were admixed in certain amounts and the electrochemical performance was evaluated in laboratory size cells via rate handling testing up to 10 A g^{-1} and voltage floating over 100 h in a standard organic electrolyte (1 M TEA-BF_4 in ACN). A decreased sheet resistance for an increased amount of conductive additive does not necessarily translate to an improved rate handling. Especially at low rates, the gravimetric capacitance drops generally after adding carbons with low SSA to AC. However, the rate performance can be increased up to 20% at 10 A g^{-1} by optimizing the amount of conductive particles to AC (in our study between 2.5-5 mass%). The long-time stability via voltage floating of composite electrodes is always inferior to electrodes composed of either AC or the conductive additive materials. In our study we explain this effect with the generation of water at the electrolyte-electrode interface by mixing alkaline and basic surface groups from different carbons. We demonstrate for the first time that mixing acidic and basic carbon materials leads also to a deterioration of long-time performance, especially at the contact area of basic and alkaline decorated surfaces. Thus, further work will have to investigate this effect in more detail.

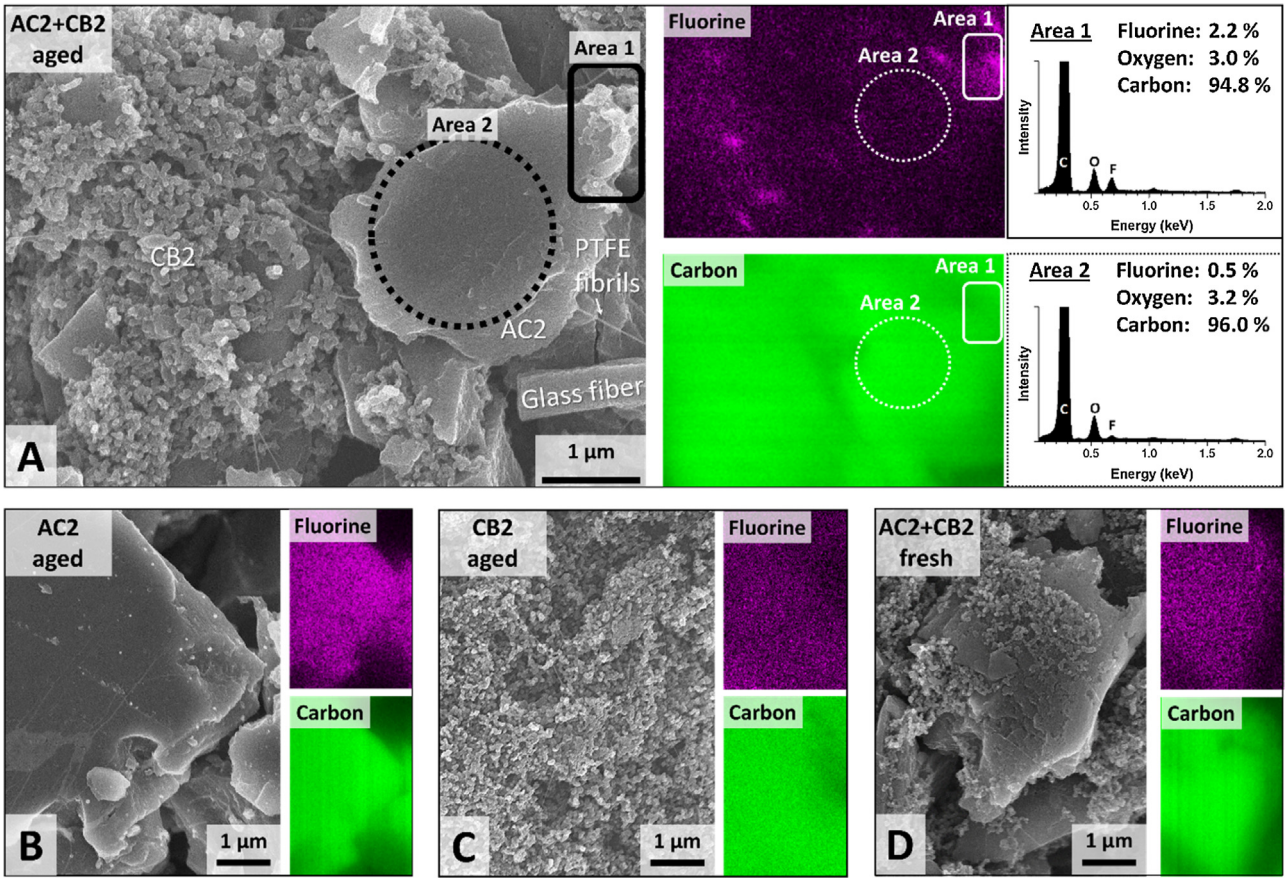

Fig. 11. SEM micrographs and EDX mapping for fluorine and carbon of (A) aged composite electrode AC2 + 10% CB2 + 5% PTFE (AC2 + CB2 aged), (B) aged activated carbon electrode AC2 + 5% PTFE, (C) aged carbon black electrode CB2 + 10% PTFE, (D) and non-aged (fresh) composite electrode AC2 + 10% CB2 +5% PTFE.

Acknowledgements

We thank Imerys Graphite & Carbon, Switzerland, for kindly providing the additives Ensaco350, C65, and the experimental expanded graphite. We acknowledge funding from the German Federal Ministry for Research and Education (BMBF) in support of the nanoEES^{3D} project (award number 03EK3013) as part of the strategic funding initiative energy storage framework. We also acknowledge additional funding via the INM FOCUS project IZIcap and thank Prof. Eduard Arzt (INM) for his continuing support.

References

[1] A. Burke, Ultracapacitors: why, how, and where is the technology, Journal of Power Sources 91 (1) (2000) 37–50.
[2] R. Kötz, M. Carlen, Principles and applications of electrochemical capacitors, Electrochimica Acta 45 (15–16) (2000) 2483–2498.
[3] A.G. Pandolfo, A.F. Hollenkamp, Carbon properties and their role in supercapacitors, Journal of Power Sources 157 (1) (2006) 11–27.
[4] M. Lu, F. Beguin, E. Frackowiak, Supercapacitors: Materials, Systems and Applications, Wiley, 2013.
[5] B.E. Conway, Electrochemical Supercapacitors: Scientific Fundamentals and Technological Applications, Springer, 1999.
[6] D. Aurbach, Review of selected electrode-solution interactions which determine the performance of Li and Li ion batteries, Journal of Power Sources 89 (2) (2000) 206–218.
[7] C. Liu, et al., Advanced materials for energy storage, Adv Mater 22 (8) (2010) E28–62.
[8] P. Simon, Y. Gogotsi, Materials for electrochemical capacitors, Nat Mater 7 (11) (2008) 845–854.
[9] H. Marsh, F.R. Reinoso, Activated carbon, Elsevier, 2006.
[10] J. Chmiola, et al., Desolvation of ions in subnanometer pores and its effect on capacitance and double-layer theory, Angewandte Chemie - International Edition 47 (18) (2008) 3392–3395.
[11] R. Mysyk, E. Raymundo-Pinero, F. Beguin, Saturation of subnanometer pores in an electric double-layer capacitor, Electrochemistry Communications 11 (3) (2009) 554–556.
[12] L. Zhang, et al., Controlling the effective surface area and pore size distribution of sp2 carbon materials and their impact on the capacitance performance of these materials, J Am Chem Soc 135 (15) (2013) 5921–5929.
[13] F. Beguin, et al., Carbons and electrolytes for advanced supercapacitors, Adv Mater 26 (14) (2014) 2219–2251, 2283.
[14] P.J. Hall, et al., Energy storage in electrochemical capacitors: designing functional materials to improve performance, Energy & Environmental Science 3 (9) (2010) 1238–1251.
[15] S. Zhang, N. Pan, Supercapacitors Performance Evaluation, Advanced Energy Materials 5 (6) (2015) 1401401.
[16] D. Weingarth, et al., Carbon additives for electrical double layer capacitor electrodes, Journal of Power Sources 266 (2014) 475–480.
[17] A.G. Pandolfo, et al., The Influence of Conductive Additives and Inter-Particle Voids in Carbon EDLC Electrodes, Fuel Cells 10 (5) (2010) 856–864.
[18] N. Jäckel, et al., Comparison of carbon onions and carbon blacks as conductive additives for carbon supercapacitors in organic electrolytes, Journal of Power Sources 272 (2014) 1122–1133.
[19] G.X. Wang, Z.P. Shao, Z.L. Yu, Comparisons of different carbon conductive additives on the electrochemical performance of activated carbon, Nanotechnology 18 (20) (2007) 205705.
[20] M.E. Spahr, et al., Development of carbon conductive additives for advanced lithium ion batteries, Journal of Power Sources 196 (7) (2011) 3404–3413.
[21] W. Guoping, et al., The effect of different kinds of nano-carbon conductive additives in lithium ion batteries on the resistance and electrochemical behavior of the LiCoO2 composite cathodes, Solid State Ionics 179 (7–8) (2008) 263–268.
[22] C. Portet, et al., Influence of carbon nanotubes addition on carbon-carbon supercapacitor performances in organic electrolyte, Journal of Power Sources 139 (1–2) (2005) 371–378.

[23] D. Weingarth, A. Foelske-Schmitz, R. Kötz, Cycle versus voltage hold—Which is the better stability test for electrochemical double layer capacitors? Journal of Power Sources 225 (2013) 84–88.
[24] P.W. Ruch, et al., Aging of electrochemical double layer capacitors with acetonitrile-based electrolyte at elevated voltages, Electrochimica Acta 55 (15) (2010) 4412–4420.
[25] P. Azais, et al., Causes of supercapacitors ageing in organic electrolyte, Journal of Power Sources 171 (2) (2007) 1046–1053.
[26] M. Hahn, et al., Gas evolution in activated carbon/propylene carbonate based double-layer capacitors, Electrochemistry Communications 7 (9) (2005) 925–930.
[27] D. Weingarth, et al., Graphitization as a Universal Tool to Tailor the Potential-Dependent Capacitance of Carbon Supercapacitors, Advanced Energy Materials 4 (13) (2014).
[28] D. Weingarth, et al., PTFE bound activated carbon—A quasi-reference electrode for ionic liquids, Electrochemistry Communications 18 (0) (2012) 116–118.
[29] P.W. Ruch, et al., On the use of activated carbon as a quasi-reference electrode in non-aqueous electrolyte solutions, Journal of Electroanalytical Chemistry 636 (1–2) (2009) 128–131.
[30] S. Brunauer, P.H. Emmett, E. Teller, Adsorption of Gases in Multimolecular Layers, Journal of the American Chemical Society 60 (2) (1938) 309–319.
[31] G.Y. Gor, et al., Quenched solid density functional theory method for characterization of mesoporous carbons by nitrogen adsorption, Carbon 50 (4) (2012) 1583–1590.
[32] P.I. Ravikovitch, G.L. Haller, A.V. Neimark, Density functional theory model for calculating pore size distributions: pore structure of nanoporous catalysts, Advances in Colloid and Interface Science 76 (0) (1998) 203–226.
[33] A. Vishnyakov, P.I. Ravikovitch, A.V. Neimark, Molecular level models for CO_2 sorption in nanopores, Langmuir 15 (25) (1999) 8736–8742.
[34] F. Beguin, et al., Carbons and electrolytes for advanced supercapacitors, Advanced Materials 26 (14) (2014) 2219–2251.
[35] F. Tuinstra, J.L. Koenig, Raman Spectrum of Graphite, Journal of Chemical Physics 53 (3) (1970) 1126–1130.
[36] C. Thomsen, S. Reich, Double resonant raman scattering in graphite, Phys Rev Lett 85 (24) (2000) 5214–5217.
[37] A.C. Ferrari, J. Robertson, Raman spectroscopy of amorphous, nanostructured, diamond—like carbon, and nanodiamond, Philosophical Transactions of the Royal Society of London Series A 362 (1824) (2004) 2477–2512.
[38] N. Shimodaira, A. Masui, Raman spectroscopic investigations of activated carbon materials, Journal of Applied Physics 92 (2) (2002) 902–909.
[39] M. Thommes, et al., Physisorption of gases, with special reference to the evaluation of surface area and pore size distribution (IUPAC Technical Report), Pure and Applied Chemistry 87 (9–10) (2015).
[40] S. Porada, et al., Capacitive Deionization using Biomass-based Microporous Salt-Templated Heteroatom-Doped Carbons, ChemSusChem 8 (11) (2015) 1867–1874.
[41] A.Y. Mottlau, N.E. Fisher, Measurement of pore volume by a titration technique, Analytical Chemistry 34 (6) (1962) 714–715.
[42] M. Aslan, et al., Polyvinylpyrrolidone as binder for castable supercapacitor electrodes with high electrochemical performance in organic electrolytes, Journal of Power Sources 266 (1) (2014) 374–383.
[43] Q. Abbas, et al., Effect of binder on the performance of carbon/carbon symmetric capacitors in salt aqueous electrolyte, Electrochimica Acta 140 (2014) 132–138.
[44] H. Gerischer, The Impact of Semiconductors on the Concepts of Electrochemistry, Electrochimica Acta 35 (11–12) (1990) 1677–1699.
[45] A.A. Kornyshev, N.B. Luque, W. Schmickler, Differential capacitance of ionic liquid interface with graphite: the story of two double layers, Journal of Solid State Electrochemistry 18 (5) (2013) 1345–1349.
[46] C. Schütter, et al., Activated Carbon, Carbon Blacks and Graphene Based Nanoplatelets as Active Materials for Electrochemical Double Layer Capacitors: A Comparative Study, Journal of the Electrochemical Society 162 (1) (2015) A44–A51.
[47] H.A. Andreas, Self-discharge in electrochemical capacitors: A perspective article, Journal of the Electrochemical Society 162 (5) (2015) A5047–A5053.
[48] C.R. Pérez, et al., Structure and electrochemical performance of carbide-derived carbon nanopowders, Advanced Functional Materials 23 (8) (2013) 1081–1089.
[49] J.K. McDonough, et al., Influence of the structure of carbon onions on their electrochemical performance in supercapacitor electrodes, Carbon 50 (9) (2012) 3298–3309.
[50] P. Krtil, L. Kavan, P. Novak, Oxidation of Acetonitrile-Based Electrolyte Solutions at High Potentials, Journal of The Electrochemical Society 140 (12) (1993) 3390.
[51] P. Kurzweil, M. Chwistek, Electrochemical stability of organic electrolytes in supercapacitors: Spectroscopy and gas analysis of decomposition products, Journal of Power Sources 176 (2) (2008) 555–567.
[52] D. Cericola, et al., Effect of Water on the Aging of Activated Carbon Based Electrochemical Double Layer Capacitors During Constant Voltage Load Tests, International Journal of Electrochemical Science 6 (4) (2011) 988–996.

4.2 Anomalous or Regular Capacitance? The Influence of Pore Size Dispersity on Double-layer Formation

N. Jäckel [a,b], M. Rodner [a,b], A. Schreiber [a], J. Jeongwook [a], M. Zeiger [a,b], M. Aslan [a], D. Weingarth [a], V. Presser [a,b]

[a] INM—Leibniz Institute for New Materials, Campus D2 2, 66123 Saarbrücken, Germany

[b] Department of Materials Science and Engineering, Saarland University, Campus D2 2, 66123 Saarbrücken, Germany

published in Journal of Power Sources, 2016. 326: p. 660-671

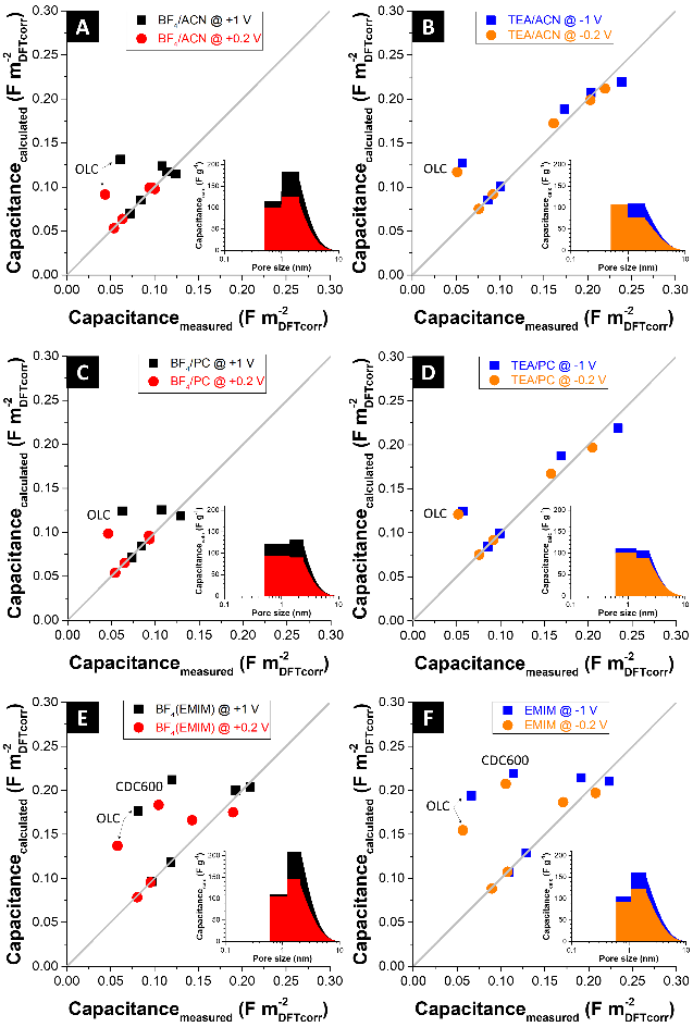

Own contribution:

Data generation 25 %

Data analysis 80 %

Interpretation 90 %

Writing 85 %

Supporting Information:

Appendix A

Journal of Power Sources 326 (2016) 660–671

Contents lists available at ScienceDirect

Journal of Power Sources

journal homepage: www.elsevier.com/locate/jpowsour

Anomalous or regular capacitance? The influence of pore size dispersity on double-layer formation

N. Jäckel [a, b], M. Rodner [a, b], A. Schreiber [a], J. Jeongwook [a], M. Zeiger [a, b], M. Aslan [a], D. Weingarth [a], V. Presser [a, b, *]

[a] INM - Leibniz Institute for New Materials, Saarbrücken, Germany
[b] Department of Materials Science and Engineering, Saarland University, Saarbrücken, Germany

HIGHLIGHTS

- Pore size incremental analysis shows non-constant capacitive contribution.
- Differential capacitance depends on type of ion and solvent.
- Ion desolvation may become more important at higher electrode potentials.
- Ionic liquids exhibit cation-anion coordination.

ARTICLE INFO

Article history:
Received 27 January 2016
Received in revised form
2 March 2016
Accepted 4 March 2016
Available online 30 March 2016

Keywords:
Electrochemical energy storage
Microporous carbon
Porosity
Supercapacitor

ABSTRACT

The energy storage mechanism of electric double-layer capacitors is governed by ion electrosorption at the electrode surface. This process requires high surface area electrodes, typically highly porous carbons. In common organic electrolytes, bare ion sizes are below one nanometer but they are larger when we consider their solvation shell. In contrast, ionic liquid electrolytes are free of solvent molecules, but cation-anion coordination requires special consideration. By matching pore size and ion size, two seemingly conflicting views have emerged: either an increase in specific capacitance with smaller pore size or a constant capacitance contribution of all micro- and mesopores. In our work, we revisit this issue by using a comprehensive set of electrochemical data and a pore size incremental analysis to identify the influence of certain ranges in the pore size distribution to the ion electrosorption capacity. We see a difference in solvation of ions in organic electrolytes depending on the applied voltage and a cation-anion interaction of ionic liquids in nanometer sized pores.

1. Introduction

Electrical double-layer capacitors (EDLCs, members of the family of supercapacitors or ultracapacitors) are energy storage devices with high efficiency and long cycling stability [1–3]. Today, EDLCs are used, for example, in (hybrid) electric vehicles, systems for uninterrupted power supply, or trams [4,5]. In EDLCs, energy storage is accomplished via ion electrosorption in the electrical double-layer (EDL) at the electrically charged interface of high surface area carbon electrodes in contact with an electrolyte [6]. The electrolyte can be aqueous, organic, or an ionic liquid and the electrochemical stability window determines the ratings for the maximum operational cell voltage [7]. While EDLCs show a moderate energy density compared to lithium-ion batteries, they enable high power performance [8]. It is commonly known that the electrochemical performance of EDLCs varies as a function of the electrode material and the pore structure has been identified as an important parameter governing power and energy ratings [9–11]. Optimized electrochemical performance requires careful matching of the electrode properties to the specifics of a certain electrolyte [7,12].

The most common parameter to describe a supercapacitor's energy storage capacity used in the community is capacitance (Farad = Coulomb/Volt). Currently, this parameter is more extensively used than the energy storage capacity (with the unit Watthour, Wh). The capacitance is usually normalized by mass of active

* Corresponding author. INM - Leibniz Institute for New Materials, Saarbrücken, Germany.
E-mail address: volker.presser@leibniz-inm.de (V. Presser).

http://dx.doi.org/10.1016/j.jpowsour.2016.03.015
0378-7753/

material ($F \cdot g^{-1}$) and in a symmetrical cell assembly recalculated for one electrode ($C_{single\text{-}electrode} = 4 \cdot C_{device}$). Per definition, capacitance reflects on the prime requisite of supercapacitors, namely, to exhibit a capacitive charge/discharge profile [9]. This means that there should be a monotonic, linear relation between applied potential or cell voltage and accumulated charge. Yet, we note (at least) three general complications to this simplification.

(1) Capacitance may even intrinsically not be a constant material property [13]. Fundamentally shown for graphite by Gerischer et al., the capacitance of carbon may increase when increasing the cell voltage [14]. This effect is not related with nanoconfinement of ions, but is a result of the non-metallic nature of carbon: as higher potentials are applied, increasingly more charges (more than predicted from a linear capacitive correlation) can be accumulated as the density of states of charge carriers changes during charging [15]. In the literature, this effect has been denoted as electrochemical doping and the resulting symmetric distortion measured during cyclic voltammetry (CV) has been coined as butterfly-shape. By this virtue, we may have to consider for carbons a non-constant capacitance as a function of applied potential, called differential capacitance. This effect depends on the structure of carbon and was found to be very pronounced for graphite [14], highly graphitic carbon onions [16], zeolite-templated carbon [17], nitrogen-doped carbon nanotubes [18], and metallic carbon nanotubes [19], but much smaller for more amorphous activated carbon [16].
(2) Another complication to non-constant differential capacitance arises from the structure of the double-layer [20–22]. At very dilute concentrations in the mM range, a constant increase in differential capacitance needs to be considered for very low potentials (e.g., below 200 mV). This effect can be explained in terms of the Gouy-Chapman-Stern model and relates to the dependency of the total potential drop at the fluid-solid-interface on the bulk concentration [22–24]. Using high potentials, we can also see a drastic reduction of the measured capacitance as an effect of ion starvation, causing a characteristic narrowing in the shape of a corresponding CV [25].
(3) A further issue relates to nomenclature and the conceptual basis of capacitance. Be it either by non-faradaic (double-layer capacitor) or faradaic (pseudocapacitor) charge transfer: the prerequisite of a system to qualify as a supercapacitor is the electric behavior of a capacitor (including the small deviations thereof caused, for example, by (1) and (2)). If clear redox-peaks are encountered, then the behavior contains battery-like components up to the point where only insignificant capacitor-like contributions to the charge storage capacity are found and the concept of capacitance becomes unsuitable [26,27]. This issue has led to the report of very large capacitance values recalculated from battery-like systems and incorrect calculation of corresponding energy ratings (esp. specific energy, $Wh \cdot kg^{-1}$). A critical discussion of this issue can be found, for example, in Ref. [28].

The large capacitance of EDLCs, compared to electrolytic capacitors, is accomplished by using nanoporous carbons with high specific surface area. Typical ACs show a large volume of micropores (i.e., pore size <2 nm) and surface area values of 1500 $m^2 \cdot g^{-1}$ or higher [3,29]. Their use brings along a further complication to capacitive considerations for pores smaller than the Debye length with typically a few nanometers. Starting with overlapping potential profiles of the double-layers and ending with pores so small that ions can only enter when (partially) shedding a solvation shell, there is a large complexity in ion electrosorption processes in nanometer sized pores [30,31]. The seminal work of 2006 published by the Béguin Group [32] (in organic and aqueous media) and by the Gogotsi/Simon Groups [33] (in organic media) demonstrated an increase of the (surface area normalized) capacitance for microporous carbons with decreasing pore size. Similar conclusions were drawn from enhanced salt removal capacity from aqueous saline electrolytes via capacitive deionization by Porada et al. when comparing ACs and carbide-derived carbons (CDCs) [34]. However, (partial) desolvation of ions entering sub-nanometer-sized pores was discussed even earlier, for example by Salitra et al. in the year 2000 [35]. Remarkable are also the conclusions in the 1986 paper of Kastening and Spinzig [36] investigating ion electrosorption in sub-nanometer pores: "*In these narrow pores, however, the usual Gouy-Chapman layer (thickness about 1.3 nm under the conditions applied) cannot be developed because it would require a diameter of at least 2.6 nm. The ions will apparently be partially desolvated when entering these narrow pores.*" [36].

The conclusiveness of the reported experimental data is challenged by several complications.

(1) A first issue concerns the measurement of the pore structure and specific surface area of the dry powder, and relating such data to the electrochemical performance of binder-containing film electrodes induces inconsistencies. The use of polymer binder (esp. when being used in excess of 5 mass %) may lead to a significant reduction of the pore volume/surface area, while the pore size distribution remains less affected [37,38]. Thus, normalizing the measured electrochemical performance to the electrode pore structure should be favored over the porosity of the dry carbon powder only.
(2) Another issue arises from pore size dispersity. No actual carbon material has an ideal monodisperse pore size distribution (PSD). While some optimized AC [39] or CDC [40] materials may come close to being unimodal, we commonly have to consider a spread of the pore volume across a certain pore size range from sub-nanometer to several nanometers. A microporous carbon's pore structure with multimodal PSDs or very broad distributions cannot adequately be expressed by stating one average pore size value [41]. As such, the concept of average pore size may not be suitable when comparing very diverse carbons. Nevertheless, the term average pore size, defined as the pore size up to which 50% of the pore volume is encompassed, itself remains useful for structural comparison.
(3) A third complication is caused by the way values for the surface area or pore volume are determined. Most commonly, gas sorption techniques are used to derive pore characteristics [42]. For example, it has been widely accepted that the BET method [43] fails to accurately represent the pore structure of microporous carbons [44]. Relating electrochemical data to the BET surface area, for microporous carbons, is not recommended and more adequate models have been devised. In particular, deconvolution of nitrogen, carbon-dioxide, or argon sorption data with density functional theory (DFT) approaches have been proven to be powerful tools to investigate microporous carbons [44–46]. The mathematical approach of such complex carbon surface structures with DFT methods leads to certain artefacts. Regarding nitrogen sorption analysis, the most known artifact in non-local DFT (1D-NLDFT) is the gap at about 1 nm pore width which is related to the inadequate assumption of infinite flat, homogenous pore walls and corresponds to the pressure where the first layer of nitrogen fluid is formed [47]. This was improved by the implementation of molecularly

heterogeneity in quenched-solid DFT (QSDFT) [46,47] and by the NLDFT calculation in two dimensions (2D-NLDFT) [45]. Today, QSDFT kernels with different pore shapes are available, like slit-, cylindrical-, or spherical-shaped and hybrid kernels with assumption of certain pore shape in defined pore ranges [46]. The comparison of both new DFT models (i.e., 2D-NLDFT and QSDFT) showed comparable results as presented by Puziy et al. [48]. However, the unavailability of QSDFT kernels for carbon-dioxide sorption currently limits the comprehensiveness of sub-nanometer pore size distribution (there is only a 1D-NLDFT kernel available at the moment). The general variation of pore geometry as a function of synthesis parameters was shown, for example, for carbide-derived carbons via small angle neutron scattering, showing a transition from rather spherical to slit-shaped pores with higher processing temperatures [49]. However, in most cases, there is a good agreement between porosity data from gas sorption and scattering methods (typically within 10–20%) [42]. We also note that the measured surface area and pore volume may also contain pores which are electrochemically not relevant, meaning, which are inaccessible to the ion electrosorption process by being smaller than the actual ion size.

Mostly motivated by (3), Centeno and Stoeckli have stimulated a very important discussion on the question if the enhanced capacitance identified for small pore diameters may be an artifact of the porosity data obtained from gas sorption analysis [50,51]. The postulated regular pattern of capacitance vs. pore size average (0.7–15 nm) was demonstrated for polymer-containing film electrodes of a large array of microporous carbons in organic media by using immersion calorimetry to obtain a more realistic representation of the electrochemically relevant porosity [50]. A constant capacitance over pore size between ca. 0.6 nm and 2 nm was also demonstrated by the Centeno group for monolithic carbon, and it was shown that a presumably anomalous increase in capacitance with decreasing pore size would be obtained when using the BET surface area (BET-SSA) instead of using just pore volume larger than the ion size [52].

In contrast, a non-regular pattern was identified for organic electrolytes and ionic liquids using computer simulation [53,54]. For ionic liquids, and using a model with a perfectly monodisperse pore size dispersion, an oscillatory dependency between ion size and pore size was identified. This oscillatory behavior was shown to disappear for organic solutions in favor of one main peak of enhanced differential capacitance when matching the ion size to the pore size [55]. Modelling may also adopt the pore size dispersity of microporous carbons [56], and it was demonstrated for ionic liquids that a large PSD amplitude may transition the anomalous capacitance vs. pore size pattern to a regular one [57].

These conflicting results make the impact of sub-nm pores to the capacitance controversial. Recently, a number of studies have engaged in a more detailed analysis of this topic. Mentioning a few, Pohlmann et al. investigated the influence of anion-cation combinations on different activated carbons in ionic liquids or dissolved in propylene carbonate in certain concentrations [58,59]. Galhena et al. provided data on an enhanced specific capacitance in the sub-nanometer range when the pore size in graphene oxide paper matches the non-solvated ion size in organic electrolyte [60]. Jiang et al. used a DFT model to describe the packing density of solvent molecules and ions in certain pore sizes [55]. They reported (partial) ion desolvation inside narrow pores and showed a constant differential capacitance for pores larger than 1 nm [61]. For ionic liquids, Monte-Carlo simulations by Kondrat et al. indicate that higher voltages favor facile ion storage in larger pores (>1–2 nm) with saturation of smaller pores occurring at lower potentials [56]. The former work also mentions an expected loss in theoretical energy storage capacity when a perfect monodisperse pore size distribution transitions towards a broader dispersity [56]. Zhang et al. showed the importance of accessible SSA in the sp^2-hybridized material for two different ionic liquids (ILs) [62]. Since they used a slit/cylindrical NLDFT kernel to calculate the pore size distribution, the PSD contained two mathematical artefacts at 1 nm and 2 nm [47]. The disappearing peak capacitance for pore size matching the ion size in case of broader distributed pore sizes has also been demonstrated for organic electrolytes [63]. Lee et al. developed a model including the combined effects of pore size and ionophobility/ionophobicity on the capacitance in slit-like pores [64]. Furthermore, Hsieh et al. adopted a model for overlapping double-layers and applied it to the experimental NLDFT-derived porosity data of micro- and mesoporous carbons. By employing a length-dependent value for the dielectric permittivity, they postulated for aqueous and organic solutions constant differential capacitance in micropores because of electrostriction effects [65].

This work will investigate the possible pore size dependence of capacitance and venture to establish that both the regular and the anomalous pattern can be consolidated by rigorous application of the concept of differential capacitance. We employed organic solutions and ionic liquid electrolytes and an array of different microporous carbons. Our data will separate the pore characteristics of the dry powder from the film electrodes and by use of a reference electrode. The electrochemical performance is surveyed for the positively and negatively polarized electrodes separately. By this way, we can separate the data in dependence of the size of anions and cations. We also apply a model that we have recently introduced for the highly accurate prediction of the desalination capacity via capacitive deionization in saline aqueous media [66]. This model uses discretization of the pore volume and calculation of differential capacitance for such segments to investigate the correlation between differential capacitance (rather than device capacitance) and pore size segment (rather than average pore size).

2. Experimental description

2.1. Electrode materials and preparation

Activated carbon YP-50 F from Kuraray (called AC), carbon black BP2000 from Cabot (called CB1), were used as received from the suppliers. Carbide-derived carbon (CDC) materials were synthesized from titanium carbide (TiC) powder placed in glass crucibles and thermally annealed in a furnace in chlorine gas at either 600, 800, or 1000 °C for 3 h and named CDC600, CDC800, or CDC1000, respectively. To remove residual chlorine, all samples were subsequently annealed at 600 °C in hydrogen for 2 h and after cooling placed in vacuum (0.1 mPa) for several hours. Carbon onions, named OLC, were derived from nanodiamond powder (NaBond) by placing the material in graphite crucibles for thermal annealing in argon at 1700 °C for 1 h with a heating rate of 20 $°C \cdot min^{-1}$ (Thermal Technology Furnace).

For electrode preparation, carbon powder was soaked with ethanol and agitated in a mortar. We added 10 mass% of dissolved polytetrafluoroethylene (PTFE, 60 mass% solution in water from Sigma Aldrich) as binder. The resulting dough-like material was rolled with a rolling machine (MTI HR01, MTI Corp.) to a 200 ± 20 μm thick free standing film electrode and finally dried at 120 °C at 2 kPa for 24 h before use.

2.2. Cell preparation, electrical, and electrochemical measurements

For electrochemical testing, we employed a custom-built

polyether ether ketone (PEEK) cell with spring loaded titanium pistons as a three electrode system described elsewhere [16]. The working electrode was punched from a free-standing electrode containing 10 mass% PTFE with 12 mm diameter and 200 ± 20 μm thickness with a total mass of 10–20 mg. An oversized YP-80 F (Kuraray) electrode with 500 μm thickness and 25 mg served as counter electrode. We employed a glass-fiber separator (GF/A from Whatman) and a carbon-coated aluminum foil current collector (type Zflo 2653 from Coveris Advanced Coatings). Further, we used PTFE-bound YP-50 F as a stable quasi-reference electrode [67,68]. The assembled cells were dried at 120 °C for 12 h at 2 kPa in an inert gas glove box (MBraun Labmaster 130, O_2 and H_2O < 1 ppm) and, after cooling to room temperature, vacuum-filled with 1 M tetraethylammonium-tetrafluoroborate (TEA-BF_4) in electrochemical grade (i.e., water content <20 ppm) acetonitrile (ACN) or propylene carbonate (PC) purchased from BASF. The ionic liquid 1-ethyl-3-methylimidazolium tetrafluoroborate (EMIM-BF_4; >99%, Sigma Aldrich) was degassed using a Schlenck flask in a Si-oil bath heated to 100 °C while applying a vacuum of 1 Pa for at least 6 h to remove residual gas and water and cells were vacuum-filled as described before.

Electrochemical measurements were carried out using a potentiostat/galvanostat VSP300 from Bio-Logic, France, with cyclic voltammetry (CV) at 2 $mV \cdot s^{-1}$, galvanostatic cycling with potential limitation (GCPL) with a 15 min holding step at each potential to bring the system to an equilibrated state. The specific (gravimetric) capacitance during discharging was calculated via Eq. (1):

$$C_{sp} = \frac{\int_{t_0}^{t_{end}} Idt}{U} \cdot \frac{1}{m} \quad (1)$$

with specific capacitance C_{sp}, time t (t_0: starting time of discharge, t_{end}: end of discharging time), applied potential difference U, discharge current I, and total mass of the working electrode m (i.e., considering carbon and the binder). For every type of electrode composition, two electrodes were prepared and these two cells were tested individually to calculate mean values with a standard deviation always below 5%.

2.3. Porosity analysis

Nitrogen gas sorption measurements were carried out with an Autosorb iQ system (Quantachrome) at the temperature of liquid nitrogen (−196 °C) after degassing at 10^2 Pa and 150 °C for 10 h for binder containing film electrodes and at 300 °C for 24 h for powder samples. For the measurements, the relative pressure (P/P_0) was varied from $5 \cdot 10^{-7}$ to 1.0 in 68 steps. The specific surface area (SSA) was calculated with the ASiQwin-software using the Brunauer-Emmett-Teller (BET) equation in the linear relative pressure range of 0.01–0.2 [43]. We also calculated the SSA and pore size distribution (PSD) via quenched-solid DFT (QSDFT) with a slit pore shape model between 0.56 and 37.5 nm [46]. As shown elsewhere, the error in assuming slit-like pores for OLC is not insignificant, but smaller than using other kernels [16]. Values for the total pore volume correspond to $p/p_0 = 0.95$. Carbon dioxide gas sorption measurements were carried out at 0 °C in the relative pressure range from $1 \cdot 10^{-4}$ to $1 \cdot 10^{-2}$ in 40 steps. SSA and PSD values were calculated for pore sizes between 0.3 nm and 1 nm with the ASiQwin software using nonlocal density functional theory (NLDFT) for CO_2 sorption [69]. 1D-NLDFT kernel suffer from the assumption of infinite flat, homogenous carbon surface which results in the incorrect pore size distribution with many sharp maxima and gaps in-between [70]. Nevertheless, CO_2 adsorption is favorable for measuring of ultramiropores [44,71]. The calculated PSD was incremented by a linear approximation of the calculated pore volume (CO_2-sorption-derived PSD was used up to a pore size of 0.9 nm and N_2-sorption-derived PSD for pores larger than 0.9 nm) to an equidistant point density of 0.1 nm in the range 0.3–2 nm and a point-to-point distance of 1 nm for pores larger than 2 nm. In some cases, especially for highly microporous carbons, the calculated SSA or pore volume of CO_2 sorption at the intercept-spot 0.9 nm was higher than the one calculated from nitrogen sorption. In this case, the offset was added to the PSD data obtained from nitrogen sorption, as described in previous work [72].

2.4. Structural and chemical characterization

Raman spectra of the raw materials were recorded with a Renishaw inVia Raman system using an Nd-YAG laser (532 nm) with 0.2 mW power at the sample's surface. The spectral resolution of ca. 1.2 cm^{-1} corresponds to a grating with 2400 $lines \cdot mm^{-1}$ and the spot size on the sample was in the focal plane ca. 2 μm (numeric aperture = 0.9). The acquisition time was 30 s and 50 accumulations were recorded. Peak analysis and peak fitting were performed assuming one Lorentzian peak for both, the D-mode and the G-mode.

Elemental analysis (EDX) of carbon powder was measured with a Thermo Fisher Scientific system placed in a JSM-7500 F from JEOL. Samples were placed on a conductive carbon tape and spectra were recorded at 50 different positions for each sample with 10 kV acceleration voltage.

2.5. Model description

Our approach entails the combination of SSA and electrochemical data to obtain the influence of certain pore ranges on the total capacitance. We take into account the ion size and influence of solvation shell or ion-ion attraction in IL. In our model we start with a correction of the surface area to obtain an accessible SSA compensating for the finite size of the ions. We subtract the surface area calculated from DFT for pores smaller than the bare ion size ($SSA_{DFTcorr}$). With this corrected SSA, we then calculate the cumulated SSA for a certain pore size range. The range is determined by the bare ion size and the size of fully solvated ions. The first range goes from the bare ion size to the size of the fully solvated ion, for example, TEA^+ in ACN from 0.7 to 1.3 nm, BF_4^- in PC from 0.5 to 1.3 nm. The second range expands from the size of one solvated ion up to the size of two solvated ions. With this approach we assume no desolvation of ions in pores larger than the size of one fully solvated ion [73,74]. Regarding the Coulombic repulsion of two equal polarized ions, we also assume that only for a pore as large as two solvated ions, both of them will be able to enter the pore [73,74]. For pores larger than two solvated ions, we calculate an exponential decrease of the contribution of pores to the total capacitance, starting from the capacitance value of 2 nm and ending at zero for pore width of 10 nm [66]. Since we use only highly microporous carbons, the SSA is strongly dominated by pores smaller than 2 nm and the charge is mainly accommodated in nanopores [55,73]. The kernel used a linear least-squares solver with two bounds, the total capacitance and the total SSA of each material. With this model, we can back calculate the theoretical capacitance in $F \cdot g^{-1}$ normalized to the average density of microporous carbon (approx. 2 $g \cdot cm^{-3}$). For the aprotic ionic liquid, we assumed bare ion sizes without a solvation shell and the used thresholds are the size of one and two ion diameters. For larger pore sizes, we assumed an exponential decrease in importance of pores, as described before.

The mean square error values are calculated following equation 2

$$MSE = \frac{1}{n}\sum_{i=1}^{n}\sqrt{\left(C_{meas,i} - C_{calc,i}\right)^2} \quad (2)$$

with calculated capacitance C_{calc} and measured capacitance C_{meas}.

3. Results and discussion

3.1. Porosity and general analysis of carbon electrodes

The porosity was characterized by gas sorption analysis. For a better assessment of the sub-nanometer pores down to 0.3 nm, we have employed CO_2 gas sorption at 0 °C in addition to nitrogen gas sorption at −196 °C. The combined result of both methods contains the deconvoluted data of carbon-dioxide adsorption in the range of 0.3–0.9 nm and nitrogen sorption in the range of 0.9–30 nm. The cumulative PSD pattern for the different dry powders and the consolidated electrode films are shown in Fig. 1, with the full isotherms provided in the *Supporting Information* Fig. S1 and the resulting PSD of all materials in Fig. S2. The CO_2 sorption isotherms (*Supporting Information*, Fig. S1A + B) at 0 °C can be split in two groups: (1) almost linear correlations (AC + CB1 + OLC) and (2) non-linear sorption isotherms. We note that in all cases, by virtue of measuring up to atmospheric pressure, only a small segment of the entire isotherm is accessible at 0 °C. For the first group, we can assume a constant adsorption increase of CO_2 at all measured relative pressures resulting in a homogenous distribution of pores over the range of 0.3–0.9 nm [47,75]. For CDC600 and CDC800, the adsorbed amount is higher in the beginning for a relative pressure below 0.007 compared to the other samples, resulting in a large amount of pores smaller than 0.5 nm [47,75]. The N_2 sorption isotherms in Fig. S1C-F (*Supporting Information*) present a characteristic type I(a) shape for all CDCs and type I(b) for AC, which is related to microporous materials with pores smaller than 1 nm or 2.5 nm, respectively [44]. CB1 shows a mixture of type I(b) isotherm, related to the internal microporosity, and type IV(b) isotherm (mesopores) with a slight H4 hysteresis, which is an indicator for a predominantly microporous and mesoporous material [44]. The high amount of adsorbed nitrogen of CB1 with a specific pore volume of 1.83 $cm^3 \cdot g^{-1}$ (Table 1) is related to its high internal porosity and the large amount of interparticle voids due to the primary particle size of about 50 nm. OLC displays only type IV(b) isotherm (mesopores) with a slight H4 hysteresis since there is no internal porosity, only the nanometer-sized pores between the spheres of OLC particles and agglomerates [76], and the strong increase in the amount of adsorbed nitrogen above a relative pressure of 0.95 is related to voids between OLC agglomerates [77].

Based on the cumulative pore size distribution data (Fig. 1A), we can differentiate (1) exclusive (ultra)microporous carbons (CDCs), (2) micro-mesoporous carbons (AC and CB1), and (3) non-porous carbon onions with a large interparticle pore volume (OLC). In case of CB1, the pore volume above 10 nm is related to interparticle voids, whereas the smaller pores are internal, and in case of OLC there are only interparticle pores due to the closed shell of OLCs. Since the primary OLC particle size is about 5 nm in diameter, there are also micropores between the spherical particles [76]. The general shape of such interparticle pores in OLC materials (i.e., continuously narrowing of ogee-shaped pores) is a severe complication when adapting currently available DFT models which assume slit-, spherical-, or cylindrical shapes (or mixtures thereof) [16,76]. For the studied carbons, a division into two materials with high specific surface area, SSA, (AC, CDCs, CB1) and low SSA (OLC) is possible (Fig. 1B). As seen from Table 1, the DFT-SSA of AC is 1784 $m^2 \cdot g^{-1}$, of CDC ranges from 1346 $m^2 \cdot g^{-1}$ (CDC600) to 1538 $m^2 \cdot g^{-1}$ (CDC1000), of CB1 is 1331 $m^2 \cdot g^{-1}$, and of OLC is

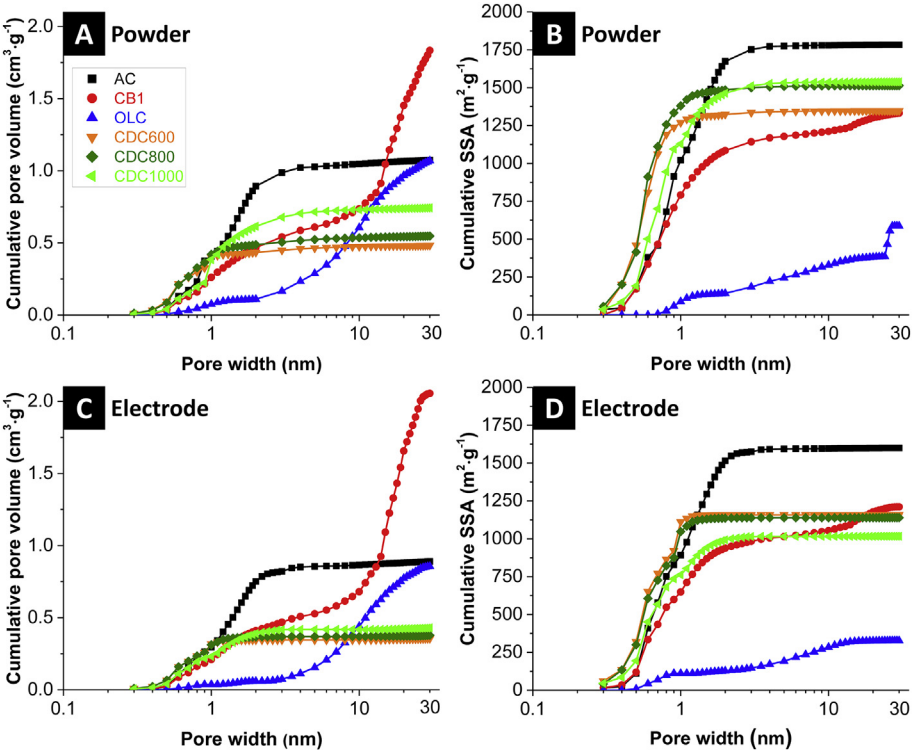

Fig. 1. Cumulative pore volume of (A) powder materials and (C) electrodes containing 10 mass% PTFE. Combined cumulative specific surface area (derived from CO_2 and N_2 sorption data) of (B) powder materials and (D) electrodes containing 10 mass% PTFE.

Table 1
Gas sorption results assuming BET model and combined NLDFT model for CO_2 sorption for pores smaller than 0.9 nm and QSDFT model for N_2 sorption for pores larger than 0.9 nm. Average pore size relates to the volume-weighted arithmetic mean value.

	BET SSA ($m^2 \cdot g^{-1}$)	DFT SSA ($m^2 \cdot g^{-1}$)	Pore volume ($cm^3 \cdot g^{-1}$)	Average pore size (nm)
Powder				
AC	2347	1784	1.08	1.3
CB1	1389	1331	1.83	15
OLC	398	586	1.07	9.7
CDC600	1195	1346	0.48	0.63
CDC800	1324	1513	0.55	0.67
CDC1000	1598	1538	0.74	0.88
Electrode				
AC	1839	1599	0.89	1.3
CB1	1097	1210	2.06	15
OLC	232	328	0.86	9.5
CDC600	934	1159	0.36	0.64
CDC800	977	1140	0.38	0.69
CDC1000	967	1016	0.43	0.90

586 $m^2 \cdot g^{-1}$. The corresponding values for the pore volume are in the range from 0.48 $cm^3 \cdot g^{-1}$ (CDC600) to 1.83 $cm^3 \cdot g^{-1}$ for CB1.

By comparison of powder and electrode data, one can see a general decrease of pore volume and SSA in all but one case (Table 1). The decrease in pore volume ranges between 18% for AC and 42% for CDC1000. A similar trend was found for the DFT-SSA, with a loss between 9% (CB1) and 44% (OLC) when comparing powder data with electrode films. As the only exception, we see for CB1 a decrease in surface area (DFT-SSA decreases by 9%), but the pore volume increases by 13%. This effect may relate to the spatial separation of carbon black nanoparticles during electrode manufacturing. With such great differences, correlation of dry powder pore values (volume or surface) with electrochemical performance of the film electrodes may yield a significant discrepancy (in our case: up to 44%). It is important to note that the pore size distribution remains largely unchanged and the values for average pore size change within a range of only ±5% with or without binder. This indicates that the predominant effect of adding binder is a certain amount of pore blocking over the sub-nanometer pore range.

Characterization of the carbon structure of the used materials by Raman spectroscopy is provided in the *Supporting Information* Table S1 and Fig. S4. In short, all materials were incompletely graphitized with different degrees of carbon ordering; the highest carbon ordering was seen for OLC, the highest disorder for CDC600. Regarding possible heteroatoms and functional surface groups, we have employed EDX analysis and the results show less than 2 atom % oxygen (*Supporting Information*, Table S2). The influence of such low amount of oxygen in aprotic electrolytes can be considered insignificant [78]. With this information and the rectangular shape of the CVs (*Supporting Information*, Fig. S3) we expect a mere double-layer capacitive energy storage for the investigated samples without Faradaic contribution.

3.2. Electrochemical analysis of carbon electrodes

All carbons expressed a pronouncedly capacitive behavior in all used electrolytes (see *Supporting Information*, Fig. S3 for CV data). The electrochemical results are plotted in Fig. 2 as specific capacitance vs. applied voltage for all studied electrolytes using galvanostatic charge/discharge measurements. Table 2 also provides data for the ion sizes (bare/solvated). As it is expected for materials with low or moderate surface area, a low capacitance is measured in all electrolytes for OLC with values typically below 20 $F \cdot g^{-1}$. Higher values, up to ca. 130 $F \cdot g^{-1}$, can be seen for CDC600 (DFT-SSA: 1346 $m^2 \cdot g^{-1}$). For the latter, we already see profound differences between the electrolytes. While a high specific capacitance is seen for CDC600 at +1 V vs. carbon with 1 M TEA-BF_4 in either ACN (127 $F \cdot g^{-1}$) or PC (132 $F \cdot g^{-1}$), only very small values are found in EMIM-BF_4 (61 $F \cdot g^{-1}$ at +1 V vs. carbon). It is important to note that in all three cases, at positive polarization, electrosorption of the same anion (BF_4^-) occurs, but leads to very different charge storage capacities in organic electrolytes or ionic liquid medium. In EMIM-BF_4, CDC800 and AC show the highest specific capacitance at +1 V vs. carbon, namely, 112 $F \cdot g^{-1}$ and 115 $F \cdot g^{-1}$, respectively.

We also note that the capacitance for positive and negative polarization is almost identical at +0.2 and −0.2 V vs. carbon, but increases to various degrees at higher absolute potential. The studied range of applied potential from −1 V to +1 V vs. carbon corresponds with symmetrical full cell voltages between −2 V and +2 V. Within that range, we see to a different degree for all carbons an increase in capacitance at higher potential. With carbon not being a perfect metallic conductor, the density of states (DOS) of charge carriers remains limited, but increases during charging; this gives rise to electrochemical doping and an effective increase in charge screening ability [14,16].

3.3. Normalization of the electrochemical data by total surface area

The electrochemical results normalized to the electrode SSA values are plotted in Fig. 3. In the left column, the specific capacitance is normalized by the BET-SSA and normalized by the DFT-SSA in the right column. The results for 1 M TEA-BF_4 in both organic solvents show a similar behavior of all studied carbons (Fig. 3A–D). The specific capacitance remains quite constant at negative polarization and the larger increase at positive polarization is comparable for all carbon film electrodes. At a potential of +1 V vs. carbon and for both organic solvents, the spread of values for all carbons stretches between 0.06 $F \cdot m^{-2}$ and 0.14 $F \cdot m^{-2}$ for capacitance values normalized by BET-SSA and between 0.05 $F \cdot m^{-2}$ and 0.12 $F \cdot m^{-2}$ for DFT-SSA normalized data. A slightly smaller spread of the values for the different materials is seen when normalizing by DFT-SSA.

The areal capacitance is similar for the ionic liquid electrolyte, ranging from 0.06 $F \cdot m^{-2}$ to 0.11 $F \cdot m^{-2}$ (BET-SSA) and between 0.05 $F \cdot m^{-2}$ and 0.12 $F \cdot m^{-2}$ (DFT-SSA). For OLC, we see also a pronounced increase in capacitance for increased positive polarization. The values for CDC600 are very low (around 0.05 $F \cdot m^{-2}$, see Fig. 3F) compared to TEA-BF_4 in either organic solvent. This aligns with the conflict of small average pore size (0.63 nm) and large size $EMIM^+$ (0.76 × 0.43 nm^2) and a calculated van-der Waals diameter of 0.61 nm [79], so ion access to such small sub-nanometer pores is limited [80]. Yet, the anisotropic shape of the $EMIM^+$ ion can be approximated by a sphere with the diameter of the van-der-Waals

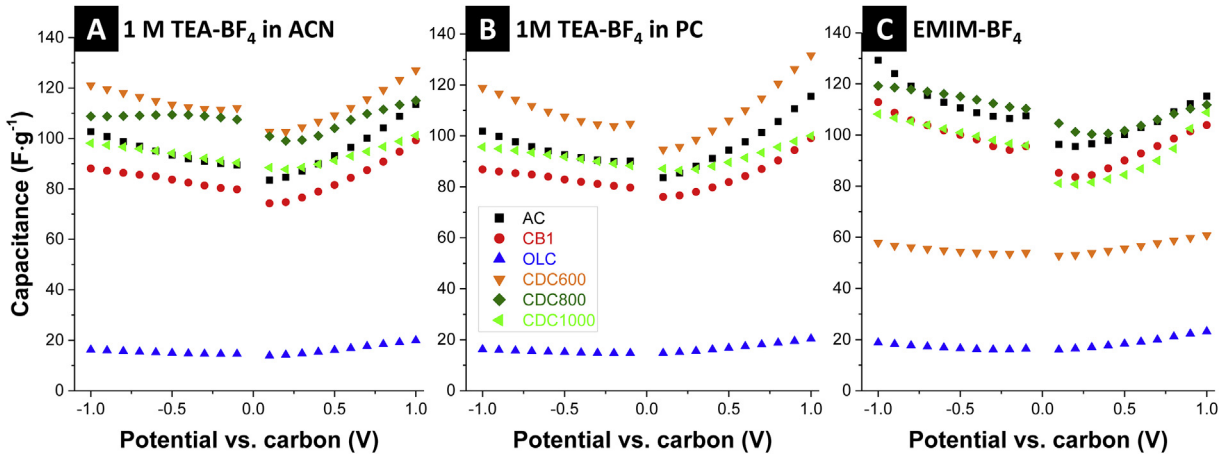

Fig. 2. Specific capacitance in (A) TEA-BF_4/ACN, (B) TEA-BF_4/PC, and (C) EMIM-BF_4. The *y*-axis unit in panel (A) pertains also to panel (B) and (C).

Table 2
Ion size and solvated ion size of the used electrolytes, according to Ref. [84]. Data for the solvent molecule size according to Ref. [91,92].

Ion	TEA^+(nm)	BF_4^-(nm)	$EMIM^+$(nm)	Bare solvent molecule (nm)
Bare ion	0.67	0.45	0.76 × 0.43	–
In ACN	1.3	1.1	–	0.47
In PC	1.4	1.35	–	0.55

calculation [81]. Noticeably, the capacitance at positive polarization remains low, which is surprising when considering the small size of the BF_4^- anion (0.45 nm). We explain this discrepancy by the rather strong cation-anion interaction of the ionic liquid, which does not allow the BF_4^- to enter the pore alone considering its attraction to $EMIM^+$ and a high energy barrier for counter ion repulsion [82,83]. For comparison, CDC800 with an average pore size of 0.69 nm yielded an area-normalized capacitance higher for the IL than for TEA-BF_4/ACN, even though the average pore size is still a bit smaller than the length of the $EMIM^+$, but larger than the van-der-Waals diameter.

3.4. Normalization of the electrochemical data by corrected total surface area

The considerations so far were based on specific capacitance normalized by the entire surface area, measured either by BET or DFT calculations. The data presented so far introduced the issue of ion size conflicting with pore size considerations. We see that the anion is the same in all three studied electrolytes, the capacitance in organic media (normalized by mass or area) varies between solvents and when compared to the neat ionic liquid. As seen from Table 2, the ion size of BF_4^- (0.45 nm) increases because of solvation to 1.1 nm for ACN and to 1.35 nm for PC. The bare ion size of TEA^+ is 0.67 nm and the size increases with solvation to 1.3 nm in case of ACN and 1.4 nm in case of PC [84]. For the IL cation $EMIM^+$, size consideration is complicated by its non-spherical shape. Thus, it is reasonable to assume a lower cut-off value in the pore size distribution and to calculate a surface area corrected for the amount of pores which are non-accessible by the bare ion for geometric reasons [35].

In Fig. 4 we plot the capacitance normalized by the DFT-SSA after subtraction of the inaccessible SSA for ions. The cut-off pore width is related to the bare ion size and the value for BF_4^- is 0.4 nm, for TEA^+ 0.6 nm, and for $EMIM^+$ 0.6 nm. Accordingly, the calculated SSA for pores smaller than the cut-off size was subtracted from the total SSA. With this correction, the areal capacitances of CDC materials increase because of their large amount of sub-nanometer pores. Considering with the difference in anion and cation size, we see a large difference in calculated areal capacitance for positive and negative polarization. For the latter, the values almost double for CDC materials. As an example, we see in 1 M TEA-BF_4 in ACN at +1 V vs. carbon for CDC600 a corrected areal capacitance of 0.12 $F \cdot m^{-2}$, while we obtain 0.24 $F \cdot m^{-2}$ at −1 V vs. carbon. For a material with a very broad pore size dispersion like OLC, we see very small variations of the areal capacitance, for example in 1 M TEA-BF_4 in ACN between 0.04 $F \cdot m^{-2}$ and 0.06 $F \cdot m^{-2}$ (corrected DFT-SSA) up to ±1 V vs. carbon.

3.5. Pore size incremental analysis of electrochemical data

Having a comprehensive set of porosity and electrochemical data, we now compare our results with the values reported by Chmiola et al. [33], namely plotting the BET-SSA normalized capacitance vs. the volume-weighted average pore size (Fig. 5A). As seen, our data align well with the literature and are in line with the recent study by Garcia-Gomez et al. [52] confirming an "anomalous" increase in areal capacitance. It is important to note that we used for this plot data normalized by the electrode surface area, whereas in the literature (with exception of work on monoliths; [52]) only powder data were utilized. We also remind that the BET model is not an accurate tool to investigate highly microporous media, as well-known from the scientific literature and international standards [43,44,51,85]. Second, we used the approach by the Centeno group, namely to normalize the electrochemical data by the "relevant" porosity (Fig. 5B). The "regular pattern" in capacitance normalized to the DFT-SSA with a mean capacitance about 0.09 ± 0.2 F m^{-2} (grey box in Fig. 5B) is also confirmed by our measurements in accordance with the data from Centeno et al. [50] and Chmiola et al. [33]. In conclusion, depending on the normalization, our data are seemingly in agreement with both the anomalous and the regular pattern model.

Calculation of a single value (average pore size) for carbons with not perfectly unimodal pore size dispersity will generate a severe complication [56], making a pore size incremental analysis of capacitive contribution necessary. In our model, we corrected the DFT-SSA by subtracting the inaccessible SSA for the respective bare ions in the electrolyte as described in *Section 3.4*. This aligns well with the procedure by which the data in Fig. 4 were obtained. For organic electrolytes, the DFT-SSA is subtracted by the cumulative SSA value for pores to 0.4 nm in case of positive polarization

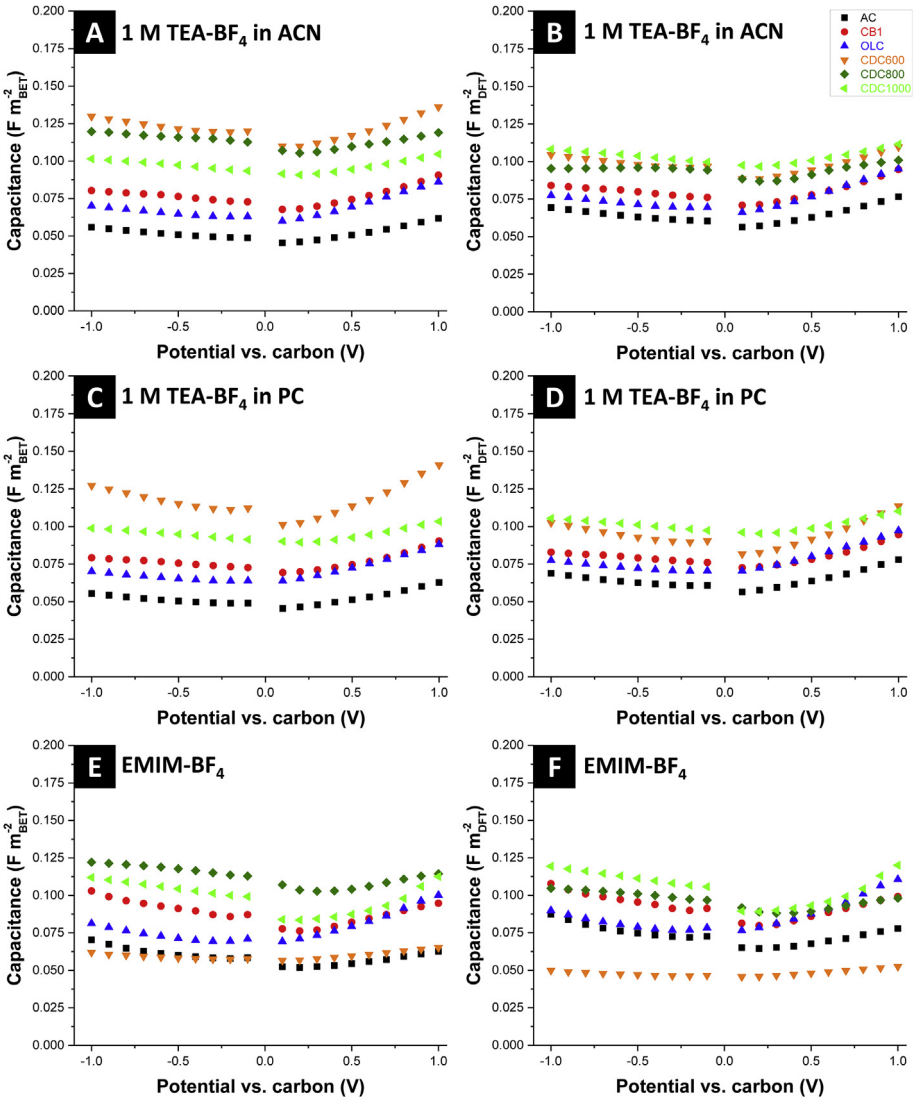

Fig. 3. Areal capacitance of all materials in (A + B) TEA-BF_4/ACN, (C + D) TEA-BF_4/PC, and (E + F) EMIM-BF_4. (A + C + E) Capacitance normalized to BET-SSA and (B + D + F) to entire DFT-SSA assuming slit-shaped pores.

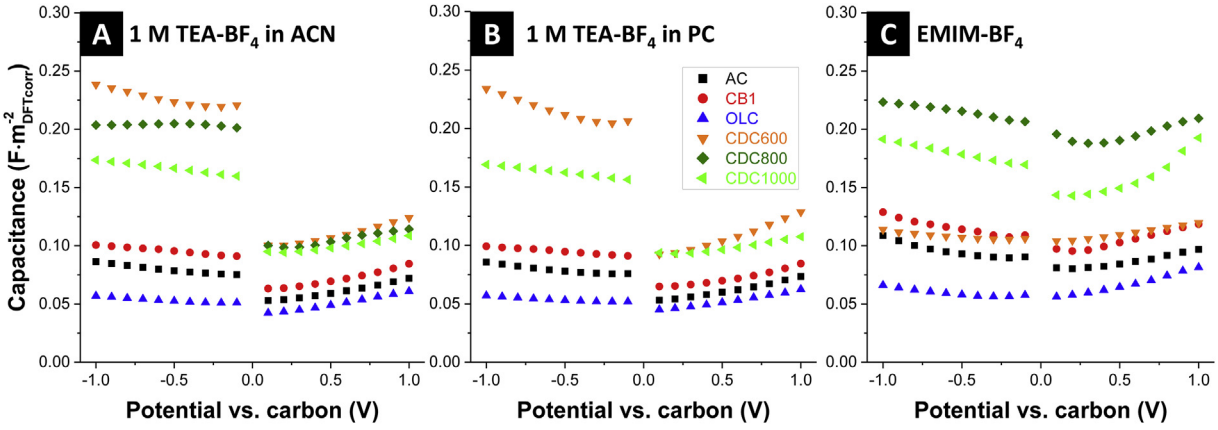

Fig. 4. Areal capacitance normalized to the DFT-SSA after subtraction of inaccessible SSA for ions. (A) TEA-BF_4/ACN, (B) TEA-BF_4/PC, (C) EMIM-BF_4. Cut-off pore width for BF_4^- 0.4 nm, for TEA^+ 0.6 nm, and for $EMIM^+$ 0.6 nm.

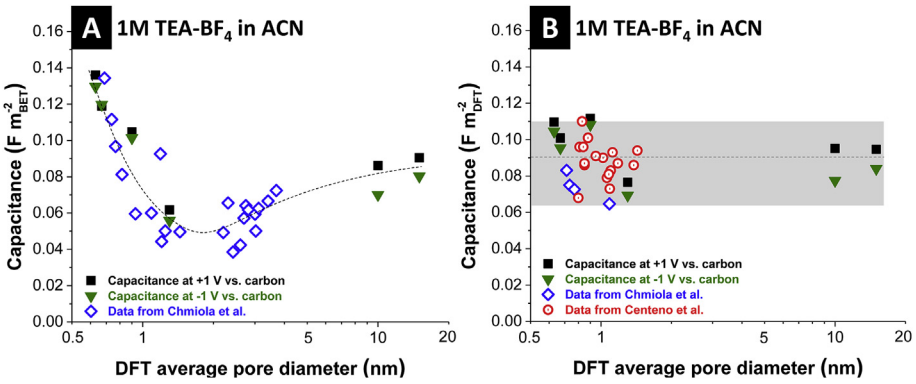

Fig. 5. (A) Specific capacitance normalized to the BET-SSA and the volume-weighted DFT average pore diameter, including data from Ref. [33]. (B) Specific capacitance normalized to the DFT-SSA assuming slit-like pores and the DFT average pore diameter, including data from Ref. [33] and Ref. [50]. The dashed lines and the grey box have been added as a guide to the eye.

(diameter BF_4^- is 0.45 nm) and 0.6 nm for negative polarization (diameter TEA^+ is 0.67 nm). For IL, the DFT-SSA data were corrected for both polarization directions by the cumulative SSA at 0.6 nm.

At first, we follow the approach of Centeno et al. [50] and calculate the capacitance of the studied materials assuming the same "importance" of all pores. This was done in Fig. 6A in 1 M TEA-BF_4 in ACN for +1 V vs. carbon. The results are plotted in a parity plot, where the measured capacitance is related to the *x*-axis vs. the calculated capacitance at the *y*-axis. This mean value calculation of capacitance (106 $F \cdot g^{-1}$) results in a strong difference between calculated and measured capacitance (mean squared error, MSE = 1.3%). Especially the values for OLC diverge in a 6 times higher calculated capacitance than measured. In case of CDC600, the calculated capacitance is 15% smaller than the measured value.

To reduce the deviation between calculated and measured value, we implemented the assumption of a pore size dependent ion electrosorption capacity (Fig. 6B). By fitting the values for all materials, we find an optimal solution at +0.2 V vs. carbon for 100 $F \cdot g^{-1}$ for pores smaller 1 nm and 124 $F \cdot g^{-1}$ for 1–2 nm pores. In agreement with the literature [66,86], we assumed an exponential decrease of the capacitive contribution of pores larger than the size of two (solvated) ions. With this assumption, we significantly reduced the average error (MSE = 0.09%) and the discrepancy between calculated and measured capacitance is below 10%. Larger deviations were only observed for OLC. The average error increases significantly (MSE = 0.73%, Fig. 6C) if we use the capacitance of the measured dry powder SSA with cutting-off pores smaller than the bare ion diameter.

An overview of the calculated data with the new model is provided in Fig. 7 in the form of parity plots. The insets show the calculated capacitance values in $F \cdot g^{-1}$ normalized by the mean density of all studied materials, since the areal and the gravimetric capacitance are linked by the density of the material. With the data of Fig. 7A, we first explored the positive polarization regime for 1 M TEA-BF_4 in ACN at +0.2 V and +1 V vs. carbon. The capacitance increased with higher applied potential, as seen already for the total gravimetric capacitance depicted in Fig. 4A. Regarding the calculated contribution of (partially) desolvated BF_4^- and fully solvated ions, we can see in accordance to the literature a strong increase of importance of pores large enough to accommodate solvated ions in the range of 1–2 nm when we apply higher voltage [73,87]. For (partially) desolvated ions, the importance does only slightly increase. At +0.2 V vs. carbon, the ratio between solvated and desolvated ions is 1.25:1 and this ratio increases to 1.6:1 at +1 V vs. carbon. The very small bare ion size of 0.45 nm and the strong electronegative field of BF_4^- resulting in typically 9 ACN molecules in the solvation shell [88] cause almost immediate desolvation even without applied potential and the degree of solvation increases only slightly with applied voltage [73]. Noticeably, OLC does not fit well into this correlation. This can be explained by the

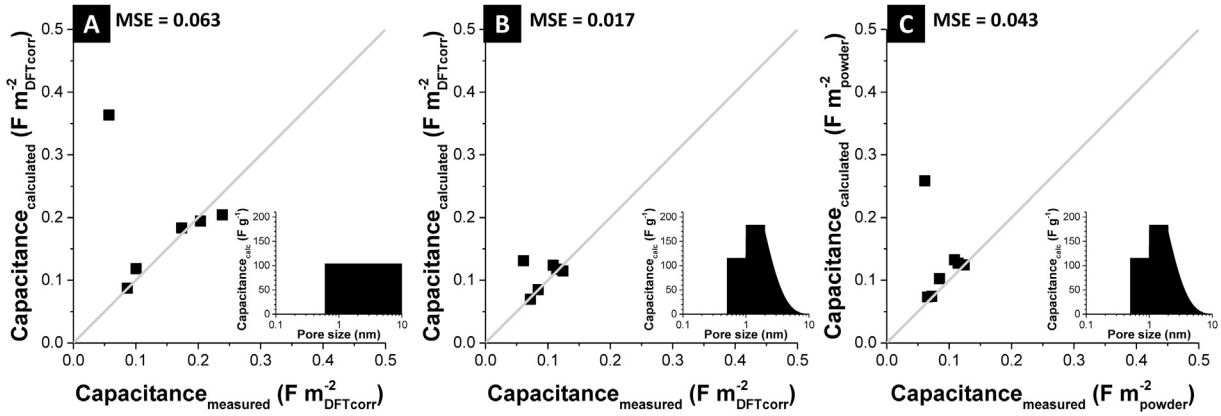

Fig. 6. Parity plot of measured capacitance normalized to the corrected DFT-SSA vs. calculated capacitance for positive (BF_4^- adsorption) polarization at 1 V vs. carbon in TEA-BF_4/ACN. (A) Results with assuming same contribution of capacitance for all pores, (B) results normalized to the value of the film electrode SSA with weighting the pore increments, and (C) results normalized to the corrected DFT-SSA of dry powder with weighting importance of pores. The grey lines indicate the parity line (i.e., perfect agreement between calculated and measured values). MSE: mean squared error.

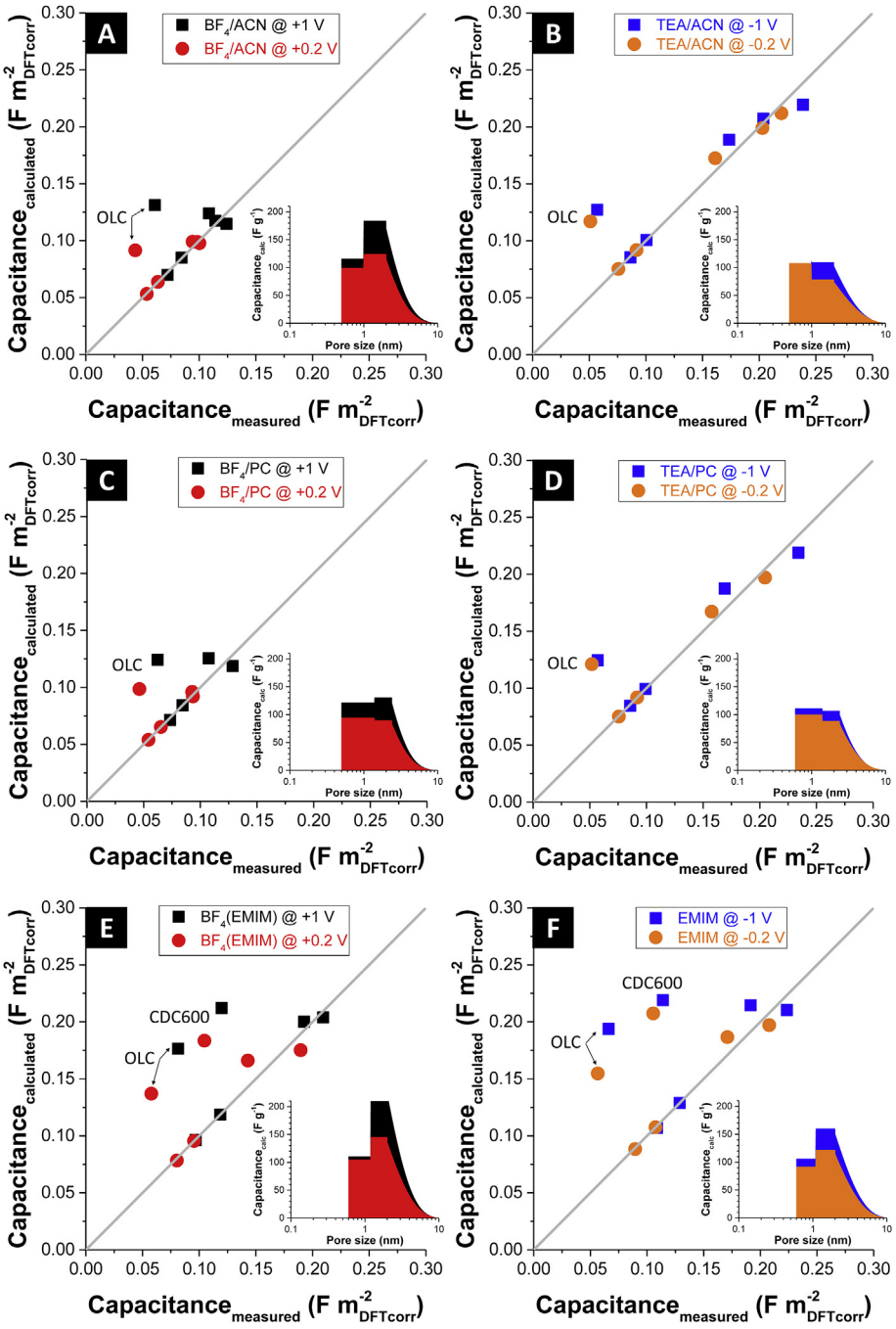

Fig. 7. Parity plots for all systems. First row TEA-BF_4/ACN, second row TEA-BF_4/PC, and third row the ionic liquid EMIM-BF_4. Results in the left column belong to positive polarization, on the right column for negative polarization (potential vs. carbon). Insights show the weighting factors for certain pore sizes, recalculated in Farad per gram. Outliers are marked and explained in text.

profoundly different porosity character: OLC has ogee-shaped pores with continuous narrowing between single (spherical) carbon onion particles. Yet, none of the currently available DFT pore models adequately can handle such nanometer sized pores with positive curvature and we assume the calculated differences to stem from possible fluctuation in the pore size distribution data by assuming incorrectly slit-shaped pores [16].

For negative polarization and the electrosorption of TEA^+ (Fig. 7B), the values for gravimetric capacitance are generally lower since the ion is much larger than BF_4^- and there are much more inaccessible pores. The importance of pores with desolvated ions remains constant over the studied voltage range, but the amount of solvated ions increases with higher voltage (Fig. 7B) since the energetic minimum is reached by accommodation of solvated ions instead of more desolvation and "squeezing" into the smallest accessible pores.

Now, we compare the aforementioned data of 1 M TEA-BF_4 in ACN with the same salt in PC, which exhibits a higher viscosity [89]. The amount of PC molecules in the solvation shell decrease to 8 for BF_4^- and 4 for TEA^+, resulting in a different solvated ion size compared to ACN (Table 2) [88]. This explains a different degree of (partially) desolvation. The plot for positive polarization (Fig. 7C)

shows a slightly larger contribution of fully solvated ions for +1 V vs carbon. This ratio now favors an enhanced importance of (partially) desolvated ions at lower potential. We conclude a more pronounced desolvation of ions, especially at low potentials compared to ACN as a result of the smaller polarity of PC and a larger molecule size (Table 2). Ions prefer (partial) desolvation in PC more than in ACN, even when there are fewer molecules in the solvation shell in PC. The outlier OLC is related to the aforementioned issues with the PSD calculations. At negative potentials (Fig. 7D), the ratio of solvated and (partially) desolvated remains constant for both potentials (i.e., −0.2 V and −1 V vs. carbon) at 1:1.1 with more impact of desolvated ions than solvated ones. For an optimized EDLC electrode material design strategy, we note that for ACN the amount of sub-nanometer pores may not need to be as high as it is for PC because of the preferred desolvation in PC and the stronger ion-solvent interaction for ACN.

Finally, we investigate the behavior of solvent-free ionic liquid electrolyte (EMIM-BF_4; Fig. 7E–F). For positive polarization (Fig. 7E), we calculated a very high contribution of pores larger than one BF_4^- ion. The ratio of impact for pores containing one and two ions is 1:2.2 at +1 V vs. carbon and 1:1.3 at +0.2 V vs. carbon. For these results we have to consider the very high viscosity of IL compared to organic electrolytes and the large attractive force of cations and anions in the electrolyte. The strong influence of pores larger than the size of one ion can be correlated to the report of Wang et al. where a confinement of ions in nanometer sized pores is resulting in certain favorable ion packing mechanisms [81]. The authors reported an effective ion diameter of 0.97 nm for $EMIM^+$, which means access for these ions to our second range from 1 to 2 nm [81]. The outlier CDC600 is related to the large amount of pores smaller than the ion size of $EMIM^+$. BF_4^- seems not to enter the pores without $EMIM^+$ because of their high affinity to the cation, even though the pores would provide ample size for preferential anion adsorption. Even though some ions can enter the pore the high packing density of the ions in the IL and the absence of solvation molecules produce a high energy barrier for co-ion adsorption or counter-ion repulsion at the pore entrance [90]. The results are similar for negative polarization (Fig. 7F), but with lower values for the incremental capacitance due to the larger size of $EMIM^+$ and a consequent larger force needed to fit into the smallest pores.

4. Conclusions

This study provides a comprehensive dataset of six microporous carbons tested in three different electrolytes (i.e., two organic electrolytes and one room temperature ionic liquid). The electrochemical results and the pore size distribution are correlated by a model considering the size of ions and the impact of the solvation shell. From these data, a few key considerations can be projected onto future carbon design strategies for EDLC electrode materials. First, it is important to consider all pores and the entirety of the pore volume and we have to consider that carbon electrodes differ in porosity from the dry carbon powders, while the average pore size can be assumed to remain rather unchanged. Second, by applying a pore size incremental model we see that pores too small for the fully solvated ion must also contribute to the charge storage mechanism since the observed capacitances cannot be explained without ion desolvation. Yet, the latter does not account for the majority of electrosorbed ions and even at elevated potentials the pores with sufficient diameter to accommodate solvated ions are relatively more important. Our data can be explained when assuming a stronger solvation for BF_4^- in ACN than in PC and the impact of pores larger than one solvated ion is much larger in the case of ACN. For negative polarization, the values are quite constant for both organic electrolytes with a less strong solvation shell adherence and a higher impact of pores containing (partially) desolvated ions. For the ionic liquid, the impact of pores larger than the bare ion size is much larger (up to 2.3-times) than the pores containing only one ion for positive and negative polarization. Summarizing, in organic media with solvent molecules, size differences between anions and cations have a strong impact on the single electrode capacitance when accounting for the difference in ion accessible pore volume. However, these considerations cannot be directly translated to ionic liquids, where the strong interaction between cations and anions excludes the possibility to treat ions quasi as “desolvated”.

As for the validity of either the anomalous or regular pattern, we conclude that both models do not adequately implement the issue of pore size dispersity of practical carbon materials. Both patterns can be recreated by our data, depending on the normalization strategy. Yet, a predictive tool to calculate the expected capacitance of a material should rather be based on a pore size incrementing approach which adopts a varying contribution of certain pores to the total capacitance of the electrodes.

Acknowledgements

We acknowledge funding from the German Federal Ministry for Research and Education (BMBF) in support of the nanoEES^{3D} project (award number 03EK3013) as part of the strategic funding initiative energy storage framework. The authors acknowledge additional funding via the INM FOCUS project IZIcap and thank Prof. Eduard Arzt (INM) for his continuing support and Prof. Guang Feng (HUST) and Dr. Lars Borchardt (TU Dresden) for helpful discussions.

Appendix A. Supplementary data

Supplementary data related to this article can be found at http://dx.doi.org/10.1016/j.jpowsour.2016.03.015.

References

[1] J.R. Miller, Science 335 (2012) 1312–1313.
[2] F. Beguin, E. Frackowiak, Supercapacitors, Wiley, Weinheim, 2013.
[3] W. Gu, G. Yushin, Wiley Interdiscip. Rev. Energy Environ. 3 (2014) 424–473.
[4] P. Ball, MRS Bull. 37 (2012) 802–803.
[5] J.R. Miller, P. Simon, Science 321 (2008) 651–652.
[6] B.E. Conway, Electrochemical Supercapacitors, Springer, Berlin, 1999.
[7] F. Beguin, V. Presser, A. Balducci, E. Frackowiak, Adv. Mater. 26 (2014) 2219–2251.
[8] P. Simon, Y. Gogotsi, B. Dunn, Science 343 (2014) 1210–1211.
[9] S. Zhang, N. Pan, Adv. Energy Mater. 5 (2015) aenm.201401401.
[10] G. Wang, L. Zhang, J. Zhang, Chem. Soc. Rev. 41 (2012) 797–828.
[11] Y. Zhai, Y. Dou, D. Zhao, P.F. Fulvio, R.T. Mayes, S. Dai, Adv. Mater. 23 (2011) 4828–4850.
[12] A.G. Pandolfo, A.F. Hollenkamp, J. Power Sources 157 (2006) 11–27.
[13] A.A. Kornyshev, N.B. Luque, W. Schmickler, J. Solid State Electr. 18 (2014) 1345–1349.
[14] H. Gerischer, R. McIntyre, D. Scherson, W. Storck, J. Phys. Chem. 91 (1987) 1930–1935.
[15] P.W. Ruch, R. Kötz, A. Wokaun, Electrochimica Acta 54 (2009) 4451–4458.
[16] D. Weingarth, M. Zeiger, N. Jäckel, M. Aslan, G. Feng, V. Presser, Adv. Energy Mater. 4 (2014) 1400316.
[17] J.S. Moon, H. Kim, D.-C. Lee, J.T. Lee, G. Yushin, J. Electrochem. Soc. 162 (2015) A5070–A5076.
[18] J.D. Wiggins-Camacho, K.J. Stevenson, J. Phys. Chem. C 113 (2009) 19082–19090.
[19] Y. Yamada, T. Tanaka, K. Machida, S. Suematsu, K. Tamamitsu, H. Kataura, H. Hatori, Carbon 50 (2012) 1422–1424.
[20] P.M. Biesheuvel, Y. Fu, M.Z. Bazant, Phys. Rev. E 83 (2011) 061507.
[21] P.M. Biesheuvel, J. Colloid Interface Sci. 238 (2001) 362–370.
[22] O. Stern, Z. für Elektrochem. Angew. Phys. Chem. 30 (1924) 508–516.
[23] D.L. Chapman, Philos. Mag. 25 (1913) 475–481.
[24] L.G. Gouy, J. de Physique Théorique Appliquée 9 (1910) 457–468.
[25] J. Segalini, E. Iwama, P.-L. Taberna, Y. Gogotsi, P. Simon, Electrochem. Commun. 15 (2012) 63–65.

[26] T. Brousse, D. Bélanger, J.W. Long, J. Electrochem. Soc. 162 (2015) A5185–A5189.
[27] A. Laheäär, P. Przygocki, Q. Abbas, F. Béguin, Electrochem. Commun. 60 (2015) 21–25.
[28] B. Akinwolemiwa, C. Peng, G.Z. Chen, J. Electrochem. Soc. 162 (2015) A5140–A5147.
[29] M. Inagaki, H. Konno, O. Tanaike, J. Power Sources 195 (2010) 7880–7903.
[30] P.B. Peters, R. van Roij, M.Z. Bazant, P.M. Biesheuvel, ArXiv, 1512.04261 (2016).
[31] P.R. Bandaru, H. Yamada, R. Narayanan, M. Hoefer, Mater. Sci. Eng. R 96 (2015) 1–69.
[32] E. Raymundo-Piñero, K. Kierzek, J. Machnikowski, F. Béguin, Carbon 44 (2006) 2498–2507.
[33] J. Chmiola, G. Yushin, Y. Gogotsi, C. Portet, P. Simon, P.L. Taberna, Science 313 (2006) 1760–1763.
[34] S. Porada, L. Weinstein, R. Dash, A. van der Wal, M. Bryjak, Y. Gogotsi, P.M. Biesheuvel, ACS Appl. Mater. Interfaces 4 (2012) 1194–1199.
[35] G. Salitra, A. Soffer, L. Eliad, Y. Cohen, D. Aurbach, J. Electrochem. Soc. 147 (2000) 2486–2493.
[36] B. Kastening, S. Spinzig, J. Electroanal. Chem. 214 (1986) 295–302.
[37] B. Dyatkin, V. Presser, M. Heon, M.R. Lukatskaya, M. Beidaghi, Y. Gogotsi, Chemsuschem 6 (2013) 2269–2280.
[38] M. Aslan, D. Weingarth, N. Jäckel, J.S. Atchison, I. Grobelsek, V. Presser, J. Power Sources 266 (2014) 374–383.
[39] P. Kleszyk, P. Ratajczak, P. Skowron, J. Jagiello, Q. Abbas, E. Frąckowiak, F. Béguin, Carbon 81 (2015) 148–157.
[40] Y. Gogotsi, A. Nikitin, H. Ye, W. Zhou, J.E. Fischer, B. Yi, H.C. Foley, M.W. Barsoum, Nat. Mater. 2 (2003) 591–594.
[41] A. Jänes, T. Thomberg, H. Kurig, E. Lust, Carbon 47 (2009) 23–29.
[42] G. Laudisio, R.K. Dash, J.P. Singer, G. Yushin, Y. Gogotsi, J.E. Fischer, Langmuir 22 (2006) 8945–8950.
[43] S. Brunauer, P.H. Emmett, E. Teller, J. Am. Chem. Soc. 60 (1938) 309–319.
[44] M. Thommes, K. Kaneko, A.V. Neimark, J.P. Olivier, F. Rodriguez-Reinoso, J. Rouquerol, K.S.W. Sing, Pure Appl. Chem. 87 (2015) 1051–1069.
[45] J. Jagiello, C. Ania, J.B. Parra, C. Cook, Carbon 91 (2015) 330–337.
[46] G.Y. Gor, M. Thommes, K.A. Cychosz, A.V. Neimark, Carbon 50 (2012) 1583–1590.
[47] J. Landers, G.Y. Gor, A.V. Neimark, Colloids Surf. A Physicochem. Eng. Asp. 437 (2013) 3–32.
[48] A.M. Puziy, O.I. Poddubnaya, B. Gawdzik, M. Sobiesiak, Adsorption (2015) 1–6.
[49] L.L. He, S.M. Chathoth, Y.B. Melnichenko, V. Presser, J. McDonough, Y. Gogotsi, Microporous Mesoporous Mater. 149 (2012) 46–54.
[50] T.A. Centeno, O. Sereda, F. Stoeckli, Phys. Chem. Chem. Phys. 13 (2011) 12403–12406.
[51] F. Stoeckli, T.A. Centeno, Phys. Chem. Chem. Phys. 14 (2012) 11589–11591.
[52] A. Garcia-Gomez, G. Moreno-Fernandez, B. Lobato, T.A. Centeno, Phys. Chem. Chem. Phys. 17 (2015) 15687–15690.
[53] D. Jiang, Z. Jin, J. Wu, Nano Lett. 11 (2011) 5373–5377.
[54] G. Feng, P.T. Cummings, J. Phys. Chem. Lett. 2 (2011) 2859–2864.
[55] D. Jiang, Z. Jin, D. Henderson, J. Wu, J. Phys. Chem. Lett. 3 (2012) 1727–1731.
[56] S. Kondrat, C.R. Perez, V. Presser, Y. Gogotsi, A. Kornyshev, Energ Environ. Sci. 5 (2012) 6474–6479.
[57] G. Feng, S. Li, V. Presser, P.T. Cummings, J. Phys. Chem. Lett. 4 (2013) 3367–3376.
[58] S. Pohlmann, B. Lobato, T.A. Centeno, A. Balducci, Phys. Chem. Chem. Phys. 15 (2013) 17287–17294.
[59] S. Pohlmann, R.-S. Kühnel, T.A. Centeno, A. Balducci, ChemElectroChem 1 (2014) 1301–1311.
[60] D.T.L. Galhena, B.C. Bayer, S. Hofmann, G.A.J. Amaratunga, ACS Nano (2015).
[61] J. Chmiola, C. Largeot, P.-L. Taberna, P. Simon, Y. Gogotsi, Angew. Chem. Int. Ed. 47 (2008) 3392–3395.
[62] L. Zhang, X. Yang, F. Zhang, G. Long, T. Zhang, K. Leng, Y. Zhang, Y. Huang, Y. Ma, M. Zhang, Y. Chen, J. Am. Chem. Soc. 135 (2013) 5921–5929.
[63] D. Jiang, J. Wu, J. Phys. Chem. Lett. 4 (2013) 1260–1267.
[64] A.A. Lee, D. Vella, A. Goriely, S. Kondrat, ArXiV, 1510.05595 (2015).
[65] W. Hsieh, T.-L.A. Horng, H.-C. Huang, H. Teng, J. Mater. Chem. A 3 (2015) 16535–16543.
[66] S. Porada, L.O. Borchardt, M.M. Bryjak, J.S. Atchison, K.J. Keesman, S. Kaskel, P.M. Biesheuvel, V. Presser, Energ Environ. Sci. 6 (2013) 3700–3712.
[67] D. Weingarth, A. Foelske-Schmitz, A. Wokaun, R. Kötz, Electrochem. Commun. 18 (2012) 116–118.
[68] P.W. Ruch, D. Cericola, M. Hahn, R. Kötz, A. Wokaun, J. Electroanal. Chem. 636 (2009) 128–131.
[69] P.I. Ravikovitch, A. Vishnyakov, A.V. Neimark, Phys. Rev. E 64 (2001) 011602.
[70] J. Jagiello, M. Thommes, Carbon 42 (2004) 1227–1232.
[71] J. Silvestre-Albero, A. Silvestre-Albero, F. Rodríguez-Reinoso, M. Thommes, Carbon 50 (2012) 3128–3133.
[72] V. Presser, J. McDonough, S.H. Yeon, Y. Gogotsi, Energ Environ. Sci. 4 (2011) 3059–3066.
[73] J.M. Griffin, A.C. Forse, W.Y. Tsai, P.L. Taberna, P. Simon, C.P. Grey, Nat. Mater. 14 (2015) 812–819.
[74] M. Sevilla, S. Álvarez, T.A. Centeno, A.B. Fuertes, F. Stoeckli, Electrochimica Acta 52 (2007) 3207–3215.
[75] A. Vishnyakov, P.I. Ravikovitch, A.V. Neimark, Langmuir 15 (1999) 8736–8742.
[76] M. Zeiger, N. Jäckel, M. Aslan, D. Weingarth, V. Presser, Carbon 84 (2015) 584–598.
[77] N. Jäckel, D. Weingarth, M. Zeiger, M. Aslan, I. Grobelsek, V. Presser, J. Power Sources 272 (2014) 1122–1133.
[78] T.A. Centeno, M. Hahn, J.A. Fernández, R. Kötz, F. Stoeckli, Electrochem. Commun. 9 (2007) 1242–1246.
[79] H. Tokuda, K. Hayamizu, K. Ishii, M.A.B.H. Susan, M. Watanabe, J. Phys. Chem. B 109 (2005) 6103–6110.
[80] C. Largeot, C. Portet, J. Chmiola, P.-L. Taberna, Y. Gogotsi, P. Simon, J. Am. Chem. Soc. 130 (2008) 2730–2731.
[81] X. Wang, H. Zhou, E. Sheridan, J.C. Walmsley, D. Ren, D. Chen, Energ Environ. Sci. 9 (2016) 232–239.
[82] S. Baldelli, Acc. Chem. Res. 41 (2008) 421–431.
[83] S. Baldelli, J. Phys. Chem. B 109 (2005) 13049–13051.
[84] M.M. Hantel, D. Weingarth, R. Kötz, Carbon 69 (2014) 275–286.
[85] T.A. Centeno, F. Stoeckli, Carbon 48 (2010) 2478–2486.
[86] J. Huang, B.G. Sumpter, V. Meunier, G. Yushin, C. Portet, Y. Gogotsi, J. Mater. Res. 25 (2010) 1525–1531.
[87] M. Deschamps, E. Gilbert, P. Azais, E. Raymundo-Piñero, M.R. Ammar, P. Simon, D. Massiot, F. Béguin, Nat. Mater. 12 (2013) 351–358.
[88] Y.-J. Kim, Y. Masutzawa, S. Ozaki, M. Endo, M.S. Dresselhaus, J. Electrochem. Soc. 151 (2004) E199–E205.
[89] M. Arulepp, L. Permann, J. Leis, A. Perkson, K. Rumma, A. Jänes, E. Lust, J. Power Sources 133 (2004) 320–328.
[90] M.V. Fedorov, A.A. Kornyshev, Chem. Rev. 114 (2014) 2978–3036.
[91] M. Ue, J. Electrochem. Soc. 141 (1994) 3336–3342.
[92] B.J. Loughnane, R.A. Farrer, A. Scodinu, J.T. Fourkas, J. Chem. Phys. 111 (1999) 5116–5123.

4.3 Increase in Capacitance by Subnanometer Pores in Carbon

N. Jäckel [a,b], P. Simon [c,d], Y. Gogotsi [e], V. Presser [a,b]

[a] INM—Leibniz Institute for New Materials, Campus D2 2, 66123 Saarbrücken, Germany

[b] Department of Materials Science and Engineering, Saarland University, Campus D2 2, 66123 Saarbrücken, Germany

[c] Université Paul Sabatier, CIRIMAT UMR, CNRS 5085, 5085, 31062 Toulouse Cedex 4, France

[d] Réseau sur le Stockage Electrochimique de l'Energie, RS2E FR CNRS 3459, France

[e] Department of Materials Science and Engineering & A. J. Drexel Nanotechnology Institute, PA 19104 Philadelphia, USA

published in ACS Energy Letters, 2016. 1(6): p. 1262-1265

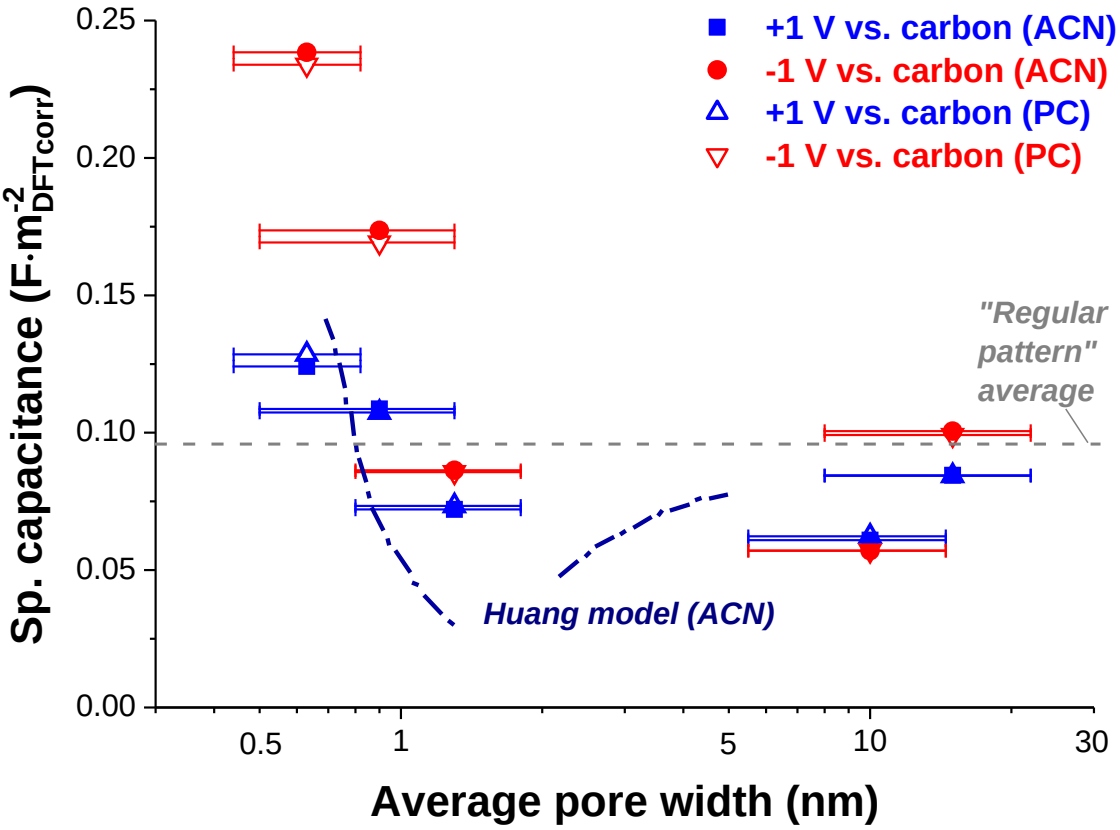

Own contribution:

Data generation 25 %

Data analysis 90 %

Interpretation 90 %

Writing 80 %

Supporting Information:

Appendix B

ACS Energy LETTERS

http://pubs.acs.org/journal/aelccp

VIEWPOINT

Increase in Capacitance by Subnanometer Pores in Carbon

Electrical double-layer capacitors (EDLCs, also known as supercapacitors or ultracapacitors) store energy by electrosorption of ions at the electrode/electrolyte interface.[1] To achieve a high-energy storage capacity, electrodes with a high surface area and well-developed pore structure in the range from several Angstroms to several tens of nanometers are required.[2] However, neither natural precursor-derived carbons nor templated carbon materials present an ideal, infinitesimally narrow pore size dispersion.[3]

In EDLCs, the use of salt dissolved in an organic or aqueous solvent makes it important to consider the solvation shell around the ions. The bare ion size is usually below 1 nm, whereas the solvation shell can increase the size significantly.[3] Several studies have provided strong evidence of ion desolvation during electrosorption, which is the only way to explain why carbon materials with pore sizes smaller than the solvated ion but larger than the bare ion have high charge storage capacities.[4−8] A maximized capacitance (normalized by the surface area) was found in experimental and theoretical studies when matching the pore size with the ion size.[9] This effect seems to be universally applicable for solvent-containing and solvent-free electrolytes (ionic liquids), while important secondary differences are to be considered for the latter. For example, the oscillatory dependency of capacitance on pore size predicted for neat ionic liquids and ideal carbons with slit pores is lost when introducing a solvent, where a single maximum is observed when the ion size and the pore size are identical.[10,11]

This Viewpoint clarifies the correlation between capacitance and pore size, which is of high practical importance for the design of advanced carbon electrode materials. Two extreme cases are obvious: excessively large pores, accompanied by large pore volumes and limited specific surface area, will lead to a low energy storage capacity, whereas very small pores will limit the ion access due to steric effects (Figure 1), in addition to imposing obstacles to ion transport.[12,13] Yet, for the intermediate range, down to the point when the pores are too small for the bare ion to fit, there is no consent in the literature about the correlation between the pore size and the corresponding area-normalized capacitance. For example, there has been criticism about the method of surface area determination and normalization, especially considering the inadequacy of the Brunauer−Emmett−Teller (BET) model for microporous carbons.[14,15] Benchmarking various kinds of carbons, including carbon monoliths, a "regular pattern" was presented, suggesting that the area-normalized capacitance does not depend on the pore size.[14,16] This lack of dependence can be explained by neither the ab initio or molecular dynamics models[17,18] nor geometric considerations as when the pore diameter increases by 50−90%, there is still just one ion in each pore contributing to charge storage and the remaining surface area and pore volume remain unused, decreasing the capacitance normalized by the pore surface or volume.

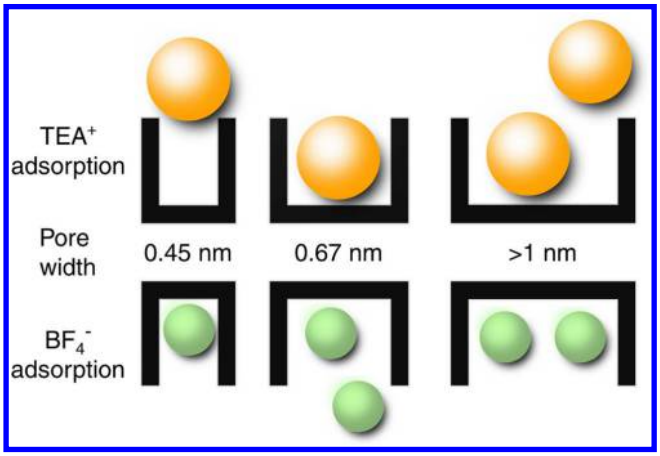

Figure 1. Electrosorption of specific ions with a finite size is only possible if the pore size is at least equal to the ion size. Therefore, the specific surface area of pores smaller than the bare ion size is inaccessible for energy storage. Larger pores can adsorb more than one ion per pore.

Recently, we developed a model for understanding the capacitance of microporous carbons, taking into account the entire measured pore size distribution, and have established a comprehensive data set of electrochemical measurements.[6] Density functional theory (DFT) kernels were used, which are currently the most advanced methodology to extract porosity data from gas sorption isotherms for meso- and microporous carbons and effectively avoid the fundamental limitations of the BET theory.[19] Activated carbon showed the highest specific surface area (SSA), followed by two different titanium carbide-derived carbons (CDCs),[20] activated carbon black (CB), and carbon onions.[21] Yet, when normalizing electrochemical performance data on porosity values, we first have to consider differences between dry powder and film electrodes.[6] Then, we have to assess the differences in pore size distributions; these are shown in Figure 2A normalized to 100% for the aforementioned carbon materials. Many carbons display a significant dispersion width; this is why the often-used volume-weighted average pore size d_{50} does not fully capture the pore size distribution width, as we show by adding values for d_{25} and d_{75}, representing the pore width encompassing 25 and 75% of the total pore volume, respectively (Table 1, Figure 2A).

More differences in the surface area of the different electrode materials become evident when we calculate the electrochemically active surface, that is, the ion-accessible surface area (Table 1, Figure 2B). Taking into account the bare ion size of BF_4^- (0.45 nm) and TEA^+ (0.67 nm), pores smaller than these

Received: October 9, 2016
Accepted: November 4, 2016
Published: November 21, 2016

DOI: 10.1021/acsenergylett.6b00516
ACS Energy Lett. 2016, 1, 1262−1265

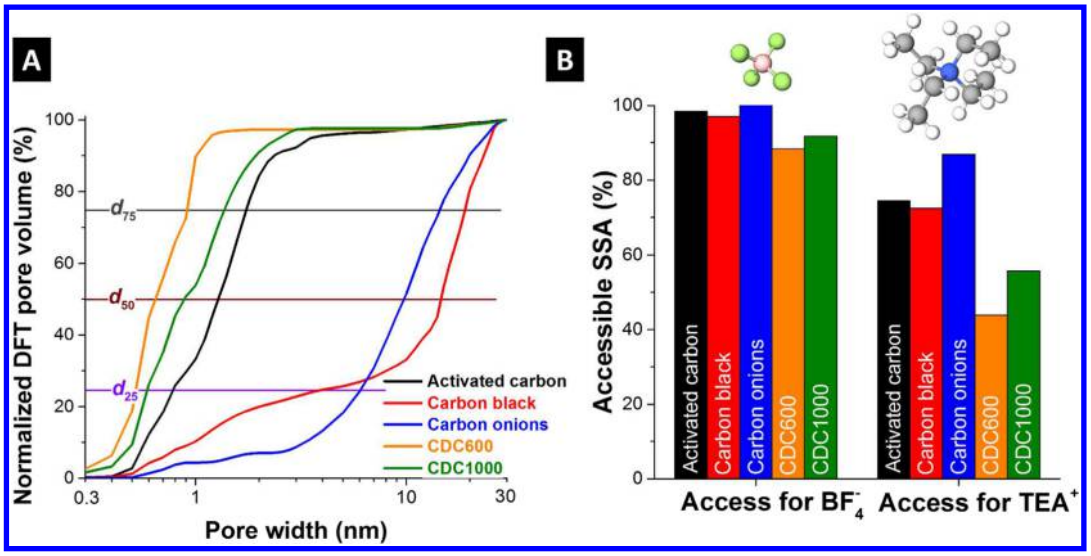

Figure 2. (A) The cumulative pore size distribution of electrodes was derived by combining CO_2 and N_2 sorption and normalizing all data to 100%. (B) Porosity analysis of different carbon electrode materials using a DFT model. Data are normalized for SSA of electrodes containing 10 mass% PTFE as 100% and the calculated accessible surface area for BF_4^- anions (0.4 nm, BF_4^- accessible) and TEA^+ cations (0.6 nm, TEA^+ accessible).

Table 1. Combined NLDFT Model for CO_2 Sorption for Pores Smaller than 0.9 nm and QSDFT Model for N_2 Sorption for Pores Larger than 0.9 nm[a]

Material	DFT SSA ($m^2 \cdot g^{-1}$)	d_{50}(d_{25}–d_{75}) pore width (nm)	capacitance at +1 V in ACN ($F \cdot g^{-1}$)	Coulomb efficiency (%)	capacitance at +1 V in PC ($F \cdot g^{-1}$)	Coulomb efficiency (%)	capacitance at −1 V in ACN ($F \cdot g^{-1}$)	Coulomb efficiency (%)	capacitance at −1 V in PC ($F \cdot g^{-1}$)	Coulomb efficiency (%)
AC	1839	1.3 (0.8–1.8)	113	96	115	99	103	99	102	99
CB	1097	15 (5–19)	99	99	99	99	88	99	87	99
OLC	232	9.5 (6–14)	20	98	20	99	16	99	16	99
CDC600	934	0.64 (0.53–0.93)	127	97	132	98	121	98	119	99
CDC1000	967	0.90 (0.62–1.4)	101	97	100	98	98	98	96	99

[a]The average pore size relates to the volume-weighted arithmetic mean value d_{50} with the standard deviation from d_{25} to d_{75}. Capacitance values were recorded at +1 V vs carbon and −1 V vs carbon in a three-electrode setup (half-cell).

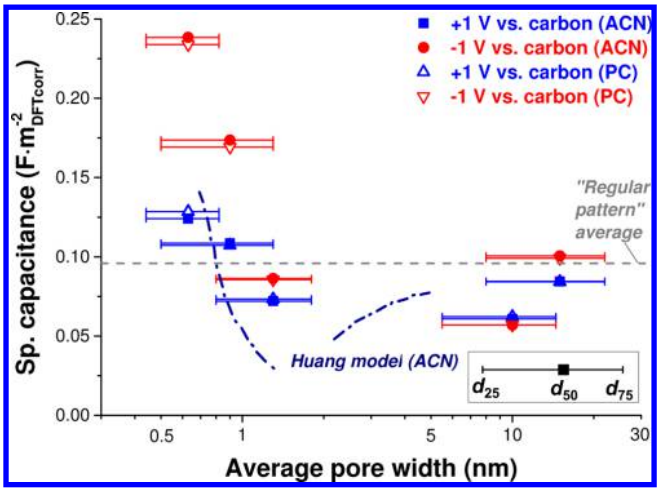

Figure 3. Capacitance of porous carbons normalized to the accessible surface area for each ion in both solvents. The regular pattern average of 0.95 F m^{-2} from ref 15 is added, and data for the Huang model is from ref 17.

values are inaccessible to the ions.[7] The result is a further reduction of the specific surface area, and we have to consider different cutoff values for the positively (cutoff pore size of 0.4 nm) and negatively (cutoff at 0.6 nm) polarized electrodes. In the case of CDC, only about 40–50% of the total SSA is accessible to TEA^+ compared to about 70% for activated carbon and carbon black (Figure 2A).

The reported electrochemical measurements using a three-electrode configuration (for experimental methods see the Supporting Information) showed a nonlinear correlation of SSA and gravimetric capacitance measured in $F \cdot g^{-1}$ (Table 1) for 1 M TEA-BF_4 in acetonitrile (ACN) or propylene carbonate (PC).[6] A very high Coulombic efficiency (up to 99%) underlines the absence of significant Faradaic reactions in the chosen potential window (Table 1). When we normalize the measured electrode capacitance by the surface area accessible to cations or anions at +1 and −1 V vs carbon, respectively, we see a clear difference between positive and negative polarization (Figure 3, Table 1). Instead of just discussing the electrochemical data in the context of average pore width (d_{50}), we added error bars for the x-axis, which spread between d_{25} and d_{75} (Figure 3). Even when considering pore size dispersity, we still see a clear trend of increased normalized capacitance in subnanometer pores, which is significantly larger for negative polarization (i.e., electrosorption of the larger TEA^+ cation). The more effective use of available pores in the case of matching sizes results in a strong increase in capacitance, which was already shown by a geometric model of Huang et al. (ref 22; see also the data line in Figure 3). For larger pore sizes, in

DOI: 10.1021/acsenergylett.6b00516
ACS Energy Lett. 2016, 1, 1262–1265

particular, for mesopores, the capacitance converges toward an average value below 0.1 $F \cdot m^{-2}$, which aligns well with the "regular pattern" value reported by Centeno et al. (ref 15) and with the calculated value limiting the double-layer capacitance at the planar carbon interface (or larger than the few-nm pores; ref 17).

For electrolytes with significant differences between the size of anions and cations, our data clearly show the importance of differentiating between ion electrosorption during positive or negative polarization with use of half-cell measurements (Figure 3). With a larger size of TEA^+, and smaller corresponding surface area accessible to the cations, the values of areal capacitance during negative polarization are significantly larger than those for BF_4^- electrosorption (i.e., positive polarization). Accordingly, advanced EDLC cell design could achieve performance enhancement by developing nanoporous carbon with slightly different pore sizes for the positive and negative electrodes.[23,24]

In summary, our data analysis clearly supports the increase in surface-normalized capacitance when most of the pores are below 1 nm, in agreement with previous studies (e.g., see refs 7 and 25). This was shown for carbons with very different pore structures considering the complexity of pore size dispersity and for two different solvents (i.e., PC and ACN). This effect is seen at different amplitudes for positive and negative polarization, with a smaller increase for BF_4^- within the range of investigated pore sizes.

Nicolas Jäckel[†,‡]
Patrice Simon[*,§,∥]
Yury Gogotsi[*,⊥]
Volker Presser[*,†,‡]

[†]INM - Leibniz Institute for New Materials, 66123 Saarbrücken, Germany

[‡]Department of Materials Science and Engineering, Saarland University, 66123 Saarbrücken, Germany

[§]Université Paul Sabatier, CIRIMAT UMR, CNRS 5085, 5085, 31062 Toulouse Cedex 4, France

[∥]Réseau sur le Stockage Electrochimique de l'Energie, RS2E FR CNRS 3459, 80039 Amiens Cedex, France

[⊥]Department of Materials Science and Engineering, and A. J. Drexel Nanotechnology Institute, Drexel University, Philadelphia, Pennsylvania 19104, United States

■ ASSOCIATED CONTENT

Supporting Information

The Supporting Information is available free of charge on the ACS Publications website at DOI: 10.1021/acsenergylett.6b00516.

Experimental methods (PDF)

■ AUTHOR INFORMATION

Corresponding Authors

*E-mail: simon@chimie.ups-tlse.fr (P.S.).
*E-mail: gogotsi@drexel.edu (Y.G.).
*E-mail: volker.presser@leibniz-inm.de (V.P.).

Notes

Views expressed in this viewpoint are those of the authors and not necessarily the views of the ACS.
The authors declare no competing financial interest.

■ ACKNOWLEDGMENTS

The authors thank Dr. Weingarth, Dr. Aslan, Anna Schreiber, Jeon Jeongwook (all at INM), and Katherine Van Aken (Drexel University) for their technical support and helpful discussion. N.J. and V.P. also thank Prof. Eduard Arzt (INM) for his continuing support. Y.G. was supported by the Fluid Interface Reactions, Structures and Transport (FIRST) Center, an Energy Frontier Research Center funded by the U.S. Department of Energy, Office of Science, Office of Basic Energy Sciences.

■ REFERENCES

(1) Beguin, F.; Frackowiak, E. *Supercapacitors*; Wiley: Weinheim, Germany, 2013.
(2) Salanne, M.; Rotenberg, B.; Naoi, K.; Kaneko, K.; Taberna, P. L.; Grey, C. P.; Dunn, B.; Simon, P. Efficient storage mechanisms for building better supercapacitors. *Nature Energy* **2016**, *1*, 16070.
(3) Kondrat, S.; Perez, C. R.; Presser, V.; Gogotsi, Y.; Kornyshev, A. A. Effect of pore size and its dispersity on the energy storage in nanoporous supercapacitors. *Energy Environ. Sci.* **2012**, *5*, 6474−6479.
(4) Kastening, B.; Spinzig, S. Electrochemical polarization of activated carbon and graphite powder suspensions: Part II. Exchange of ions between electrolyte and pores. *J. Electroanal. Chem. Interfacial Electrochem.* **1986**, *214*, 295−302.
(5) Levi, M. D.; Sigalov, S.; Salitra, G.; Aurbach, D.; Maier, J. The effect of specific adsorption of cations and their size on the charge-compensation mechanism in carbon micropores: The role of anion desorption. *ChemPhysChem* **2011**, *12*, 854−862.
(6) Jäckel, N.; Rodner, M.; Schreiber, A.; Jeongwook, J.; Zeiger, M.; Aslan, M.; Weingarth, D.; Presser, V. Anomalous or regular capacitance? The influence of pore size dispersity on double-layer formation. *J. Power Sources* **2016**, *326*, 660−671.
(7) Chmiola, J.; Yushin, G.; Gogotsi, Y.; Portet, C.; Simon, P.; Taberna, P. L. Anomalous increase in carbon capacitance at pore sizes less than 1 nm. *Science* **2006**, *313*, 1760−1763.
(8) Raymundo-Pinero, E.; Kierzek, K.; Machnikowski, J.; Beguin, F. Relationship between the nanoporous texture of activated carbons and their capacitance properties in different electrolytes. *Carbon* **2006**, *44*, 2498−2507.
(9) Largeot, C.; Portet, C.; Chmiola, J.; Taberna, P.-L.; Gogotsi, Y.; Simon, P. Relation between the ion size and pore size for an electric double-layer capacitor. *J. Am. Chem. Soc.* **2008**, *130*, 2730−2731.
(10) Jiang, D.; Jin, Z.; Henderson, D.; Wu, J. Solvent effect on the pore-size dependence of an organic electrolyte supercapacitor. *J. Phys. Chem. Lett.* **2012**, *3*, 1727−1731.
(11) Feng, G.; Qiao, R.; Huang, J.; Sumpter, B. G.; Meunier, V. Ion distribution in electrified micropores and its role in the anomalous enhancement of capacitance. *ACS Nano* **2010**, *4*, 2382−2390.
(12) Segalini, J.; Iwama, E.; Taberna, P.-L.; Gogotsi, Y.; Simon, P. Steric effects in adsorption of ions from mixed electrolytes into microporous carbon. *Electrochem. Commun.* **2012**, *15*, 63−65.
(13) Levi, M. D.; Levy, N.; Sigalov, S.; Salitra, G.; Aurbach, D.; Maier, J. Electrochemical quartz crystal microbalance (EQCM) studies of ions and solvents insertion into highly porous activated carbons. *J. Am. Chem. Soc.* **2010**, *132*, 13220−13222.
(14) Thommes, M.; Kaneko, K.; Neimark, A. V.; Olivier, J. P.; Rodriguez-Reinoso, F.; Rouquerol, J.; Sing, K. S. W. Physisorption of gases, with special reference to the evaluation of surface area and pore size distribution. *Pure Appl. Chem.* **2015**, *87*, 1051−1069.
(15) Centeno, T. A.; Sereda, O.; Stoeckli, F. Capacitance in carbon pores of 0.7 to 15 nm: a regular pattern. *Phys. Chem. Chem. Phys.* **2011**, *13*, 12403−6.
(16) Garcia-Gomez, A.; Moreno-Fernandez, G.; Lobato, B.; Centeno, T. A. Constant capacitance in nanopores of carbon monoliths. *Phys. Chem. Chem. Phys.* **2015**, *17*, 15687−90.

DOI: 10.1021/acsenergylett.6b00516
ACS Energy Lett. 2016, 1, 1262−1265

(17) Huang, J.; Sumpter, B. G.; Meunier, V.; Yushin, G.; Portet, C.; Gogotsi, Y. Curvature effects in carbon nanomaterials: Exohedral versus endohedral supercapacitors. *J. Mater. Res.* **2010**, *25*, 1525−1531.
(18) Merlet, C.; Rotenberg, B.; Madden, P. A.; Taberna, P. L.; Simon, P.; Gogotsi, Y.; Salanne, M. On the molecular origin of supercapacitance in nanoporous carbon electrodes. *Nat. Mater.* **2012**, *11*, 306−10.
(19) Gor, G. Y.; Thommes, M.; Cychosz, K. A.; Neimark, A. V. Quenched solid density functional theory method for characterization of mesoporous carbons by nitrogen adsorption. *Carbon* **2012**, *50*, 1583−1590.
(20) Presser, V.; Heon, M.; Gogotsi, Y. Carbide-derived carbons − from porous networks to nanotubes and graphene. *Adv. Funct. Mater.* **2011**, *21*, 810−833.
(21) Zeiger, M.; Jäckel, N.; Aslan, M.; Weingarth, D.; Presser, V. Understanding structure and porosity of nanodiamond-derived carbon onions. *Carbon* **2015**, *84*, 584−598.
(22) Huang, J.; Sumpter, B. G.; Meunier, V. A universal model for nanoporous carbon supercapacitors applicable to diverse pore regimes, carbon materials, and electrolytes. *Chem. - Eur. J.* **2008**, *14*, 6614−6626.
(23) Sigalov, S.; Levi, M. D.; Salitra, G.; Aurbach, D.; Jänes, A.; Lust, E.; Halalay, I. C. Selective adsorption of multivalent ions into TiC-derived nanoporous carbon. *Carbon* **2012**, *50*, 3957−3960.
(24) Weingarth, D.; Zeiger, M.; Jäckel, N.; Aslan, M.; Feng, G.; Presser, V. Graphitization as a universal tool to tailor the potential-dependent capacitance of carbon supercapacitors. *Adv. Energy Mater.* **2014**, *4*, 1400316.
(25) Chmiola, J.; Largeot, C.; Taberna, P.-L.; Simon, P.; Gogotsi, Y. Desolvation of Ions in subnanometer pores and its effect on capacitance and double-layer theory. *Angew. Chem., Int. Ed.* **2008**, *47*, 3392−3395.

DOI: 10.1021/acsenergylett.6b00516
ACS Energy Lett. 2016, 1, 1262−1265

4.4 Quantitative Information about Electrosorption of Ionic Liquids in Carbon Nanopores from Electrochemical Dilatometry and Quartz Crystal Microbalance Measurements

N. Jäckel [a,b], S. P. Emge [c,d], B. Krüner [a,b], B. Roling [c], V. Presser [a,b]

[a] INM-Leibniz Institute for New Materials, Campus D2 2, 66123 Saarbrücken, Germany

[b] Department of Materials Science and Engineering, Saarland University, Campus D2 2, 66123 Saarbrücken, Germany

[c] Department of Chemistry, Philipps-Universität, Marburg, Germany

[d] Department of Chemistry, University of Cambridge, United Kingdom

published in The Journal of Physical Chemistry C, 2017. 121(35): p. 19120-19128

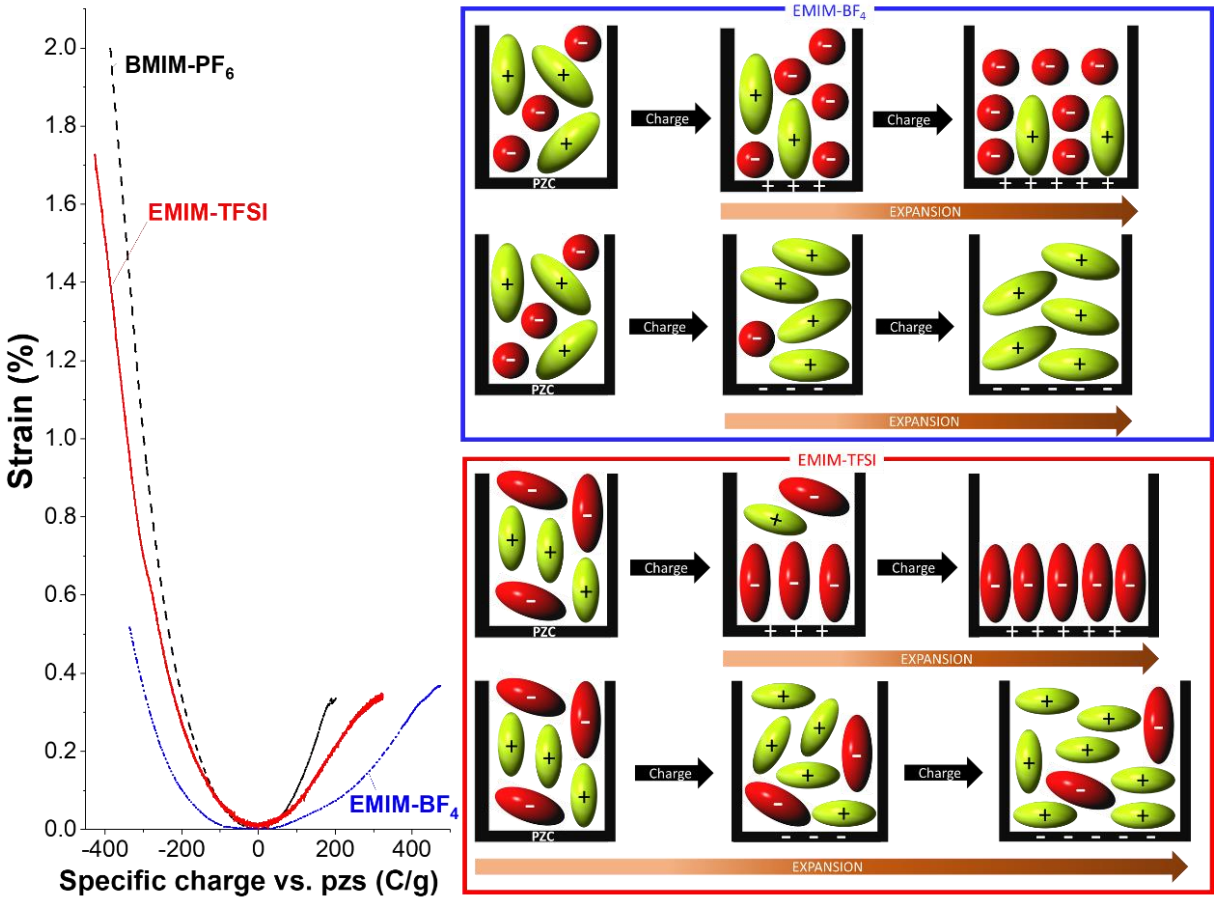

Own contribution:

Data generation 60 %

Data analysis 75 %

Interpretation 80 %

Writing 80 %

Supporting Information:

Appendix C

THE JOURNAL OF PHYSICAL CHEMISTRY C

Article

pubs.acs.org/JPCC

Quantitative Information about Electrosorption of Ionic Liquids in Carbon Nanopores from Electrochemical Dilatometry and Quartz Crystal Microbalance Measurements

Nicolas Jäckel,[†,‡] Steffen Patrick Emge,[§,∥] Benjamin Krüner,[†,‡] Bernhard Roling,*[,§] and Volker Presser*[,†,‡]

[†]INM-Leibniz Institute for New Materials, Saarbrücken 66123, Germany

[‡]Department of Materials Science and Engineering, Saarland University, Saarbrücken 66123, Germany

[§]Department of Chemistry, Philipps-Universität, Marburg 35032, Germany

[∥]Department of Chemistry, University of Cambridge, Cambridge CB2 1EW, United Kingdom

Supporting Information

ABSTRACT: Electrochemical energy storage using nanoporous carbons and ionic liquids enables large cell voltages and is a promising way to increase the energy density of electrical double-layer capacitors. The structure of the double layer in solvent-free electrolytes is fundamentally different from other systems with organic or aqueous solvents. In our study, we investigate the physical behavior of nanoporous carbon electrodes in contact with ionic liquids with a multilength scale approach by combining electrochemical quartz-crystal microbalance and electrochemical dilatometry. Synergistic combination of both in situ methods allows one to correlate system properties on particle and electrode level. We find that the charging mechanism at low charge is characterized by the exchange of more smaller ions by fewer larger ions. At higher charges, the system is changing to preferred counterion adsorption, which is resulting in a strong increase in the electrode volume. The maximum linear strain for a bulk electrode is 2% in our study, which is quite high for a supercapacitor system.

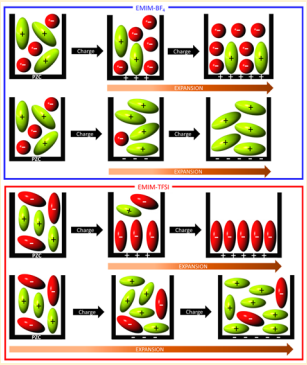

1. INTRODUCTION

Energy storage in electrical double-layer capacitors (EDLCs, also known as supercapacitors or ultracapacitors) via physical ion electrosorption at the electrode/electrolyte interface is highly reversible.[1] To achieve a high energy density, this process requires electrodes with a high surface area, and an enhanced capacitance can be achieved when most of the pores are of similar size as the ion.[2−5] Possible electrolytes are aqueous, organic, or ionic liquids (or mixtures thereof), and depending on the electrolyte, the electrochemical stability window determines the maximum operational cell voltage.[6] Ionic liquids are attractive because their use enables cell voltages above 3 V and very high capacitance of up to 180 F/g.[7−9] Yet, the power output is drastically reduced by the low ion mobility in ionic liquids at room temperature compared to organic electrolytes.[10,11] It is known that, in general, the charging mechanism depends on the pore size, ion size, and applied voltage.[12] Several competing mechanisms, such as bond-length stretching, electrowetting, electrostatic screening, and steric effects, which are all changing according to pore size and amount of functional groups, make a precise prediction of carbon swelling impossible at present.[13]

To devise further ways to enhance supercapacitor performance, it is important to understand the double-layer formation mechanism in nanoconfined spaces, like in (sub)nanometer-sized pores of carbon electrodes. In general, the charge compensation in an electrical double layer can be achieved either by co-ion expulsion, that is, expelling ions of the same charge as the electrode from the interface, or by counterion adsorption, that is, attraction of oppositely charged ions to the interface.[14] To clearly identify the governing mechanism, studies employing different in situ methods have revealed key insights. For example, the ionic liquid spontaneously wets the carbon surface but is unlikely to achieve full wetting. Such partial filling was shown, for example, for microporous activated carbon (YP-50F from Kuraray) in 1-ethyl-3-methylimidazolium bis(trifluoromethylsulfonyl)imide (EMIM-TFSI) and *N*-propyl-*N*-methylpyrrolidinium bis(trifluoromethanesulfonyl)imide (Pyr_{13}-TFSI).[15,16] Further, cations play a dominant role in the double-layer formation, which results in a more pronounced counterion adsorption at negative potentials.[15,17]

Molecular dynamic simulations show that for ionic liquids, counterions can enter the micropores faster than co-ions can exit.[18] For larger pores (i.e., mesopores), the diffusion of cations in confined space is faster than in the bulk electrolyte, and cations also seem to have a higher mobility in micropores.[16,17,19] Additionally, screening effects in highly porous electrodes allow for ions to adsorb in closer proximity

Received: July 14, 2017
Revised: August 15, 2017
Published: August 16, 2017

DOI: 10.1021/acs.jpcc.7b06915
J. Phys. Chem. C 2017, 121, 19120−19128

to the pore walls in nanoconfined spaces as it would be possible on a planar surface.[16] Also, over most potential ranges, the electrical double layer does not contain only counterions, but both kinds of ions influence the structure of the double layer. A significant number of co-ions can remain inside the micropores, and a so-called superionic state of ions is created.[20,21] Calculations and experimental work showed that a preferential adsorption of counterions (permselectivity) will only occur at high voltages of 1.0−1.5 V above the point of zero charge (pzc),[17,22,23] and the ion population in micropores increases up to a certain threshold voltage (i.e., at 1.6 V above pzc) and stays constant for higher voltages.[24]

In the case of ionic liquids, the Gouy−Chapman−Stern model cannot be used to predict electrowetting and the potential-dependent structuring of ions in the double layers at electrified interfaces but a different theoretical approach is required.[25,26] In a simplistic two-dimensional simulation of slit-like pores and ions considered as hard spheres an oscillating behavior of the capacitance was observed.[27,28] This oscillating capacitance vanishes as soon as the pore model is no longer an ideal slit pore with infinitesimally narrow size dispersity, and a broader, more natural pore size distribution is assumed.[29,30] The structural ordering becomes even more complex when taking into account the three-dimensional structure of ionic liquids in confined spaces.[31] In addition, molecular dynamic studies proclaim an exchange of ions with the bulk electrolyte without changing the volume of liquid inside the electrode.[16]

To further advance our nanoscale understanding of the electrical double layer in ionic liquids, a thorough correlation of atomistic/molecular simulations with experimental measurements is required.[32] With state-of-the-art in situ methods a quantification of volumetric changes of carbon particles or bulk electrodes can be monitored. These measurements are usually done by means of electrochemical dilatometry,[33−36] atomic force microscopy,[37,38] or (small-angle) X-ray diffraction.[39] In situ electrochemical dilatometry (eD) has confirmed that the reversible (linear) expansion of microporous carbons in contact with organic electrolytes can range up to several percent.[33−35] In the case of highly porous carbons, ionic liquid ions in nanoconfinement may enable favorable ion packing and crowding,[22,40] causing pore swelling of the electrode material.[41] In all cases of previous dilatometric studies,[42] either with organic electrolytes or with ionic liquids, the expansion for negative potentials exceeds the expansion in the positive potential regime, also at the same charge.[33−35] Moreover, a general trend was observed by an increased expansion for smaller pores,[33,35] and in ionic liquids, the expansion has a linear correlation with the amount of micropores.[42]

It was found that the theoretical expansion according to either ion insertion into bulk electrodes or generated pressure due to crowding of ions in the pores or carbon bond-length variation has been smaller than the measured values on electrodes. This results from the void volume inside the bulk electrode and the possibility of particle rearrangement.[43] To avoid such secondary effects and to gain further insights on the particle level, different measurement techniques should be used. In situ atomic force microscopy (AFM) with ionic liquids evidenced the reversible expansion and compression of porous carbon electrodes.[37,38] The AFM results combined with molecular dynamic calculations showed that cations inside of micropores contribute to increasing pressure to a greater extent than anions, even at the same state of charge.[38] This is in line with the results from eD.[33,42]

Although nanoscale expansions can be tracked by in situ AFM, it remains a very localized probing of single particles.[37,44,45] Therefore, such results cannot be extrapolated directly to the behavior of bulk electrodes with a thickness of a few hundred micrometers and characteristic scales of heterogeneity depending on particle size and the use of binder. The development of noninvasive in situ techniques for the continuous monitoring of mechanical properties of composite electrodes is therefore in high demand. Electrochemical quartz-crystal microbalance (EQCM) measurements are known for very sensitive tracking of mass differences resulting from ion (de)insertion in supercapacitors.[17,20,46−51] In this way, we can quantify the irreversible mass change after cycling or the desolvation of ions in organic electrolytes, that is, stripping off the solvation shell, when approaching narrow pores. To date, there has been only a single paper with EQCM in ionic liquid (EMIM-TFSI) published,[17] but there are no studies comparing in situ measurements with different ionic liquids and a precise description of the charging mechanism depending on the choice of ions.

In our multilength scale approach, we combine EQCM to monitor low mass changes and eD to observe volume changes of the electrode on a bulk level. During EQCM measurements, we monitor simultaneously the charge flow and the mass changes. Since the ionic liquids contain only two mobile ionic species (i.e., one type of cation and one type of anion) with different mass and no solvent molecules, the simultaneous mass and charge measurements allow us to quantify the contribution of counterion and co-ions to the double-layer charge storage. Considering the molar volumes of the ions, we can calculate potential-dependent volume changes due to the ionic liquid ions inside the pores. We show that these volume changes are in good agreement with the measured volumetric expansion from eD measurements. The much wider potential window applied in eD further allows us to see the influence of both ions on the structure of the double layer and the resulting dilatometric behavior.

2. EXPERIMENTAL SECTION

The synthesis of the novolac-derived carbon beads (NovoCarb) is described elsewhere.[52,53] In short, the novolac pellets (20 g) with 10 mass% of methenamine were dissolved in 100 mL of ethanol. The solution was added to 500 mL of water in an autoclave, heated up to 160 °C with a heating rate of 5 °C/min, and held at this temperature for 8 h. The resulting dispersion was freeze dried with liquid nitrogen. The novolac beads were afterward pyrolyzed in a graphite heating furnace (Thermal Technology) in argon atmosphere at 1000 °C with a heating rate of 20 °C/min. CO_2 activation was carried out in a quartz tube furnace (VG Scienta) at 1000 °C for 2 h.

Nitrogen gas sorption measurements were carried out with an Autosorb iQ system (Quantachrome) with liquid nitrogen (−196 °C). The electrode was degassed under vacuum at 150 °C for 10 h; the powder was degassed at 300 °C. Isotherms were recorded at relative pressures (p/p_0) from 5×10^{-7} to 1.0 in 74 steps. The specific surface area (SSA) and pore size distribution were calculated with the ASiQwin software using the quenched-solid density function theory assuming slit pores.[54]

CHNSO analysis was carried out with a Vario Micro Cube (Elementar GmbH). The temperature of the reduction tube was 850 and 1150 °C in the combustion tube. The device was calibrated with sulfanilamide. Oxygen quantification was

DOI: 10.1021/acs.jpcc.7b06915
J. Phys. Chem. C 2017, 121, 19120−19128

Table 1. Physical Properties of the Used Ionic Liquids at 25 °C

	cation size (nm^3)	anion size (nm^3)	conductivity (mS/cm)	density (g/cm^3)	viscosity (cp)	melting point (°C)	ref
EMIM-BF_4	0.156 ± 0.018	0.073 ± 0.021	14	1.28	43	+14.85	70−72
EMIM-TFSI	0.156 ± 0.018	0.232 ± 0.015	9.2	1.52	34	−15.15	70,71,73
BMIM-PF_6	0.196 ± 0.021	0.109 ± 0.008	1.4	1.36	207	+9.85	69−72

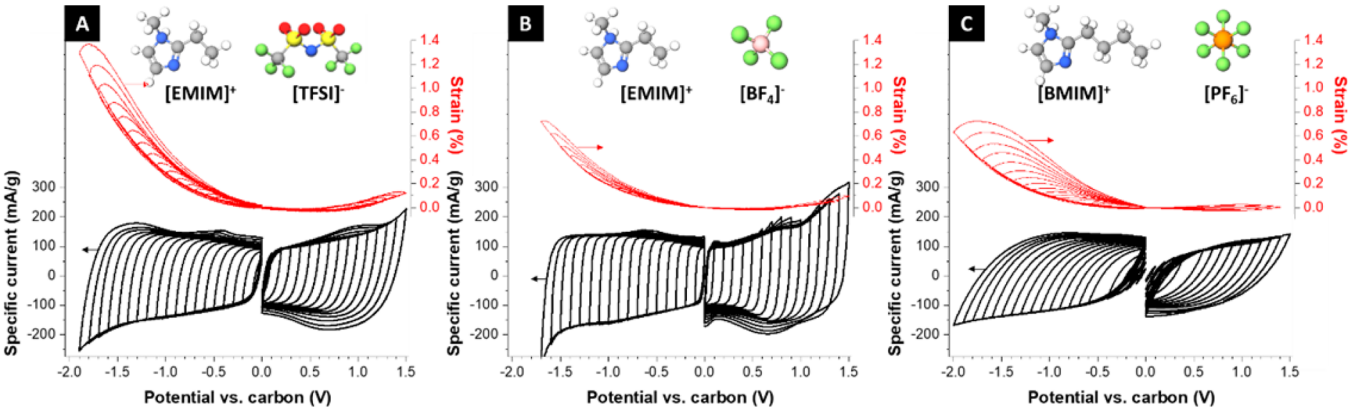

Figure 1. In situ dilatometric measurements of NovoCarb in (A) EMIM-TFSI, (B) EMIM-BF_4, and (C) BMIM-PF_6 with cyclic voltammetry at 1 mV/s. Electrochemical response of the working electrode (black line) can be simultaneously tracked with the height change (red).

conducted in a rapid OXY Cube with silver crucibles at 1450 °C. The calibration was done with benzoic acid. Room-temperature ionic liquids (RTIL) from Iolitec were degassed under vacuum at 120 °C for 24 h. The three used RTIL 1-ethyl-3-methylimidazolium tetrafluoroborate (EMIM-BF_4), 1-ethyl-3-methylimidazolium bis(trifluoromethylsulfonyl)imide (EMIM-TFSI), and 1-butyl-3-methylimidazolium hexafluorophosphate (BMIM-PF_6) were stored in an argon-filled glovebox (MBraun, H_2O and O_2 content below 1 ppm).

In situ electrochemical dilatometry was carried out with an ECD-3-nano dilatometer from EL-CELL (setup adopting the design in ref 35 and following the procedure from ref 55). The measurements were conducted at 25.0 ± 0.1 °C in a three-electrode setup. The working electrode with 90 mass % NovoCarb and 10 mass % sodium carboxymethyl cellulose (NaCMC) in water were dropcasted on the platinum current collector and dried at 200 °C for 30 min. The cell contained an oversized activated carbon electrode and a carbon quasi-reference electrode (type YP-50F, Kuraray) and was vacuum backfilled with electrolyte (approximately 0.5 mL) in the glovebox.[56] The working electrode was loaded with a constant force of 1 N, and the strain was tracked with a DP1S displacement transducer (Solartron Metrology, accuracy ±15 nm). After a resting period of 48 h, cyclic voltammograms were recorded at 1 mV/s and galvanostatic data was recorded after an appropriate equilibrium time (10−60 min) at the applied potential. We used a VMP-300 from Bio-Logic.

Electrochemical quartz-crystal microbalance (EQCM) measurements were conducted with RenLux Crystals at 10 MHz resonance frequency with gold-sputtered electrodes and an active surface area of 0.204 cm^2. The electrodes were airbrushed with a suspension of 90 mass % NovoCarb and 10 mass % NaCMC in water on the gold surface at 200 °C and dried afterwards in a vacuum oven at 60 °C for 24 h. According to the electrochemical behavior and the assumption of exclusively capacitive charge, we can calculate the active mass (i.e., carbon mass, m_C) via $m_C = I/(C_C \cdot \nu)$ with the current I during cyclic voltammetry measurements, the calculated capacitance C_C, and the scan rate ν. The electrochemical cell TSC surface from RHD Instruments was assembled with the coated quartz crystal as working electrode, a silver wire as quasi-reference electrode, and a gold disc as counter electrode. The cell was filled with electrolyte (approximately 0.6 mL) and sealed in the glovebox. The electrochemical measurements were controlled with an Interface 1000 system from Gamry, while the resonance frequency of the crystal was tracked with a Gamry eQCM 10M. Calculations for the number of ions and the volume changes are presented in the Supporting Information.

3. RESULTS AND DISCUSSION

3.1. Electrode Characterization. The novolac-derived carbon beads (NovoCarb) were produced as described elsewhere.[52,53] This type of porous carbon provides a very narrow pore size distribution[3] with an average pore size of about 1.2 nm, which is larger than the ion size of the used ionic liquids (Table 1). Furthermore, the noncarbon content is about 5 mass % (Supporting Information, Table S1). The quenched-solid DFT specific surface area (QSDFT-SSA) of the dry carbon powder is 1958 m^2/g with a total pore volume of 1.13 cm^3/g and an average pore size of 1.2 nm. The electrodes containing 90 mass% carbon and 10 mass% sodium carboxymethyl cellulose (NaCMC) show a strongly reduced SSA of 1338 m^2/g (−32%) and a pore volume of 0.82 cm^3/g (−27%), whereas the average pore diameter does not change (Supporting Information, Figure S1). The reduced SSA is related to pore blocking effects of the NaCMC binder, which especially blocks subnanometer pores.[57,58]

3.2. Ionic Liquid Properties. We used three room-temperature ionic liquids (RTILs), namely, EMIM-TFSI, EMIM-BF_4, and BMIM-PF_6, with five different ion species. These ionic liquids differ regarding the sizes, shapes, and masses of the ions. For instance, in the case of EMIM-TFSI, the molar volume and molar mass of the anions are larger than the molar volume and molar mass of the cations, while the situation is reversed in the case of EMIM-BF_4 (Table 1). Furthermore, the ionic liquids show distinct transport properties (viscosity and conductivity), which thus lead to different electrochemical properties.[59] Our work critically requires us to stay within a

DOI: 10.1021/acs.jpcc.7b06915
J. Phys. Chem. C 2017, 121, 19120−19128

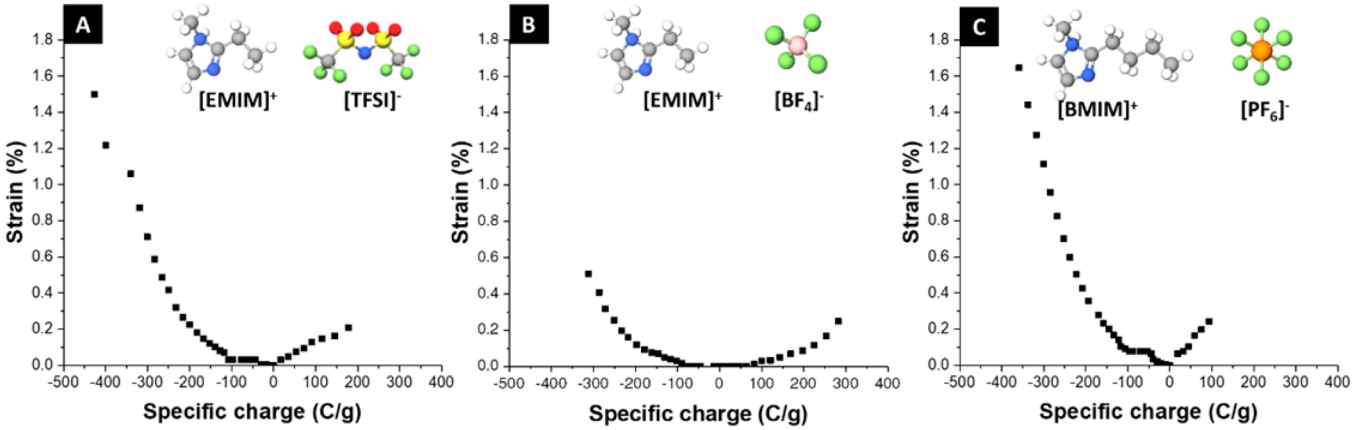

Figure 2. Galvanostatic results of NovoCarb in (A) EMIM-TFSI, (B) EMIM-BF_4, and (C) BMIM-PF_6 with normalization of charge to the point of zero strain (pzs).

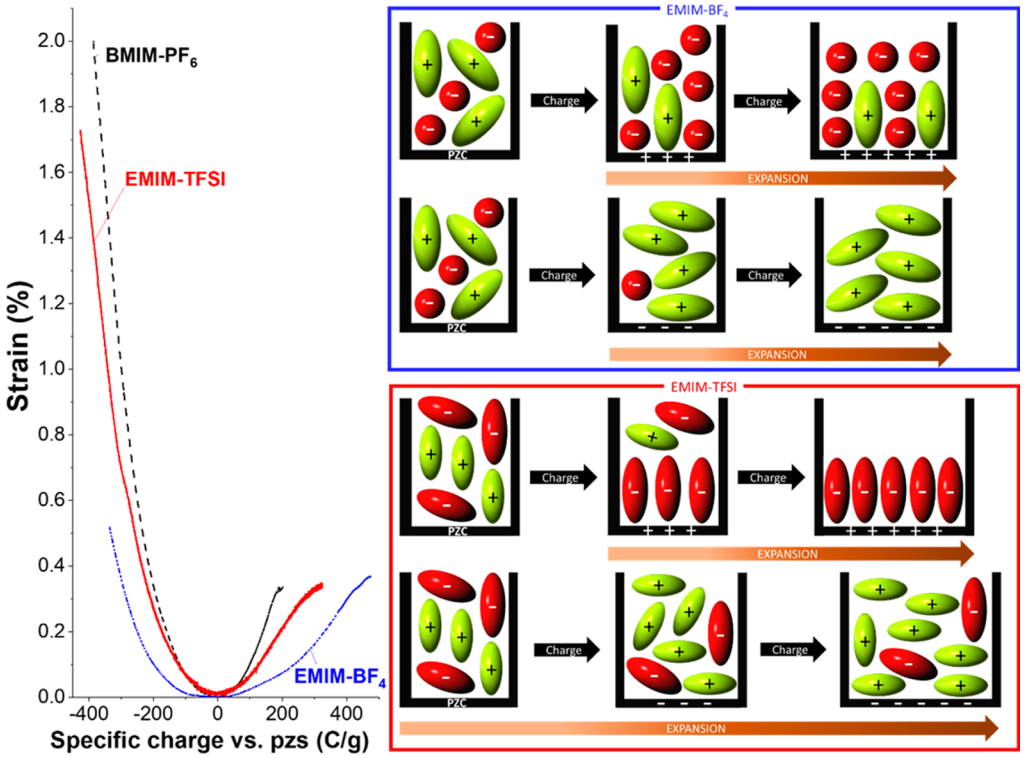

Figure 3. Galvanostatic response of the system at a specific current of 0.1 A/g. Data is derived from the in situ dilatometry system. Charge is normalized to the point of zero strain (pzs) and plotted versus the resulting strain of the working electrode. Schematic drawings show the different charging behavior according to the shape of the adsorbed ions with spherical anions (BF_4^- and PF_6^-) and nonspherical ions ($TFSI^-$). Effect is exaggerated in the drawing to illustrate the trend but not to reproduce the amplitude shown in the eD data. In all cases the smaller ion is more involved in energy storage, which results in either preferred co-ion expulsion or counter-ion adsorption.

stable electrochemical voltage window to avoid any Faradaic reactions at the fluid/solid interface between ionic liquid and carbon electrodes. To find the maximum potential window when using NovoCarb, we conducted cyclic voltammetry at a scan rate of 1 mV/s with increasing voltage window in 100 mV increments (Figure 1).[60] All RTILs were tested until an upper vertex voltage limit of +1.5 V vs carbon. In the cathodic regime, the lower vertex voltage differs with the limits for EMIM-BF_4 at −1.6 V vs carbon, for EMIM-TFSI at −1.8 V vs carbon, and for BMIM-PF_6 at −2.0 V vs carbon. In accordance with the viscosity and conductivity properties of the different RTILs, a rectangular-shaped cyclic voltammogram (CV) is observed for EMIM-BF_4 and EMIM-TFSI, while a more distorted CV with a large resistive knee is seen for BMIM-PF_6 because of the 10-fold lower conductivity of the latter (Table 1).

3.3. Electrochemical Dilatometry. Using in situ electrochemical dilatometry (eD) we can simultaneously record the CV and the displacement of the working electrode (Figure 1). This displacement is divided by the thickness of the electrode to obtain the normalized strain values. We can see a clear influence of the RTIL on the expansion of NovoCarb electrodes. The largest expansion of 1.4% is measured for EMIM-TFSI at a negative potential of −1.8 V vs carbon. This is followed by the expansion in EMIM-BF_4 (0.8%) and then BMIM-PF_6 (0.7%). It can be observed that the expansion is always more pronounced in the negative potential regime.

DOI: 10.1021/acs.jpcc.7b06915
J. Phys. Chem. C 2017, 121, 19120−19128

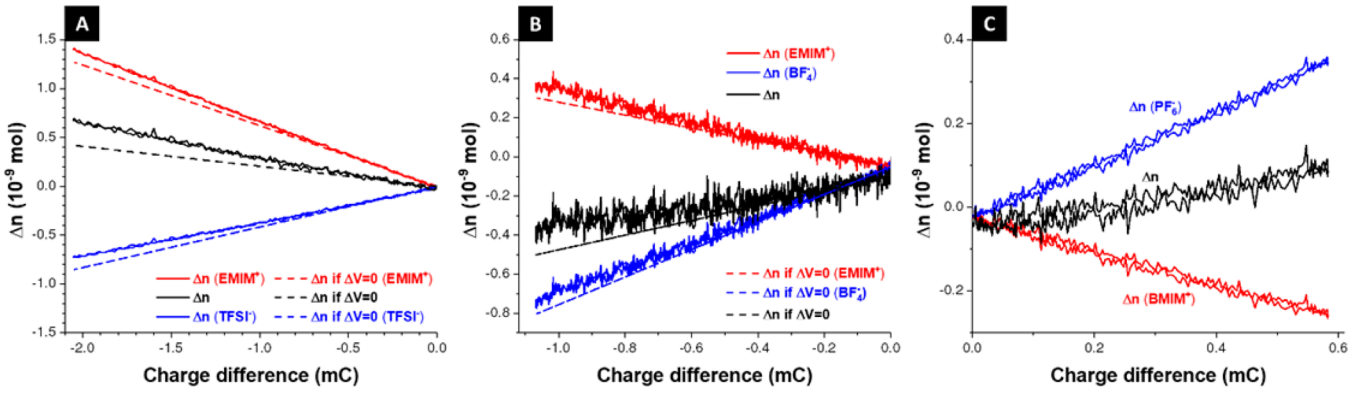

Figure 4. Calculated number of ions in the pores according to the charge difference in (A) EMIM-TFSI, (B) EMIM-BF_4, and (C) BMIM-PF_6. (A and B) Measurements are compared with the calculated changes which would result in a nonvolumetric exchange of ions (dashed lines).

However, the measured expansion cannot solely be related to the electroadsorbing cation, as both EMIM-containing electrolytes drastically differ in expansion depending on the type of anion present. At the most positive potentials (+1.5 V vs carbon), the expansion is largest for the nonspherical $TFSI^-$, which is also the largest anion, followed by PF_6^- and the smallest BF_4^-.

A strain hysteresis occurs during voltage sweeping at 1 mV/s and is enhanced for RTILs with lower ion mobility/higher viscosity as can be seen for BMIM-PF_6. The hysteresis is related to the limited ion migration inside narrow pores and the high viscosity of the used ionic liquids (Table 1). To avoid the strain hysteresis, we conducted galvanostatic measurements with the same voltage steps and an appropriate equilibrium time (Figure 2). The system is quasi-equilibrated at each voltage step, and we can now correlate charge and strain. The curves are normalized to zero charge at the minimum strain measured; we call this point the point of zero strain (pzs). This point is assumed to be close to the point of zero charge (pzc). Therefore, an equal number of cations and anions can be expected in the pores.[15,61] A higher strain is seen again at negative charge compared to positive charge for all RTILs. The smallest expansion is observed for EMIM-BF_4 with 0.25% at +300 C/g and 0.5% at −300 C/g. In the case of EMIM-TFSI, we observe a large strain of 0.7% at negative charges (−300 C/g) compared to a smaller strain of 0.2% at positive charges (+190 C/g). At a positive charge of 100 C/g, the expansion is 0.25% for BMIM-PF_6, 0.13% for EMIM-TFSI and 0.03% for EMIM-BF_4,which shows that in general a larger strain at negative potentials results also in a more pronounced expansion at positive charges. For BMIM-PF_6 the strain at −300 C/g is already 1.1%, which can be explained by the larger volume occupied by the $BMIM^+$ in comparison to $EMIM^+$ (Table 1). The effect of a more pronounced expansion at negative voltages is measured for all RTILs, but it is not fully understood yet.

In the case of EMIM-TFSI, the slope in the strain versus charge plot is smaller than that found for BMIM-PF_6. The higher strain can be correlated to the larger size of $BMIM^+$ (Table 1). It seems likely that the orientation of ions (co-ions and counterions) influences the strain, especially for the nonspherical ions.[62] A parabolic shape in the strain curve is generated by the spherical BF_4^-, whereas a more linear increase in strain can be observed for $TFSI^-$ and for the PF_6^- that is paired with the $BMIM^+$ cation. Hence, for the two $EMIM^+$-containing electrolytes, the strain at −300 C/g differs, with 0.5% for EMIM-BF_4 and 0.7% for EMIM-TFSI.[42] Moreover, the total charge values also strongly differ, which is related to the slightly different voltage windows and the surface coverage per ion, which is changing in the case of nonspherical ions (Figure 3).[62,63] The higher total charge values for EMIM-TFSI and EMIM-BF_4 in comparison to BMIM-PF_6, which has the largest cation and a spherical anion, are related to the bare ion size and the volume occupied by each ion (Table 1). Hence, we would expect higher energy E for higher potentials or larger cell voltages according to $E = 1/2CV^2$ (with capacitance C and cell voltage V), but the size of the adsorbed ions seems to have a greater impact on the possible surface charge.

The electrochemical stability of ionic liquids in the literature does not show a clear trend.[4,60,64,65] The different pzs (+0.2 V vs carbon for EMIM-BF_4 and 0.7 V vs carbon for EMIM-TFSI) might have an influence on the preferred electrosorption of ions, but there might be also a steric hindrance according to the different shapes of the ions.[66] In the case of EMIM-TFSI, both ions are nonspherical and can be approximated as cylindrically shaped. In confinement of nanometer-sized pores, these ions might slide easier along each other than spherical ions.[26,42] Nonspherical ions may create a steric barrier for other ions to slide along each other by generating the double layer inside the small pores due to their larger diameter in the $x-y$ direction, and the shape of the double layer is more affected by the larger nonspherical ions (Figure 3). In our case, the strain created at the highest potential is similar for all three types of anions within a margin of about 0.3% (Figure 3). This is counterintuitive considering the different sizes of the ions, but considering the vastly different charges a direct comparison is not possible this way.

In general, we observe a larger strain at negative polarization compared to positive potentials. The expansion is not only related to the bare ion size as described above for EMIM-TFSI and EMIM-BF_4. Even at the same amount of charge, the expansion differs for the same type of counterion, which is ascribed to an influence of the co-ions.

3.4. Electrochemical Quartz-Crystal Microbalance (EQCM). To better understand the charging mechanism in the carbon nanopores, we conducted electrochemical quartz-crystal microbalance (EQCM) measurements. We note that in the EQCM experiments the electrodes are much thinner compared to the bulk electrodes in electrochemical dilatometry. This results in a more flooded electrode (the amount of electrolyte in comparison to the mass of electrode) and faster charge transport in the electrolyte but should not affect the charging mechanism of the nanopores in the quasi-equilibrated

DOI: 10.1021/acs.jpcc.7b06915
J. Phys. Chem. C 2017, 121, 19120−19128

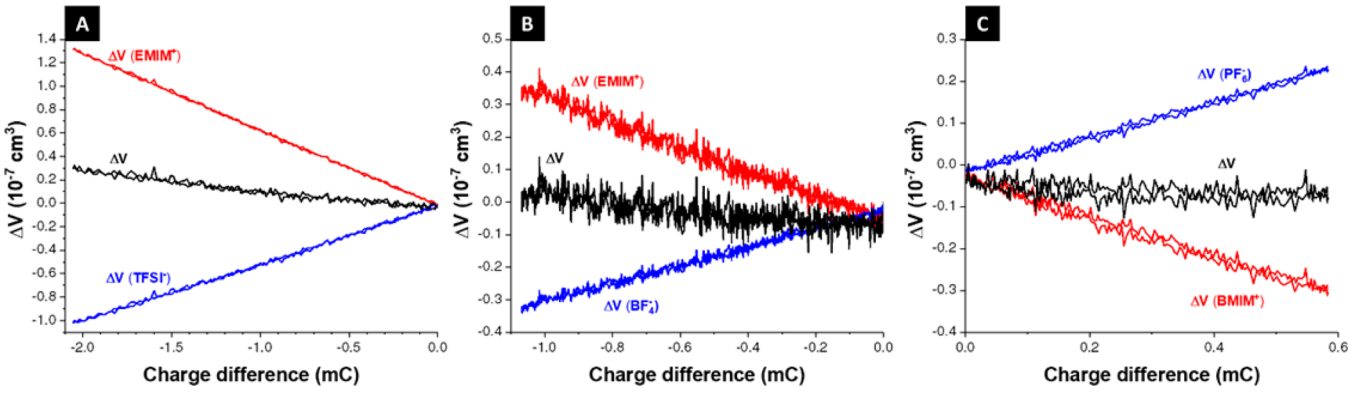

Figure 5. Calculation of volumetric changes ΔV according to the changes of number of ions Δn in the double layer in (A) EMIM-TFSI, (B) EMIM-BF_4, and (C) BMIM-PF_6. All graphs are plotted versus the charge difference for each system. Black line is the total volumetric change according to the sum of anion and cation expulsion and/or adsorption.

state. The thickness of the active mass should be in a range where the full width at half-maximum (fwhm) of the resonance peak does not change significantly. A change of the fwhm indicates viscoelastic behavior of the electrodes, and in this case, the origin of the frequency changes would not be exclusively related to mass changes. Consequently, the Sauerbrey equation would not be applicable.[47,49,67,68] However, in our measurements, the viscoelastic effects were small, since the fwhm of the resonance peak changed only by about 50−100 Hz, whereas the frequency shift was about 300−700 Hz (Supporting Information, Figure S2).

Gravimetric in situ measurements of the electrodes with adsorbed ions can be used to calculate the change of the number of ions in the pores. In all cases, the mass of the electrode is highest at the highest potential (Supporting Information, Figure S3). The different masses of cations and anions allow us to track adsorbing and desorbing ions in the pores, even if there is just a 1:1 exchange of cations and anions. A higher mass at positive potential results from a larger number of ions in the pores or is just a result of ion swapping if the mass difference of cation and anion is large. A clear differentiation of the changes in ion population is possible when calculating the change in the number of ions as described in the Supporting Information. We see that for EMIM-TFSI, more cations enter the pores than anions are ejected when applying a negative potential (Figure 4A). Accordingly, the total number of ions (Δn) increases. This is in contrast to the measured and simulated behavior of supercapacitors with aqueous or organic electrolytes.[5,14,20,32] This implies that the absence of a solvation shell leads to a different double-layer structure in the nanoconfined space.[22,26] We see a stronger increase in the number of cations $\Delta n(EMIM^+)$ compared to the decrease of anions $\Delta n(TFSI^-)$ for negative polarization. Thus, the charge storage is dominated by the insertion or expulsion of the smaller ion (i.e., $EMIM^+$, Figure 4A). This charge storage mechanism leads only to a small increase of the volume for negative polarization (Figure 5A).

The mechanism changes when using EMIM-BF_4 or BMIM-PF_6 as electrolyte (Figure 4B and 4C). In the case of these ionic liquids, the sizes of the spherical anions are smaller compared to the sizes of the cations. When the electrode is charged negatively, the number of anions decreases more strongly than the number of cations increases. This mechanism leads also to an almost constant volume of the ionic liquids within the pores (Figure 5B and 5C).

3.5. Multilength Scale Behavior. The EQCM results in the previous subsection reveal that movement of smaller ions is the dominating part of the charging mechanism at lower surface charges. We see at larger potentials an increase of the amount of counterion adsorption (Figure 3) due to the strong depletion of the smaller ions and the need of further surface charge compensation. Considering the theoretical volume of each ion,[69,70] we can estimate the volume change of the ionic liquid inside the porous electrode (Figure 4) for the low charges in the EQCM measurements. Since we have different sized ions, the structure of the electric double layer can change without yielding strong volumetric changes. The volumetric ratio of $EMIM^+$ to BF_4^- is, for example, more than 2:1; accordingly, two BF_4^- ions occupy the same volume as just one $EMIM^+$ (Table 1).

The chosen potential window for the eD measurements is much wider, so we can see the effect of ion swapping without volumetric changes and then a drastic increase in strain according to crowding the pores with counterions to compensate for the higher surface charge. In contrast to systems with solvated ions, where the total number of ions in the pore is constant,[5] we can see a crowding of pores which get filled with more ions to compensate for the surface charge. For EMIM-BF_4, the volume neutral ion swapping occurs at very low charge difference according to EQCM measurements and confirmed by eD where no strain is measured for low charges until −70 C/g (Figure 2B). This means that more BF_4^- migrates than $EMIM^+$ since two anions fit into the space of one cation. When applying more negative potentials, the strain increases, as seen by eD. Hence, the slope in EMIM-BF_4 is much smaller compared to EMIM-TFSI, which is caused by the size difference of anions and the fact that the smaller ions are more involved in the charge compensation. For BMIM-PF_6, the mechanism of charge storage is similar to EMIM-BF_4 without any significant volumetric change around the pzc (Figure 5C) due to the larger $BMIM^+$ being exchanged for more of the smaller PF_6^- ions (volumetric ratio $BMIM^+$ to PF_6^- is 1.8:1). The volume increases for more negative charges, where the amount of counterion adsorption increases. Considering that $BMIM^+$ is the largest ion in this study, the expected volumetric changes are highest, too. Moreover, the strain at the most negative charge is less for the quasi-equilibrated state (Figure 2C) in comparison to the dynamic measurement in Figure 3, which is related to the very high viscosity of this IL.

DOI: 10.1021/acs.jpcc.7b06915
J. Phys. Chem. C 2017, 121, 19120−19128

In summary, we see at first always smaller ions are being exchanged for fewer large ions until a critical point is reached, where the mechanism due to strong diminution of co-ions must change to a larger amount of counterion adsorption. This aligns with the dilatometer measurements, where no strain was measured (up to ±100 C/g for EMIM-BF_4), while for higher negative charges the increased counterion adsorption causes the slope to rise (Figure 3).

A rigorous quantification is difficult since the pores are not completely filled without an applied voltage and secondary effects like electrowetting may occur.[15] In the absence of solvent molecules, ideal RTIL counterion adsorption must cause an increase in the volume of the electrical double layer and a crowding of ions in the pores.[17,22,26] For potentials far from pzc, counterion adsorption dominates as the charging mechanism and the slope of volume expansion increases for larger ions since each ion occupies a larger volume fraction inside a narrow pore (Figure 3). However, the expansion differs for EMIM-TFSI and EMIM-BF_4 even though both systems employ the same cation. This must be related to strong ion−ion interactions and a non-negligible number of the co-ions are involved in the charging mechanism. According to the shape and degree of freedom, also the adsorption sites inside of micropores might differ strongly (Figure 3).[41,42] The spherical anions seem to create less strain compared to the cylindrical $TFSI^-$, which also might be caused by a lower degree of freedom and a larger steric hindrance as co-ion in the double layer.[66]

4. CONCLUSIONS

We present a systematic study on capacitive energy storage at a microporous carbon surface with different ionic liquids. The electrochemical properties at the fluid/solid interface were investigated in situ by a multilength scale approach. Electrochemical dilatometry on bulk electrodes and electrochemical quartz-crystal microbalance on thin electrodes were used to fundamentally understand the charging mechanism and the resulting bulk behavior. Close to the potential of zero charge, smaller ions are more involved in the charging mechanism. Since more smaller ions are exchanged by less larger ions, the charging takes place at almost constant volume. For potentials far from the pzc, the mechanism changes to a preferred counterion adsorption due to depletion of co-ions. Moreover, a spherical anion creates less strain compared to a nonspherical one, which might be caused by a lower degree of freedom and a larger steric hindrance as co-ion in the electrical double layer.

■ ASSOCIATED CONTENT

Supporting Information

The Supporting Information is available free of charge on the ACS Publications website at DOI: 10.1021/acs.jpcc.7b06915.

Description of quantification of ions, clarification of volumetric changes, supporting Information for gas sorption analysis, supporting Information on EQCM measurements, chemical analysis via CHNSO analysis (PDF)

■ AUTHOR INFORMATION

Corresponding Authors

*E-mail: roling@staff.uni-marburg.de.
*E-mail: volker.presser@leibniz-inm.de.

ORCID

Volker Presser: 0000-0003-2181-0590

Notes

The authors declare no competing financial interest.

■ ACKNOWLEDGMENTS

The authors thank Prof. Eduard Arzt (INM) for his continuing support. N.J. and V.P. acknowledge funding from the German-Israeli Foundation for Scientific Research and Development (GIF) via Research Grant Agreement No. 1-1237-302.5/2014. B.K. and V.P. acknowledge support by the Minerva Foundation via the Award for Research Cooperation and High Excellence in Science Award (ARCHES). We appreciate the discussions with Simon Fleischmann (INM) and Prof. Mikhael Levi (Bar-Ilan University). B.R. and S.E. acknowledge financial support of this work by the Federal State of Hesse within the LOEWE program of excellence (project initiative STORE-E).

■ REFERENCES

(1) Simon, P.; Gogotsi, Y. Materials for Electrochemical Capacitors. *Nat. Mater.* **2008**, *7*, 845−854.
(2) Salanne, M.; Rotenberg, B.; Naoi, K.; Kaneko, K.; Taberna, P. L.; Grey, C. P.; Dunn, B.; Simon, P. Efficient Storage Mechanisms for Building Better Supercapacitors. *Nat. Energy* **2016**, *1*, 16070.
(3) Jäckel, N.; Simon, P.; Gogotsi, Y.; Presser, V. The Increase in Capacitance by Subnanometer Pores in Carbon. *ACS Energy Lett.* **2016**, *1*, 1262−1265.
(4) Pohlmann, S.; Kühnel, R.-S.; Centeno, T. A.; Balducci, A. The Influence of Anion−Cation Combinations on the Physicochemical Properties of Advanced Electrolytes for Supercapacitors and the Capacitance of Activated Carbons. *ChemElectroChem* **2014**, *1*, 1301−1311.
(5) Prehal, C.; Koczwara, C.; Jäckel, N.; Schreiber, A.; Burian, M.; Amenitsch, H.; Hartmann, M. A.; Presser, V.; Paris, O. Quantification of Ion Confinement and Desolvation in Nanoporous Carbon Supercapacitors with Modelling and in Situ X-Ray Scattering. *Nat. Energy* **2017**, *2*, 16215.
(6) Beguin, F.; Presser, V.; Balducci, A.; Frackowiak, E. *Adv. Mater.* **2014**, *26*, 2219−2251.
(7) Zhong, C.; Deng, Y.; Hu, W.; Qiao, J.; Zhang, L.; Zhang, J. A Review of Electrolyte Materials and Compositions for Electrochemical Supercapacitors. *Chem. Soc. Rev.* **2015**, *44*, 7484−539.
(8) Redondo, E.; Tsai, W.-Y.; Daffos, B.; Taberna, P.-L.; Simon, P.; Goikolea, E.; Mysyk, R. Outstanding Room-Temperature Capacitance of Biomass-Derived Microporous Carbons in Ionic Liquid Electrolyte. *Electrochem. Commun.* **2017**, *79*, 5−8.
(9) Salanne, M. Ionic Liquids for Supercapacitor Applications. *Top. Curr. Chem.* **2017**, *375*, 63.
(10) Brandt, A.; Balducci, A. Theoretical and Practical Energy Limitations of Organic and Ionic Liquid-Based Electrolytes for High Voltage Electrochemical Double Layer Capacitors. *J. Power Sources* **2014**, *250*, 343−351.
(11) Burt, R.; Breitsprecher, K.; Daffos, B.; Taberna, P. L.; Simon, P.; Birkett, G.; Zhao, X. S.; Holm, C.; Salanne, M. Capacitance of Nanoporous Carbon-Based Supercapacitors Is a Trade-Off between the Concentration and the Separability of the Ions. *J. Phys. Chem. Lett.* **2016**, *7*, 4015−4021.
(12) Forse, A. C.; Merlet, C.; Griffin, J. M.; Grey, C. P. New Perspectives on the Charging Mechanisms of Supercapacitors. *J. Am. Chem. Soc.* **2016**, *138*, 5731−44.
(13) Rochester, C. C.; Pruessner, G.; Kornyshev, A. A. Statistical Mechanics of 'Unwanted Electroactuation' in Nanoporous Supercapacitors. *Electrochim. Acta* **2015**, *174*, 978−984.
(14) Griffin, J. M.; Forse, A. C.; Wang, H.; Trease, N. M.; Taberna, P. L.; Simon, P.; Grey, C. P. Ion Counting in Supercapacitor Electrodes Using Nmr Spectroscopy. *Faraday Discuss.* **2015**, *176*, 49−68.

DOI: 10.1021/acs.jpcc.7b06915
J. Phys. Chem. C 2017, 121, 19120−19128

(15) Forse, A. C.; Griffin, J. M.; Merlet, C.; Bayley, P. M.; Wang, H.; Simon, P.; Grey, C. P. Nmr Study of Ion Dynamics and Charge Storage in Ionic Liquid Supercapacitors. *J. Am. Chem. Soc.* **2015**, *137*, 7231−42.
(16) Merlet, C.; Rotenberg, B.; Madden, P. A.; Taberna, P. L.; Simon, P.; Gogotsi, Y.; Salanne, M. On the Molecular Origin of Supercapacitance in Nanoporous Carbon Electrodes. *Nat. Mater.* **2012**, *11*, 306−10.
(17) Tsai, W.-Y.; Taberna, P.-L.; Simon, P. Electrochemical Quartz Crystal Microbalance (Eqcm) Study of Ion Dynamics in Nanoporous Carbons. *J. Am. Chem. Soc.* **2014**, *136*, 8722−8728.
(18) Pean, C.; Rotenberg, B.; Simon, P.; Salanne, M. Understanding the Different (Dis)Charging Steps of Supercapacitors: Influence of Potential and Solvation. *Electrochim. Acta* **2016**, *206*, 504−512.
(19) Chathoth, S. M.; Mamontov, E.; Dai, S.; Wang, X.; Fulvio, P. F.; Wesolowski, D. J. Fast Diffusion in a Room Temperature Ionic Liquid Confined in Mesoporous Carbon. *Epl-Europhys. Lett.* **2012**, *97*, 66004.
(20) Griffin, J. M.; Forse, A. C.; Tsai, W. Y.; Taberna, P. L.; Simon, P.; Grey, C. P. In Situ Nmr and Electrochemical Quartz Crystal Microbalance Techniques Reveal the Structure of the Electrical Double Layer in Supercapacitors. *Nat. Mater.* **2015**, *14*, 812−9.
(21) Kondrat, S.; Kornyshev, A. Superionic State in Double-Layer Capacitors with Nanoporous Electrodes. *J. Phys.: Condens. Matter* **2011**, *23*, 022201.
(22) Bazant, M. Z.; Storey, B. D.; Kornyshev, A. A. Double Layer in Ionic Liquids: Overscreening Versus Crowding. *Phys. Rev. Lett.* **2011**, *106*, 046102.
(23) He, Y.; Huang, J.; Sumpter, B. G.; Kornyshev, A. A.; Qiao, R. Dynamic Charge Storage in Ionic Liquids-Filled Nanopores: Insight from a Computational Cyclic Voltammetry Study. *J. Phys. Chem. Lett.* **2015**, *6*, 22−30.
(24) Kondrat, S.; Georgi, N.; Fedorov, M. V.; Kornyshev, A. A. A Superionic State in Nano-Porous Double-Layer Capacitors: Insights from Monte Carlo Simulations. *Phys. Chem. Chem. Phys.* **2011**, *13*, 11359−66.
(25) Kornyshev, A. A. Double-Layer in Ionic Liquids: Paradigm Change? *J. Phys. Chem. B* **2007**, *111*, 5545−5557.
(26) Fedorov, M. V.; Kornyshev, A. A. Ionic Liquids at Electrified Interfaces. *Chem. Rev.* **2014**, *114*, 2978−3036.
(27) Jiang, D.; Jin, Z.; Wu, J. Oscillation of Capacitance inside Nanopores. *Nano Lett.* **2011**, *11*, 5373−5377.
(28) Ma, K.; Wang, X.; Forsman, J.; Woodward, C. E. Molecular Dynamic Simulations of Ionic Liquid's Structural Variations from Three to One Layers inside a Series of Slit and Cylindrical Nanopores. *J. Phys. Chem. C* **2017**, *121*, 13539−13548.
(29) Eikerling, M.; Kornyshev, A. A.; Lust, E. Optimized Structure of Nanoporous Carbon-Based Double-Layer Capacitors. *J. Electrochem. Soc.* **2005**, *152*, E24−E33.
(30) Kondrat, S.; Perez, C. R.; Presser, V.; Gogotsi, Y.; Kornyshev, A. A. Effect of Pore Size and Its Dispersity on the Energy Storage in Nanoporous Supercapacitors. *Energy Environ. Sci.* **2012**, *5*, 6474−6479.
(31) Kornyshev, A. A.; Qiao, R. Three-Dimensional Double Layers. *J. Phys. Chem. C* **2014**, *118*, 18285−18290.
(32) Forse, A. C.; Griffin, J. M.; Merlet, C.; Carretero-Gonzalez, J.; Raji, A.-R. O.; Trease, N. M.; Grey, C. P. Direct Observation of Ion Dynamics in Supercapacitor Electrodes Using In situ Diffusion Nmr Spectroscopy. *Nat. Energy* **2017**, *2*, 16216.
(33) Hantel, M. M.; Presser, V.; Kötz, R.; Gogotsi, Y. In Situ Electrochemical Dilatometry of Carbide-Derived Carbons. *Electrochem. Commun.* **2011**, *13*, 1221−1224.
(34) Hahn, M.; Barbieri, O.; Campana, F. P.; Kötz, R.; Gallay, R. Carbon Based Double Layer Capacitors with Aprotic Electrolyte Solutions: The Possible Role of Intercalation/Insertion Processes. *Appl. Phys. A: Mater. Sci. Process.* **2006**, *82*, 633−638.
(35) Hahn, M.; Barbieri, O.; Gallay, R.; Kötz, R. A Dilatometric Study of the Voltage Limitation of Carbonaceous Electrodes in Aprotic Edlc Type Electrolytes by Charge-Induced Strain. *Carbon* **2006**, *44*, 2523−2533.
(36) Ruch, P. W.; Hahn, M.; Cericola, D.; Menzel, A.; Kötz, R.; Wokaun, A. A Dilatometric and Small-Angle X-Ray Scattering Study of the Electrochemical Activation of Mesophase Pitch-Derived Carbon in Non-Aqueous Electrolyte Solution. *Carbon* **2010**, *48*, 1880−1888.
(37) Arruda, T. M.; Heon, M.; Presser, V.; Hillesheim, P. C.; Dai, S.; Gogotsi, Y.; Kalinin, S. V.; Balke, N. In Situ Tracking of the Nanoscale Expansion of Porous Carbon Electrodes. *Energy Environ. Sci.* **2013**, *6*, 225−231.
(38) Black, J. M.; Feng, G.; Fulvio, P. F.; Hillesheim, P. C.; Dai, S.; Gogotsi, Y.; Cummings, P. T.; Kalinin, S. V.; Balke, N. Strain-Based in Situ Study of Anion and Cation Insertion into Porous Carbon Electrodes with Different Pore Sizes. *Adv. Energy Mater.* **2014**, *4*, 1300683.
(39) Hantel, M. M.; Kaspar, T.; Nesper, R.; Wokaun, A.; Kötz, R. Persistent Electrochemical Pillaring of Graphene Ensembles. *Electrochem. Commun.* **2013**, *34*, 189−191.
(40) Wang, X.; Zhou, H.; Sheridan, E.; Walmsley, J. C.; Ren, D.; Chen, D. Geometrically Confined Favourable Ion Packing for High Gravimetric Capacitance in Carbon-Ionic Liquid Supercapacitors. *Energy Environ. Sci.* **2016**, *9*, 232−239.
(41) Kaasik, F.; Tamm, T.; Hantel, M. M.; Perre, E.; Aabloo, A.; Lust, E.; Bazant, M. Z.; Presser, V. Anisometric Charge Dependent Swelling of Porous Carbon in an Ionic Liquid. *Electrochem. Commun.* **2013**, *34*, 196−199.
(42) Hantel, M. M.; Weingarth, D.; Kötz, R. Parameters Determining Dimensional Changes of Porous Carbons During Capacitive Charging. *Carbon* **2014**, *69*, 275−286.
(43) Hantel, M. M.; Nesper, R.; Wokaun, A.; Kötz, R. In-Situ Xrd and Dilatometry Investigation of the Formation of Pillared Graphene Via Electrochemical Activation of Partially Reduced Graphite Oxide. *Electrochim. Acta* **2014**, *134*, 459−470.
(44) Black, J. M.; Okatan, M. B.; Feng, G.; Cummings, P. T.; Kalinin, S. V.; Balke, N. Topological Defects in Electric Double Layers of Ionic Liquids at Carbon Interfaces. *Nano Energy* **2015**, *15*, 737−745.
(45) Balke, N.; Jesse, S.; Carmichael, B.; Okatan, M. B.; Kravchenko, I. I.; Kalinin, S. V.; Tselev, A. Quantification of in-Contact Probe-Sample Electrostatic Forces with Dynamic Atomic Force Microscopy. *Nanotechnology* **2017**, *28*, 065704.
(46) Pean, C.; Daffos, B.; Rotenberg, B.; Levitz, P.; Haefele, M.; Taberna, P. L.; Simon, P.; Salanne, M. Confinement, Desolvation, and Electrosorption Effects on the Diffusion of Ions in Nanoporous Carbon Electrodes. *J. Am. Chem. Soc.* **2015**, *137*, 12627−32.
(47) Levi, M. D.; Daikhin, L.; Aurbach, D.; Presser, V. Quartz Crystal Microbalance with Dissipation Monitoring (Eqcm-D) for in-Situ Studies of Electrodes for Supercapacitors and Batteries: A Mini-Review. *Electrochem. Commun.* **2016**, *67*, 16−21.
(48) Levi, M. D.; Levy, N.; Sigalov, S.; Salitra, G.; Aurbach, D.; Maier, J. Electrochemical Quartz Crystal Microbalance (Eqcm) Studies of Ions and Solvents Insertion into Highly Porous Activated Carbons. *J. Am. Chem. Soc.* **2010**, *132*, 13220−13222.
(49) Levi, M. D.; Shpigel, N.; Sigalov, S.; Dargel, V.; Daikhin, L.; Aurbach, D. In Situ Porous Structure Characterization of Electrodes for Energy Storage and Conversion by Eqcm-D: A Review. *Electrochim. Acta* **2017**, *232*, 271−284.
(50) Levi, M. D.; Salitra, G.; Levy, N.; Aurbach, D.; Maier, J. Application of a Quartz-Crystal Microbalance to Measure Ionic Fluxes in Microporous Carbons for Energy Storage. *Nat. Mater.* **2009**, *8*, 872−875.
(51) Sigalov, S.; Levi, M. D.; Daikhin, L.; Salitra, G.; Aurbach, D. Electrochemical Quartz Crystal Admittance Studies of Ion Adsorption on Nanoporous Composite Carbon Electrodes in Aprotic Solutions. *J. Solid State Electrochem.* **2014**, *18*, 1335−1344.
(52) Krüner, B.; Lee, J.; Jäckel, N.; Tolosa, A.; Presser, V. Sub-Micrometer Novolac-Derived Carbon Beads for High Performance Supercapacitors and Redox Electrolyte Energy Storage. *ACS Appl. Mater. Interfaces* **2016**, *8*, 9104−9115.
(53) Krüner, B.; Srimuk, P.; Fleischmann, S.; Zeiger, M.; Schreiber, A.; Aslan, M.; Quade, A.; Presser, V. Hydrogen-Treated, Sub-

DOI: 10.1021/acs.jpcc.7b06915
J. Phys. Chem. C 2017, 121, 19120−19128

Micrometer Carbon Beads for Fast Capacitive Deionization with High Performance Stability. *Carbon* **2017**, *117*, 46−54.
(54) Gor, G. Y.; Thommes, M.; Cychosz, K. A.; Neimark, A. V. Quenched Solid Density Functional Theory Method for Characterization of Mesoporous Carbons by Nitrogen Adsorption. *Carbon* **2012**, *50*, 1583−1590.
(55) Jäckel, N.; Krüner, B.; van Aken, K. L.; Alhabeb, M.; Anasori, B.; Kaasik, F.; Gogotsi, Y.; Presser, V. Electrochemical in Situ Tracking of Volumetric Changes in Two-Dimensional Metal Carbides (Mxenes) in Ionic Liquids. *ACS Appl. Mater. Interfaces* **2016**, *8*, 32089−32093.
(56) Weingarth, D.; Foelske-Schmitz, A.; Wokaun, A.; Kötz, R. Ptfe Bound Activated Carbon—a Quasi-Reference Electrode for Ionic Liquids. *Electrochem. Commun.* **2012**, *18*, 116−118.
(57) Kumagai, S.; Mukaiyachi, K.; Tashima, D. Rate and Cycle Performances of Supercapacitors with Different Electrode Thickness Using Non-Aqueous Electrolyte. *J. Energy Stor.* **2015**, *3*, 10−17.
(58) Varzi, A.; Raccichini, R.; Marinaro, M.; Wohlfahrt-Mehrens, M.; Passerini, S. Probing the Characteristics of Casein as Green Binder for Non-Aqueous Electrochemical Double Layer Capacitors' Electrodes. *J. Power Sources* **2016**, *326*, 672−679.
(59) Jäckel, N.; Rodner, M.; Schreiber, A.; Jeongwook, J.; Zeiger, M.; Aslan, M.; Weingarth, D.; Presser, V. Anomalous or Regular Capacitance? The Influence of Pore Size Dispersity on Double-Layer Formation. *J. Power Sources* **2016**, *326*, 660−671.
(60) Weingarth, D.; Noh, H.; Foelske-Schmitz, A.; Wokaun, A.; Kötz, R. A Reliable Determination Method of Stability Limits for Electrochemical Double Layer Capacitors. *Electrochim. Acta* **2013**, *103*, 119−124.
(61) Nanjundiah, C.; McDevitt, S. F.; Koch, V. R. Differential Capacitance Measurements in Solvent-Free Ionic Liquids at Hg and C Interfaces. *J. Electrochem. Soc.* **1997**, *144*, 3392−3397.
(62) Baldelli, S. Surface Structure at the Ionic Liquid−Electrified Metal Interface. *Acc. Chem. Res.* **2008**, *41*, 421−431.
(63) Rivera-Rubero, S.; Baldelli, S. Surface Spectroscopy of Room-Temperature Ionic Liquids on a Platinum Electrode: A Sum Frequency Generation Study. *J. Phys. Chem. B* **2004**, *108*, 15133−15140.
(64) Mousavi, M. P. S.; Dittmer, A. J.; Wilson, B. E.; Hu, J.; Stein, A.; Bühlmann, P. Unbiased Quantification of the Electrochemical Stability Limits of Electrolytes and Ionic Liquids. *J. Electrochem. Soc.* **2015**, *162*, A2250−A2258.
(65) Brandt, A.; Pohlmann, S.; Varzi, A.; Balducci, A.; Passerini, S. Ionic Liquids in Supercapacitors. *MRS Bull.* **2013**, *38*, 554−559.
(66) Segalini, J.; Iwama, E.; Taberna, P.-L.; Gogotsi, Y.; Simon, P. Steric Effects in Adsorption of Ions from Mixed Electrolytes into Microporous Carbon. *Electrochem. Commun.* **2012**, *15*, 63−65.
(67) Sauerbrey, G. Verwendung Von Schwingquarzen Zur Wägung Dünner Schichten Und Zur Mikrowägung. *Eur. Phys. J. A* **1959**, *155*, 206−222.
(68) Shpigel, N. In Situ Hydrodynamic Spectroscopy for Structure Characterization of Porous Energy Storage Electrodes. *Nat. Mater.* **2016**, *15*, 570−575.
(69) Slattery, J. M.; Daguenet, C.; Dyson, P. J.; Schubert, T. J. S.; Krossing, I. How to Predict the Physical Properties of Ionic Liquids: A Volume-Based Approach. *Angew. Chem., Int. Ed.* **2007**, *46*, 5384−5388.
(70) Zhang, S.; Sun, N.; He, X.; Lu, X.; Zhang, X. Physical Properties of Ionic Liquids: Database and Evaluation. *J. Phys. Chem. Ref. Data* **2006**, *35*, 1475−1517.
(71) Krossing, I.; Slattery, J. M.; Daguenet, C.; Dyson, P. J.; Oleinikova, A.; Weingärtner, H. Why Are Ionic Liquids Liquid? A Simple Explanation Based on Lattice and Solvation Energies. *J. Am. Chem. Soc.* **2006**, *128*, 13427−13434.
(72) Resende Prado, C. E.; Gomide Freitas, L. C. Molecular Dynamics Simulation of the Room-Temperature Ionic Liquid 1-Butyl-3-Methylimidazolium Tetrafluoroborate. *J. Mol. Struct.: THEOCHEM* **2007**, *847*, 93−100.
(73) Largeot, C.; Portet, C.; Chmiola, J.; Taberna, P.-L.; Gogotsi, Y.; Simon, P. Relation between the Ion Size and Pore Size for an Electric Double-Layer Capacitor. *J. Am. Chem. Soc.* **2008**, *130*, 2730−2731.

DOI: 10.1021/acs.jpcc.7b06915
J. Phys. Chem. C 2017, 121, 19120−19128

4.5 In situ Measurement of Electrosorption-induced Deformation Reveals the Importance of Micropores in Hierarchical Carbons

C. Koczwara [a], S. Rumswinkel [b], C. Prehal [b], N. Jäckel [c,d], M. Elsässer [b], H. Amenitsch [e], V. Presser [c,d], N. Hüsing [b], O. Paris [a]

[a] Institute of Physics, Montanuniversitaet Leoben, Franz-Josef Straße 18, 8700 Leoben, Austria

[b] Paris Lodron University of Salzburg, Materials Chemistry, Jakob-Haringer Str. 2A , 5020 Salzburg, Austria

[c] INM-Leibniz Institute for New Materials, Campus D2 2, 66123 Saarbrücken, Germany

[d] Department of Materials Science and Engineering, Saarland University, Campus D2 2, 66123 Saarbrücken, Germany

[e] Institute of Inorganic Chemistry, Graz University of Technology, Stremayrgasse 9/IV, 8010 Graz, Austria

published in ACS Applied Materials & Interfaces, 2017. 9(28): p. 23319-23324.

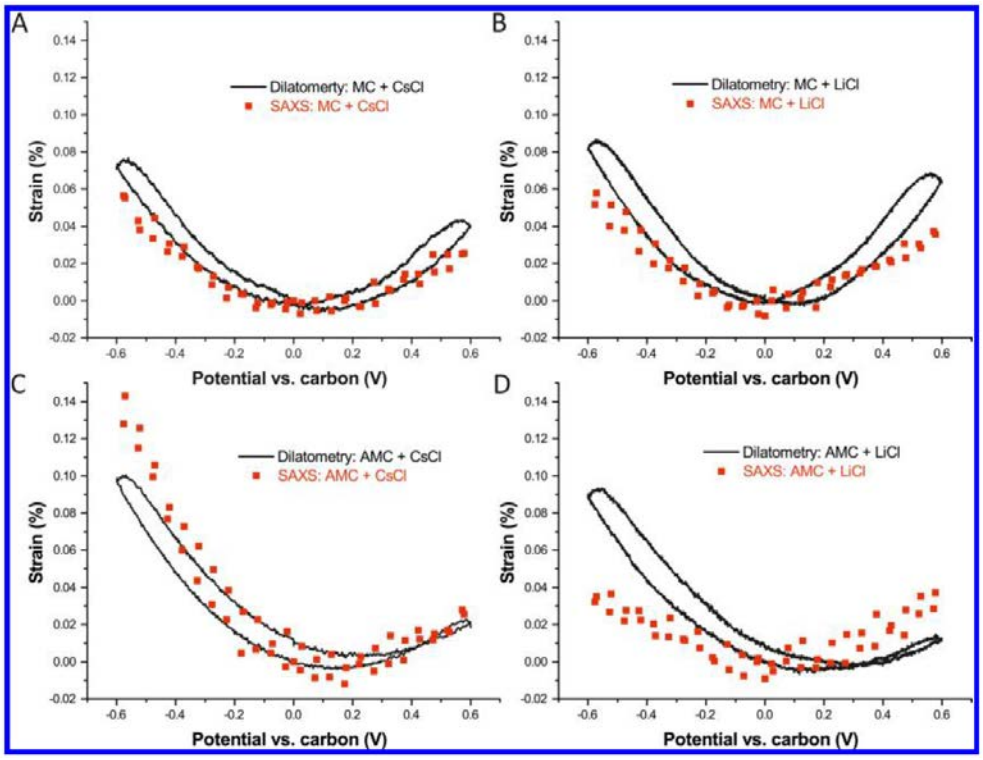

Own contribution:

Data generation 50 %

Data analysis 50 %

Interpretation 40 %

Writing 30 %

Supporting Information:

Appendix D

ACS APPLIED MATERIALS & INTERFACES

Letter

www.acsami.org

In Situ Measurement of Electrosorption-Induced Deformation Reveals the Importance of Micropores in Hierarchical Carbons

Christian Koczwara,[†] Simon Rumswinkel,[‡] Christian Prehal,[†] Nicolas Jäckel,[§,∥] Michael S. Elsässer,[‡] Heinz Amenitsch,[⊥] Volker Presser,[*,§,∥] Nicola Hüsing,[*,‡] and Oskar Paris[*,†]

[†]Institute of Physics, Montanuniversitaet Leoben, Franz-Josef Straße 18, 8700 Leoben, Austria

[‡]Materials Chemistry, Paris Lodron University Salzburg, Jakob-Haringer Strasse 2a, 5020 Salzburg, Austria

[§]INM - Leibniz Institute for New Materials, Campus D2 2, 66123 Saarbrücken, Germany

[∥]Department of Materials Science and Engineering, Saarland University, Campus D2 2, 66123 Saarbrücken, Germany

[⊥]Institute of Inorganic Chemistry, Graz University of Technology, Stremayrgasse 9/IV, 8010 Graz, Austria

Supporting Information

ABSTRACT: Dimensional changes in carbon-based supercapacitor electrodes were investigated using a combination of electrochemical dilatometry and in situ small-angle X-ray scattering. A novel hierarchical carbon material with ordered mesoporosity was synthesized, providing the unique possibility to track electrode expansion and shrinkage on the nanometer scale and the macroscopic scale simultaneously. Two carbons with similar mesopore structure but different amounts of micropores were investigated, employing two different aqueous electrolytes. The strain of the electrodes was always positive, but asymmetric with respect to positive and negative applied voltages. The asymmetry strongly increased with increasing microporosity, giving hints to the possible physical origin of electrosorption induced pore swelling.

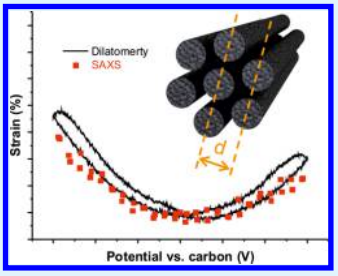

KEYWORDS: *electrical double-layer capacitor, supercapacitor, dilatometry, small-angle X-ray scattering, swelling, in situ, ordered porous carbon*

Electrical double-layer capacitors (EDLCs, also known as supercapacitors) have become a widely used energy storage technology[1] because of their high power density and long cycle life.[2,3] Unraveling the nature of ion charge storage in nanoporous electrode materials has been an ambitious goal for years, leading to a variety of in situ experimental, theoretical, and (atomistic) simulation attempts.[4−6] A combination of in situ X-ray scattering and atomistic modeling has recently elucidated unknown details on the local arrangement and desolvation of ions in disordered nanoporous carbons as a function of the applied cell voltage.[7] An important side effect caused by ion electrosorption is the volumetric expansion of the carbon electrodes during operation. Although electrode deformation is usually much smaller as compared to batteries,[8] repeated expansion and contraction of the electrode may contribute toward electrode degradation. Moreover, this deformation must not necessarily be unwanted, as it opens a facile way to build highly efficient bilayer actuators of astonishing simplicity.[9,10] So far, dimensional changes of electrodes in EDLCs were analyzed using in situ dilatometry or atomic force microscopy.[11−16] In situ dilatometry was even proposed as a method of choice to investigate ion transport in and out of the electrode pores to gain insight on ion-size effects and optimized electrolyte/electrode combinations.[12] However, studies trying to relate volume changes unambiguously to ion concentration and ion-size related steric effects are contradicting.[14] In Li-ion battery electrode swelling, Li intercalation plays by far the dominant role. In contrast, in porous supercapacitor electrodes, several contributions may be of the same order of magnitude, including electronic effects on the surface carbon atoms caused by electrosorbed ions.[14,17,18] In order to exploit the full potential of in situ dilatometry for studying ion charge storage and transport phenomena, those contributions have to be identified and understood in detail.

X-ray scattering is considered advantageous in studying electrosorption-induced pore swelling in EDLCs, as it can probe concurrently the microscopic strain of the carbon and the ion location within the nanopores. To the best of our knowledge, there exists only one X-ray based report on the dimensional changes so far, where the layer spacing in reduced graphite oxide was analyzed by X-ray diffraction.[19] For disordered nanoporous carbons, the crystalline order is usually too low to enable X-ray diffraction for the quantitative study of expansion/contraction processes. In the small-angle scattering (SAXS) regime, pore swelling is a second order effect which is hardly extractable from the data.[20] Therefore, we synthesized a tailored carbon material with an ordered mesoporous structure, giving rise to sharp Bragg reflections from the mesopore lattice in the SAXS regime. This allows analyzing the electrosorption induced strain at the mesopore level via the shift of a distinct

Received: May 18, 2017
Accepted: June 28, 2017
Published: June 28, 2017

DOI: 10.1021/acsami.7b07058
ACS Appl. Mater. Interfaces 2017, 9, 23319−23324

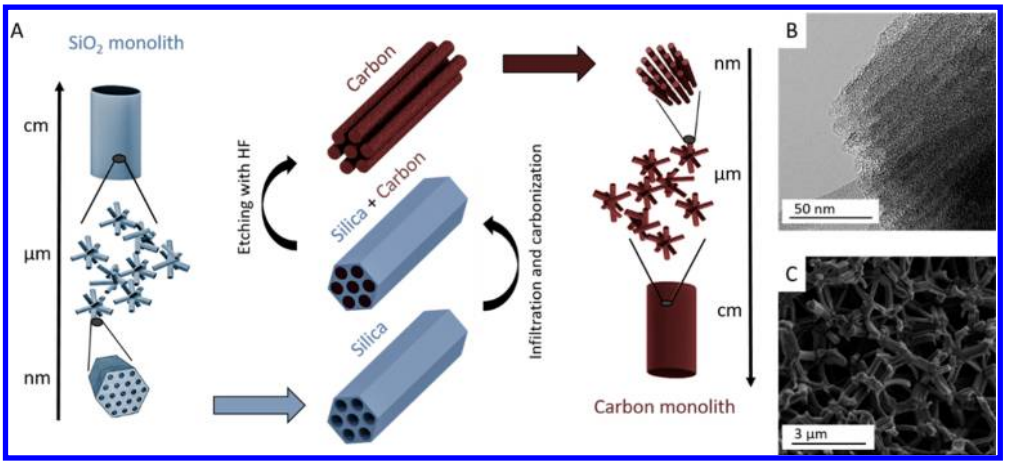

Figure 1. (A) schematic representation of the synthesis of the ordered mesoporous carbon (see the Supporting Information for details). (B) TEM image of the nonactivated carbon (sample MC). (C) SEM image of the macroporous structure of MC.

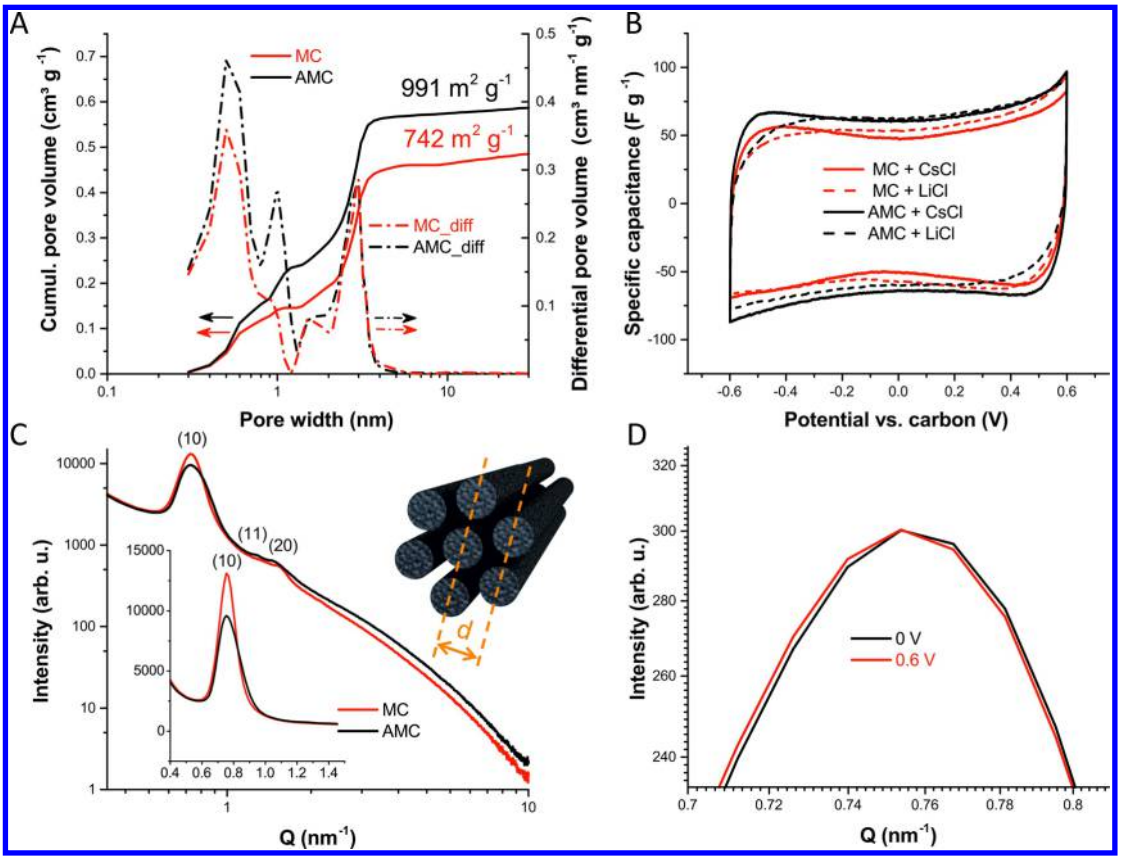

Figure 2. (A) Cumulative specific pore volume and differential pore size distribution of the carbon electrodes containing 10 mass% PTFE binder, determined from CO_2 and N_2 sorption isotherms. (B) cyclic voltammetry measurement of both electrode materials with 1 mV s^{-1} scan rate in 1 M CsCl and 1 M LiCl aqueous electrolyte using a half cell design. (C) SAXS curves of the dry electrodes and schematic drawing of the carbon rods with lattice spacing *d* calculated from the (10) Bragg peak position. (D) Visualization of the (10) peak position for 0 and 0.6 V for MC with aqueous 1 M CsCl.

diffraction peak. Here, we present a novel in situ approach of studying the microscopic (by in situ SAXS) and macroscopic (by in situ dilatometry) swelling behavior of supercapacitor carbon electrodes with ordered mesopores and different amounts of disordered micropores.

We synthesized carbon monoliths via nanocasting using silica monoliths with hierarchical porosity (Figure 1). The silica monoliths were prepared according to Brandhuber et al.[21] via a soft templating approach, resulting in a cellular network structure with interconnected macropores of several hundreds of nanometers in diameter. The struts forming the network are composed of amorphous silica comprising a well-ordered mesostructure with periodically arranged mesopores of about 6−7 nm in diameter (see also the Supporting Information).[21] These silica gels were infiltrated prior to drying with a resorcinol-formaldehyde solution followed by carbonization at 850 °C and template removal by HF etching (see the Supporting Information for details). The final carbon material

DOI: 10.1021/acsami.7b07058
ACS Appl. Mater. Interfaces 2017, 9, 23319−23324

Table 1. Carbon Structure and Properties

	total SSA[a] (m^2 g^{-1})	SSA between 0.63 and 1.3 nm (m^2 g^{-1})	total pore volume (0.95 p/p_0) (cm^3 g^{-1})	micropore volume (cm^3 g^{-1})	mesopore volume (cm^3 g^{-1})	lattice spacing d[b] (nm)	specific capacitance[c] (F g^{-1})
MC	742	113	0.48	0.19	0.29	8.34	56
AMC	991	250	0.59	0.29	0.30	8.34	68

[a]Pore structure and electrochemical performance of the carbon were obtained from electrodes containing 10 mass% PTFE binder. [b]Lattice spacing was calculated from the nonelectrolyte-filled (empty) electrode. [c]Capacitance values were obtained from cyclic voltammetry at 1 mV s^{-1} with 1 M CsCl in the range of ±0.6 V vs carbon.

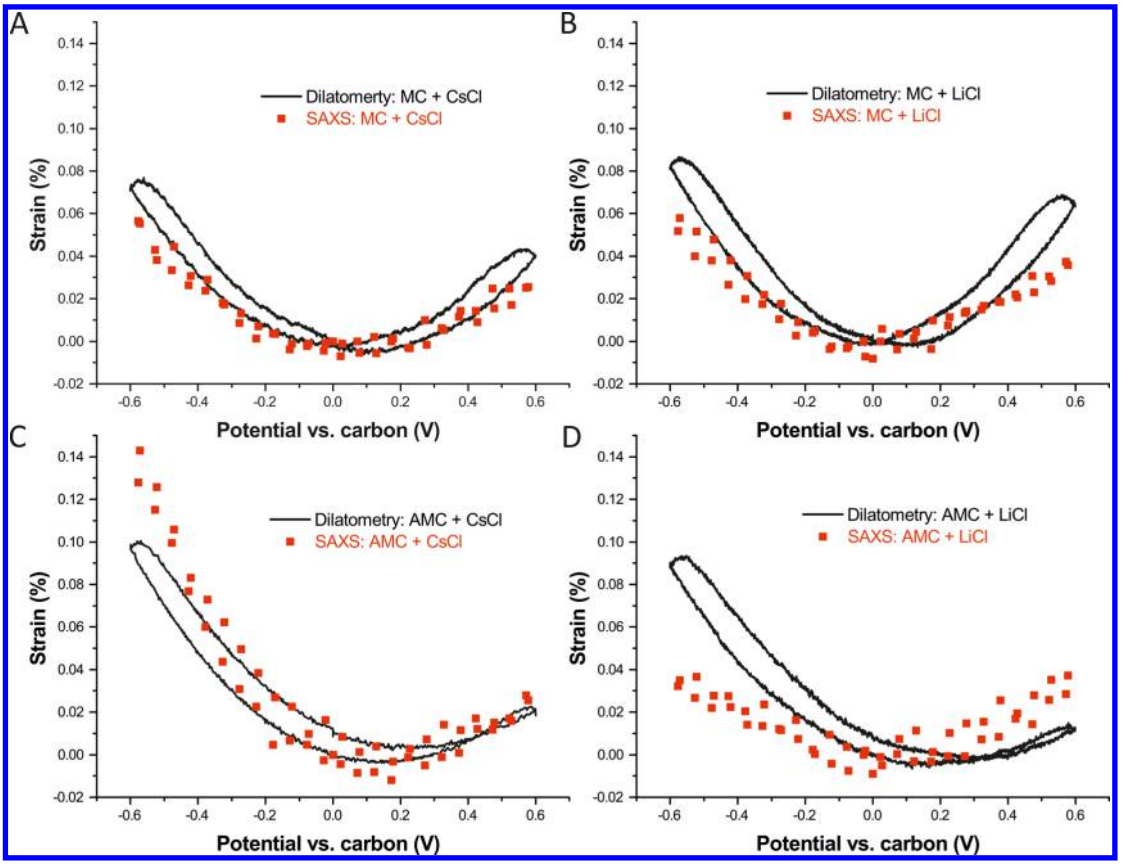

Figure 3. Strain versus potential from in situ SAXS (red) and in situ dilatometry (black) for (A) MC with aqueous 1 M CsCl, (B) MC with aqueous 1 M LiCl, (C) AMC with 1 M CsCl, and (D) AMC with 1 M LiCl. All strain curves were recorded with a scan rate of 1 mV s^{-1}.

consisted of a macroporous network of carbon struts (Figure 1C) indicating a positive replication at the macropore level, with each strut resembling a bundle of monodisperse carbon nanorods which are highly ordered on a 2D hexagonal lattice (Figure 1A). Thus, templating in the mesoscopic regime resulted in a negative replication of the periodically arranged mesopores of the silica mold due to complete filling of the mesopore with the organic polymer. The nanorods exhibited some disordered microporosity already after the carbonization (material MC, Figure 1B), which could be further increased by physical activation with CO_2 (material AMC). Besides the micropore structure, cylindrical carbon struts are identifiable at a higher level of hierarchy (Figure 1C). Specific pore volume, specific surface area (SSA), and pore size distributions (PSD) were calculated from N_2 and CO_2 sorption analysis (Figure 2A, Table 1, and the Supporting Information).[22] The differential PSD of the MC material shows two distinct peaks, one in the micropore region at ∼0.5 nm and one in the mesopore region at ∼3 nm. Activation increased the amount of the smallest pores, and an additional micropore population at ∼1 nm appeared, while the amount of mesopores remained essentially unchanged. Cyclic voltammetry (CV) of the MC and the AMC electrodes was performed in 1 M CsCl and 1 M LiCl aqueous electrolyte (see the Supporting Information for electrode fabrication and electrochemical characterization). Figure 2B shows the typical behavior of a pure EDLC device without any pseudocapacitive contributions. As expected, the mass-specific capacitance of the AMC electrode is higher than the one of the MC electrode due to the increased SSA (Table 1).

The main difference between previously investigated carbons using in situ SAXS[7,20,23] and the new materials presented in this work is the ordered mesoporous structure created by the 2D hexagonally ordered carbon rods as shown in Figure 1A. This resulted in well resolved Bragg reflections in the SAXS curve (Figure 2C), the main reflection corresponding to a lattice spacing of d = 8.34 nm. The lattice spacing did not change upon activation, although the Bragg peak from the activated sample became broader indicating that the mesopore order is somewhat reduced by the activation process. The diffuse scattering below the Bragg peak originates from the disordered

DOI: 10.1021/acsami.7b07058
ACS Appl. Mater. Interfaces 2017, 9, 23319−23324

micropores. The increase of the intensity at large q as a consequence of activation (Figure 2C), being proportional to the increase in SSA via Porod's law,[24] is in good agreement with gas sorption analysis.

To quantify the volumetric changes of the working electrode during charging and discharging, the change of the peak position (Figure 2D) was measured in situ providing the lattice strain as a function of the applied voltage. In situ SAXS experiments were performed at the Austrian SAXS beamline at the synchrotron radiation facility Elettra in Trieste.[25] CV's with a scan rate of 1 mV s^{-1} were recorded using a two-electrode setup in a custom-built cell,[20] while recording a SAXS pattern every five seconds. The mesopore lattice parameter was obtained from the SAXS data by fitting the first order Bragg peak (see the Supporting Information), and the strain was determined by calculating the relative peak shift with respect to the peak position at 0 V. These nanoscopic strains from the swelling of the mesopore lattice were compared to macroscopic strains derived from in situ electrochemical dilatometry performed on electrodes made with the same material (see the Supporting Information). The results are shown in Figure 3 for two different aqueous electrolytes (1 M CsCl and 1 M LiCl). As the electron densities of the cations in these two salts are different, this approach represents a kind of contrast variation. A similar approach (although with other salts) turned out suitable to systematically analyze the changes in disordered carbons with in situ SAXS.[20] As shown in Figure 3A-B for the MC sample, there is a good correspondence between the SAXS and the dilatometry measurements for both electrolytes. Both methods show slightly asymmetric curves with higher strain at negative potentials, which is already known from literature.[14,15,18,26] The good qualitative and reasonable quantitative agreement between strains from SAXS and dilatometry makes us confident that the tiny peak shifts (Figure 2D) are in this case not obscured by contrast induced changes of the SAXS curves due to the rearrangement of ions.[20]

The agreement is less satisfactory for the AMC sample shown in Figure 3C–D. The strain curves measured with dilatometry are pronouncedly asymmetric, but similar for the two electrolytes. In the strain curves obtained from SAXS we observed a distinct dependence on the used electrolyte. For aqueous 1 M CsCl, the SAXS curve is highly asymmetric, even exceeding the asymmetry of the dilatometry curve. For aqueous 1 M LiCl, however, the shape of the SAXS curve is almost symmetric. To be more precise, for positive applied voltage, the strain curves from SAXS are similar for both electrolytes and qualitatively consistent with the findings from dilatometry. For negative potential and aqueous 1 M CsCl, the maximum SAXS strain exceeds the one from dilatometry by almost a factor of 1.5, whereas for LiCl the situation is reversed. We believe that these differences are caused by contrast effects due to local ion rearrangement,[7] because upon charging, counterions will accumulate near the carbon strut surface and within the micropores. At negative polarization, the carbon pores are populated dominantly by Cs^+ and Li^+, respectively, whose electron densities are strongly different. Therefore, we expect so-called "pseudostrains" influencing the measured peak shift.[27] The deviation from the macroscopic strain measured by dilatometry depends on the counterion electron density and the amount of micropores within the carbon struts. Considering additionally a higher strain at negative voltage as compared to positive voltage in the AMC sample as suggested from dilatometry, the data become qualitatively consistent.

An asymmetric shape with higher strains for cation electrosorption as compared to anion electrosorption has been reported for in situ dilatometry studies on carbon electrodes before.[12,28] Using in situ SAXS and carbon materials with an ordered mesopore structure, it is shown here for the first time experimentally that this strain unambiguously originates from the micro/mesopore scale by evaluating the shift of a Bragg reflection from the ordered mesopore lattice. The magnitude and the asymmetry of the strain with respect to the sign of the applied voltage was found to depend on the amount of micropores within the otherwise identical carbon nanorods of the model material. Therefore, ion size effects can be rejected to be exclusively responsible for the asymmetry, implying that the overall strain must be a combination of at least two individual effects. First, an increase in the total (cation plus anion) concentration upon electrode charging,[20] either globally (in all micro- and mesopores) or locally (only in sites with high degree of confinement[7]), would lead to a positive osmotic pressure and thus to an expansion for both, positive and negative polarizations.[13,26] A second effect being in the right order of magnitude is the variation of the C–C bond length. Electron/hole doping during electrode charging influences the band structure and hence the length of the C–C bonding.[18,29] Applying a negative potential elongates the bonding, which in consequence leads to an expansion, and vice versa. Such effects have been explicitly calculated for a simple model of the axial elongation of cylindrical nanopores with an ionic liquid as electrolyte, and have been successfully compared with experiments.[26] Adding to this, we report here that an increase of microporosity (corresponding to an increase of the relative amount of surface carbon atoms) strongly enhances this asymmetry, being in good agreement with previous studies on different carbon materials.[14] A simple estimation of two strain contributions (symmetric and asymmetric) supports the prediction that asymmetric swelling is a surface related effect and caused by electron/hole doping. Comparing the two carbons investigated in this work reveals a just slightly changed symmetric strain contribution (osmotic pressure) and roughly a doubling of the asymmetric contribution (electron/hole doping) in the micropore rich carbon. This corresponds roughly to the doubling of the micropore surface area in the pore size range between 0.63 and 1.3 nm (where the biggest change occurs) due to the activation process (Table 1). This is indeed expected because the influence of electron/hole doping should roughly scale with the surface area.

In conclusion, it was demonstrated that hierarchical carbons with hexagonally ordered microporous carbon nanorods are useful model materials to investigate dimensional changes of supercapacitor electrodes during operation. The unique combination of a tailored material and novel in situ techniques makes the pore strain accessible on different length scales. The use of different electrolytes containing ions with different electron densities represents a contrast variation approach which allowed to qualitatively separate X-ray contrast effects from real strains. By also performing in situ electrochemical dilatometry we could compare macroscopic swelling with dimensional changes on the length scale of the ordered mesopores. The investigation of two materials with different PSD's revealed that the amount of micropores inside the carbon nanorods considerably influences the polarization dependent magnitude of dimensional changes during operation.

DOI: 10.1021/acsami.7b07058
ACS Appl. Mater. Interfaces 2017, 9, 23319–23324

■ ASSOCIATED CONTENT

Supporting Information

The Supporting Information is available free of charge on the ACS Publications website at DOI: 10.1021/acsami.7b07058.

Additional details about the synthesis and experiments mentioned in this letter (PDF)

■ AUTHOR INFORMATION

Corresponding Authors

*E-mail: volker.presser@leibniz-inm.de.
*E-mail: nicola.huesing@sbg.ac.at.
*E-mail: oskar.paris@unileoben.ac.at.

ORCID

Christian Koczwara: 0000-0002-8905-0586
Volker Presser: 0000-0003-2181-0590

Author Contributions

C.K., C.P., and H.A. performed the in situ SAXS experiments. S.R. and M.E. synthesized the carbon material. N.J. performed the dilatometry and sorption analysis. V.P., N.H., and O.P. conceptualized the work. C.K., C.P., H.A., N.J., and O.P. contributed to the data analysis. The manuscript was written with contributions from all authors. All authors have given approval to the final version of the manuscript.

Funding

Funding of this research was provided by the Austrian Klima- and Energiefonds via the FFG program "Energieforschung" (Project: Hybrid Supercap).

Notes

The authors declare no competing financial interest.

■ ACKNOWLEDGMENTS

We acknowledge financial support from the Austrian Klima- und Energiefonds via the FFG program "Energieforschung" (Project: Hybrid Supercap). N.J. and V.P. thank Prof. Eduard Arzt (INM) for his continuing support and acknowledge funding from the German-Israeli Foundation for Scientific Research and Development (GIF) via Research Grant Agreement No. 1-1237-302.5/2014.

■ ABBREVIATIONS

SAXS, small-angle X-ray scattering
CE, counter electrode
WE, working electrode
PSD, pore size distribution
SSA, specific surface area
PTFE, polytetrafluoroethylene
MC, mesoporous carbon
AMC, activated mesoporous carbon
EDLC, electrical double-layer capacitor

■ REFERENCES

(1) Yang, Z.; Zhang, J.; Kintner-Meyer, M. C. W.; Lu, X.; Choi, D.; Lemmon, J. P.; Liu, J. Electrochemical Energy Storage for Green Grid. *Chem. Rev.* **2011**, *111*, 3577−3613.

(2) Simon, P.; Gogotsi, Y. Materials for Electrochemical Capacitors. *Nat. Mater.* **2008**, *7*, 845−854.

(3) Beguin, F.; Presser, V.; Balducci, A.; Frackowiak, E. Carbons and Electrolytes for Advanced Supercapacitors. *Adv. Mater.* **2014**, *26*, 2219−2251.

(4) Deschamps, M.; Gilbert, E.; Azais, P.; Raymundo-Pinero, E.; Ammar, M. R.; Simon, P.; Massiot, D.; Beguin, F. Exploring Electrolyte Organization in Supercapacitor Electrodes with Solid-state NMR. *Nat. Mater.* **2013**, *12*, 351−358.

(5) Salanne, M.; Rotenberg, B.; Naoi, K.; Kaneko, K.; Taberna, P.-L.; Grey, C. P.; Dunn, B.; Simon, P. Efficient Storage Mechanisms for Building Better Supercapacitors. *Nat. Energy* **2016**, *1*, 16070.

(6) Richey, F. W.; Dyatkin, B.; Gogotsi, Y.; Elabd, Y. A. Ion Dynamics in Porous Carbon Electrodes in Supercapacitors Using in situ Infrared Spectroelectrochemistry. *J. Am. Chem. Soc.* **2013**, *135*, 12818−12826.

(7) Prehal, C.; Koczwara, C.; Jäckel, N.; Schreiber, A.; Burian, M.; Amenitsch, H.; Hartmann, M. A.; Presser, V.; Paris, O. Quantification of Ion Confinement and Desolvation in Nanoporous Carbon Supercapacitors with Modelling and in situ X-ray scattering. *Nat. Energy* **2017**, *2*, 16215.

(8) Nitta, N.; Wu, F.; Lee, J. T.; Yushin, G. Li-Ion Battery Materials: Present and Future. *Mater. Today* **2015**, *18*, 252−264.

(9) Torop, J.; Palmre, V.; Arulepp, M.; Sugino, T.; Asaka, K.; Aabloo, A. Flexible Supercapacitor-like Actuator with Carbide-derived Carbon Electrodes. *Carbon* **2011**, *49*, 3113−3119.

(10) Torop, J.; Arulepp, M.; Leis, J.; Punning, A.; Johanson, U.; Palmre, V.; Aabloo, A. Nanoporous Carbide-derived Carbon Material-based Linear Actuators. *Materials* **2010**, *3*, 9−25.

(11) Black, J. M.; Feng, G.; Fulvio, P. F.; Hillesheim, P. C.; Dai, S.; Gogotsi, Y.; Cummings, P. T.; Kalinin, S. V.; Balke, N. Strain-based in situ Study of Anion and Cation Insertion into Porous Carbon Electrodes with Different Pore Sizes. *Adv. Energy Mater.* **2014**, *4*, 1300683.

(12) Hantel, M. M.; Presser, V.; Kötz, R.; Gogotsi, Y. In situ Electrochemical Dilatometry of Carbide-derived Carbons. *Electrochem. Commun.* **2011**, *13*, 1221−1224.

(13) Hantel, M. M.; Presser, V.; McDonough, J. K.; Feng, G.; Cummings, P. T.; Gogotsi, Y.; Kotz, R. In situ Electrochemical Dilatometry of Onion-like Carbon and Carbon Black. *J. Electrochem. Soc.* **2012**, *159*, A1897−A1903.

(14) Hantel, M. M.; Weingarth, D.; Kötz, R. Parameters Determining Dimensional Changes of Porous Carbons during Capacitive Charging. *Carbon* **2014**, *69*, 275−286.

(15) Ruch, P. W.; Kötz, R.; Wokaun, A. Electrochemical Characterization of Single-Walled Carbon Nanotubes for Electrochemical Double Layer Capacitors using non-aqueous Electrolyte. *Electrochim. Acta* **2009**, *54*, 4451−4458.

(16) Kaasik, F.; Tamm, T.; Hantel, M. M.; Perre, E.; Aabloo, A.; Lust, E.; Bazant, M. Z.; Presser, V. Anisometric Charge Dependent Swelling of Porous Carbon in an Ionic Liquid. *Electrochem. Commun.* **2013**, *34*, 196−199.

(17) Hahn, M.; Barbieri, O.; Gallay, R.; Kötz, R. A Dilatometric Study of the Voltage Limitation of Carbonaceous Electrodes in Aprotic EDLC Type Electrolytes by Charge-induced Strain. *Carbon* **2006**, *44*, 2523−2533.

(18) Hahn, M.; Barbieri, O.; Campana, F. P.; Kötz, R.; Gallay, R. Carbon based Double Layer Capacitors with Aprotic Electrolyte Solutions: The Possible Role of Intercalation/Insertion Processes. *Appl. Phys. A: Mater. Sci. Process.* **2006**, *82*, 633−638.

(19) Hantel, M. M.; Kaspar, T.; Nesper, R.; Wokaun, A.; Kötz, R. Partially Reduced Graphite Oxide for Supercapacitor Electrodes: Effect of Graphene Layer Spacing and Huge Specific Capacitance. *Electrochem. Commun.* **2011**, *13*, 90−92.

(20) Prehal, C.; Weingarth, D.; Perre, E.; Lechner, R. T.; Amenitsch, H.; Paris, O.; Presser, V. Tracking the Structural Arrangement of Ions in Carbon Supercapacitor Nanopores Using in situ Small-Angle X-ray Scattering. *Energy Environ. Sci.* **2015**, *8*, 1725−1735.

(21) Brandhuber, D.; Torma, V.; Raab, C.; Peterlik, H.; Kulak, A.; Hüsing, N. Glycol-modified Silanes in the Synthesis of Mesoscopically Organized Silica Monoliths with Hierarchical Porosity. *Chem. Mater.* **2005**, *17*, 4262−4271.

(22) Jäckel, N.; Rodner, M.; Schreiber, A.; Jeongwook, J.; Zeiger, M.; Aslan, M.; Weingarth, D.; Presser, V. Anomalous or Regular Capacitance? The Influence of Pore Size Dispersity on Double-Layer Formation. *J. Power Sources* **2016**, *326*, 660−671.

DOI: 10.1021/acsami.7b07058
ACS Appl. Mater. Interfaces 2017, 9, 23319−23324

(23) Prehal, C.; Koczwara, C.; Jäckel, N.; Amenitsch, H.; Presser, V.; Paris, O. A Carbon Nanopore Model to Quantify Structure and Kinetics of Ion Electrosorption with In Situ Small-Angle X-ray Scattering. *Phys. Chem. Chem. Phys.* **2017**, *19*, 15549−15561.
(24) Glatter, O.; Kratky, O. *Small-Angle X-ray Scattering*; Academic Press: London, 1982.
(25) Amenitsch, H.; Rappolt, M.; Kriechbaum, M.; Mio, H.; Laggner, P.; Bernstorff, S. First Performance Assessment of the Small-Angle X-ray Scattering Beamline at ELETTRA. *J. Synchrotron Radiat.* **1998**, *5*, 506−508.
(26) Rochester, C. C.; Pruessner, G.; Kornyshev, A. A. Statistical Mechanics of 'Unwanted Electroactuation' in Nanoporous Supercapacitors. *Electrochim. Acta* **2015**, *174*, 978−984.
(27) Prass, J.; Müter, D.; Erko, M.; Paris, O. Apparent Lattice Expansion in Ordered Nanoporous Silica During Capillary Condensation of Fluids. *J. Appl. Crystallogr.* **2012**, *45*, 798−806.
(28) Shao, L.-H.; Biener, J.; Kramer, D.; Viswanath, R. N.; Baumann, T. F.; Hamza, A. V.; Weissmuller, J. Electrocapillary Maximum and Potential of Zero Charge of Carbon Aerogel. *Phys. Chem. Chem. Phys.* **2010**, *12*, 7580−7587.
(29) Sun, G.; Kürti, J.; Kertesz, M.; Baughman, R. H. Dimensional Changes as a Function of Charge Injection in Single-Walled Carbon Nanotubes. *J. Am. Chem. Soc.* **2002**, *124*, 15076−15080.

NOTE ADDED AFTER ASAP PUBLICATION

This paper was published on the Web on July 3, 2017, with minor errors in Figure 2C. The corrected version was reposted on July 7, 2017.

DOI: 10.1021/acsami.7b07058
ACS Appl. Mater. Interfaces 2017, 9, 23319−23324

4.6 Electrochemical in Situ Tracking of Volumetric Changes in Two-Dimensional Metal Carbides (MXenes) in Ionic Liquids

N. Jäckel [a,b], B. Krüner [a,b], K. L. Van Aken [c], M. Alhabeb [c], B. Anasori [c], F. Kaasik [a], Y. Gogotsi [c], V. Presser [a,b]

[a] INM-Leibniz Institute for New Materials, Campus D2 2, 66123 Saarbrücken, Germany

[b] Department of Materials Science and Engineering, Saarland University, Campus D2 2, 66123 Saarbrücken, Germany

[c] Department of Materials Science and Engineering & A. J. Drexel Nanotechnlogy Institute, PA 19104 Philadelphia, USA

published in ACS Applied Materials & Interfaces, 2016. 8(47): p. 32089-32093

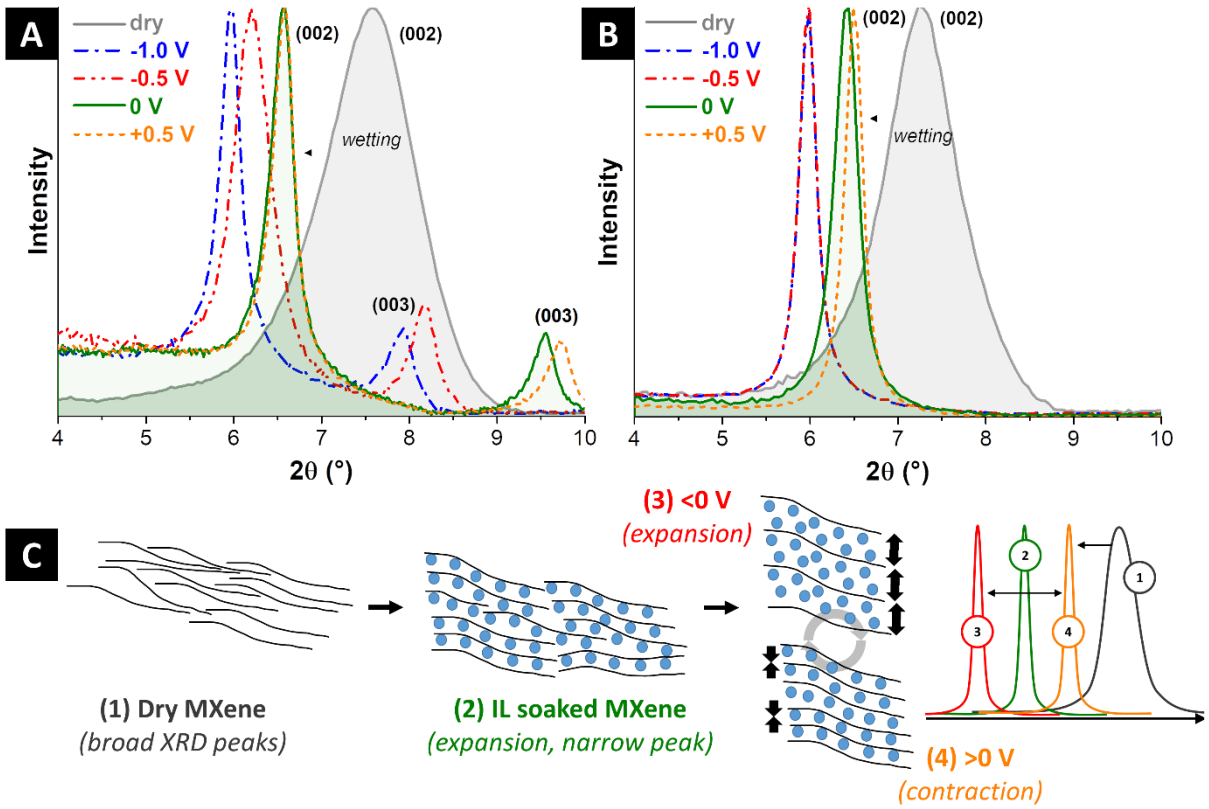

Own contribution:

Data generation 75 %

Data analysis 85 %

Interpretation 80 %

Writing 85 %

Supporting Information:

Appendix E

ACS APPLIED MATERIALS & INTERFACES

Letter

www.acsami.org

Electrochemical in Situ Tracking of Volumetric Changes in Two-Dimensional Metal Carbides (MXenes) in Ionic Liquids

Nicolas Jäckel,[†,‡] Benjamin Krüner,[†,‡] Katherine L. Van Aken,[§] Mohamed Alhabeb,[§] Babak Anasori,[§] Friedrich Kaasik,[†] Yury Gogotsi,[*,§] and Volker Presser[*,†,‡]

[†]INM-Leibniz Institute for New Materials, 66123 Saarbrücken, Germany

[‡]Department of Materials Science and Engineering, Saarland University, 66123 Saarbrücken, Germany

[§]Department of Materials Science and Engineering & A.J. Drexel Nanomaterials Institute, Drexel University, Philadelphia, Pennsylvania 19104, United States

Supporting Information

ABSTRACT: We report the volumetric changes of MXenes in contact with different ionic liquids and the swelling/contraction during electrochemical voltage cycling by complementing electrochemical dilatometry with in situ X-ray diffraction measurements. A drastic, initial, and irreversible volume expansion of MXenes occurs during first contact to ionic liquids (wetting). Voltage cycling evidenced a highly reversible expansion and contraction of electrodes at a very large amplitude of strain (corresponding with max. 12 vol %), which may allow the use of MXene as a high-performance electrochemical actuator.

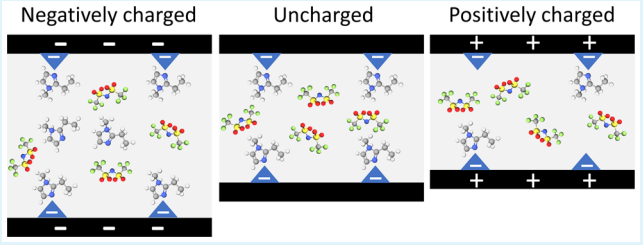

KEYWORDS: *MXene, pseudocapacitance, ionic liquid, electrochemical dilatometry, in situ XRD*

An increasing number of research studies have explored the two-dimensional (2D) early transition metal carbides and nitrides, called MXenes.[1−3] MXene has shown tremendous potential as pseudocapacitive electrode material in aqueous,[4] organic,[5] and ionic liquid (IL) electrolytes.[6,7] The latter two are attractive because of the possible high cell voltages (>3 V),[8] yet may lead to significant volumetric changes of the electrode material.[9] With so far only two studies on MXene in IL electrolyte,[6,7] there is a great need to study volumetric changes as a possible mechanical limitation for supercapacitors or as a promising actuation material.[10]

In aqueous electrolytes, promising results with high volumetric capacitance[11,12] and highly reversible mechanical changes of MXenes were observed.[4,10] MXenes have shown the unique possibility to expand and contract without any damage.[4,7] This is in contrast to the inability of nanoporous carbons to contract below the initial volume after electrolyte wetting during capacitive charging and discharging.[13] We report here the strain of MXene in contact with ILs, namely EMIM-TFSI (1-ethyl-3-methylimidazolium bis(trifluoromethylsulfonyl)imide) and BMIM-BF_4 (1-butyl-3-methylimidazolium tetrafluoroborate).

We have investigated the highly reversible swelling and contraction of Ti_3C_2-MXene during voltage cycling. In situ X-ray diffraction (XRD) was complemented by electrochemical dilatometry measurements. Two ILs with different ion sizes were selected, one with comparable sizes of anion and cation and the other one with a large size difference between anion and cation. As will be shown later, the ion size plays a key role in explaining the observed irreversible and reversible volumetric changes of MXenes.

Electrochemical investigations were carried out first by sequential window opening toward negative potentials, in parallel with electrochemical dilatometry to track the volumetric response (Figure 1). During negative polarization, there is neither a significant capacitive response nor a corresponding significant volume change for EMIM-TFSI up to a potential of −0.6 V vs carbon (Figure 1A). At more negative potentials, there is a large current increase and a peak emerging at −1 V vs carbon during anodic sweeping and a corresponding peak at −0.5 V vs carbon during cathodic sweeping. By sweeping from 0 to −1.5 V vs carbon at a scan rate of 1 mV/s, we see the concurrence of an increased current signal and an electrode strain of up to 6% (Figure 1A) in the *z*-direction (i.e., perpendicular to the aligned layered nanosheets of the MXene paper electrode). Considering the large size of $EMIM^+$ ions, the expansion seemingly is related to intercalation of ions between the MXene nanosheets. That shows the possibility for even very large ions to intercalate MXene, in line with a recently published in situ XRD study.[7]

During positive polarization of EMIM-TFSI, there is a very low current signal and no expansion is detected. Instead, a contractive strain of up to −1% is measured at a maximum potential of +1 V vs carbon. This behavior cannot be explained by deintercalation of $EMIM^+$, insertion of $TFSI^-$, or the exchange of

Received: September 15, 2016
Accepted: November 10, 2016
Published: November 10, 2016

DOI: 10.1021/acsami.6b11744
ACS Appl. Mater. Interfaces 2016, 8, 32089−32093

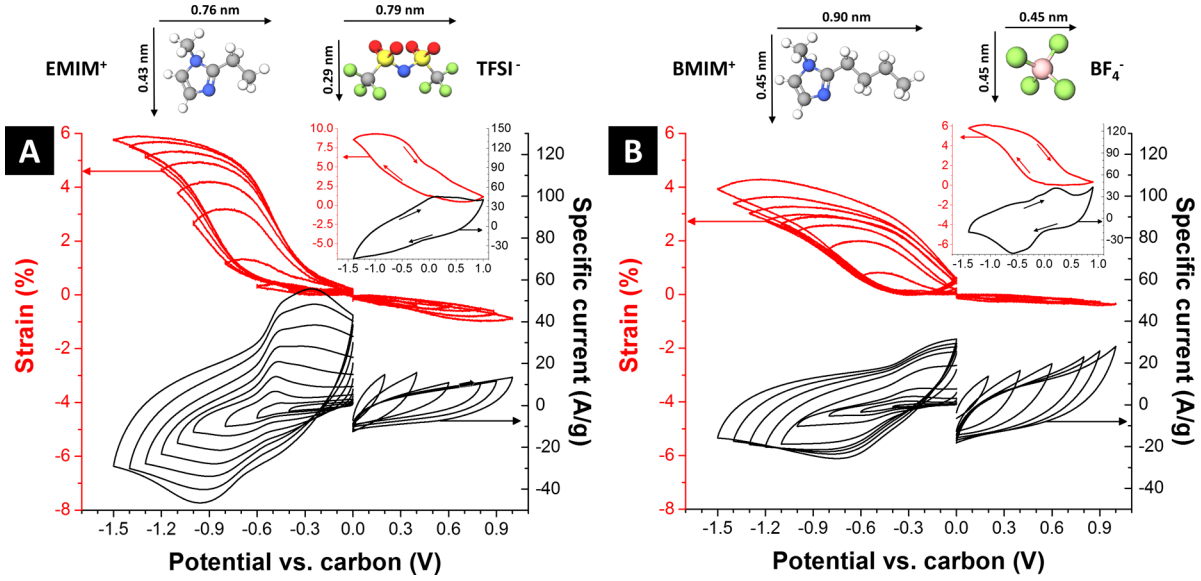

Figure 1. Voltage window opening with in situ electrical dilatometry in CV mode at 1 mV/s sweep rate. The expansion/contraction is normalized to the equilibrium thickness (after 24 h) at 0 V vs carbon. (A) In EMIM-TFSI and (B) in BMIM-BF_4. Insets: full range CV with related displacement with arrows indicating the direction of potential sweeping.

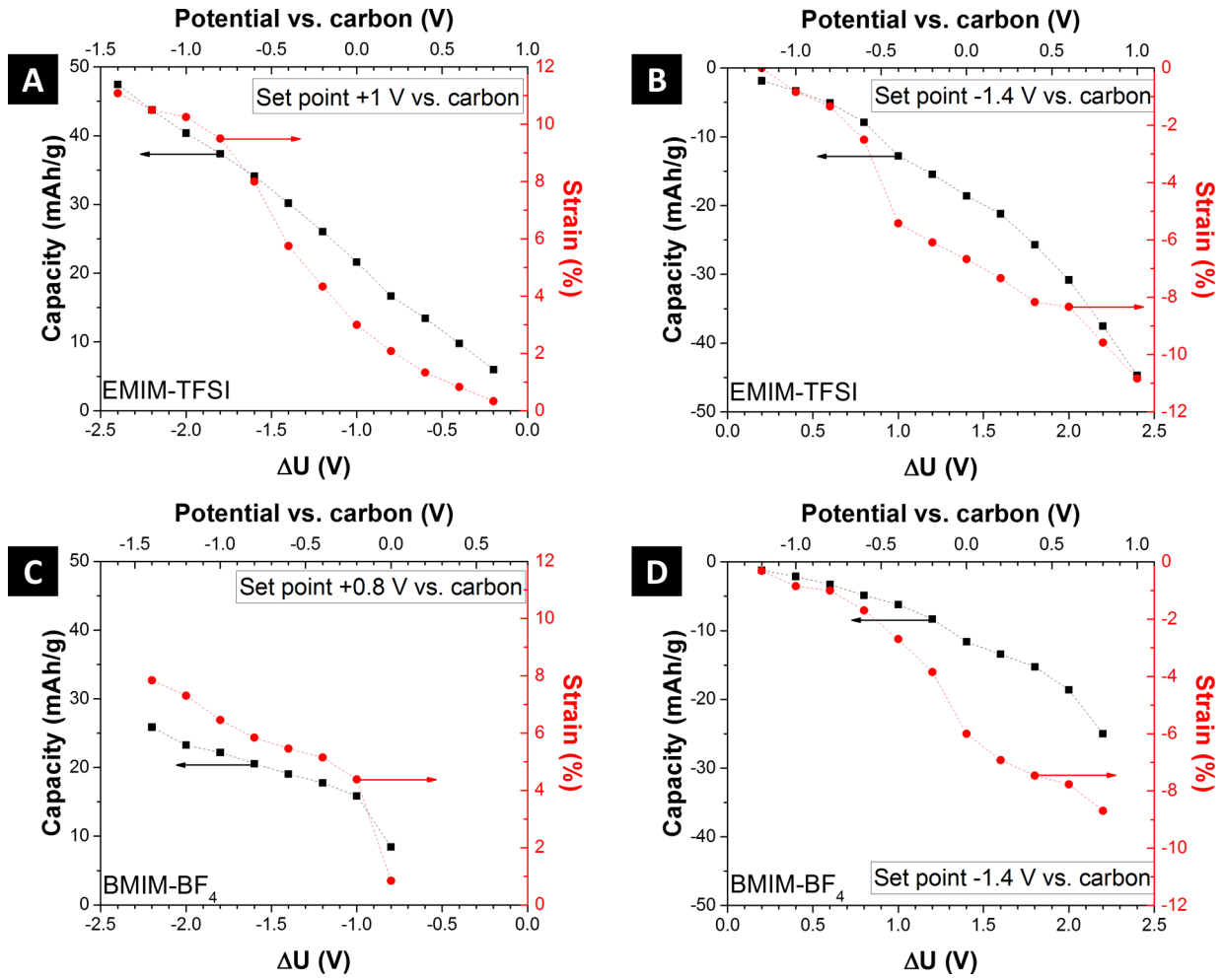

Figure 2. Chronoamperometric measurements with (A, C) fully contracted electrodes as reference thickness at the most positive potential and (B, D) fully swollen electrodes with reference to the most negative potential. (A, B) In EMIM-TFSI and (C, D) in BMIM-BF_4.

cation and anion between the MXene sheets because the size difference is too small. We also see differences when cycling Ti_3C_2-MXene in EMIM-TFSI between −1.4 V to +1 V vs carbon compared to just positive or just negative voltage sweeping

DOI: 10.1021/acsami.6b11744
ACS Appl. Mater. Interfaces 2016, 8, 32089−32093

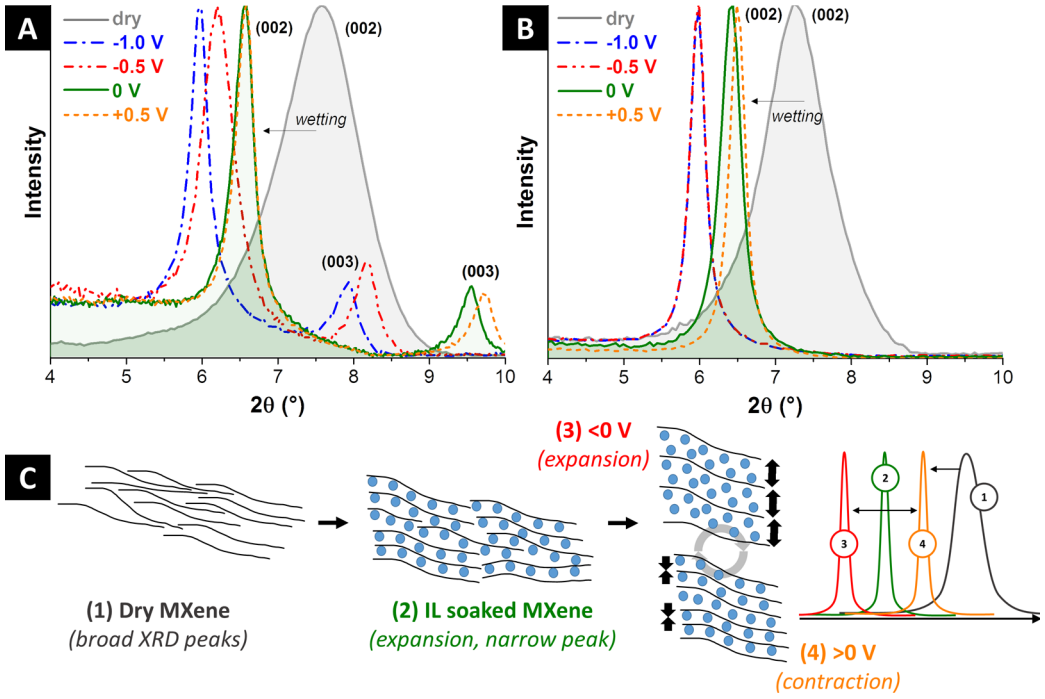

Figure 3. In situ XRD patterns for (A) EMIM-TFSI and (B) BMIM-BF_4 recorded after wetting with ILs and applying different potentials; data normalized to the (002)-peak. (C) Schematic of increased MXene layer spacing (*d*-value) and ordering after IL intercalation (wetting) and influence of positive and negative applied potentials on the lattice spacing.

(Figure 1A, inset). By doing so, we see an onset of expansion at +0.5 V vs carbon and an onset of contraction at −0.7 V vs carbon. The emerging peaks in CV (smeared out due to high internal resistance in the dilatometer assembly) correspond with the measured strain. Most notably, the maximum strain increases to 9% at −1.4 V vs carbon after sweeping from the upper to the lower stable potential.

A different behavior is seen during voltage cycling Ti_3C_2-MXene in BMIM-BF_4, where the cation is much larger than the anion (Figure 1B). We must also consider the difference in viscosity. This results in a higher resistivity and reduced kinetics during electrochemical operation with BMIM-BF_4, as can be seen from lowered and broadened signals of charge and strain, especially during anodic voltage sweeping to −1.4 V vs carbon. At this maximum vertex potential, we measured a maximum strain of 4%. Also, MXene contraction during positive polarization in BMIM-BF_4 is smaller than for EMIM-TFSI with a maximum contraction of 0.4% at +1 V vs carbon. The size difference of cation and anion makes it difficult to geometrically explain the smaller contraction in the case of BMIM-BF_4. We found in the cyclic voltammogram during cycling between −1.4 V and +0.8 V vs carbon, prominent current peaks at −0.6 V and at +0.2 V vs carbon. These peaks coincide with the maximum slope of expansion and contraction (inset Figure 1B). We assume de-intercalation of ions mainly at these potentials.[6] The hysteresis width between expansion and contraction of 0.8 V is related to the cell assembly and internal kinetics. The maximum expansion at −1.4 V during this extended voltage cycling (6%) is higher compared to when cycling between 0 and −1.4 V vs carbon (i.e., 4%). In general, we see much lower strain for BMIM-BF_4 compared to EMIM-TFSI.

To eliminate kinetic effects caused by different ion mobility, we employed chronoamperometry (CA) with 1 h of equilibrium time at each potential to achieve the maximum (equilibrium) expansion for the maximum charged state at the given electrode potential (Figure 2). In our experiments, we condition the cells either at the maximum positive electrode potential (i.e., + 1 V vs carbon for EMIM-TFSI (Figure 2A) or +0.8 V vs carbon for BMIM-BF_4 (Figure 2C) or the maximum negative electrode potential (i.e., −1.4 V vs carbon for both electrolytes (Figure 2B, D). When first conditioning at a high positive potential (maximum contraction) and then lowering the voltage, we observed an increasing electrode expansion (Figure 2A, C) for both electrolytes. The opposite case was observed when the maximum negative potential was kept constant and the voltage increased. In this case, the electrode started as fully expanded and higher voltages lead to a continuous compression (Figure 2B, D).

For EMIM-TFSI (Figure 2A, B), the charge increased nearly linearly with potential, as expected for a capacitive/pseudocapacitive material like MXene. Yet, the strain does not exhibit a linear dependency and we see a drastic increase/decrease at −0.5 V vs carbon in expansion or contraction, respectively. This correlates with the onset of the current peak seen in the CV presented in Figure 1A. Seemingly, $EMIM^+$ ions gain further access to initially less accessible sites between the MXene nanosheets when the potential exceeds −0.5 V vs carbon. It is possible that at this potential, surface charges are fully compensated and the material accomplishes counterion electrosorption on the surface of the nanosheets (ions with opposite charge as the electrode). Furthermore, the total strain does not change if the electrode expands or shrinks, which can be attributed to the high reproducibility and reversibility of ion insertion and extraction between the nanosheets.

In the case of BMIM-BF_4, the correlation of charge (capacity) and applied voltage is no longer linear (Figure 2C, D). When the initial conditioning was set at +0.8 V vs carbon, we observed maximum contraction and only small strain occurred when lowering the potential to 0 V (Figure 2C). This behavior aligns with the results shown in Figure 1B (inset) where almost no change in strain occurs in the potential range of +0.8 to 0 V vs

DOI: 10.1021/acsami.6b11744
ACS Appl. Mater. Interfaces 2016, 8, 32089−32093

Table 1. Results of the in Situ XRD Tracking of the (002) Reflection of Ti_3C_2 MXene with Calculated Strain from XRD and Resulting Strain from Chronoamperometric Dilatometry Measurements (eD)

	EMIM-TFSI				BMIM-BF_4			
condition/applied potential	(002) *d*-spacing (Å)	fwhm (° 2θ)	strain XDR (%)	strain eD (%)	(002) *d*-spacing (Å)	fwhm (° 2θ)	strain XRD (%)	strain eD (%)
dry MXene	11.6	1.21			11.6	1.21		
+0.5 V	13.4	0.29	−1	−1	13.5	0.25	−1	−1
0 V	13.5	0.32	0	0	13.7	0.33	0	0
−0.5 V	14.2	0.49	+5	+3	14.8	0.24	+7	+4
−1.0 V	14.8	0.28	+9	+6	14.8	0.22	+7	+5

carbon. There is a strong increase in slope for charge and strain as the potential reaches −0.2 V vs carbon. This also correlates with the peak emerging in the CV (Figure 1B, inset). Continuing toward lower potentials, we see a capacitor-like, linear increase of charge and the same trend for strain.

The behavior is different when starting with a fully expanded electrode, that is, after conditioning the system at −1.4 V vs carbon. Instead of a linear correlation between charge and potential, a parabolic dependence is observed for both electrolytes. We also see two discontinuities in capacity at 0 and at 0.6 V vs carbon. Concurrently, the strain drastically decreases at these voltages. By comparison with CV (Figure 1B, inset), the slope in strain signal is the highest at 0 V by sweeping positive and this matches with the strong decrease in strain in CA measurements.

The CA results together with information from CVs identify a certain voltage at which a strong increase in current and strain occur. Since the surface of MXene is terminated by −OH, ═O and −F and acquires negative static charge in solution, intercalation of cations between the MXene sheets may become possible at this or lower potentials.[14] We can conclude that insertion of cations results in a large expansion of the electrode. The contraction during sweeping to positive potentials cannot be explained by ion swapping or anion insertion because the contraction is more pronounced for EMIM-TFSI with similar ion sizes, whereas the values are much lower for BMIM-BF_4 with a much smaller anion. Cation intercalation (negative potential) and de-intercalation (positive potential) seems to control the expansion as well as contraction, as has been recently suggested.[6] Because $BMIM^+$ has a lower mobility than $EMIM^+$, it is removed slower and the strain is lower in the former case. The negatively charged surface lead to a preferred orientation of cations close to the surface with the same number of anions due to counter-balanced charge without applied potential.

To further understand the structural changes during electrochemical cycling and to also investigate the initial wetting process, we carried out an in situ XRD study (Figure 3, full XRD pattern Figure S1). The peak in the range of 6−8° 2θ is from the (002) reflection of Ti_3C_2-MXene.[11] This initially broad (002) peak at 7.5° 2θ (fwhm 1.212° 2θ) for dry MXene shifts for EMIM-BF_4 at 0 V to lower angles (6.5° 2θ) and becomes considerably more narrow (fwhm = 0.321° 2θ). This means the stacking ordering along the *c*-axis is drastically increased, whereas the interlayer spacing of the MXene sheets is also increased during initial wetting (Figure 3A, B). The relative interlayer spacing increases and becomes more narrowly distributed when the IL ions intercalate, leading to a better alignment of MXene sheets, as schematically shown in Figure 3C. We can see a drastic initial swelling when the dry nanosheets contact the IL with *d*-values increasing from 11.6 to 13.5 Å (Table 1), whereas the negatively charged surface groups may lead to an enhanced wetting with cations followed by anions to achieve charge neutrality.

For EMIM-TFSI, when applying a voltage, we see the expected swelling (increase in *d*-value) at negative voltage and compression (decrease in *d*-value) at positive potential (Table 1 and Figure 3A). The fwhm values are lowest at +0.5 V and −1 V vs carbon, which is attributed to the best ordering of MXene sheets resulting from a homogeneous coverage of ions. Furthermore, a peak emerges at 9.5° 2θ. This peak shifts to slightly higher angles under applied positive potential (9.7° 2θ) and strongly shifts to smaller angles under negative potentials (8.2° 2θ at −0.5 V and 7.9° 2θ at −1 V vs carbon). This additional peak can be explained as a (003) reflection typically found after phase transitions of two-dimensional materials.[15]

The XRD data of Ti_3C_2-MXene during electrochemical cycling in BMIM-BF_4 are plotted in Figure 3B. As has already been seen for EMIM-TFSI, the (002) peak shifts to lower angles after initial contact with the IL (initial swelling due to IL intercalation) and moves to even lower values as the potential decreases. The calculated strain values from XRD measurements (Table 1) follow the same trend as observed in dilatometry (Figure 1), with expansion during negative polarization (up to +9% strain) and contraction during negative sweeping (up to −1% strain). We also see a much larger expansion at −1.0 V vs carbon for EMIM-TFSI (9%) compared to BMIM-BF_4 (7%). The slightly lower strain values seen in Figure 1 result from the much more dynamic probing during voltage sweeping at 1 mV/s, compared to the more equilibrated values recorded by in situ XRD (Table 1). Higher strain seen from XRD also relates to the expansion/contraction of individual MXene flakes, whereas slightly lower values are expected for dilatometry, where the entire electrode is measured and there is a small applied constant pressure on the electrode in the device (1 N).

There seems to be a saturation of $BMIM^+$ at −0.5 V vs carbon because the (002) peak does not shift further at −1 V vs carbon. Yet, the peak intensity increases and the fwhm decreases which could be explained by increasing ordering of MXenes due to more complete filling of interlayer spacing with $BMIM^+$ ions, forming a complete monolayer on each MXene sheet. Furthermore, no secondary peak at 10° 2θ emerges in the BMIM-BF_4 pattern because $BMIM^+$ with lower ion mobility intercalates less compared to $EMIM^+$, which results in the absence of a phase transition.

In conclusion, we identified a large initial swelling of the MXene electrode after initial contact with ILs which suggests spontaneous ion intercalation.[16] This swelling occurs without the application of an external voltage, but is enhanced when applying negative voltage, suggesting preferential insertion of cations. Under positive potentials the electrode contracts even further compared to the thickness at 0 V. Taking into account the difference in size of $BMIM^+$ and BF_4^-, this can be explained by

DOI: 10.1021/acsami.6b11744
ACS Appl. Mater. Interfaces 2016, 8, 32089−32093

swapping of cations and anions, but we assume only cation intercalation at negative potentials and cation deintercalation at positive potentials.[7,17] After applying positive potentials, a depletion of $EMIM^+$/$BMIM^+$ occurs, whereas the lower ion mobility of $BMIM^+$ results in lower total expansion/contraction at applied voltage.

The observed large expansion and contraction of MXene electrodes in IL electrolytes may explain their fast strain fading in IL (Figure S2), which may require pillaring of MXene layers with polymers or other molecules before using in supercapacitor electrodes.[6,19] However, the same large volume change may be beneficial for the use in electrochemical actuators, especially taking into account the high strength of MXene paper and MXene-polymer composites.[18,19]

EXPERIMENTAL DESCRIPTION

See the Supporting Information.

ASSOCIATED CONTENT

Supporting Information

The Supporting Information is available free of charge on the ACS Publications website at DOI: 10.1021/acsami.6b11744.

Experimental description, full-range XRD pattern (Figure S1), longtime performance (Figure S2), information about the used ionic liquids and additional information about MAX and MXene phases (PDF)

AUTHOR INFORMATION

Corresponding Authors

*E-mail: gogotsi@drexel.edu.
*E-mail: volker.presser@leibniz-inm.de.

ORCID

Volker Presser: 0000-0003-2181-0590

Notes

The authors declare no competing financial interest.

ACKNOWLEDGMENTS

K.L.V., M.A., and Y.G. were supported by the Fluid Interface Reactions, Structures and Transport (FIRST) Center, an Energy Frontier Research Center funded by the U.S. Department of Energy, Office of Science, Office of Basic Energy Sciences. The authors thank Dr. Aslan, Dr. Grobelsek, Aura Tolosa, and Anna Schreiber (all at INM), for discussions. N.J., B.K., F.K., and V.P. also thank Prof. Arzt (INM) for his continuing support. F.K. and V.P. thank the Prof. Lenz Foundation (Stiftungspreis).

REFERENCES

(1) Naguib, M.; Mochalin, V. N.; Barsoum, M. W.; Gogotsi, Y. 25th Anniversary Article: MXenes: a New Family of Two-Dimensional Materials. *Adv. Mater.* **2014**, *26* (7), 992−1005.

(2) Ghidiu, M.; Lukatskaya, M. R.; Zhao, M. Q.; Gogotsi, Y.; Barsoum, M. W. Conductive Two-Dimensional Titanium Carbide 'Clay' with High Volumetric Capacitance. *Nature* **2014**, *516* (7529), 78−81.

(3) Srimuk, P.; Kaasik, F.; Krüner, B.; Tolosa, A.; Fleischmann, S.; Jäckel, N.; Tekeli, M. C.; Aslan, M.; Suss, M. E.; Presser, V. MXene as a novel intercalation-type pseudocapacitive cathode and anode for capacitive deionization. *J. Mater. Chem. A* **2016**, DOI: 10.1039/C6TA07833H.

(4) Levi, M. D.; Lukatskaya, M. R.; Sigalov, S.; Beidaghi, M.; Shpigel, N.; Daikhin, L.; Aurbach, D.; Barsoum, M. W.; Gogotsi, Y. Solving the Capacitive Paradox of 2D MXene using Electrochemical Quartz-Crystal Admittance and In Situ Electronic Conductance Measurements. *Adv. Energy Mater.* **2015**, *5* (1), 1400815.

(5) Byeon, A.; Glushenkov, A. M.; Anasori, B.; Urbankowski, P.; Li, J.; Byles, B. W.; Blake, B.; Van Aken, K. L.; Kota, S.; Pomerantseva, E.; Lee, J. W.; Chen, Y.; Gogotsi, Y. Lithium-Ion Capacitors with 2D Nb_2CT_x (MXene) − Carbon Nanotube Electrodes. *J. Power Sources* **2016**, *326*, 686−694.

(6) Lin, Z.; Barbara, D.; Taberna, P.-L.; Van Aken, K. L.; Anasori, B.; Gogotsi, Y.; Simon, P. Capacitance of $Ti_3C_2T_x$ MXene in Ionic Liquid Electrolyte. *J. Power Sources* **2016**, *326*, 575−579.

(7) Lin, Z.; Rozier, P.; Duployer, B.; Taberna, P.-L.; Anasori, B.; Gogotsi, Y.; Simon, P. Electrochemical and In-situ X-ray Diffraction Studies of $Ti_3C_2T_x$ MXene in Ionic Liquid Electrolyte. *Electrochem. Commun.* **2016**, *72*, 50−53.

(8) Zhong, C.; Deng, Y.; Hu, W.; Qiao, J.; Zhang, L.; Zhang, J. A Review of Electrolyte Materials and Compositions for Electrochemical Supercapacitors. *Chem. Soc. Rev.* **2015**, *44* (21), 7484−539.

(9) Kaasik, F.; Tamm, T.; Hantel, M. M.; Perre, E.; Aabloo, A.; Lust, E.; Bazant, M. Z.; Presser, V. Anisometric Charge Dependent Swelling of Porous Carbon in an Ionic Liquid. *Electrochem. Commun.* **2013**, *34*, 196−199.

(10) Come, J.; Xie, Y.; Naguib, M.; Jesse, S.; Kalinin, S. V.; Gogotsi, Y.; Kent, P. R. C.; Balke, N. Nanoscale Elastic Changes in 2D $Ti_3C_2T_x$ (MXene) Pseudocapacitive Electrodes. *Adv. Energy Mater.* **2016**, *6*, 1502290.

(11) Lukatskaya, M. R.; Mashtalir, O.; Ren, C. E.; Dall'Agnese, Y.; Rozier, P.; Taberna, P. L.; Naguib, M.; Simon, P.; Barsoum, M. W.; Gogotsi, Y. Cation Intercalation and High Volumetric Capacitance of Two-Dimensional Titanium Carbide. *Science* **2013**, *341* (6153), 1502−1505.

(12) Xie, X.; Zhao, M.-Q.; Anasori, B.; Maleski, K.; Ren, C. E.; Li, J.; Byles, B. W.; Pomerantseva, E.; Wang, G.; Gogotsi, Y. Porous Heterostructured MXene/Carbon Nanotube Composite Paper with High Volumetric Capacity for Sodium-Based Energy Storage Devices. *Nano Energy* **2016**, *26*, 513−523.

(13) Hantel, M. M.; Weingarth, D.; Kötz, R. Parameters Determining Dimensional Changes of Porous Carbons During Capacitive Charging. *Carbon* **2014**, *69*, 275−286.

(14) Hope, M. A.; Forse, A. C.; Griffith, K. J.; Lukatskaya, M. R.; Ghidiu, M.; Gogotsi, Y.; Grey, C. P. NMR Reveals the Surface Functionalisation of Ti_3C_2 MXene. *Phys. Chem. Chem. Phys.* **2016**, *18* (7), 5099−5102.

(15) Xie, X.; Makaryan, T.; Zhao, M.; Van Aken, K. L.; Gogotsi, Y.; Wang, G. MoS_2 Nanosheets Vertically Aligned on Carbon Paper: A Freestanding Electrode for Highly Reversible Sodium-Ion Batteries. *Adv. Energy Mater.* **2016**, *6* (5), 1502161.

(16) Mashtalir, O.; Naguib, M.; Mochalin, V. N.; Dall'Agnese, Y.; Heon, M.; Barsoum, M. W.; Gogotsi, Y. Intercalation and Delamination of Layered Carbides and Carbonitrides. *Nat. Commun.* **2013**, *4*, 1716.

(17) Dall'Agnese, Y.; Rozier, P.; Taberna, P.-L.; Gogotsi, Y.; Simon, P. Capacitance of Two-Dimensional Titanium Carbide (MXene) and MXene/Carbon Nanotube Composites in Organic Electrolytes. *J. Power Sources* **2016**, *306*, 510−515.

(18) Ling, Z.; Ren, C. E.; Zhao, M.-Q.; Yang, J.; Giammarco, J. M.; Qiu, J.; Barsoum, M. W.; Gogotsi, Y. Flexible and Conductive MXene Films and Nanocomposites with High Capacitance. *Proc. Natl. Acad. Sci. U. S. A.* **2014**, *111* (47), 16676−16681.

(19) Come, J.; Black, J. M.; Lukatskaya, M. R.; Naguib, M.; Beidaghi, M.; Rondinone, A. J.; Kalinin, S. V.; Wesolowski, D. J.; Gogotsi, Y.; Balke, N. Controlling the Actuation Properties of MXene Paper Electrodes upon Cation Intercalation. *Nano Energy* **2015**, *17*, 27−35.

DOI: 10.1021/acsami.6b11744
ACS Appl. Mater. Interfaces 2016, 8, 32089−32093

4.7 In Situ Multi-length Scale Approach to Understand the Mechanics of Soft and Rigid Binder in Composite Lithium Ion Battery Electrodes

N. Jäckel [a,b], V. Dargel [c], N. Shpigel [c], S. Sigalov [c], M.D. Levi [c], L. Diakhin [d], D. Aurbach [c], V. Presser [a,b]

[a] INM-Leibniz Institute for New Materials, Campus D2 2, 66123 Saarbrücken, Germany

[b] Department of Materials Science and Engineering, Saarland University, Campus D2 2, 66123 Saarbrücken, Germany

[c] Department of Chemistry, Bar-Ilan University, Ramat-Gan, 52900, Israel

[d] School of Chemistry, Raymond and Beverly Sackler Faculty of Exact Sciences, Tel-Aviv University, Ramat Aviv, 69978, Israel

published in Journal of Power Sources, 2017. 371: p. 162-166

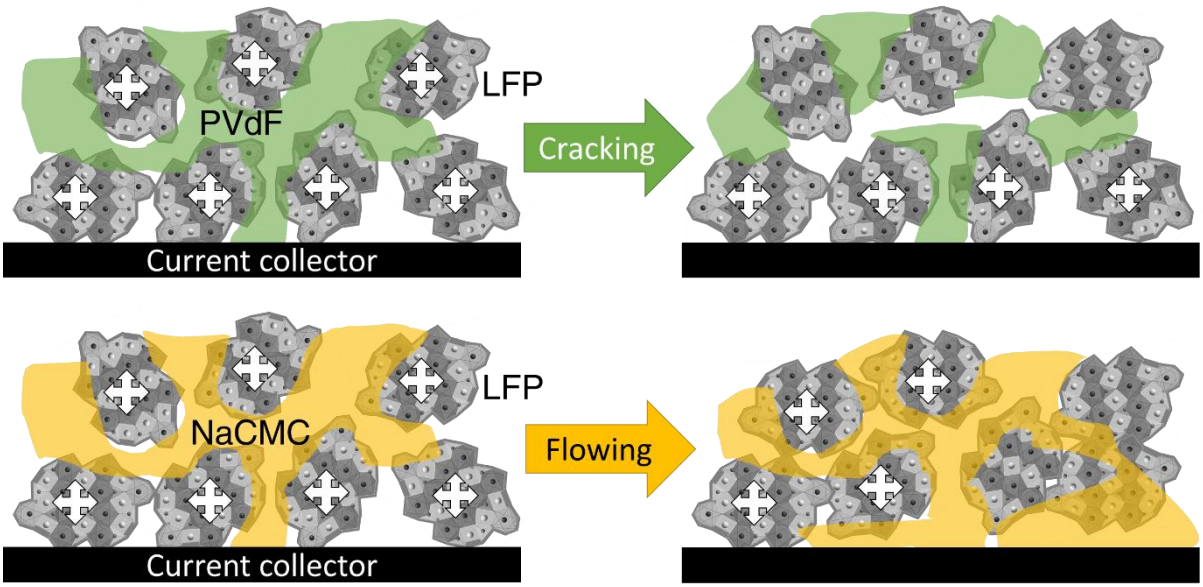

Own contribution:

Data generation 80 %

Data analysis 90 %

Interpretation 80 %

Writing 85 %

Journal of Power Sources 371 (2017) 162–166

Contents lists available at ScienceDirect

Journal of Power Sources

journal homepage: www.elsevier.com/locate/jpowsour

Short communication

In situ multi-length scale approach to understand the mechanics of soft and rigid binder in composite lithium ion battery electrodes

Nicolas Jäckel[a,b], Vadim Dargel[c], Netanel Shpigel[c], Sergey Sigalov[c], Mikhael D. Levi[c,*], Leonid Daikhin[d], Doron Aurbach[c,**], Volker Presser[a,b,***]

[a] INM - Leibniz Institute for New Materials, 66123 Saarbrücken, Germany
[b] Department of Materials Science and Engineering, Saarland University, 66123 Saarbrücken, Germany
[c] Department of Chemistry, Bar-Ilan University, Ramat-Gan 52900, Israel
[d] School of Chemistry, Raymond and Beverly Sackler Faculty of Exact Sciences, Tel-Aviv University, Ramat Aviv, 69978, Israel

HIGHLIGHTS

- Combination of dilatometry and quartz-crystal microbalance measurements.
- Synergy of in situ techniques with different characteristic measurement scales.
- Identification of suitable binder properties: not too soft, not too rigid.

GRAPHICAL ABSTRACT

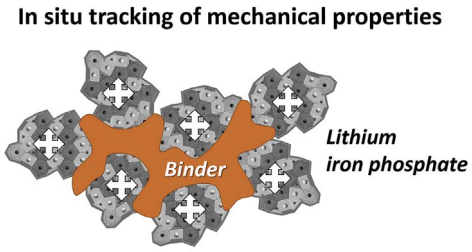

ARTICLE INFO

Keywords:
Electrochemical quartz crystal microbalance
EQCM-D
Electrochemical dilatometry
LIB
Polymer binder

ABSTRACT

Intercalation-induced dimensional changes of composite battery electrodes containing either a stiff or a soft polymeric binder is one of the many factors determining the cycling performance and ageing. Herein, we report dimensional changes in bulk composite electrodes by in situ electrochemical dilatometry (eD) combined with electrochemical quartz-crystal microbalance with dissipation monitoring (EQCM-D). The latter tracks the mechanical properties on the level of the electrode particle size. Lithium iron phosphate ($LiFePO_4$, LFP) electrodes with a stiff binder (PVdF) and a soft binder (NaCMC) were investigated by cycling in lithium sulfate (Li_2SO_4) aqueous solution. The electrochemical and mechanical electrode performances depend on the electrode cycling history. Based on combined eD and EQCM-D measurements we provide evidence which properties are preferred for a binder used for a composite Li-ion battery electrode.

1. Introduction

State-of-the-art lithium-ion batteries (LIB) offer a very broad spectrum of applications, from portable devices to all-electric vehicles [1–3]. Common industrial scale batteries contain porous composite electrodes with at least three components [4]: the active electrode material (e.g., particles of lithium iron phosphate, $LiFePO_4$, LFP) [5,6], a binder (e.g., polyvinylidene fluoride, PVdF, or Na salt of carboxymethyl cellulose, NaCMC) [7], and a conductive additive (typically carbon black) [8]. The movement of Li^+ ions in LIBs electrodes during cycling results in potential-dependent changes of the active material, for example, phase transformation with related volumetric changes

* Corresponding author.
** Corresponding author.
*** Corresponding author. INM - Leibniz Institute for New Materials, 66123 Saarbrücken, Germany.
E-mail addresses: levimi@mail.biu.ac.il (M.D. Levi), doron.aurbach@biu.ac.il (D. Aurbach), volker.presser@leibniz-inm.de (V. Presser).

http://dx.doi.org/10.1016/j.jpowsour.2017.10.048
Received 14 August 2017; Received in revised form 5 October 2017; Accepted 15 October 2017

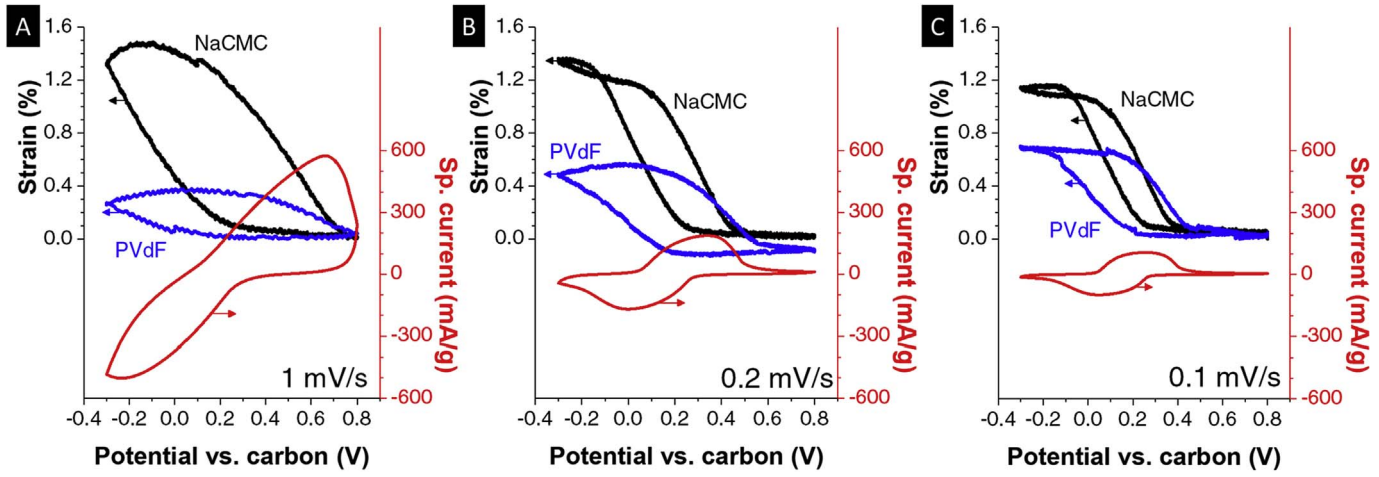

Fig. 1. Cyclic voltammogram (red) of the composite electrodes and simultaneously recorded strain signal for PVdF and NaCMC binder at (A) 1 mV/s, (B) 0.2 mV/s, and (C) 0.1 mV/s. (For interpretation of the references to colour in this figure legend, the reader is referred to the web version of this article.)

[9,10]. These volumetric changes cause mechanical stress, fatigue, and ultimate delamination from the current collector [11,12]. To determine the failure mechanisms of batteries, we need to understand the correlation between volumetric changes and the resulting performance degradation of the composite electrodes. Binders play a key role since they ensure tight electrical contact between the particles and the current collector and must be able to withstand and buffer the volumetric changes of the active material in the range of several percent [7,9].

We have recently developed a methodology called in situ hydrodynamic spectroscopy to quantify dimensional changes in olivine-type $LiFePO_4$ (a typical composite intercalation-type LIB cathode material) using electrochemical quartz-crystal microbalance with dissipation monitoring (EQCM-D) [12–16]. A unique feature of this approach is the simultaneous recording of changes of frequency shifts and changes in resonance peak width as a function of the applied potential [12]. The response of thin rigid electrode coatings on the gold-covered quartz crystal is due to the gravimetric changes caused by Li^+ (de-)intercalation, and hydrodynamic solid-liquid interactions if there are intercalation-dependent changes of the electrode rough/porous structure [17]. If the electrode is viscoelastic, the extent of viscoelasticity can strongly depend on the insertion of solvent molecules and intercalated ions (intercalation-induced viscoelastic changes), as is the case for electrodes of $Ti_3C_2(OH)_2$ (MXene) [18].

Electrochemical dilatometry (eD) was introduced as a facile tool to understand the mechanical properties of common thick electrodes (i.e., 20–100 μm) [19–22]. The effective nanometer-scale tracking of volumetric changes of bulk composite electrodes with eD has been demonstrated for battery and supercapacitor materials [19,23–26].

In the present work, our approach is focused on the investigation of the behavior of composite electrodes containing different binders on several probing length scales, ranging from a few tenths to several hundred-nanometer using EQCM-D on multiple overtone orders and in the range from a few tenth nanometers to several micrometers with eD. With these complementary in situ experiments, we can track the charge induced changes in the composite electrodes of a single/few particles layers level (EQCM-D) and correlate the properties with the results from bulk electrode measurements (eD).

2. Experimental description

Carbon-coated $LiFePO_4$ powder (battery grade, LFP) was purchased from Süd-Chemie AG. The investigated binders with always 10 mass% content in the electrode, namely polyvinylidene fluoride (PVdF) and sodium carboxy-methyl cellulose (NaCMC), were purchased from Sigma Aldrich. For dilatometer measurements 10 mass% Super C65 (Imerys) were added as conductive additive. All in situ experiments were conducted in 0.1 M Li_2SO_4 in de-aerated water.

The height change (strain) of the composite electrodes during charging and discharging was measured with an ECD-2-nano dilatometer from EL-CELL. The dilatometer cell is based on a two-electrode design using an oversized PTFE-bound activated carbon (AC, YP-80F from Kuraray) as counter and quasi-reference electrode [27]. The working electrode was dip casted on a Pt disc with 10 mm diameter. The investigated electrodes were compressed between the separator and a movable titanium plunger with a constant weight load of 1 N. A DP1S displacement transducer (Solartron Metrology), with an accuracy of 15 nm was used and connected to the VMP300 (Bio-logic) potentiostat. The experiments were performed at constant temperature of 25.0 ± 0.5 °C using a Binder climate chamber.

Electrodes for EQCM-D measurements were prepared by coating of LFP/PVdF in *n*-methyl-2-pyrrolidone (NMP) or LFP/NaCMC in water on 5 MHz Au polished quartz crystal (14 mm diameter, Biolin Scientific) by airbrush method [12,15,28]. Multiharmonic EQCM-D measurements were performed with Q-Sense E1 module (QCM-D from Biolin Scientific) using overtone orders from 3 to 13.

A slurry containing LFP powder and the binder was dispersed in a suitable solvent by sonication and immediately sprayed on the surface of a to a quartz crystal surface on a hot plate. The mass ratio of LFP to binder was also 9:1.

Electrochemical measurements were performed using a BioLogic VSP-300 potentiostat/galvanostat. The coated Au-quartz crystal was set as working electrode in a customized electrochemical flooded cell with Pt counter electrode and Ag/AgCl/KCl (sat.) reference electrode. The electrolyte solution was aqueous 0.1 M Li_2SO_4 (Sigma-Aldrich) in double-distilled H_2O. This electrolyte solution was chosen to study a system with an extremely soft and an extremely stiff binder. PVdF and NaCMC in aqueous solution ideally corresponds to these conditions. Moreover, aqueous systems containing LFP as active material are attractive for green and cost-attractive future batteries.

3. Results and discussion

For a first characterization of the aqueous battery system, in situ electrochemical dilatometry (eD) was recorded during cyclic voltammetric operation at different scan rates (Fig. 1). The plots show the current signal (red curve, similar for both binders) together with the resulting strain (blue and black curve) versus the electrode potential (measured vs. activated carbon QRE) [27]. Reversible lithium (de-)intercalation is evidenced by the current peaks in the CV. As seen, the strain for electrodes containing NaCMC is much larger than for PVdF at

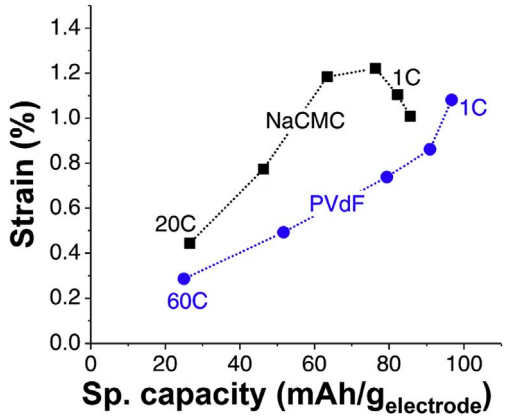

Fig. 2. Galvanostatic rate handling with accumulated charge from the discharge branch and related changes in strain values of the entire composite electrode using either PVdF or NaCMC binder.

all scan rates (Fig. 1). The strain hysteresis during potentiostatic cycling increases and the current peaks related to lithium (de-)intercalation become narrower at low sweep rates (Fig. 1B–C). While for samples with PVdF binder, the total strain at the negative vertex potential is gradually increasing from 0.3% to 0.55% at 1 mV/s and 0.1 mV/s, respectively, we see for NaCMC a reduced stain amplitude (fading from 1.3% to 1.1% at 1 mV/s and 0.1 mV/s, respectively). At 0.1 mV/s, the strain signal at the vertex potentials reaches a plateau as the electrodes become fully lithiated or fully delithiated. In general, the soft binder NaCMC allows more strain in the composite electrode than the rigid PVdF. Note that rigid or soft behavior of binder is also strongly dependent on the type of electrolyte and differ in non-aqueous media [14].

We further conducted galvanostatic measurements with different specific currents from high rate (up to 60 °C) to low rate (about C/3; Fig. 2). As typical for an intercalation material with a two-phase process at (de-)intercalation, the highest current leads to the lowest charge and this gradually changes by an increase of charge for lower rates [5,12,29].

In the case of the PVdF binder, the linear correlation between charge and strain is indicative of a good correlation between phase transformation related volume change and stored charge. As mentioned in our earlier publication, PVdF binder behaves rigidly in aqueous electrolytes [14]. A different behavior is observed for NaCMC bound electrodes: the initial strain at high loads is larger compared to PVdF and in line with the earlier monitored CV measurements. The strain increases as a function of the charge to about 1.2%. Interestingly, a further decrease in current with lower discharge rate leads to a higher amount of charge but to a lower value of strain. This behavior seems to be inconsistent with the intercalation mechanism as the progressing

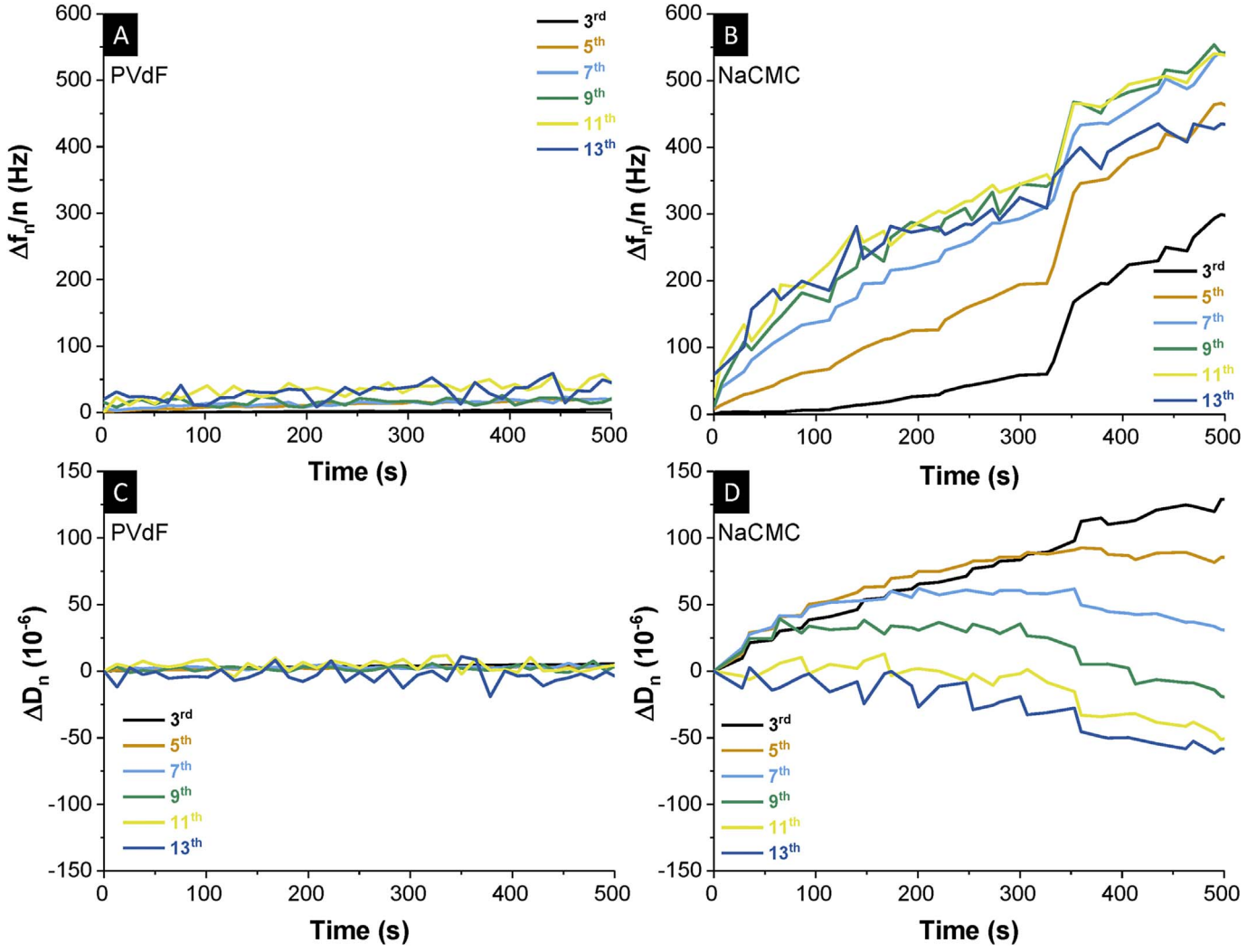

Fig. 3. Monitoring of (A + B) frequency change $\Delta f_n/n$ and (C + D) dissipation change ΔD_n over time after contact of the electrode with electrolyte (set as zero) at OCV for composite electrodes containing (A + C) PVdF and (B + D) NaCMC.

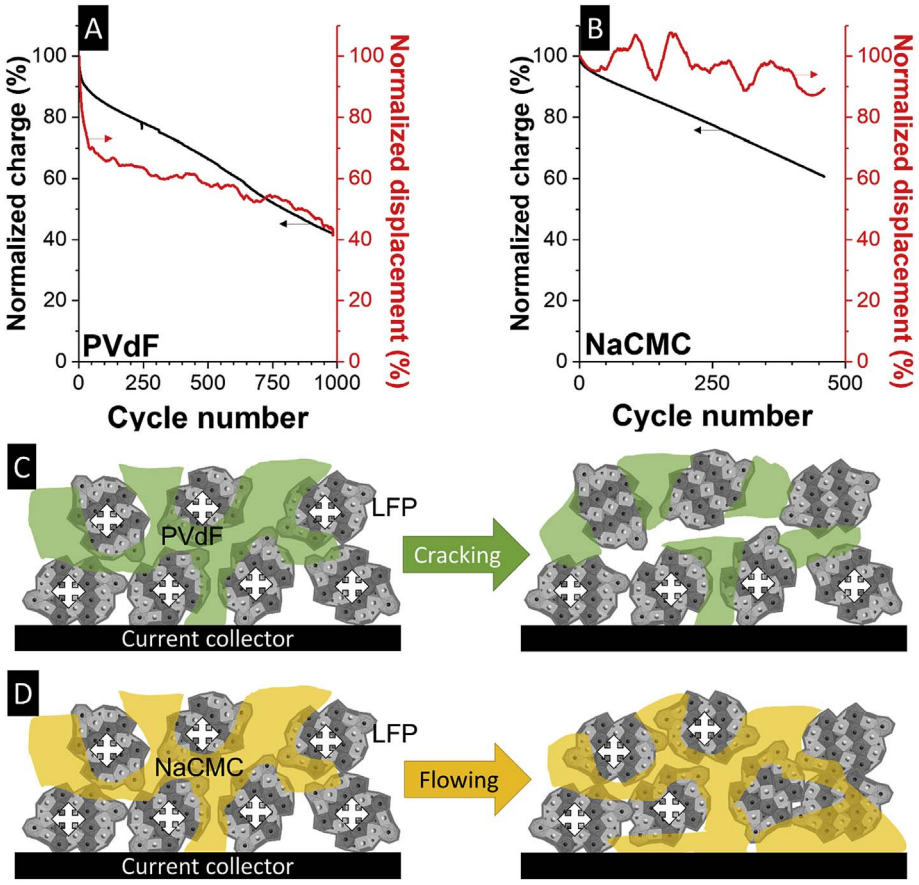

Fig. 4. Longtime cycling of composite electrodes at a rate of 1 °C with (A) PVdF binder and (B) NaCMC binder. Displacement refers to the difference in thickness of the electrode between lithiated and delithiated state. Values for the charge and displacement are normalized to the initial values in the first cycle as 100%. (C–D) Schematic drawing of ageing mechanisms according to the influence of binder.

lithium intercalation is achieved by the phase transformation and the accompanying strain in LFP [5,30]. Furthermore, the rate handling is poorer in the case of NaCMC in comparison to PVdF. We explain this by the very soft behavior of NaCMC in aqueous electrolyte solutions and the imperfect contact between the active material and the current collector [31].

A deeper understanding of the mechanical response can be gained by employing EQCM-D and studying the properties of a thin composite electrode. By this way, the behavior of particles in contact with the binder and the electrolyte can be traced with high precision. The basis for the quantitative analysis of EQCM-D data for composite electrodes containing both large and small particles as well as rigid and soft binders is the use of hydrodynamic and viscoelastic models for the layers of small particles, together with original sliding friction models for the large particles [32]. The initial changes in frequency and dissipation over the time after the electrode was immersed into the electrolytes are negligible for the PVdF-containing electrode (Fig. 3A + C). The absence of changes in both $\Delta f_n/n$ and ΔD_n is consistent with the rigid character of PVdF [14]. In contrast, a significant change in $\Delta f_n/n$ and ΔD_n with time in case of NaCMC binder is related with its viscoelastic character when in contact with aqueous solutions (Fig. 3B + D).

Combining now the results from the EQCM-D measurements with the results from eD, we can explain the decrease in strain at low rates for NaCMC-containing electrode by a rearrangement of particles. The constant load of 1 N on the working electrode and the softness of the binder allow to subject the intercalation particles to a viscous creep. Consequently, the exclusive information along the *z*-direction in eD does not fully reflect the actual volumetric change of the electrode particles, since significant viscoelastic changes occur at low rates. This is complicating the intercalation-induced translation in the *x*-*y* direction at a mesoscopic scale. Indeed, as follows from our viscoelastic modeling for the LFP electrode with NaCMC binder [32], the loss modulus exceeds by a factor of 2 to the related storage modulus. Therefore, it is important to carefully interpret eD data related to composite electrodes containing viscoelastic binders when the viscous creep distorts the vertical translation of the electrode volume changes. Moreover, the sliding friction coefficient is 1.7-times higher in the case of PVdF-bound electrodes in comparison to the NaCMC-bound electrodes. This can be understood as an inability of NaCMC to keep the particles properly bound to the current collector [32]. The complex shear moduli of NaCMC in aqueous solutions was quantified in a previous work with a storage modulus of 50.4 kPa and a loss modulus of 40.8 kPa [32].

To understand the influence of the binders on the longtime performance of thicker electrodes, we measured the strain during galvanostatic cycling with eD at a rate of 1 C up to 900 cycles (Fig. 4). The plot correlates with the charge transferred during lithiation of LFP with the resulting displacement in the dilatometer signal. We measured displacements, that is, the difference in thickness of the working electrode in lithiated and delithiated state. Both values, charge and displacement, are normalized to the initial values (= 100%). In the case of PVdF the initial decrease in charge after 50 cycles amounting to 88% corresponds to a significant drop in the displacement down to 69% (Fig. 4A). The EQCM-D measurements of the LFP electrode reported elsewhere [32] imply that rigid binder surrounding intercalation particles of the composite electrode does not allow their full and fully-reversible volumetric change. This can lead to accumulation of stresses in the contact area (aggravated by non-uniform character of charging of large intercalation particles), and may in some severe cases result in the formation of cracks deteriorating cycling performance (Fig. 4C) [14]. Due to deterioration of cycling performance, further cycling leads to a linear decrease in charge down to 45% after 900 cycles accompanied by the displacement decreasing to around 49%. We believe that both responses, that is: the charge and displacement decrease due to the ageing

of the composite LFP electrode [5,33] and the gradual loss of the electric contact to the current collector [9].

In the case of NaCMC-bound composite electrodes, the charge also decreases linearly but without a significant initial drop (Fig. 4B). Notably, the displacement response does not significantly change over the whole period of 500 cycles. The fluctuations of displacement data are related to the statistical signal noise of the eD system. We must consider that aging of LFP electrodes in aqueous electrolyte solutions is depending on many factors, but since we changed only the binder and kept (to the best possible extent) all other conditions unchanged, we can correlate the displacement with the battery performance.

We assume the enhanced viscoelasticity revealed by the LFP electrode with NaCMC binder at slow charging rate is both responsible for the deterioration of the reversible electrode capacity (leading to a loss of electrical contact) and more efficient and stable intercalation-induced displacement of the electrode. The fading in charge accumulation might be related to the inactivation of particles by NaCMC flowing between the active mass and the current collector (Fig. 4D). In general, a viscoelastic binder effectively accommodates volume changes of the intercalation particles but can cause a decreased capacity over lifetime due to inactivation of the LFP particles.

4. Conclusions

The use of a stiff or a soft polymeric binder has a strong influence on the cycling performance of composite LIB electrodes. The combination of data obtained from in situ electrochemical dilatometry and electrochemical quartz-crystal microbalance with dissipation monitoring provides important insights into the mechanical properties of the composite electrode both as a function of its charging level and cycling number. In our work, we cycled LFP electrodes in aqueous solution of Li_2SO_4. This electrolyte leads to a pronouncedly soft behavior of NaCMC and rigid behavior of PVdF. We found that the charge storage ability and the mechanical response depend on the electrode cycling history and the ability of the binder to compensate volume-change related stress. Based on the combined eD and EQCM-D measurements, we believe that the optimal polymeric binder for the composite electrode experiencing moderate intercalation-induced volume changes should neither be completely rigid nor too soft to allow unrestricted electrode volume changes but prevent the binder from viscous creep in the active material.

Acknowledgements

The authors acknowledge funding from the German-Israeli Foundation for Scientific Research and Development (GIF) via Research Grant Agreement No. 1-1237-302.5/2014. N.J. and V.P. thank Eduard Arzt for his continuing support and Marius Rodner for technical assistance (both at INM).

References

[1] D. Aurbach, Y. Talyosef, B. Markovsky, E. Markevich, E. Zinigrad, L. Asraf, J.S. Gnanaraj, H.-J. Kim, Electrochimica Acta 50 (2004) 247–254.
[2] V. Etacheri, R. Marom, R. Elazari, G. Salitra, D. Aurbach, Energ Environ. Sci. 4 (2011) 3243–3262.
[3] E.M. Erickson, C. Ghanty, D. Aurbach, J. Phys. Chem. Lett. 5 (2014) 3313–3324.
[4] R. Wagner, N. Preschitschek, S. Passerini, J. Leker, M. Winter, J. Appl. Electrochem 43 (2013) 481–496.
[5] A.K. Padhi, K.S. Nanjundaswamy, J.B. Goodenough, J. Electrochem. Soc. 144 (1997) 1188–1194.
[6] L.-X. Yuan, Z.-H. Wang, W.-X. Zhang, X.-L. Hu, J.-T. Chen, Y.-H. Huang, J.B. Goodenough, Energ Environ. Sci. 4 (2011) 269–284.
[7] S.-L. Chou, Y. Pan, J.-Z. Wang, H.-K. Liu, S.-X. Dou, Phys. Chem. Chem. Phys. 16 (2014) 20347–20359.
[8] M.E. Spahr, D. Goers, A. Leone, S. Stallone, E. Grivei, J. Power Sources 196 (2011) 3404–3413.
[9] J. Vetter, P. Novák, M.R. Wagner, C. Veit, K.C. Möller, J.O. Besenhard, M. Winter, M. Wohlfahrt-Mehrens, C. Vogler, A. Hammouche, J. Power Sources 147 (2005) 269–281.
[10] M.D. Levi, S. Sigalov, G. Salitra, P. Nayak, D. Aurbach, L. Daikhin, E. Perre, V. Presser, J. Phys. Chem. C 117 (2013) 15505–15514.
[11] J.B. Goodenough, Energ Environ. Sci. 7 (2014) 14–18.
[12] M.D. Levi, S. Sigalov, G. Salitra, R. Elazari, D. Aurbach, L. Daikhin, V. Presser, J. Phys. Chem. C 117 (2013) 1247–1256.
[13] M.D. Levi, L. Daikhin, D. Aurbach, V. Presser, Electrochem. Commun. 67 (2016) 16–21.
[14] N. Shpigel, M.D. Levi, S. Sigalov, O. Girshevitz, D. Aurbach, L. Daikhin, N. Jäckel, V. Presser, Angew. Chem. Int. Ed. 54 (2015) 12353–12356.
[15] N. Shpigel, M.D. Levi, S. Sigalov, O. Girshevitz, D. Aurbach, L. Daikhin, P. Pikma, M. Marandi, A. Jänes, E. Lust, N. Jäckel, V. Presser, Nat. Mater. 15 (2016) 570–575.
[16] A.R. Hillman, J. Solid State Electr. 15 (2011) 1647–1660.
[17] M.D. Levi, N. Shpigel, S. Sigalov, V. Dargel, L. Daikhin, D. Aurbach, Electrochimica Acta 232 (2017) 271–284.
[18] N. Shpigel, M.R. Lukatskaya, S. Sigalov, C.E. Ren, P. Nayak, M.D. Levi, L. Daikhin, D. Aurbach, Y. Gogotsi, ACS Energy Lett. (2017) 1407–1415.
[19] P.W. Ruch, M. Hahn, D. Cericola, A. Menzel, R. Kötz, A. Wokaun, Carbon 48 (2010) 1880–1888.
[20] M.M. Hantel, T. Kaspar, R. Nesper, A. Wokaun, R. Kotz, ECS Electrochem. Lett. 1 (2012) A1–A3.
[21] M.M. Hantel, R. Nesper, A. Wokaun, R. Kötz, Electrochimica Acta 134 (2014) 459–470.
[22] M. Hahn, H. Buqa, P.W. Ruch, D. Goers, M.E. Spahr, J. Ufheil, P. Novak, R. Kötz, Electrochem. Solid-State Lett. 11 (2008) A151–A154.
[23] D. Sauerteig, S. Ivanov, H. Reinshagen, A. Bund, J. Power Sources 342 (2017) 939–946.
[24] M. Nagayama, K. Ariyoshi, Y. Yamamoto, T. Ohzuku, J. Electrochem. Soc. 161 (2014) A1388–A1393.
[25] M.M. Hantel, V. Presser, J.K. McDonough, G. Feng, P.T. Cummings, Y. Gogotsi, R. Kötz, J. Electrochem. Soc. 159 (2012) A1897–A1903.
[26] N. Jäckel, B. Krüner, K.L. van Aken, M. Alhabeb, B. Anasori, F. Kaasik, Y. Gogotsi, V. Presser, ACS Appl. Mater. Interfaces 8 (2016) 32089–32093.
[27] J. Lee, N. Jäckel, D. Kim, M. Widmaier, S. Sathyamoorthi, P. Srimuk, C. Kim, S. Fleischmann, M. Zeiger, V. Presser, Electrochimica Acta 222 (2016) 1800–1805.
[28] Z. Yang, B.J. Ingram, L. Trahey, J. Electrochem. Soc. 161 (2014) A1127–A1131.
[29] G.K.P. Dathar, D. Sheppard, K.J. Stevenson, G. Henkelman, Chem. Mater. 23 (2011) 4032–4037.
[30] A.S. Andersson, B. Kalska, L. Häggström, J.O. Thomas, Solid State Ionics 130 (2000) 41–52.
[31] F. Jeschull, D. Brandell, M. Wohlfahrt-Mehrens, M. Memm, Energy Technol. (2017), http://dx.doi.org/10.1002/ente.201700200.
[32] V. Dargel, N. Jäckel, N. Shpigel, S. Sigalov, M.D. Levi, L. Daikhin, V. Presser, D. Aurbach, ACS Appl. Mater. Interfaces 9 (2017) 27664–27675.
[33] N. Omar, M.A. Monem, Y. Firouz, J. Salminen, J. Smekens, O. Hegazy, H. Gaulous, G. Mulder, P. Van den Bossche, T. Coosemans, J. Van Mierlo, Appl. Energ 113 (2014) 1575–1585.

5. CONCLUSIONS AND OUTLOOK

In this thesis, the role of the four main parts of supercapacitors and Li-ion batteries are investigated. Electric double-layer capacitors have a better power performance with approx. 5 mass% conductive additives, but the longevity can be drastically reduced by the combination of carbons with very different surface functional groups. The possible generation of water at the interface between activated carbon and carbon black is catalyzing the decomposition of the organic electrolyte.

Further, the ongoing discussion about the relation between average pore size and surface-normalized capacitance is terminated when properly considering the total pore size distribution and the accessibility of ions into pores. An ion with a finite size cannot enter a pore with a diameter smaller than the bare ion size which can result in a drastically reduced accessible SSA, especially for large ions. The volume-weighted average pore size influences on the capacitance and a maximum energy storage capability arise when the pore width matches the bare ion size. Still, the whole pore size distribution should be considered since the solvation energy and the size of the solvated ion also have an influence on the capacitance. Ions with a strong bond to the solvation molecules will prefer to electrosorb in pores with the size of solvated ions. If the solvation is less strong, the influence of pores in the range of the bare ion size will rise. However, carbon with most pores in the range of the bare ion size will have a reduced power performance. These insights can be useful for the future development of industrial-scale capacitors.

A more fundamental understanding of ion movement in nanoconfinement using the new in situ multi-length scale and multi-apparatus approach showed the power of combined measurements. A correlation between electrochemical performance and structural changes on particle and electrode level is possible using several in situ techniques with different characteristic length-scales.

Small ions in an ionic liquid always move first when applying a potential and this is directly correlated with the macroscopic expansion of the PTFE-bound carbon electrode. In aqueous electrolytes, the volume of micropores determines the total expansion of the electrode and an increase in expansion together with an emerging asymmetry of a larger expansion at negative potentials is correlated to the total amount of micropores. Future research on double-layer capacitors should be based on a combined approach of in situ methods together with simulations. The chronometric in situ measurements can be directly correlated to the time-resolved simulations and results can be gained on different kinetical and dimensional scales. With this approach a throughout understanding of charging mechanisms and charge-related structural changes might be possible.

In the field of two-dimensional materials, with the example of Ti_3C_2X-MXene, the charging mechanism is mostly based on cation (de-)intercalation. This is a new insight and can be very useful for the use of those cells in actuation. A total volumetric change of more than 10 % is huge in comparison to the

expansion of activated carbons. Furthermore, the fast and autonomous wetting of MXenes with ionic liquids together with the very high conductivity of MXenes can generate a high-energy density and high-power energy storage device. Yet, the longevity of those systems is currently small in comparison to EDLCs and this should be considered for further research.

For Li-ion batteries, the influence of many parameters and correlations of each part of the complex devices are known and intensively researched. In this study, an environmentally friendly approach with an aqueous electrolyte is chosen. The importance of binders on power and longevity is investigated with the multi-length scale approach. It is the inactive material (binder) which can influence the total performance in a non-neglectable way as shown. Consequently, the adjustment of active material with binder and electrolyte must always be considered.

REFERENCES

1. Smalley, R.E., *Future Global Energy Prosperity: The Terawatt Challenge.* MRS Bulletin, 2011. **30**(6): p. 412-417.
2. Gore, A., *The Future*. 2013: Ebury Publishing.
3. *Advancing the Science of Climate Change*. 2010, Washington, DC: The National Academies Press. 526.
4. International Energy Agency, *World Energy Outlook 2016 Part B: Special Focus on Renewable Energy*. 2016.
5. Lu, J., et al., *The role of nanotechnology in the development of battery materials for electric vehicles.* Nature Nanotechnology, 2016. **11**(12): p. 1031-1038.
6. Lu, J., T. Wu, and K. Amine, *State-of-the-art characterization techniques for advanced lithium-ion batteries.* Nature Energy, 2017. **2**(3): p. 17011.
7. Huggins, R.A., *Energy Storage*. 2010: Springer US.
8. Dunn, B., H. Kamath, and J.-M. Tarascon, *Electrical Energy Storage for the Grid: A Battery of Choices.* Science, 2011. **334**(6058): p. 928-935.
9. Scrosati, B. and J. Garche, *Lithium batteries: Status, prospects and future.* Journal of Power Sources, 2010. **195**(9): p. 2419-2430.
10. Energy, A., *The Worldwide Rechargeable Battery Market 2015-2025*, C. Pillot, Editor. 2016.
11. Yoo, H.D., et al., *On the challenge of developing advanced technologies for electrochemical energy storage and conversion.* Materials Today, 2014. **17**(3): p. 110-121.
12. Mankowski, P.J., et al., *Cellular phone collateral damage: A review of burns associated with lithium battery powered mobile devices.* Burns, 2016. **42**(4): p. e61-4.
13. Ball, P. and Y. Gogotsi, *Super-capacitors take charge in Germany.* MRS Bulletin, 2012. **37**(09): p. 802-803.
14. Schoeggl, P., A. Haimann, and L. Ress, *Electrification in Motorsports.* ATZautotechnology, 2012. **12**(1): p. 32-39.
15. Winter, M. and R.J. Brodd, *What Are Batteries, Fuel Cells, and Supercapacitors?* Chemical Reviews, 2004. **104**(10): p. 4245-4270.
16. Aurbach, D., et al., *Common Electroanalytical Behavior of Li Intercalation Processes into Graphite and Transition Metal Oxides.* Journal of The Electrochemical Society, 1998. **145**(9): p. 3024-3034.
17. Liu, C., et al., *Advanced materials for energy storage.* Adv Mater, 2010. **22**(8): p. E28-62.
18. Simon, P. and Y. Gogotsi, *Materials for electrochemical capacitors.* Nature Materials, 2008. **7**(11): p. 845-854.
19. Zhong, C., et al., *A review of electrolyte materials and compositions for electrochemical supercapacitors.* Chem Soc Rev, 2015. **44**(21): p. 7484-539.
20. Wang, G., L. Zhang, and J. Zhang, *A review of electrode materials for electrochemical supercapacitors.* Chem Soc Rev, 2012. **41**(2): p. 797-828.
21. Ragone, D.V., *Review of Battery Systems for Electrically Powered Vehicles*. 1968, SAE International.
22. Christen, T. and M.W. Carlen, *Theory of Ragone plots.* Journal of Power Sources, 2000. **91**(2): p. 210-216.
23. Jäckel, N., et al., *Increase in Capacitance by Subnanometer Pores in Carbon*. ACS Energy Letters, 2016. **1**(6): p. 1262-1265.
24. Boos, D.L., *Electrolytic capacitor having carbon paste electrodes*. 1970.
25. Hosokawa, M., K. Sanada, and T. Kawamura, *Laminated structure of double-layer capacitor*, L. Nippon Electric Co., Tokyo, Japan, Editor. 1982.
26. Sharma, P. and T.S. Bhatti, *A review on electrochemical double-layer capacitors.* Energy Conversion and Management, 2010. **51**(12): p. 2901-2912.
27. Conway, B.E., *Electrochemical Supercapacitors: Scientific Fundamentals and Technological Applications*. 1999: Springer US.

28. Grahame, D.C., *Properties of the Electrical Double Layer at a Mercury Surface. I. Methods of Measurement and Interpretation of Results.* Journal of the American Chemical Society, 1941. **63**(5): p. 1207-1215.
29. Helmholtz, H., *Ueber einige Gesetze der Vertheilung elektrischer Ströme in körperlichen Leitern mit Anwendung auf die thierisch-elektrischen Versuche.* Annalen der Physik, 1853. **165**(6): p. 211-233.
30. Grahame, D.C., *The Electrical Double Layer and the Theory of Electrocapillarity.* Chemical Reviews, 1947. **41**(3): p. 441-501.
31. Marsh, H. and F.R. Reinoso, *Activated Carbon*. 2006: Elsevier Science.
32. Jäckel, N., et al., *Quantitative Information about Electrosorption of Ionic Liquids in Carbon Nanopores from Electrochemical Dilatometry and Quartz Crystal Microbalance Measurements.* The Journal of Physical Chemistry C, 2017. **121**(35): p. 19120-19128.
33. Jäckel, N., et al., *Anomalous or regular capacitance? The influence of pore size dispersity on double-layer formation.* Journal of Power Sources, 2016. **326**: p. 660-671.
34. Beguin, F., et al., *Carbons and electrolytes for advanced supercapacitors.* Advanced Materials, 2014. **26**(14): p. 2219-51, 2283.
35. Walden, P., *Ueber die Molekulargrösse und elektrische Leitfähigkeit einiger geschmolzenen Salze.* Bulletin de l'Académie Impériale des Sciences de St.-Petersburg, 1914. **8**(6): p. 405-422.
36. Fedorov, M.V. and A.A. Kornyshev, *Ionic liquids at electrified interfaces.* Chemical Reviews, 2014. **114**(5): p. 2978-3036.
37. Welton, T., *Room-Temperature Ionic Liquids. Solvents for Synthesis and Catalysis.* Chemical Reviews, 1999. **99**(8): p. 2071-2084.
38. Krossing, I., et al., *Why Are Ionic Liquids Liquid? A Simple Explanation Based on Lattice and Solvation Energies.* Journal of the American Chemical Society, 2006. **128**(41): p. 13427-13434.
39. Marcus, Y., *Thermodynamics of solvation of ions. Part 5.-Gibbs free energy of hydration at 298.15 K.* Journal of the Chemical Society, Faraday Transactions, 1991. **87**(18): p. 2995-2999.
40. Hantel, M.M., D. Weingarth, and R. Kötz, *Parameters determining dimensional changes of porous carbons during capacitive charging.* Carbon, 2014. **69**: p. 275-286.
41. Marcus, Y., G. Hefter, and T.-S. Pang, *Ionic partial molar volumes in non-aqueous solvents.* Journal of the Chemical Society, Faraday Transactions, 1994. **90**(13): p. 1899-1903.
42. Marcus, Y., *Ion solvation*. 1985: Wiley.
43. Balducci, A., *Electrolytes for high voltage electrochemical double layer capacitors: A perspective article.* Journal of Power Sources, 2016. **326**: p. 534-540.
44. Redondo, E., et al., *Outstanding room-temperature capacitance of biomass-derived microporous carbons in ionic liquid electrolyte.* Electrochemistry Communications, 2017. **79**: p. 5-8.
45. Zhao, Y., et al., *3D nanostructured conductive polymer hydrogels for high-performance electrochemical devices.* Energy & Environmental Science, 2013. **6**(10): p. 2856.
46. Bélanger, D., et al., *Characterization and Long-Term Performance of Polyaniline-Based Electrochemical Capacitors.* Journal of The Electrochemical Society, 2000. **147**(8): p. 2923-2929.
47. Carlberg, J.C. and O. Inganäs, *Poly(3,4-ethylenedioxythiophene) as Electrode Material in Electrochemical Capacitors.* Journal of The Electrochemical Society, 1997. **144**(4): p. L61-L64.
48. Cuentas Gallegos, A.K. and M.E. Rincón, *Carbon nanofiber and PEDOT-PSS bilayer systems as electrodes for symmetric and asymmetric electrochemical capacitor cells.* Journal of Power Sources, 2006. **162**(1): p. 743-747.
49. Makgopa, K., P.M. Ejikeme, and K.I. Ozoemena, *Nanostructured Manganese Oxides in Supercapacitors*, in *Nanomaterials in Advanced Batteries and Supercapacitors*. 2016, Springer. p. 345-376.
50. Ardizzone, S., G. Fregonara, and S. Trasatti, *"Inner" and "outer" active surface of RuO_2 electrodes.* Electrochimica Acta, 1990. **35**(1): p. 263-267.
51. Augustyn, V., P. Simon, and B. Dunn, *Pseudocapacitive oxide materials for high-rate electrochemical energy storage.* Energy & Environmental Science, 2014. **7**(5): p. 1597.

52. Augustyn, V., et al., *High-rate electrochemical energy storage through Li+ intercalation pseudocapacitance.* Nat Mater, 2013. **12**(6): p. 518-22.
53. Conway, B.E., V. Birss, and J. Wojtowicz, *The role and utilization of pseudocapacitance for energy storage by supercapacitors.* Journal of Power Sources, 1997. **66**(1–2): p. 1-14.
54. Nernst, W., *Zur kinetik der in lösung befindlichen körper.* Zeitschrift für physikalische Chemie, 1888. **2**(9): p. 613-679.
55. Eftekhari, A., *Energy efficiency: a critically important but neglected factor in battery research.* Sustainable Energy & Fuels, 2017. **1**(10): p. 2053-2060.
56. Laheäär, A., et al., *Appropriate methods for evaluating the efficiency and capacitive behavior of different types of supercapacitors.* Electrochemistry Communications, 2015. **60**: p. 21-25.
57. Armand, M., *Intercalation electrodes*, in *Materials for Advanced Batteries*, D.W. Murphy, J. Broadhead, and B.C.H. Steele, Editors. 1980, Plenum Press: New York. p. 145.
58. Mizushima, K., et al., *Li_xCoO_2 (0<x<-1): A new cathode material for batteries of high energy density.* Materials Research Bulletin, 1980. **15**(6): p. 783-789.
59. Lazzari, M. and B. Scrosati, *A Cyclable Lithium Organic Electrolyte Cell Based on Two Intercalation Electrodes.* Journal of The Electrochemical Society, 1980. **127**(3): p. 773-774.
60. Yoshino, A., K. Sanechika, and T. Nakajima, *Secondary battery*. 1987.
61. Nitta, N., et al., *Li-ion battery materials: present and future.* Materials Today, 2015. **18**(5): p. 252-264.
62. Thackeray, M., *Lithium-ion batteries: An unexpected conductor.* Nature Materials, 2002. **1**(2): p. 81-82.
63. Blomgren, G.E., *The Development and Future of Lithium Ion Batteries.* Journal of The Electrochemical Society, 2017. **164**(1): p. A5019-A5025.
64. Goodenough, J.B. and Y. Kim, *Challenges for Rechargeable Li Batteries.* Chemistry of Materials, 2010. **22**(3): p. 587-603.
65. Imhof, R. and P. Novák, *In Situ Investigation of the Electrochemical Reduction of Carbonate Electrolyte Solutions at Graphite Electrodes.* Journal of The Electrochemical Society, 1998. **145**(4): p. 1081-1087.
66. Seidl, L., et al., *In situ scanning tunneling microscopy studies of the SEI formation on graphite electrodes for Li^+-ion batteries.* Nanoscale, 2016. **8**(29): p. 14004-14.
67. Sacci, R.L., et al., *Direct visualization of initial SEI morphology and growth kinetics during lithium deposition by in situ electrochemical transmission electron microscopy.* Chem Commun (Camb), 2014. **50**(17): p. 2104-7.
68. Peled, E., D. Golodnitsky, and J. Penciner, *The Anode/Electrolyte Interface*, in *Handbook of Battery Materials*. 2011, Wiley-VCH Verlag GmbH & Co. KGaA. p. 479-523.
69. Nishi, Y., *The development of lithium ion secondary batteries.* The Chemical Record, 2001. **1**(5): p. 406-413.
70. Kaskhedikar, N.A. and J. Maier, *Lithium Storage in Carbon Nanostructures.* Advanced Materials, 2009. **21**(25-26): p. 2664-2680.
71. Ohzuku, T., A. Ueda, and N. Yamamoto, *Zero-Strain Insertion Material of $Li[Li_{1/3}Ti_{5/3}]O_4$ for Rechargeable Lithium Cells.* Journal of The Electrochemical Society, 1995. **142**(5): p. 1431-1435.
72. Hatchard, T.D. and J.R. Dahn, *In Situ XRD and Electrochemical Study of the Reaction of Lithium with Amorphous Silicon.* Journal of The Electrochemical Society, 2004. **151**(6): p. A838.
73. Borchardt, L., M. Oschatz, and S. Kaskel, *Carbon Materials for Lithium Sulfur Batteries-Ten Critical Questions.* Chemistry, 2016. **22**(22): p. 7324-51.
74. Thackeray, M.M., C. Wolverton, and E.D. Isaacs, *Electrical energy storage for transportation—approaching the limits of, and going beyond, lithium-ion batteries.* Energy & Environmental Science, 2012. **5**(7): p. 7854.
75. Manthiram, A., *Materials Challenges and Opportunities of Lithium Ion Batteries.* The Journal of Physical Chemistry Letters, 2011. **2**(3): p. 176-184.
76. Thommes, M., et al., *Physisorption of gases, with special reference to the evaluation of surface area and pore size distribution (IUPAC Technical Report).* Pure and Applied Chemistry, 2015.

77. Thommes, M., *Physical Adsorption Characterization of Nanoporous Materials.* Chemie Ingenieur Technik, 2010. **82**(7): p. 1059-1073.
78. Ravikovitch, P.I., A. Vishnyakov, and A.V. Neimark, *Density functional theories and molecular simulations of adsorption and phase transitions in nanopores.* Phys Rev E Stat Nonlin Soft Matter Phys, 2001. **64**(1 Pt 1): p. 011602.
79. Silvestre-Albero, J., et al., *Physical characterization of activated carbons with narrow microporosity by nitrogen (77.4K), carbon dioxide (273K) and argon (87.3K) adsorption in combination with immersion calorimetry.* Carbon, 2012. **50**(9): p. 3128-3133.
80. Lobato, B., et al., *Capacitance and surface of carbons in supercapacitors.* Carbon, 2017. **122**: p. 434-445.
81. Brunauer, S., P.H. Emmett, and E. Teller, *Adsorption of Gases in Multimolecular Layers.* Journal of the American Chemical Society, 1938. **60**(2): p. 309-319.
82. Langmuir, I., *The Adsorption of Gases on Plane Surfaces of Glass, Mica and Platinum.* Journal of the American Chemical Society, 1918. **40**(9): p. 1361-1403.
83. Lastoskie, C., K.E. Gubbins, and N. Quirke, *Pore size heterogeneity and the carbon slit pore: a density functional theory model.* Langmuir, 1993. **9**(10): p. 2693-2702.
84. Tarazona, P., U.M.B. Marconi, and R. Evans, *Phase equilibria of fluid interfaces and confined fluids.* Molecular Physics, 1987. **60**(3): p. 573-595.
85. Neimark, A.V., et al., *Quenched solid density functional theory and pore size analysis of micro-mesoporous carbons.* Carbon, 2009. **47**(7): p. 1617-1628.
86. Gor, G.Y., et al., *Quenched solid density functional theory method for characterization of mesoporous carbons by nitrogen adsorption.* Carbon, 2012. **50**(4): p. 1583-1590.
87. Jagiello, J. and J.P. Olivier, *2D-NLDFT adsorption models for carbon slit-shaped pores with surface energetical heterogeneity and geometrical corrugation.* Carbon, 2013. **55**: p. 70-80.
88. Puziy, A.M., et al., *Comparison of heterogeneous pore models QSDFT and 2D-NLDFT and computer programs ASiQwin and SAIEUS for calculation of pore size distribution.* Adsorption, 2015. **22**(4-6): p. 459-464.
89. Friedrich, W., P. Knipping, and M. Laue, *Interferenzerscheinungen bei Röntgenstrahlen.* Annalen der Physik, 1913. **346**(10): p. 971-988.
90. Bragg, W.H. and W.L. Bragg, *The reflection of X-rays by crystals.* Proceedings of the Royal Society of London. Series A, Containing Papers of a Mathematical and Physical Character, 1913. **88**(605): p. 428-438.
91. Anasori, B., M.R. Lukatskaya, and Y. Gogotsi, *2D metal carbides and nitrides (MXenes) for energy storage.* Nature Reviews Materials, 2017. **2**(2): p. 16098.
92. Klug, H.P. and L.E. Alexander, *X-Ray Diffraction Procedures: For Polycrystalline and Amorphous Materials*. 1974: Wiley.
93. Jäckel, N., et al., *Electrochemical in Situ Tracking of Volumetric Changes in Two-Dimensional Metal Carbides (MXenes) in Ionic Liquids.* ACS Applied Materials & Interfaces, 2016. **8**(47): p. 32089-32093.
94. Rietveld, H.M., *The Rietveld Method: A Retrospection*, in *Zeitschrift für Kristallographie Crystalline Materials*. 2010. p. 545.
95. Als-Nielsen, J. and D. McMorrow, *X-rays and their interaction with matter*, in *Elements of Modern X-ray Physics*. 2011, John Wiley & Sons, Inc. p. 1-28.
96. Thomson, G.P. *Experiments on the diffraction of cathode rays*. in *Proceedings of the Royal Society of London A: Mathematical, Physical and Engineering Sciences*. 1928. The Royal Society.
97. Compton, A.H., *A Quantum Theory of the Scattering of X-rays by Light Elements.* Physical Review, 1923. **21**(5): p. 483-502.
98. Prehal, C., et al., *A carbon nanopore model to quantify structure and kinetics of ion electrosorption with in situ small-angle X-ray scattering.* Phys Chem Chem Phys, 2017. **19**(23): p. 15549-15561.
99. Prehal, C., et al., *Quantification of ion confinement and desolvation in nanoporous carbon supercapacitors with modelling and in situ X-ray scattering.* Nature Energy, 2017. **2**: p. 16215.

100. Koczwara, C., et al., *In Situ Measurement of Electrosorption-Induced Deformation Reveals the Importance of Micropores in Hierarchical Carbons.* ACS Applied Materials & Interfaces, 2017. **9**(28): p. 23319-23324.
101. Prehal, C., et al., *Tracking the structural arrangement of ions in carbon supercapacitor nanopores using in situ small-angle X-ray scattering.* Energy & Environmental Science, 2015. **8**(6): p. 1725-1735.
102. Gibaud, A., J.S. Xue, and J.R. Dahn, *A small angle X-ray scattering study of carbons made from pyrolyzed sugar.* Carbon, 1996. **34**(4): p. 499-503.
103. Ruland, W., *Small-angle scattering of two-phase systems: determination and significance of systematic deviations from Porod's law.* Journal of Applied Crystallography, 1971. **4**(1): p. 70-73.
104. Pean, C., et al., *Confinement, Desolvation, And Electrosorption Effects on the Diffusion of Ions in Nanoporous Carbon Electrodes.* J Am Chem Soc, 2015. **137**(39): p. 12627-32.
105. Chmiola, J., et al., *Desolvation of ions in subnanometer pores and its effect on capacitance and double-layer theory.* Angewandte Chemie International Edition, 2008. **47**(18): p. 3392-5.
106. Ratkova, E.L., D.S. Palmer, and M.V. Fedorov, *Solvation thermodynamics of organic molecules by the molecular integral equation theory: approaching chemical accuracy.* Chem Rev, 2015. **115**(13): p. 6312-56.
107. Pean, C., et al., *Understanding the different (dis)charging steps of supercapacitors: influence of potential and solvation.* Electrochimica Acta, 2016. **206**: p. 504-512.
108. Weingarth, D., et al., *Graphitization as a Universal Tool to Tailor the Potential-Dependent Capacitance of Carbon Supercapacitors.* Advanced Energy Materials, 2014. **4**(13).
109. Ruch, P.W., et al., *On the use of activated carbon as a quasi-reference electrode in non-aqueous electrolyte solutions.* Journal of Electroanalytical Chemistry, 2009. **636**(1-2): p. 128-131.
110. Weingarth, D., et al., *PTFE bound activated carbon-A quasi-reference electrode for ionic liquids.* Electrochemistry Communications, 2012. **18**: p. 116-118.
111. Widmaier, M., et al., *Carbon as Quasi-Reference Electrode in Unconventional Lithium-Salt Containing Electrolytes for Hybrid Battery/Supercapacitor Devices.* Journal of The Electrochemical Society, 2016. **163**(14): p. A2956-A2964.
112. Lee, J., et al., *Porous carbon as a quasi-reference electrode in aqueous electrolytes.* Electrochimica Acta, 2016. **222**: p. 1800-1805.
113. Busom, J., et al., *Sputtering of sub-micrometer aluminum layers as compact, high-performance, light-weight current collector for supercapacitors.* Journal of Power Sources, 2016. **329**: p. 432-440.
114. Byun, S. and J. Yu, *Direct formation of a current collector layer on a partially reduced graphite oxide film using sputter-assisted metal deposition to fabricate high-power micro-supercapacitor electrodes.* Journal of Power Sources, 2016. **307**: p. 849-855.
115. Doberdò, I., et al., *Enabling aqueous binders for lithium battery cathodes – Carbon coating of aluminum current collector.* Journal of Power Sources, 2014. **248**: p. 1000-1006.
116. Simon, P., Y. Gogotsi, and B. Dunn, *Materials science. Where do batteries end and supercapacitors begin?* Science, 2014. **343**(6176): p. 1210-1.
117. Fic, K., et al., *Around the thermodynamic limitations of supercapacitors operating in aqueous electrolytes.* Electrochimica Acta, 2016. **206**: p. 496-503.
118. Lee, J., et al., *Tin/vanadium redox electrolyte combining battery-like energy storage capacity with supercapacitor-like power handling.* Energy & Environmental Science, 2016. **9**(11): p. 3392-3398.
119. Lukatskaya, M.R., B. Dunn, and Y. Gogotsi, *Multidimensional materials and device architectures for future hybrid energy storage.* Nature Communications, 2016. **7**: p. 12647.
120. Krtil, P., L. Kavan, and P. Novák, *Oxidation of Acetonitrile-Based Electrolyte Solutions at High Potentials: An In Situ Fourier Transform Infrared Spectroscopy Study.* Journal of The Electrochemical Society, 1993. **140**(12): p. 3390-3395.
121. Cericola, D., et al., *Effect of Water on the Aging of Activated Carbon Based Electrochemical Double Layer Capacitors During Constant Voltage Load Tests.* International Journal of Electrochemical Science, 2011. **6**(4): p. 988-996.

122. Ruch, P.W., et al., *A comparison of the aging of electrochemical double layer capacitors with acetonitrile and propylene carbonate-based electrolytes at elevated voltages.* Electrochimica Acta, 2010. **55**(7): p. 2352-2357.
123. Ruch, P.W., et al., *Aging of electrochemical double layer capacitors with acetonitrile-based electrolyte at elevated voltages.* Electrochimica Acta, 2010. **55**(15): p. 4412-4420.
124. Métrot, A., P. Willmann, and A. Herold, *Insertion electrochimique du complexe $BF_3(C_2H_5)_2O$ dans un pyrographite.* Materials Science and Engineering, 1977. **31**(Supplement C): p. 83-86.
125. Biberacher, W., et al., *A high resolution dilatometer for in situ studies of the electrointercalation of layered materials.* Materials Research Bulletin, 1982. **17**(11): p. 1385-1392.
126. Winter, M., et al., *Dilatometric Investigations of Graphite Electrodes in Nonaqueous Lithium Battery Electrolytes.* Journal of The Electrochemical Society, 2000. **147**(7): p. 2427-2431.
127. Hahn, M., et al., *Carbon based double layer capacitors with aprotic electrolyte solutions: the possible role of intercalation/insertion processes.* Applied Physics A, 2005. **82**(4): p. 633-638.
128. Dahn, J.R., R. Fong, and M.J. Spoon, *Suppression of staging in lithium-intercalated carbon by disorder in the host.* Physical Review B, 1990. **42**(10): p. 6424-6432.
129. Padhi, A.K., K.S. Nanjundaswamy, and J.B. Goodenough, *Phospho-olivines as Positive-Electrode Materials for Rechargeable Lithium Batteries.* Journal of The Electrochemical Society, 1997. **144**(4): p. 1188-1194.
130. Kao, Y.-H., et al., *Overpotential-Dependent Phase Transformation Pathways in Lithium Iron Phosphate Battery Electrodes.* Chemistry of Materials, 2010. **22**(21): p. 5845-5855.
131. Tarascon, J.M., et al., *The Spinel Phase of $LiMn_2O_4$ as a Cathode in Secondary Lithium Cells.* Journal of The Electrochemical Society, 1991. **138**(10): p. 2859-2864.
132. Erickson, E.M., et al., *Review—Recent Advances and Remaining Challenges for Lithium Ion Battery Cathodes: II. Lithium-Rich, $xLi_2MnO_3{\cdot}(1-x)LiNi_aCo_bMn_cO_2$.* Journal of The Electrochemical Society, 2017. **164**(1): p. A6341-A6348.
133. David, W.I.F., et al., *Structure refinement of the spinel-related phases $Li_2Mn_2O_4$ and $Li_{0.2}Mn_2O_4$.* Journal of Solid State Chemistry, 1987. **67**(2): p. 316-323.
134. Christensen, J. and J. Newman, *A Mathematical Model of Stress Generation and Fracture in Lithium Manganese Oxide.* Journal of The Electrochemical Society, 2006. **153**(6): p. A1019-A1030.
135. Thackeray, M.M., et al., *Lithium insertion into manganese spinels.* Materials Research Bulletin, 1983. **18**(4): p. 461-472.
136. Thackeray, M.M., et al., *Structural Fatigue in Spinel Electrodes in High Voltage (4 V) $Li/Li_xMn_2O_4$ Cells.* Electrochemical and Solid-State Letters, 1998. **1**(1): p. 7-9.
137. Jäckel, N., et al., *In situ multi-length scale approach to understand the mechanics of soft and rigid binder in composite lithium ion battery electrodes.* Journal of Power Sources, 2017. **371**: p. 162-166.
138. Black, J.M., et al., *Strain-Based In Situ Study of Anion and Cation Insertion into Porous Carbon Electrodes with Different Pore Sizes.* Advanced Energy Materials, 2014. **4**(3): p. 1300683.
139. Kiyohara, K., T. Sugino, and K. Asaka, *Electrolytes in porous electrodes: Effects of the pore size and the dielectric constant of the medium.* The Journal of Chemical Physics, 2010. **132**(14): p. 144705.
140. Kiyohara, K. and K. Asaka, *Voltage induced pressure in porous electrodes.* Molecular Physics, 2013. **111**(2): p. 297-308.
141. Pietronero, L. and S. Strässler, *Bond-Length Change as a Tool to Determine Charge Transfer and Electron-Phonon Coupling in Graphite Intercalation Compounds.* Physical Review Letters, 1981. **47**(8): p. 593-596.
142. Oren, Y., et al., *The electrical double layer charge and associated dimensional changes of high surface area electrodes as detected by more deflectometry.* Journal of Electroanalytical Chemistry and Interfacial Electrochemistry, 1985. **187**(1): p. 59-71.
143. Golub, D., Y. Oren, and A. Soffer, *Electro adsorption, the electrical double layer and their relation to dimensional changes of carbon electrodes.* Carbon, 1987. **25**(1): p. 109-117.

144. Hantel, M.M., et al., *In situ electrochemical dilatometry of carbide-derived carbons.* Electrochemistry Communications, 2011. **13**(11): p. 1221-1224.
145. Kaasik, F., et al., *Anisometric charge dependent swelling of porous carbon in an ionic liquid.* Electrochemistry Communications, 2013. **34**: p. 196-199.
146. Ruch, P.W., et al., *A dilatometric and small-angle X-ray scattering study of the electrochemical activation of mesophase pitch-derived carbon in non-aqueous electrolyte solution.* Carbon, 2010. **48**(7): p. 1880-1888.
147. Hahn, M., et al., *A dilatometric study of the voltage limitation of carbonaceous electrodes in aprotic EDLC type electrolytes by charge-induced strain.* Carbon, 2006. **44**(12): p. 2523-2533.
148. Rochester, C.C., G. Pruessner, and A.A. Kornyshev, *Statistical Mechanics of 'Unwanted Electroactuation' in Nanoporous Supercapacitors.* Electrochimica Acta, 2015. **174**: p. 978-984.
149. Biesheuvel, P.M., *Theory of expansion of porous carbon electrodes in aqueous solutions according to the Donnanmodel.* arXiv preprint arXiv:1702.05310, 2017.
150. Sauerbrey, G., *Verwendung von Schwingquarzen zur Wägung dünner Schichten und zur Mikrowägung.* Zeitschrift für Physik, 1959. **155**(2): p. 206-222.
151. Keiji Kanazawa, K. and J.G. Gordon, *The oscillation frequency of a quartz resonator in contact with liquid.* Analytica Chimica Acta, 1985. **175**: p. 99-105.
152. Jones, J.L. and J.P. Mieure, *Piezoelectric transducer for determination of metals at the micromolar level.* Analytical Chemistry, 1969. **41**(3): p. 484-490.
153. Buttry, D.A. and M.D. Ward, *Measurement of interfacial processes at electrode surfaces with the electrochemical quartz crystal microbalance.* Chemical Reviews, 1992. **92**(6): p. 1355-1379.
154. Schumacher, R., *The Quartz Microbalance: A Novel Approach to the In-Situ Investigation of Interfacial Phenomena at the Solid/Liquid Junction [New Analytical Methods (40)].* Angewandte Chemie International Edition in English, 1990. **29**(4): p. 329-343.
155. Levi, M.D., et al., *In Situ Porous Structure Characterization of Electrodes for Energy Storage and Conversion by EQCM-D: a Review.* Electrochimica Acta, 2017. **232**: p. 271-284.
156. Levi, M.D., et al., *Application of a quartz-crystal microbalance to measure ionic fluxes in microporous carbons for energy storage.* Nature Materials, 2009. **8**(11): p. 872-5.
157. Sigalov, S., et al., *Electrochemical quartz crystal admittance studies of ion adsorption on nanoporous composite carbon electrodes in aprotic solutions.* Journal of Solid State Electrochemistry, 2013. **18**(5): p. 1335-1344.
158. Levi, M.D., et al., *Electrochemical quartz crystal microbalance (EQCM) studies of ions and solvents insertion into highly porous activated carbons.* Journal of the Americal Chemical Society, 2010. **132**(38): p. 13220-2.
159. Griffin, J.M., et al., *In situ NMR and electrochemical quartz crystal microbalance techniques reveal the structure of the electrical double layer in supercapacitors.* Nature Materials, 2015. **14**(8): p. 812-9.
160. Tsai, W.Y., P.L. Taberna, and P. Simon, *Electrochemical quartz crystal microbalance (EQCM) study of ion dynamics in nanoporous carbons.* Journal of the Americal Chemical Society, 2014. **136**(24): p. 8722-8.
161. Levi, M.D., et al., *Assessing the Solvation Numbers of Electrolytic Ions Confined in Carbon Nanopores under Dynamic Charging Conditions.* Journal of Physical Chemisrty Letters, 2011. **2**(2): p. 120-4.
162. Levi, M.D., et al., *Collective Phase Transition Dynamics in Microarray Composite Li_xFePO_4 Electrodes Tracked by in Situ Electrochemical Quartz Crystal Admittance.* The Journal of Physical Chemistry C, 2013. **117**(30): p. 15505-15514.
163. Levi, M.D., et al., *In Situ Tracking of Ion Insertion in Iron Phosphate Olivine Electrodes via Electrochemical Quartz Crystal Admittance.* Journal of Physical Chemistry C, 2013. **117**(3): p. 1247-1256.
164. Levi, M.D., et al., *Solving The Capacitive Paradox of 2D MXene using Electrochemical Quartz-Crystal Admittance and In Situ Electronic Conductance Measurements.* Advanced Energy Materials, 2015. **5**(1): p. 1400815.

165. Geelhood, S.J., C.W. Frank, and K. Kanazawa, *Transient Quartz Crystal Microbalance Behaviors Compared.* Journal of The Electrochemical Society, 2002. **149**(1): p. H33.
166. Johannsmann, D., *Viscoelastic, mechanical, and dielectric measurements on complex samples with the quartz crystal microbalance.* Phys Chem Chem Phys, 2008. **10**(31): p. 4516-34.
167. Levi, M.D., et al., *Quartz Crystal Microbalance with Dissipation Monitoring (EQCM-D) for in-situ studies of electrodes for supercapacitors and batteries: A mini-review.* Electrochemistry Communications, 2016. **67**: p. 16-21.
168. Shpigel, N., et al., *In situ hydrodynamic spectroscopy for structure characterization of porous energy storage electrodes.* Nature Materials, 2016. **15**(5): p. 570-575.
169. Shpigel, N., et al., *Non-Invasive In Situ Dynamic Monitoring of Elastic Properties of Composite Battery Electrodes by EQCM-D.* Angewandte Chemie International Edition, 2015. **54**(42): p. 12353-12356.
170. Bear, J., *Dynamics of Fluids in Porous Media*. 2013: Dover Publications.
171. Constantin, P. and C. Foias, *Navier-Stokes Equations*. 1988: University of Chicago Press.
172. Sigalov, S., et al., *Electrochemical Quartz Crystal Microbalance with Dissipation Real-Time Hydrodynamic Spectroscopy of Porous Solids in Contact with Liquids.* Analytical Chemistry, 2016. **88**(20): p. 10151-10157.
173. Dargel, V., et al., *In Situ Multilength-Scale Tracking of Dimensional and Viscoelastic Changes in Composite Battery Electrodes.* ACS Applied Materials & Interfaces, 2017. **9**(33): p. 27664-27675.
174. Kötz, R. and M. Carlen, *Principles and applications of electrochemical capacitors.* Electrochimica Acta, 2000. **45**(15): p. 2483-2498.
175. Zhang, S. and N. Pan, *Supercapacitors Performance Evaluation.* Advanced Energy Materials, 2015. **5**(6): p. 1401401.
176. Weingarth, D., A. Foelske-Schmitz, and R. Kötz, *Cycle versus voltage hold – Which is the better stability test for electrochemical double layer capacitors?* Journal of Power Sources, 2013. **225**: p. 84-88.
177. Pandolfo, A.G., et al., *The Influence of Conductive Additives and Inter-Particle Voids in Carbon EDLC Electrodes.* Fuel Cells, 2010. **10**(5): p. 856-864.
178. Spahr, M.E., et al., *Development of carbon conductive additives for advanced lithium ion batteries.* Journal of Power Sources, 2011. **196**(7): p. 3404-3413.
179. Jäckel, N., et al., *Comparison of carbon onions and carbon blacks as conductive additives for carbon supercapacitors in organic electrolytes.* Journal of Power Sources, 2014. **272**: p. 1122-1133.
180. Yang, I., et al., *Effects of the Mixing of an Active Material and a Conductive Additive on the Electric Double Layer Capacitor Performance in Organic Electrolyte.* Korean Journal of Materials Research, 2015. **25**(3): p. 132-137.
181. Jäckel, N., et al., *Performance evaluation of conductive additives for activated carbon supercapacitors in organic electrolyte.* Electrochimica Acta, 2016. **191**: p. 284-298.
182. Chmiola, J., et al., *Anomalous increase in carbon capacitance at pore sizes less than 1 nanometer.* Science, 2006. **313**(5794): p. 1760-1763.
183. Centeno, T.A., O. Sereda, and F. Stoeckli, *Capacitance in carbon pores of 0.7 to 15 nm: a regular pattern.* Phys Chem Chem Phys, 2011. **13**(27): p. 12403-6.
184. Futamura, R., et al., *Partial breaking of the Coulombic ordering of ionic liquids confined in carbon nanopores.* Nature Materials, 2017. **16**(12): p. 1225-1232.
185. Salanne, M., *Ionic Liquids for Supercapacitor Applications.* Topics in Current Chemistry, 2017. **375**(3): p. 63.
186. Wang, X., et al., *Geometrically confined favourable ion packing for high gravimetric capacitance in carbon–ionic liquid supercapacitors.* Energy & Environmental Science, 2016. **9**(1): p. 232-239.
187. Bañuelos, J.L., et al., *Densification of Ionic Liquid Molecules within a Hierarchical Nanoporous Carbon Structure Revealed by Small-Angle Scattering and Molecular Dynamics Simulation.* Chemistry of Materials, 2013. **26**(2): p. 1144-1153.
188. Baldelli, S., *Surface structure at the ionic liquid-electrified metal interface.* Accounts of Chemical Research, 2008. **41**(3): p. 421-31.

189. Dyatkin, B., et al., *Ionic liquid structure, dynamics, and electrosorption in carbon electrodes with bimodal pores and heterogeneous surfaces.* Carbon, 2018. **129**: p. 104-118.
190. Fulik, N., et al., Electrolyte mobility in supercapacitor electrodes – Solid state NMR studies on hierarchical and narrow pore sized carbons. Energy Storage Materials, 2018. **12**: p. 183-190.
191. Humphreys, E.K., et al., *SFG Study of the Potential-Dependent Adsorption of the p-Toluenesulfonate Anion at an Activated Carbon/Propylene Carbonate Interface.* The Journal of Physical Chemistry C, 2017. **121**(38): p. 20567-20575.
192. Prass, J., et al., *Apparent lattice expansion in ordered nanoporous silica during capillary condensation of fluids.* Journal of Applied Crystallography, 2012. **45**(4): p. 798-806.
193. Naguib, M., et al., *Two-dimensional nanocrystals produced by exfoliation of Ti_3AlC_2.* Advanced Materials, 2011. **23**(37): p. 4248-53.
194. Huetter, L.J. and H.H. Stadelmaier, *Ternary carbides of transition metals with aluminum and magnesium.* Acta Metallurgica, 1958. **6**(5): p. 367-370.
195. Alhabeb, M., et al., *Guidelines for Synthesis and Processing of Two-Dimensional Titanium Carbide ($Ti_3C_2T_x$ MXene).* Chemistry of Materials, 2017. **29**(18): p. 7633-7644.
196. Shahzad, F., et al., *Electromagnetic interference shielding with 2D transition metal carbides (MXenes).* Science, 2016. **353**(6304): p. 1137-1140.
197. Anasori, B., et al., *Two-Dimensional, Ordered, Double Transition Metals Carbides (MXenes).* ACS Nano, 2015. **9**(10): p. 9507-9516.
198. Hope, M.A., et al., *NMR reveals the surface functionalisation of Ti_3C_2 MXene.* Phys Chem Chem Phys, 2016. **18**(7): p. 5099-102.
199. Lin, Z., et al., *Capacitance of $Ti_3C_2T_x$ MXene in ionic liquid electrolyte.* Journal of Power Sources, 2016. **326**: p. 575-579.
200. Lin, Z., et al., *Electrochemical and In-situ X-ray diffraction Studies of $Ti_3C_2T_x$ MXene in Ionic Liquid Electrolyte.* Electrochemistry Communications, 2016. **72**: p. 50-53.
201. Xu, K., et al., *Tracking Ionic Rearrangements and Interpreting Dynamic Volumetric Changes in Two-Dimensional Metal Carbides Supercapacitors: A Molecular Dynamics Simulation Study.* ChemSusChem, 2018. **11**: p. 1-9
202. Li, J., et al., *Achieving High Pseudocapacitance of 2D Titanium Carbide (MXene) by Cation Intercalation and Surface Modification.* Advanced Energy Materials, 2017: p. 1602725.

CURRICULUM VITAE

Nicolas Jäckel

- PhD Student, Saarland University,
  INM-Leibniz Institute for New Materials,
  Division Energy Materials
- M. Sc. Microfabrication and Nanostructures,
  Department of Physics and Mechatronics, Saarland University

Nicolas Jäckel

> M. Sc. Microfabrication and Nanostructures, Department of Physics and Mechatronics, Saarland University

> PhD Student, Saarland University, INM-Leibniz Institute for New Materials, Division Energy Materials

EDUCATION

- PhD student, since 03/2015
  Saarland University
  INM- Leibniz Institute for New Materials (Division Energy Materials)
  Title: Structure and Properties of Supercapacitors and Lithium-Ion Battery Electrodes: The role of Material, Electrolyte, Binder, and Additives
- Master of Science in Microfabrication and Nanostructures, 02/2015
  Saarland University
  INM- Leibniz Institute for New Materials (Division Energy Materials)
  Title: Influence of graphitization and pseudoactive surface decoration on the electrochemical performance of carbon and carbon hybrid supercapacitors
- Bachelor of Science in Microfabrication and Nanostructures, 07/2012
  Saarland University
  Drägerwerk AG & Co. KGaA (Basic research department)
  Title: Gasfilter für Mikrosensor

PROFESSIONAL EXPERIENCE

INM- Leibniz Institute for New Materials (Energy Materials Group), Saarbrücken, Germany

- PhD student, since 03/2015
- Master thesis, 06/2014 – 02/2015
- Student intern, 10/2013 – 05/2014

Saarland University, Saarbrücken, Germany

- Teaching experience "Introduction to thermodynamics" by Prof. Volker Presser
  Leading exercises in summer term 2014 and 2015
- Student intern – Lab of Measurement Technology, 10/2012 – 09/2013

Bar-Ilan University, Ramat-Gan, Israel

- Research internship for joint PhD work at Doron Aurbach group, 03/2015
- Research internship for joint PhD work at Doron Aurbach group, 10/2016 – 12/2016

CSIR Materials Science and Manufacturing, Pretoria, South Africa

- Research internship at Energy Materials group, Kenneth Ozoemena, 07/2016 – 08/2016

Drägerwerk AG & Co. KGaA, Lübeck, Germany

- Bachelor thesis, 02/2012 – 06/2012
- Practical intern, 11/2011 – 01/2012

SCHOLARSHIPS AND GRANTS

- DAAD Kurzzeitstipendium für Doktoranden
  2-month scholarship from German Academic Exchange Service for in situ characterization of battery materials with multiple apparatus
- Participation at the 67th Lindau Nobel Laureate Meeting
  Dedicated to the field of Chemistry

Nicolas Jäckel

- Travel grant from the ECS Battery Division
  Participation of the 232nd Meeting of the Electrochemical Society
- GradUS global scholarship for conference participation

PUBLICATIONS

Statistical summary (source: Web of Science)

- h-Index: 13
- Total citations: 462 (347 without self-citations)
- Peer-review articles: 38

(1) Prehal C, Koczwara C, **Jäckel N**, Schreiber A, Burian M, Amenitsch H, Hartmann MA, Presser V, Paris O
Quantification of ion confinement and desolvation in nanoporous carbon supercapacitors with modelling and in situ X-ray scattering.
Nature Energy, 2017. 2: 16215

(2) **Jäckel N**, Dargel V, Shpigel N, Sigalov S, Levi MD, Daikhin L, Aurbach D, Presser V
In situ multi-length scale approach to understand the mechanics of soft and rigid binder in composite lithium ion battery electrodes
Journal of Power Sources, 2017. 371: p. 162-166.

(3) **Jäckel N**, Emge SP, Krüner B, Roling B, Presser V
Quantitative Information about Electrosorption of Ionic Liquids in Carbon Nanopores from Electrochemical Dilatometry and Quartz Crystal Microbalance Measurements.
The Journal of Physical Chemistry C, 2017.

(4) Dargel V, **Jäckel N**, Shpigel N, Sigalov S, Levi MD, Daikhin L, Presser V, Aurbach D
In Situ Multilength-Scale Tracking of Dimensional and Viscoelastic Changes in Composite Battery Electrodes.
ACS Appl Mater Interfaces, 2017. 9(33): p. 27664-27675.

(5) Widmaier M, **Jäckel N**, Zeiger M, Abuzarli M, Engel C, Bommer L, Presser V
Influence of carbon distribution on the electrochemical performance and stability of lithium titanate based energy storage devices.
Electrochimica Acta, 2017. 247: p. 1006-1018.

(6) Schneidermann C., **Jäckel N**, Oswald S, Giebeler L, Presser V, Borchardt L
Solvent-Free Mechanochemical Synthesis of Nitrogen-Doped Nanoporous Carbon for Electrochemical Energy Storage.
ChemSusChem, 2017. 10(11): p. 2416-2424.

(7) Leistenschneider D, **Jäckel N**, Hippauf F, Presser V, Borchardt L
Mechanochemistry-assisted synthesis of hierarchical porous carbons applied as supercapacitors.
Beilstein Journal of Organic Chemistry, 2017. 13: p. 1332-1341.

(8) Prehal C, Koczwara C, **Jäckel N**, Amenitsch H, Presser V, Paris O
A carbon nanopore model to quantify structure and kinetics of ion electrosorption with in situ small-angle X-ray scattering.
Physical Chemistry Chemical Physics, 2017. 19(23): p. 15549-15561.

Nicolas Jäckel

(9) Koczwara C, Rumswinkel S, Prehal C, **Jäckel N**, Elsässer MS, Amenitsch H, Presser V, Hüsing N, Paris O
In Situ Measurement of Electrosorption-Induced Deformation Reveals the Importance of Micropores in Hierarchical Carbons.
ACS Applied Materials & Interfaces, 2017. 9(28): p. 23319-23324.

(10) Fleischmann S, Zeiger M, **Jäckel N**, Krüner B, Lemkova V, Widmaier M, Presser V
Tuning pseudocapacitive and battery-like lithium intercalation in vanadium dioxide/carbon onion hybrids for asymmetric supercapacitor anodes.
Journal of Materials Chemistry A, 2017. 5(25): p. 13039-13051.

(11) Srimuk P, Zeiger M, **Jäckel N**, Tolosa A, Krüner B. Fleischmann S, Grobelsek I, Aslan M, Shvartsev B, Suss ME, Presser V
Enhanced performance stability of carbon/titania hybrid electrodes during capacitive deionization of oxygen saturated saline water.
Electrochimica Acta, 2017. 224: p. 314-328

(12) Srimuk P, Lee J, Fleischmann S, Choudhury S, **Jäckel N**, Zeiger M, Kim C, Aslan M, Presser V
Faradaic deionization of brackish and sea water via pseudocapacitive cation and anion intercalation into few-layered molybdenum disulfide.
Journal of Materials Chemistry A, 2017. 5(30): p. 15640-15649.

(13) Lee J, Tolosa A, Krüner B, **Jäckel N**, Fleischmann S, Zeiger M, Kim D, Presser V
Asymmetric tin–vanadium redox electrolyte for hybrid energy storage with nanoporous carbon electrodes.
Sustainable Energy Fuels, 2017. 1(2): p. 299-307

(14) Shpigel N, Levi MD, Sigalov S, Girshevitz O, Aurbach D, Daikhin L, Pikma P, Marandi M, Janes A, Lust E, **Jäckel N**, Presser V
In situ hydrodynamic spectroscopy for structure characterization of porous energy storage electrodes.
Nature Materials. 2016. 15: p. 570–575

(15) **Jäckel N**, Simon P, Gogotsi Y, Presser V
Increase in Capacitance by Subnanometer Pores in Carbon.
ACS Energy Letters, 2016. 1: p. 1262-1265. (Viewpoint, invited)

(16) **Jäckel N**, Rodner M, Schreiber A, Jeongwook J, Zeiger M, Aslan M, Weingarth D, Presser V
Anomalous or regular capacitance? The influence of pore size dispersity on double-layer formation.
Journal of Power Sources. 2016. 326: p. 660-671

(17) **Jäckel N**, Krüner B, Van Aken KL, Alhabeb M, Anasori B, Kaasik F, Gogotsi Y, Presser V
Electrochemical in situ tracking of volumetric changes in two-dimensional metal carbides (MXenes) in ionic liquids.
ACS Applied Materials & Interfaces, 2016. 8(47): p. 32089-32093

(18) Srimuk P, Ries L, Zeiger M, Fleischmann S, **Jäckel N**, Tolosa A, Krüner B, Aslan M, Presser V
High performance stability of titania decorated carbon for desalination with capacitive deionization in oxygenated water.
RSC Advances, 2016. 6(108): p. 106081-106089.

Nicolas Jäckel

(19) Srimuk P, Kaasik F, Krüner B, Tolosa A, Fleischmann S, **Jäckel N**, Tekeli MC, Suss M, Aslan M, Presser V
MXene as a novel intercalation-type pseudocapacitive cathode and anode for capacitive deionization.
Journal of Materials Chemistry A, 2016. 4(47): p. 18265-18271

(20) Widmaier M, Krüner B, **Jäckel N**, Aslan M, Fleischmann S, Engel C, Presser V
Carbon as Quasi-Reference Electrode in Unconventional Lithium-Salt Containing Electrolytes for Hybrid Battery/Supercapacitor Devices.
Journal of The Electrochemical Society, 2016. 163(14): p. A2956-A2964.

(21) Tolosa A, Krüner B, Fleischmann S, **Jäckel N**, Zeiger M, Aslan M, Grobelsek I, Presser V
Niobium carbide nanofibers as a versatile precursor for high power supercapacitor and high energy battery electrodes.
Journal of Materials Chemistry A. 2016. 4(41): p. 16003-16016.

(22) Busom J, Schreiber A, Tolosa A, **Jäckel N**, Grobelsek I, Peter NJ, Presser V
Sputtering of sub-micrometer aluminum layers as compact, high-performance, light-weight current collector for supercapacitors.
Journal of Power Sources. 2016. 329: p. 432-440

(23) **Jäckel N**, Weingarth D, Schreiber A, Krüner B, Zeiger M, Tolosa A, Aslan M, Presser V
Performance evaluation of conductive additives for activated carbon supercapacitors in organic electrolyte.
Electrochimica Acta. 2016. 191: p. 284-298.

(24) Fleischmann S, **Jäckel N**, Zeiger M, Krüner B, Grobelsek I, Formanek P, Choudhury S, Weingarth D, Presser, V
Enhanced Electrochemical Energy Storage by Nanoscopic Decoration of Endohedral and Exohedral Carbon with Vanadium Oxide via Atomic Layer Deposition.
Chemistry of Materials, 2016. 28(8): p. 2802-2813.

(25) Zeiger M, **Jäckel N**, Mochalin VN, Presser V
Review: carbon onions for electrochemical energy storage.
Journal of Materials Chemistry A, 2016. 4(9): p. 3172-3196.

(26) Aslan M, Zeiger M, **Jäckel N**, Grobelsek I, Weingarth D, Presser V
Improved capacitive deionization performance of mixed hydrophobic/hydrophilic activated carbon electrodes.
Journal of Physics: Condensed Matter. 2016. 28(11): 114003.

(27) Tolosa A, Krüner B, **Jäckel N**, Aslan M, Vakifahmetoglu C, Presser V
Electrospinning and electrospraying of silicon oxycarbide-derived nanoporous carbon for supercapacitor electrodes.
Journal of Power Sources, 2016. 313: p. 178-188.

(28) Krüner B, Lee J, **Jäckel N**, Tolosa A, Presser V
Submicron novolac-derived carbon beads for high performance supercapacitors and redox electrolyte energy storage.
ACS Applied Materials & Interfaces, 2016. 8: p. 9104-9115.

(29) Lee J, **Jäckel N**, Kim D, Widmaier M, Sathyamoorthi S, Srimuk P, Kim C, Fleischmann S, Zeiger M, Presser V
Porous carbon as a quasi-reference electrode in aqueous electrolytes.
Electrochimica Acta, 2016. 222: p. 1800-1805 (invited)

(30) Ewert JK, Weingarth D, Denner C, Friedrich M, Zeiger M, Schreiber A, **Jäckel N**, Presser V, Kempe R
Enhanced capacitance of nitrogen-doped hierarchically porous carbide-derived carbon in matched ionic liquids.
Journal of Materials Chemistry A. 2015. 3(37): p. 18906-18912.

(31) Shpigel N, Levi MD, Sigalov S, Girshevitz O, Aurbach D, Daikhin L, **Jäckel N**, Presser V
Non-Invasive In Situ Dynamic Monitoring of Elastic Properties of Composite Battery Electrodes by EQCM-D.
Angewandte Chemie International Edition. 2015. 54(42): p. 12353-12356.

(32) Zeiger M, **Jäckel N**, Weingarth D, Presser V
Vacuum or flowing argon: What is the best synthesis atmosphere for nanodiamond-derived carbon onions for supercapacitor electrodes?
Carbon. 2015. 94: p. 507-517.

(33) Oschatz M, Zeiger M, **Jäckel N**, Strubel P, Borchardt L, Reinhold R
Emulsion soft templating of carbide-derived carbon nanospheres with controllable porosity for capacitive electrochemical energy storage.
Journal of Materials Chemistry A. 2015. 3(35): p. 17983-17990.

(34) Zeiger M, **Jäckel N**, Aslan M, Weingarth D, Presser V
Understanding structure and porosity of nanodiamond-derived carbon onions.
Carbon. 2015. 84: p. 584-598.

(35) Atchison JS, Zeiger M, Tolosa A, Funke LM, **Jäckel N**, Presser V
Electrospinning of ultrafine metal oxide/carbon and metal carbide/carbon nanocomposite fibers.
RSC Advances. 2015. 5(45): p. 35683-35692.

(36) Weingarth D, Zeiger M, **Jäckel N**, Aslan M, Feng G, Presser V
Graphitization as a Universal Tool to Tailor the Potential-Dependent Capacitance of Carbon Supercapacitors.
Advanced Energy Materials. 2014. 4(13): 1400316.

(37) Aslan M, Weingarth D, **Jäckel N**, Atchison JS, Grobelsek I, Presser V
Polyvinylpyrrolidone as binder for castable supercapacitor electrodes with high electrochemical performance in organic electrolytes.
Journal of Power Sources. 2014. 266: p. 374-383.

(38) **Jäckel N**, Weingarth D, Zeiger M, Aslan M, Grobelsek I, Presser V
Comparison of carbon onions and carbon blacks as conductive additives for carbon supercapacitors in organic electrolytes.
Journal of Power Sources. 2014. 272: p. 1122-1133.

CONFERENCE: TALKS AND POSTER

Statistical summary

- Total conference visits: 13
- Conference talks: 11 (invited: 1)
- Conference poster: 4

(1) (*invited*) **Jäckel N**, Gogotsi Y, Levi MD, Aurbach D, Presser V
In situ monitoring of energy storage systems via multi-length scale approach
232nd ECS meeting, National Harbor (USA), 2017, oral presentation

Nicolas Jäckel

(2) **Jäckel N**, Krüner B, Van Aken KL, Alhabeb M, Anasori B, Kaasik F, Gogotsi Y, Presser V
Electrochemical in situ tracking of volumetric changes in two-dimensional metal carbides (MXenes) in ionic liquids
5th ISEECap, Jena (Germany), 2017, oral presentation

(3) **Jäckel N**, Gogotsi Y, Levi MD, Aurbach D, Presser V
In situ monitoring of mechanical properties via multi-length scale approach
ISE 20th topical meeting, Buenos Aires (Argentina), 2017, oral presentation

(4) **Jäckel N**, Schreiber A, Rodner M, Krüner B, Zeiger M, Tolosa A, Weingarth D, Presser V
Influence of surface chemistry and electrode morphology on supercapacitor performance
11th EMNT 2016, Brussels (Belgium), 2016, oral presentation

(5) **Jäckel N**, Schreiber A, Rodner M, Zeiger M, Aslan M, Weingarth D, Presser V
Anomalous or regular capacitance? The influence of pore size dispersity on double-layer formation
ISE 67th annual meeting, The Hague (Netherlands), 2016, oral presentation

(6) **Jäckel N**, Weingarth D, Schreiber A, Krüner B, Zeiger M, Tolosa A, Aslan M, Presser V
Performance evaluation of conductive additives for activated carbon supercapacitors in organic electrolyte
ISE 67th annual meeting, The Hague (Netherlands), 2016, Poster

(7) **Jäckel N**, Zeiger M, Weingarth D, Presser V
Nanodiamond-derived carbon onions as conductive additive and active material for double-layer capacitors
MRS Spring Meeting, Phoenix (USA), 2016, oral presentation

(8) **Jäckel N**, Levi MD, Aurbach D, Presser V
In-situ monitoring of elastic properties of common binders via electrochemical quartz microbalance with dissipation and dilatometry
MRS Spring Meeting, Phoenix (USA), 2016, oral presentation

(9) **Jäckel N**, Weingarth D, Zeiger M, Presser V
Conductive additives for carbon-carbon supercapacitors in organic electrolytes: How much additive is needed?
Cost meeting, Poznan (Poland), 2015, oral presentation

(10) **Jäckel N**, Weingarth D, Presser V
Titanium nitride from atomic layer deposition: suitable for protic ionic liquid pseudocapacitors?
4th ISEECap, Montpellier (France), 2015, Poster

(11) **Jäckel N**, Presser V
Nanopores in carbon Supercapacitors
9th INASCON, Basel (Switzerland), 2015, oral presentation

(12) **Jäckel N**., Levi MD, Aurbach D, Presser V
In-situ monitoring of binders in Li-ion batteries via EQCM-D and electrochemical dilatometry
ISE 66th annual Meeting, Taipei (Taiwan), 2015, Poster

(13) **Jäckel N**, Zeiger M, Presser V
Carbon onions for supercapacitor and pseudocapacitor electrodes
6th CESEP, Poznan (Poland), 2015, oral presentation

(14) Aslan M, Weingarth D, Zeiger M, **Jäckel N**, Grobelsek I, Presser V
Activated carbon electrodes with improved charge storage capacity and capacitive deionization performance
1st CDI&E, Saarbrücken (Germany), 2015, Poster

(15) **Jäckel N**, Weingarth D, Zeiger M, Presser V
Carbon onions versus high and low surface area carbon black: what is the better conductive additive?
ISE 65th annual Meeting, Lausanne (Switzerland), 2014, oral presentation

INVITED SEMINAR TALKS

- Total invited talks: 3

(1) **Jäckel N**, Zeiger M, Sethuraman S, Presser V, Raju K, Ozoemena K
Manganese-oxide decorated carbon nano-onions in protic ionic liquids
CSIR Materials Science and Manufacturing, Pretoria (South Africa), 2016

(2) **Jäckel N**, Levi MD, Aurbach D, Presser V
In situ tracking volume changes
& understanding the role of nanopores in carbon supercapacitors
Drexel University, Philadelphia (USA), 2016

(3) **Jäckel N**, Presser V
How to make a good energy storage device?
Korea University of Technology and Education, Chungcheongnam-do (Republic of Korea), 2015

APPENDIZES

Appendix A Supporting Information to *Ch. 4.2*

Anomalous or regular capacitance? The influence of pore size dispersity on double-layer formation

Appendix B Supporting Information to *Ch. 4.3*

Increase in Capacitance by Subnanometer Pores in Carbon

Appendix C Supporting Information to *Ch. 4.4*

Quantitative Information about Electrosorption of Ionic Liquids in Carbon Nanopores from Electrochemical Dilatometry and Quartz Crystal Microbalance Measurements

Appendix D Supporting Information to *Ch. 4.5*

In situ Measurement of Electrosorption-induced Deformation Reveals the Importance of Micropores in Hierarchical Carbons

Appendix E Supporting Information to *Ch. 4.6*

Electrochemical in Situ Tracking of Volumetric Changes in Two-Dimensional Metal Carbides (MXenes) in Ionic Liquids

Appendix A

Supporting Information

Anomalous or regular capacitance? The influence of pore size dispersity on double-layer formation

N. Jäckel,[1,2] M. Rodner,[1,2] A. Schreiber,[1] J. Jeongwook,[1] M. Zeiger,[1,2]
M. Aslan,[1] D. Weingarth,[1] V. Presser[1,2,*]

[1]… INM - Leibniz Institute for New Materials, Saarbrücken, Germany

[2]… Department of Materials Science and Engineering, Saarland University, Saarbrücken, Germany

*… Corresponding author's email address: volker.presser@leibniz-inm.de

1. Gas sorption analysis

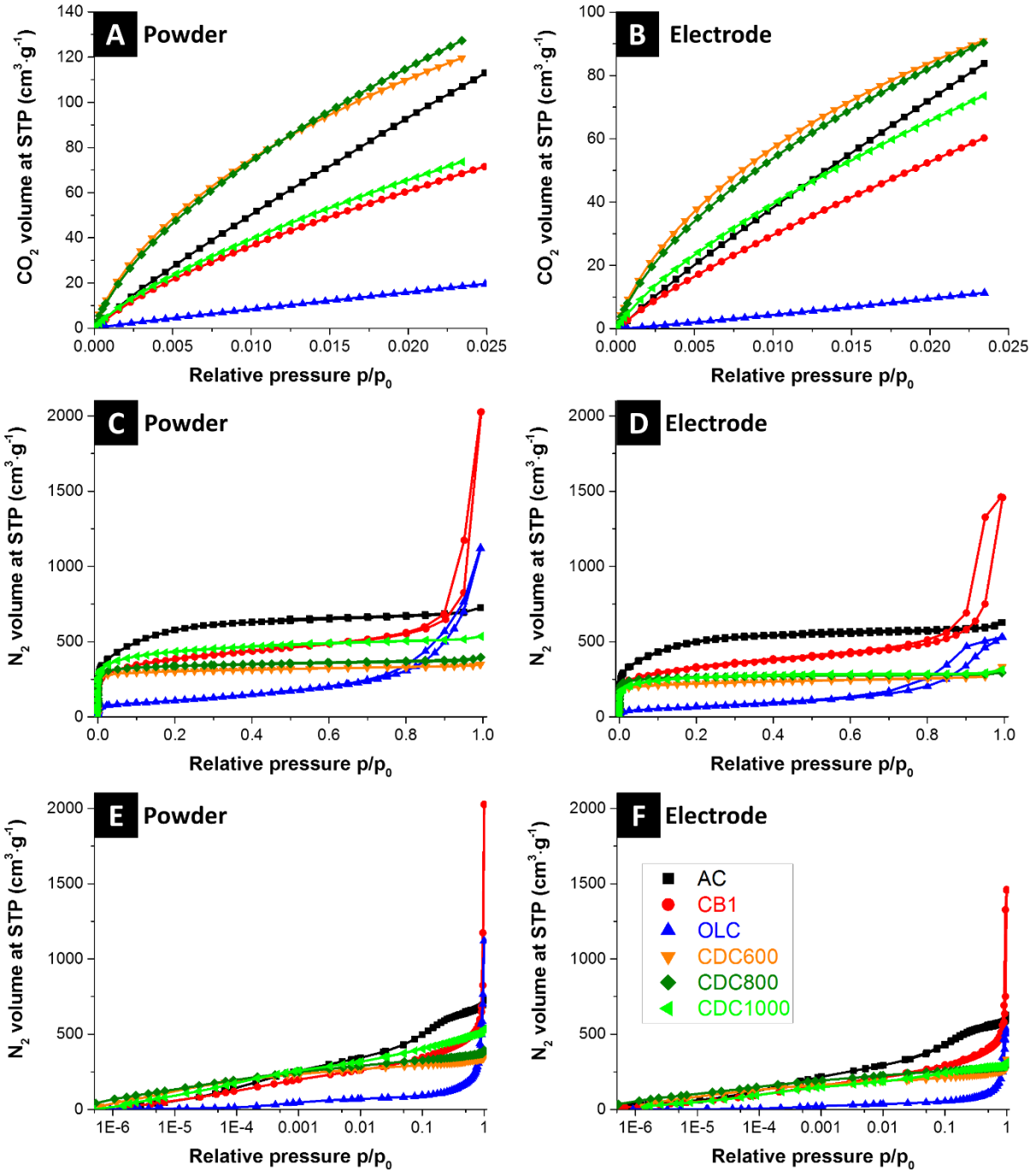

Figure S1: Sorption isotherms of the used carbons. First row (A+B) CO_2 sorption isotherms (at 0 °C) and (C-F) nitrogen sorption isotherms (at -196 °C). The left column (A+C+E) are the isotherms for dry powder and the right column (B+D+F) relate to the isotherms of electrodes containing 10 mass% PTFE. The symbol legend in panel (F) relates to all panels.

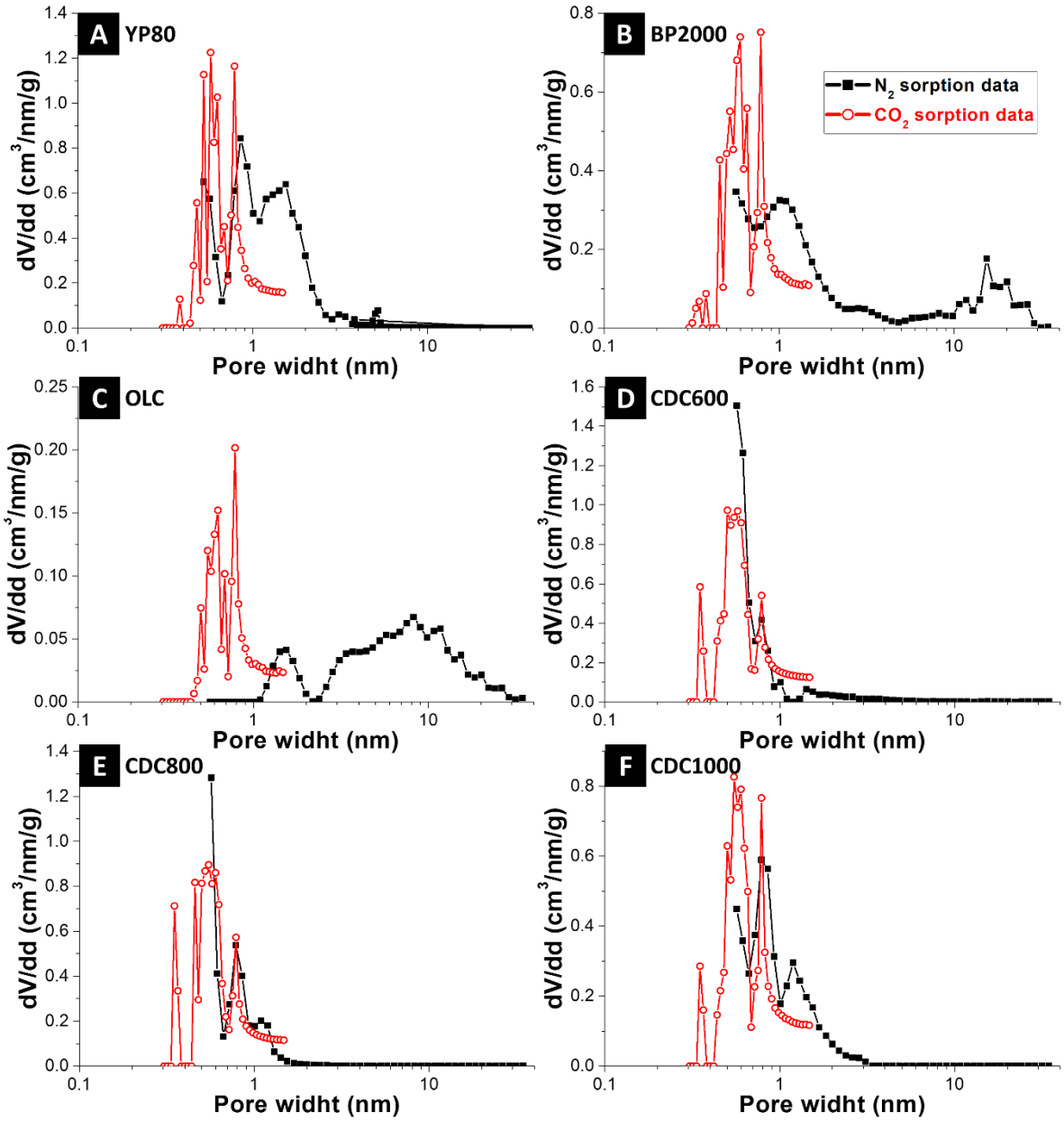

Figure S2: Calculated pore size distribution with a NLDFT kernel for carbon-dioxide (CO_2) sorption and a QSDFT kernel assuming slit-like pores for nitrogen (N_2) sorption measurements. All electrodes contain 10 mass% PTFE.

2. Cyclic voltammetry

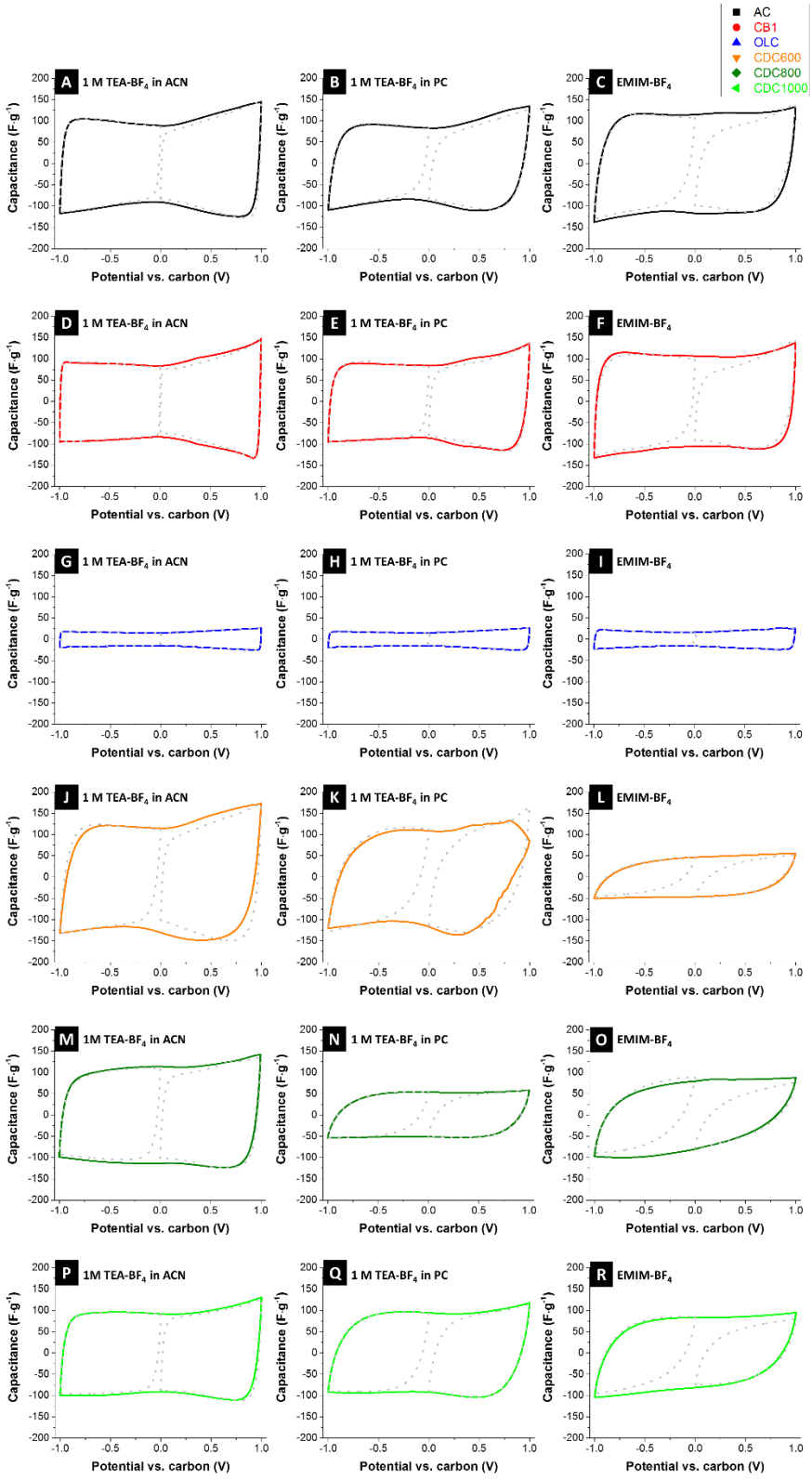

Figure S3: (A-R) Cyclic voltammograms of the studied samples recorded at 2 mV·s^{-1}. The measured current on the y-axis was normalized by the scan rate, hence, resulting in a virtual unit of F·g^{-1}.

3. Structural and chemical analysis

3.1 Raman spectroscopy

The carbon materials differ in the degree of carbon ordering, as it can be seen from Raman spectroscopy (**Fig. S4**). Raman spectra are characterized by the D-mode between 1338 and 1347 cm^{-1} and the G-mode between 1591 and 1599 cm^{-1}. The G-mode is characteristic for graphitic material and comes from the bond stretching of sp^2-hybridized carbon atoms in rings and chains according to the zone center E_{2g} mode.[1] The D-mode, or "disordered" mode, arises from a double-resonant process. It relates to the breathing of six-fold carbon rings, but is only Raman active in the presence of defects, such as related to curvature, edges, heteroatoms, or vacancies.[2]

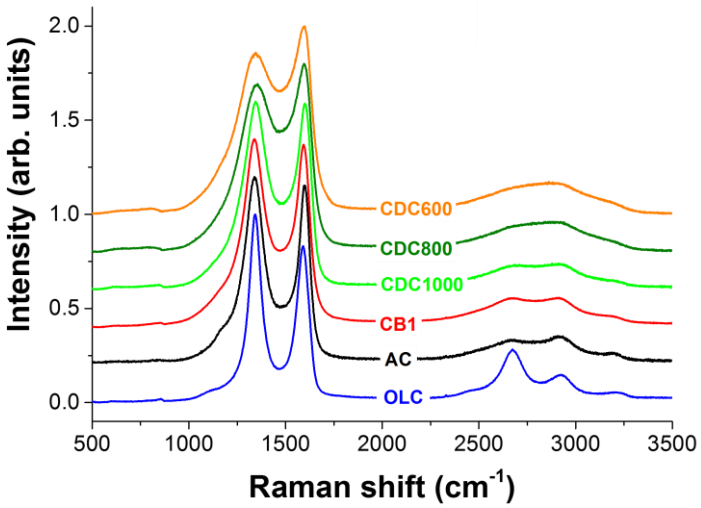

Figure S4: Raman spectra recorded using 532 nm wavelength with a power of 0.2 mW.

The position of the G-mode for all carbons is shifted to larger wavelengths compared to ideal graphite at 1581 cm^{-1} and is only slightly smaller than for nanocrystalline graphite at ~1600 cm^{-1}.[3] This indicates the existence of nanocrystalline domains in the material combined with an amorphous carbon phase. The amorphous carbon phase is supported by the broad transition between the D- and G-mode, leading to a broad signal at ~1520 cm^{-1}.

Table S1: Results of peak fitting of Raman data.

	D-mode position (cm^{-1})	G-mode position (cm^{-1})	FWHM D-mode (cm^{-1})	FWHM G-mode (cm^{-1})	Integral I_D/I_G ratio
AC	1338	1599	140	65	2.2
CB1	1339	1594	212	100	2.1
OLC	1343	1591	80	69	1.4
CDC600	1346	1594	238	103	2.1
CDC800	1347	1595	223	99	2.2
CDC1000	1347	1594	174	82	2.1

For OLC this transition is negligible, larger for AC and CB1, and decreases with the CDC synthesis temperature. This indicates the rather small fraction of amorphous carbon in high temperature carbon onions compared to, for example, low temperature CDC (CDC600). The high degree of carbon ordering for OLC, compared to all other carbons, is also underlined by the small I_D/I_G areal intensity ratio and comparable small FWHM of D- and G-mode (**Table S1**). All other carbons show a much larger I_D/I_G ratio of 2.1-2.2 compared to 1.4 for OLC. The higher degree of disorder for these materials, is also indicated by the larger FHWM of the D-mode. A broad D-peak correlates with strong distortion of six-fold rings, curvature, as well as nanocrystalline domains. The largest FWHM of the D-mode is measured for CDC600 with 238 cm^{-1}, leading to the carbon material with the highest degree of disorder. With increasing synthesis temperature, CDC materials increase in carbon ordering as indicated by the decreasing FWHM of both D- and G-mode. CB1 presents a similar degree of carbon ordering, but lower than AC. The FWHM of the G-mode is similar for the CDC and CB1, but significantly smaller for AC and OLC. The reason is the less bond-length variation in the nanocrystalline domains of AC and OLC than in the other carbons.

Summarizing, the carbons show a different degree of ordering with OLC presenting a more pronounced graphitization and with CDC600 characterized by a large fraction of amorphous carbon and high degree of disorder.

3.2 Chemical analysis (EDX)

EDX spectra show a very low amount of oxygen in the used carbon electrodes, proving the statement of little amount of heteroatoms and surface functional groups in the investigated samples. Especially the CDC samples show no detectable amount of oxygen within the error of the method, whereas the industrial produced carbon powders have some small amount below 2 atom%. For the CDC samples, the residual difference to 100% relates to residual amounts of electrochemically inert carbide species.

Table S2: Carbon and oxygen content of carbon electrodes, measured with elemental analysis. n.d.: not detectable.

Material	Carbon (atom%)	Oxygen (atom%)	Reference
AC1	97.8±0.5	2.0±0.5	[4]
CB1	98.1±0.1	1.3±0.1	[4]
OLC	98.8±0.1	1.2±0.1	[5]
CDC600	94.6±1.0	n.d.	
CDC800	98.1±0.5	n.d.	
CDC1000	98.3±0.2	n.d.	

4. Supporting references

1. Tuinstra, F. and J.L. Koenig, *Raman Spectrum of Graphite.* The Journal of Chemical Physics, 1970. **53**(3): p. 1126-1130.
2. Thomsen, C. and S. Reich, *Double Resonant Raman Scattering in Graphite.* Physical Review Letters, 2000. **85**(24): p. 5214-5217.
3. Ferrari, A.C. and J. Robertson, *Raman spectroscopy of amorphous, nanostructured, diamond–like carbon, and nanodiamond*. Vol. 362. 2004. 2477-2512.
4. Jäckel, N., et al., *Performance evaluation of conductive additives for activated carbon supercapacitors in organic electrolyte.* Electrochimica Acta, 2016. **191**: p. 284-298.
5. Zeiger, M., et al., *Vacuum or flowing argon: What is the best synthesis atmosphere for nanodiamond-derived carbon onions for supercapacitor electrodes?* Carbon, 2015. **94**: p. 507-517.

Appendix B

The increase in capacitance

by subnanometer pores in carbon

N. Jäckel,[1,2] P. Simon,[3,4,*] Y. Gogotsi,[5,*] V. Presser[1,2,*]

[1] *INM - Leibniz Institute for New Materials, 66123 Saarbrücken, Germany*

[2] *Department of Materials Science and Engineering, Saarland University, 66123 Saarbrücken, Germany*

[3] *Université Paul Sabatier, CIRIMAT UMR, CNRS 5085, 5085, 31062 Toulouse Cedex 4, France*

[4] *Réseau sur le Stockage Electrochimique de l'Energie, RS2E FR CNRS 3459, France*

[5] *Department of Materials Science and Engineering & A. J. Drexel Nanotechnology Institute, PA 19104 Philadelphia, USA*

* Corresponding authors:

Patrice Simon: simon@chimie.ups-tlse.fr

Yury Gogotsi: gogotsi@drexel.edu

Volker Presser: volker.presser@leibniz-inm.de

Supporting information

Experimental Methods

A more detailed experimental description can be found in our earlier work (Ref. [1]). Activated carbon YP-50F from Kuraray (called AC) and carbon black BP2000 from Cabot (called CB) were used as received. Carbide-derived carbon (CDC) samples were derived from titanium carbide (TiC) by chlorine gas treatment at 600 °C (TiC600) or 1000 °C (TiC1000) for 3 h (in both cases). All samples were subsequently annealed at 600 °C in hydrogen for 2 h and after cooling placed in vacuum (0.1 mPa) for several hours to remove residual volatile gas species.[2] Carbon onions (OLC, stands for: onion-like carbon) were derived from nanodiamond powder (NaBond) by thermal annealing in argon at 1700 °C for 1 h with a heating rate of 20 °C·min^{-1} (Thermal Technology Furnace).[3]

For electrode preparation, we added 10 mass% of polytetrafluoroethylene (PTFE, 60 mass% dispersion in water from Sigma Aldrich) as binder to the carbon powder, which was soaked with ethanol and ground in a mortar. The resulting dough-like material was further processed with a rolling machine (MTI HR01, MTI Corp.) to a 200±20 µm thick free standing film electrode and finally dried at 120 °C at 2 kPa for 24 h before use.

For electrochemical testing, we employed a custom-built polyether ether ketone (PEEK) cell with spring loaded titanium pistons as a three electrode system described elsewhere.[4] The working electrode was punched out with 12 mm diameter with a total mass of 10-20 mg. An overcapacitive YP-80F (Kuraray) electrode with 500 µm thickness and 25 mg served as counter electrode. We employed a glass-fiber separator (GF/A from Whatman) and a carbon-coated aluminum foil current collector (type Zflo 2653 from Coveris Advanced Coatings). PTFE-bound YP-50F was employed as a quasi-reference electrode with a potential close to 0 V vs. NHE.[5] The assembled cells were dried at 120 °C for 12 h at 2 kPa in an inert gas glove box (MBraun Labmaster 130, O_2 and H_2O <1 ppm) and, after cooling to room

temperature, vacuum-filled with 1 M tetraethylammonium-tetrafluoroborate (TEA-BF_4) in electrochemical grade (i.e., water content <20 ppm) acetonitrile (ACN) or propylene carbonate (PC), both purchased from BASF. Electrochemical measurements were carried out using a VSP300 potentiostat/galvanostat from Bio-Logic, with galvanostatic cycling with potential limitation (GCPL) applying a 15 min holding step (e.g., at +1 V vs. carbon) to bring the system to an equilibrated state. The specific (gravimetric) capacitance during discharging was calculated via *Eq. (1)*:

$$C_{sp} = \frac{\int_{t_0}^{t_{end}} Idt}{U} \cdot \frac{1}{m}, \quad (1)$$

with specific capacitance C_{sp}, time t (t_0: starting time of discharge, t_{end}: end of discharging time), applied potential difference ΔE discharge current I, and total mass of the working electrode m (i.e., considering carbon and the binder). For every type of electrode composition, two electrodes were prepared and these two cells were tested individually to calculate mean values with a standard deviation always below 5 %.

Nitrogen gas sorption measurements were carried out with an Autosorb iQ system (Quantachrome) at the temperature of liquid nitrogen (-196 °C) after degassing at 150 °C for 10 h. For the measurements, the relative pressure (P/P_0) was varied from $5 \cdot 10^{-7}$ to 1.0 in 68 steps. The specific surface area (SSA) and pore size distribution (PSD) was calculated with the ASiQwin-software via quenched-solid DFT (QSDFT) kernel with a slit pore shape model between 0.56 and 37.5 nm.[6] As shown elsewhere, the error in assuming slit-like pores for OLC is not insignificant, but smaller than using other kernels.[4] Carbon dioxide gas sorption measurements were carried out at 0 °C in the relative pressure range from $1 \cdot 10^{-4}$ to $1 \cdot 10^{-2}$ in 40 steps. SSA and PSD values were calculated for pore sizes between 0.3 nm and 1 nm with the ASiQwin software using nonlocal density functional theory (NLDFT) kernel for CO_2 sorption.[7] 1D-NLDFT kernel suffer from the assumption of infinite flat, homogenous carbon

surface which results in the incorrect pore size distribution with many sharp maxima and gaps in-between.[8] Nevertheless, CO_2 adsorption is the most favorable for measuring of ultramicropores.[9-10] The calculated PSD was incremented by a linear approximation of the calculated pore volume (CO_2-sorption-derived PSD was used up to a pore size of 0.9 nm and N_2-sorption-derived PSD for pores larger than 0.9 nm) to an equidistant point density as described elsewhere.[1]

References

1. Jäckel, N.; Rodner, M.; Schreiber, A.; Jeongwook, J.; Zeiger, M.; Aslan, M.; Weingarth, D.; Presser, V., Anomalous or regular capacitance? The influence of pore size dispersity on double-layer formation. *Journal of Power Sources* **2016,** *326* (1), 660-671.
2. Chmiola, J.; Yushin, G.; Gogotsi, Y.; Portet, C.; Simon, P.; Taberna, P. L., Anomalous increase in carbon capacitance at pore sizes less than 1 nanometer. *Science* **2006,** *313* (5794), 1760-1763.
3. Zeiger, M.; Jäckel, N.; Weingarth, D.; Presser, V., Vacuum or flowing argon: What is the best synthesis atmosphere for nanodiamond-derived carbon onions for supercapacitor electrodes? *Carbon* **2015,** *94* (1), 507–517.
4. Weingarth, D.; Zeiger, M.; Jäckel, N.; Aslan, M.; Feng, G.; Presser, V., Graphitization as a universal tool to tailor the potential-dependent capacitance of carbon supercapacitors. *Advanced Energy Materials* **2014,** *4* (13), 1400316.
5. Ruch, P. W.; Cericola, D.; Hahn, M.; Kötz, R.; Wokaun, A., On the use of activated carbon as a quasi-reference electrode in non-aqueous electrolyte solutions. *Journal of Electroanalytical Chemistry* **2009,** *636* (1-2), 128-131.
6. Gor, G. Y.; Thommes, M.; Cychosz, K. A.; Neimark, A. V., Quenched solid density functional theory method for characterization of mesoporous carbons by nitrogen adsorption. *Carbon* **2012,** *50* (4), 1583-1590.
7. Ravikovitch, P. I.; Vishnyakov, A.; Neimark, A. V., Density functional theories and molecular simulations of adsorption and phase transitions in nanopores. *Physical Review E* **2001,** *64* (1), 011602.
8. Jagiello, J.; Thommes, M., Comparison of DFT characterization methods based on N_2, Ar, CO_2, and H_2 adsorption applied to carbons with various pore size distributions. *Carbon* **2004,** *42* (7), 1227-1232.
9. Thommes, M.; Kaneko, K.; Neimark, A. V.; Olivier, J. P.; Rodriguez-Reinoso, F.; Rouquerol, J.; Sing, K. S. W., Physisorption of gases, with special reference to the evaluation of surface area and pore size distribution. *Pure Appl Chem* **2015,** *87* (9-10), 1051-1069.
10. Silvestre-Albero, J.; Silvestre-Albero, A.; Rodríguez-Reinoso, F.; Thommes, M., Physical characterization of activated carbons with narrow microporosity by nitrogen (77.4 K), carbon dioxide (273 K) and argon (87.3 K) adsorption in combination with immersion calorimetry. *Carbon* **2012,** *50* (9), 3128-3133.

Appendix C

In situ multi-length scale tracking of dimensional changes shed light on complex ion electrosorption in nanopores

Nicolas Jäckel,[1,2] Steffen Patrick Emge,[3] Benjamin Krüner,[1,2]

Bernhard Roling,[3,*] and Volker Presser[1,2,*]

[1]… INM - Leibniz Institute for New Materials, Saarbrücken, Germany

[2]… Department of Materials Science and Engineering, Saarland University, Saarbrücken, Germany

[3]… Department of Chemistry, Philipps-Universität, Marburg, Germany

*… Corresponding author's email address: roling@staff.uni-marburg.de, volker.presser@leibniz-inm.de

Supporting Information

1. Quantification of ions

To calculate the number of ions in the double-layer we expect an exclusive capacitive energy storage behavior. The surface charge *Q* is balanced by adsorption of counter-ions or expulsion of co-ions

$$Q = -F(\delta n_+ - \delta n_-) \tag{S1}$$

With the Faradaic Constant F and the change in number of cations δn_+ and the change in number of anions δn_-. All used ionic liquids contain single charged (monovalent) ions and we can simplify the equation by calculating the difference x between co-ions and counter-ions

$$-\frac{Q}{F} = \delta n_+ - \delta n_- = -x \tag{S2}$$

The total change of number of ions Δ*n* is the sum of the changes of co-ions and counter-ions:

$$\Delta n = \delta n_+ + \delta n_- \tag{S3}$$

Since there are only monovalent ions *Eq. (S3)*, we can write the following:

$$\Delta n = 2\delta n_+ + x \tag{S4}$$

The mass change according to the Sauerbrey equation $\Delta m = k \cdot \Delta f$ is linear related to the change in frequency.[1] Assuming only ion adsorption and desorption [2] we can correlate the mass change with the change in number of ions and mass of ion *M* as:

$$\Delta m = \delta n_+ \cdot M_+ + \delta n_- \cdot M_- \tag{S5}$$

By combination of *Eq. (S3)-(S5)*, we can calculate the change in number of a single type of ions as:

$$\Delta m = \delta n_+ * M_+ + (\delta n_+ + x) * M_- \tag{S6}$$

$$\Delta m = \delta n_+ * (M_+ + M_-) + x * M_- \tag{S7}$$

$$\delta n_+ = \frac{\Delta m - x * M_-}{M_+ + M_-} \tag{S8}$$

2. Volumetric changes

The changes in volume related to the changes in number of ions in the pores are correlated by the molar volume of the ions V_m and the Avogadro constant N_A

$$V_m = V \cdot N_A \tag{S9}$$

Since the voluminal of the ions are quite different there are possible changes of ions in the pores without any volumetric changes. If we know the free of volumetric change state of (dis-)charging we can calculate the number of ions which is related to the occurring volumetric change. If we assume ΔV=0, then we see:

$$\Delta V = 0 = \delta V_+ + \delta V_- = \delta n_{0+} V_{m+} + \delta n_{0-} V_{m-} \tag{S10}$$

$$\delta n_{0-} = \frac{Q * V_{m+}}{F(\delta V_{m-} * V_{m+})} \tag{S11}$$

$$\delta n_{0+} = \frac{Q}{F} - \delta n_{0-} \tag{S12}$$

with δn_0 is the number of ions which can be exchanged without any volumetric changes.

3. Gas sorption analysis

Nitrogen gas sorption measurements were carried out on the dry NovoCarb powder and the electrode containing 10 mass% NaCMC. The resulting quenched-solid density functional theory (QSDFT) plots show a decreased total pore volume in the electrode (**Fig. S1A**). This is resulted from the pore blocking of the binder, which is especially pronounced for the smallest pores below 1 nm as seen when normalizing the total pore volume to 100 % (**Fig. S1B**). Hence, the average pore volume stays constant.

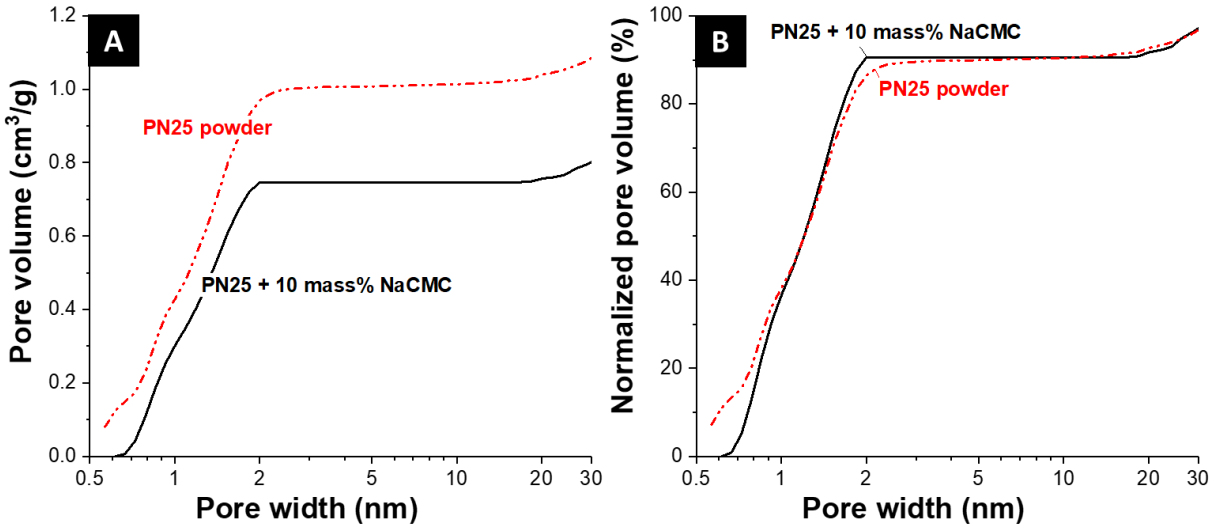

Figure S1: Cumulative pore volume for dry powder (red line, dashed) and electrode containing 10 mass% NaCMC (black line, solid).

4. EQCM measurements

The EQCM measurements for all three ionic liquids show changes in frequency Δ*f* and changes in FWHM of the peaks (dissipation Δ*W*) when applying a potential. To avoid any viscoelastic influence of the electrode on the frequency changes the change in dissipation must be much lower than the changes in peak shift Δ*f*.[3] This is confirmed by our measurements where the change in W is 3-10 times less than the change in frequency (**Fig. S2**). The signal is smoothed with a 20 point Savitzy-Golay filter.

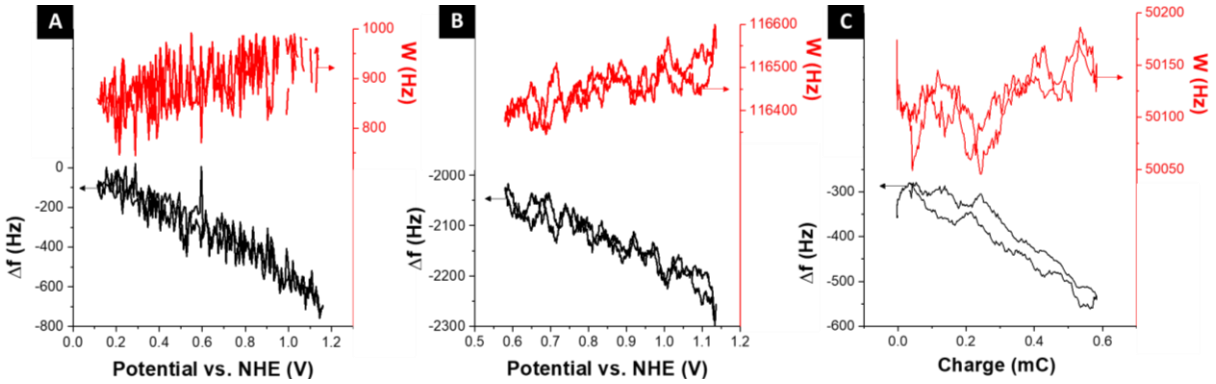

Figure S2: Change in frequency Δf and dissipation W according to the applied voltage (A,B) or to the charge (C) in (A) EMIM-TFSI, (B) EMIM-BF_4, and (C) BMIM-PF_6.

In cyclic voltammetry, the change in mass of the working electrode Δ*m* can be traced in situ with the electrochemical response of the system. In all cases the mass increased when applying positive potentials (**Fig. S3**).

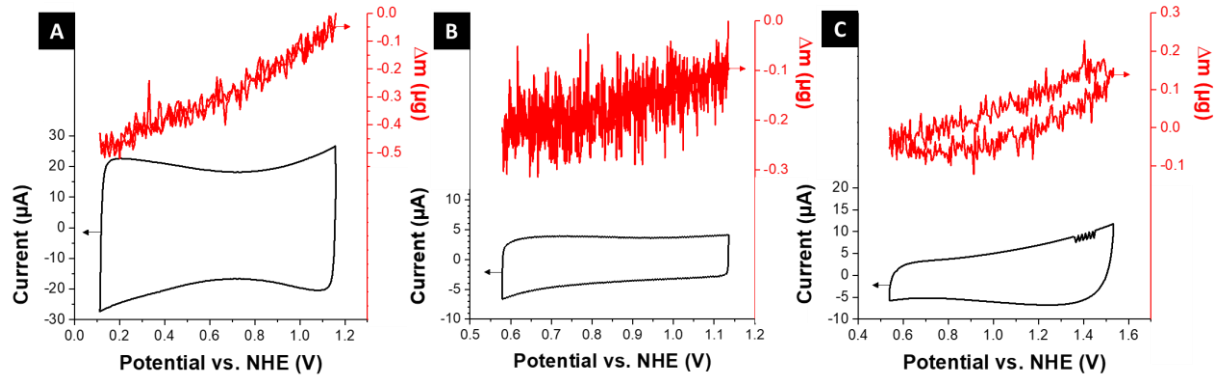

Figure S3: In situ tracing of mass changes of the working electrode (red line) and the electrochemical response (black line) of the thin EQCM electrodes in (A) EMIM-TFSI, (B) EMIM-BF_4, and (C) BMIM-PF_6.

The measured changes in mass are correlated to the change in number of adsorbed ions on the working electrode. Since we know the volume of each ion,[4] a direct calculation of volumetric changes according to the composition of the double-layer is possible (**Fig. 5**).

5. Chemical analysis

Table S1: Chemical analysis of the dry carbon powder via CHNSO analysis.

Carbon (mass%)	Hydrogen (mass%)	Nitrogen (mass%)	Sulfur (mass%)	Oxygen (mass%)
94.1±1.3	0.5±0.1	0.7±0.1	Not detectable	2.8±0.5

References

1. Shpigel, N.; Levi, M. D.; Sigalov, S.; Girshevitz, O.; Aurbach, D.; Daikhin, L.; Pikma, P.; Marandi, M.; Jänes, A.; Lust, E.; Jäckel, N.; Presser, V., In situ hydrodynamic spectroscopy for structure characterization of porous energy storage electrodes. *Nature Materials* **2016,** *15* (5), 570-575.
2. Levi, M. D.; Sigalov, S.; Salitra, G.; Aurbach, D.; Maier, J., The Effect of Specific Adsorption of Cations and Their Size on the Charge-Compensation Mechanism in Carbon Micropores: The Role of Anion Desorption. *Chemphyschem* **2011,** *12* (4), 854-862.
3. Sigalov, S.; Levi, M. D.; Daikhin, L.; Salitra, G.; Aurbach, D., Electrochemical quartz crystal admittance studies of ion adsorption on nanoporous composite carbon electrodes in aprotic solutions. *J Solid State Electr* **2013,** *18* (5), 1335-1344.
4. Krossing, I.; Slattery, J. M.; Daguenet, C.; Dyson, P. J.; Oleinikova, A.; Weingärtner, H., Why Are Ionic Liquids Liquid? A Simple Explanation Based on Lattice and Solvation Energies. *Journal of the American Chemical Society* **2006,** *128* (41), 13427-13434.

Appendix D

Supporting Information

In situ Measurement of Electrosorption-induced Deformation Reveal the Importance of Micropores in Hierarchical Carbons

Christian Koczwara[1], Simon Rumswinkel[2], Christian Prehal[1], Nicolas Jäckel[3,4], Michael Elsässer[2], Heinz Amenitsch[5], Volker Presser[3,4], Nicola Hüsing[2]*, and Oskar Paris[1]**

1. Institute of Physics, Montanuniversitaet Leoben, Franz-Josef Straße 18, 8700 Leoben, Austria
2. Materials Chemistry, Paris Lodron University of Salzburg, Jakob-Haringer Str. 2a, 5020 Salzburg, Austria
3. INM - Leibniz Institute for New Materials, Campus D2 2, 66123 Saarbrücken, Germany
4. Department of Materials Science and Engineering, Saarland University, Campus D2 2, 66123 Saarbrücken, Germany
5. Institute of Inorganic Chemistry, Graz University of Technology, Stremayrgasse 9/IV, 8010 Graz, Austria

Corresponding Authors:

* Volker Presser: volker.presser@leibniz-inm.de

* Nicola Hüsing: nicola.huesing@sbg.ac.at

* Oskar Paris: oskar.paris@unileoben.ac.at

Silica gel synthesis: The surfactant, Pluronic P123, was dissolved in 1M HCl in a ratio of P123/acid = 30/70 mass%. Tetrakis(2-hydroxyethyl)orthosilicate (EGMS) and P123/acid were mixed with a composition of the sol of Si/P123/acid = 7/30/70 mass%. The liquid mixtures were allowed to gel in a closed PP cylinder at 40 °C, and the gels were kept at this temperature as long as seven days for aging. Silanization of the whole monolith body was performed with a solution of 10 mass% trimethylchlorosilane in petroleum ether for 24 h, leading to an immediate, visible extraction of the surfactant and aqueous pore liquid. After washing with petroleum ether and ethanol, the wet gel bodies could be used for the infiltration.[1]

Carbon synthesis: Carbon monoliths were obtained from the above described silica monoliths by a nanocasting approach. The silica monoliths were infiltrated at room temperature with an aqueous solution of resorcinol (R), formaldehyde (F) and sodium carbonate (C) with a molar ratio of R/F/C/H_2O = 1/2/0.002/15, stored at 80 °C for 24 h and subsequently carbonized at 850 °C (holding time 1 h) in argon atmosphere. After cooling to room temperature, the silica-carbon-composite was immersed in 20 % hydrofluoric acid for 12 h to remove the silica mold. The resulting carbon monoliths were washed three times with a mixture of ethanol and water and dried under ambient conditions. Part of the material was activated with carbon dioxide at 925 °C for 1 h resulting in a mass loss of 20 %.

Electrode preparation and supercapacitor cell assembly: After grinding the monolithic carbon samples, electrodes were fabricated by mixing the carbon powder with ethanol and a 60 mass% polytetrafluoroethylene (PTFE) dispersion (60 % PTFE in water, Sigma-Aldrich) as a binder. The resulting slurry was rolled with a MSK-HRP-MR 100A (MTI Corporation) rolling press to a thickness of 300 µm and dried at 120 °C and 5 mbar for 24 h. Sandwich-like supercapacitor cells with platinum foil current collectors and a 300 µm glass microfiber filter (Whatman, GE) as electrode separator were assembled. The working electrode (WE, diameter 10 mm, thickness 300 µm, 10 mass% PTFE binder) consisted of the MC and AMC samples, and the five times

oversized counter electrode (CE, 5 mass% PTFE binder) was made of a commercial activated carbon (YP-80F, Kuraray Chemicals).

Sorption analysis: Nitrogen gas sorption measurements were carried out with an Autosorb iQ system (Quantachrome) with liquid nitrogen (-196 °C). The electrodes were degassed at 10^2 Pa and 150 °C for 10 h. Isotherms were recorded at relative pressures (p/p_0) from $5 \cdot 10^{-7}$ to 1.0 in 58 steps. The specific surface area (SSA) was calculated with the ASiQwin-software using the quenched-solid density function theory SSA (QSDFT-SSA) assuming slit pores. Values for the total pore volume correspond to $p/p_0 = 0.95$. Carbon dioxide sorption was carried out at 0 °C in the relative pressure range from $1 \cdot 10^{-4}$ to $1 \cdot 10^{-2}$ in 40 steps. SSA and pore size distribution (PSD) were calculated for pore sizes between 0.3 nm and 1 nm with the ASiQwin software using nonlocal density functional theory (NLDFT). The total PSD from 0.3 nm to 30 nm was incremented by a linear approximation of the calculated pore volume (CO_2-sorption-derived PSD was used up to a pore size of 0.9 nm and N_2-sorption-derived PSD for pores larger than 0.9 nm) to an equidistant point density of 0.1 nm in the range 0.3-5.0 nm and a point-to-point distance of 1 nm for pores larger than 5 nm.

In-situ SAXS measurements: In situ small-angle X-ray scattering (SAXS) measurements were performed with a custom-made cell built of polyether ether ketone (PEEK) with titanium contacts similar to the *in situ* cell published by Ruch et al.[2] A hole of 3 mm diameter through all sandwich layers except the working electrode ensured that only the scattering signal from the WE was recorded given an X-ray beam size of 1 mm. In-situ SAXS measurements were performed at the Austrian SAXS beamline at the synchrotron radiation facility Elettra in Trieste.[3] A monochromatic X-ray beam with a wavelength of 0.077 nm was used. SAXS data were recorded with a 2D Pilatus 1M detector (Dectris). The transmitted intensity was determined with an X-ray sensitive photodiode mounted on the beamstop in front of the detector. While applying cyclic voltammetry at different scan rates (1 $mV \cdot s^{-1}$ to 20 $mV \cdot s^{-1}$)

using a Gamry Reference 600 Potentiostat, 2D SAXS patterns as well as corresponding transmission values were continuously recorded every 5 s.

SAXS data evaluation: 2D SAXS patterns were azimuthally integrated using the software Fit2D.[4] The scattering intensity was normalized with respect to the corresponding monitor and transmission values. Fitting of the first order Bragg peak (10) for the different applied voltages was done as follows: In the first step, the constant background due to the change of ion concentration was determined in the Q range from 7 nm^{-1} to 9 nm^{-1} by employing Porod's law.[5] In the second step, the sum of a log-normal distribution and a power law were fitted to the data between 0.5 nm^{-1} and 2.0 nm^{-1}, where the power law captured the changes of the diffuse scattering from the micropores. The Bragg-peak position was determined from the maximum position q_0 of the fitted log-normal function. Strain as a function of applied voltage was determined by calculating the relative shift of this peak position with respect to its position at 0 V. To reduce the noise level, the peak positions from 10 consecutive SAXS curves were averaged. All data treatments were done with the software package Igor Pro 6.37 (WaveMetrics).

In situ electrochemical dilatometry was carried out with an ECD-2-nano dilatometer (EL-CELL). The measurements at 25.0±0.5 °C were conducted in a two-electrode setup with an oversized PTFE-bound activated carbon as counter and quasi-reference electrode (type YP-80F, Kuraray). The working electrode was loaded with a constant force of 1 N and the strain was tracked with a DP1S displacement transducer (Solartron Metrology, accuracy ±15 nm). After a resting period of 48 h cyclic voltammograms were recorded at 1 $mV \cdot s^{-1}$.

REFERENCES

(1) Brandhuber, D.; Torma, V.; Raab, C.; Peterlik, H.; Kulak, A.; Hüsing, N. Glycol-modified Silanes in the Synthesis of Mesoscopically Organized Silica Monoliths with Hierarchical Porosity. *Chem. Mater.* **2005**, *17*, 4262–4271.

(2) Ruch, P. W.; Hahn, M.; Cericola, D.; Menzel, A.; Kötz, R.; Wokaun, A. A dilatometric and Small-Angle X-ray Scattering Study of the Electrochemical Activation of Mesophase Pitch-Derived Carbon in Non-aqueous Electrolyte Solution. *Carbon* **2010**, *48*, 1880–1888.

(3) Amenitsch, H.; Rappolt, M.; Kriechbaum, M.; Mio, H.; Laggner, P.; Bernstorff, S. First Performance Assessment of the Small-Angle X-ray Scattering Beamline at ELETTRA. *J. Synchrotron Radiat.* **1998**, *5*, 506–508.

(4) Hammersley, A. P. FIT2D: A Multi-Purpose Data Reduction, Analysis and Visualization Program. *J. Appl. Crystallogr.* **2016**, *49*, 646–652.

(5) Glatter, O.; Kratky, O. Small angle X-ray scattering; Acad. Press: London, 1982.

Appendix E

Supporting Information

Electrochemical in situ tracking of volumetric changes in two-dimensional metal carbides (MXenes) in ionic liquids

N. Jäckel,[1,2] B. Krüner,[1,2] K. L. Van Aken,[3] M. Alhabeb,[3]

B. Anasori,[3] F. Kaasik,[1] Y. Gogotsi,[3,*] V. Presser[1,2,*]

[1] *INM - Leibniz Institute for New Materials, 66123 Saarbrücken, Germany*
[2] *Department of Materials Science and Engineering, Saarland University, 66123 Saarbrücken, Germany*
[3] *Department of Materials Science and Engineering & A. J. Drexel Nanomaterials Institute, PA 19104 Philadelphia, USA*
* Corresponding authors:
Yury Gogotsi: gogotsi@drexel.edu
Volker Presser: volker.presser@leibniz-inm.de

Experimental

Ti_3AlC_2 powder as MAX phase was synthesized as described by Naguib et al.[1] and Ti_3C_2 MXene was synthesized by etching aluminum from Ti_3AlC_2 (400 mesh size) using minimally intensive layer delamination (MILD) method thoroughly described elsewhere.[2-3] Free standing films of MXene were made using vacuum assisted filtration of aqueous colloidal solution Ti_3C_2 (1 mg/mL) using polypropylene filter membrane (Celgard 3501, 0.064 μm pore size).

We purchased 1-ethyl-3-methylimidazolium bis(trifluoromethylsulfonyl)imide (EMIM-TFSI) from IoLiTec Ionic Liquids Technologies, and 1-butyl-3-methylimidazolium tetrafluoroborate (BMIM-BF_4) from Sigma-Aldrich. Prior to use, the electrolytes were dried at 1 mbar and 120 °C for 24 h.

The height change (strain) of the carbon electrodes during charging and discharging was measured with an ECD-2-nano dilatometer from EL-CELL. The dilatometer cell is based on a two-electrode design using an oversized PTFE-bound activated carbon (AC, YP-80F from Kuraray) as counter and quasi-reference electrode. The investigated electrodes were compressed between the separator and a movable titanium plunger with a constant weight load of 1 N. Prior to the experiments, the cell was dried for 24 h at 120 °C under vacuum (20 mbar). A DP1S displacement transducer (Solartron Metrology), with an accuracy of 15 nm was used and connected to the VMP300 (Bio-logic) potentiostat. The experiments were performed at constant temperature of 25.0±0.5 °C using a climate chamber (Binder). All cyclic voltammograms were recorded at a sweep rate of 1 mV/s. Chronoamperometry (CA) was carried out using an equilibrium time of 1 h at each potential step.

X-ray diffraction (XRD) experiments were conducted with a D8 Advance diffractometer (Bruker AXS) with a copper X-ray source (Cu Kα, 40 kV, 40 mA) and a nickel filter. Air scattering at low angles is subtracted by a linear curve and intensities are normalized to the corresponding (002) peak of MXene. The in-situ cell contains an oversized AC electrode acting as the counter and quasi-reference electrode. The poly-ether ether ketone cell employed platinum current collectors and a glass fiber separator (GF/D from Whatman). The cell was operated by a Gamry Reference 600 potentiostat. After applying a constant voltage, a 2

Supporting information on ionic liquid electrolytes

The ionic liquids EMIM-TFSI (1-ethyl-3-methylimidazolium bis(trifluoromethylsulfonyl)imide) with ion sizes of $EMIM^+$ 0.43x0.76 nm^2 and $TFSI^-$ 0.29x0.79 nm^2 and BMIM-BF_4 (1-butyl-3-methylimidazolium tetrafluoroborate) with $BMIM^+$ 0.45x0.90 nm^2, BF_4^- 0.45x0.45 nm^2 were used.[4-5] The viscosity of ionic liquids, namely, 28 mPa·s for EMIM-TFSI and 180 mPa·s for BMIM-BF_4, is vastly different even if the conductivities are comparable (3.6 mS/cm for EMIM-TFSI and 3.5 mS/cm for BMIM-BF_4).[6-7]

Supporting Information on in situ XRD experiments

The full XRD patterns show two strong peaks at 26° 2Θ form the Hostaphan foil (strain crystallized poly(ethylene terephthalate); PDF-00-061-1413) covering the cell and a sharp peak at 46.2° 2Θ from the platinum current collector (PDF-04-0802) (**Fig. S1**).

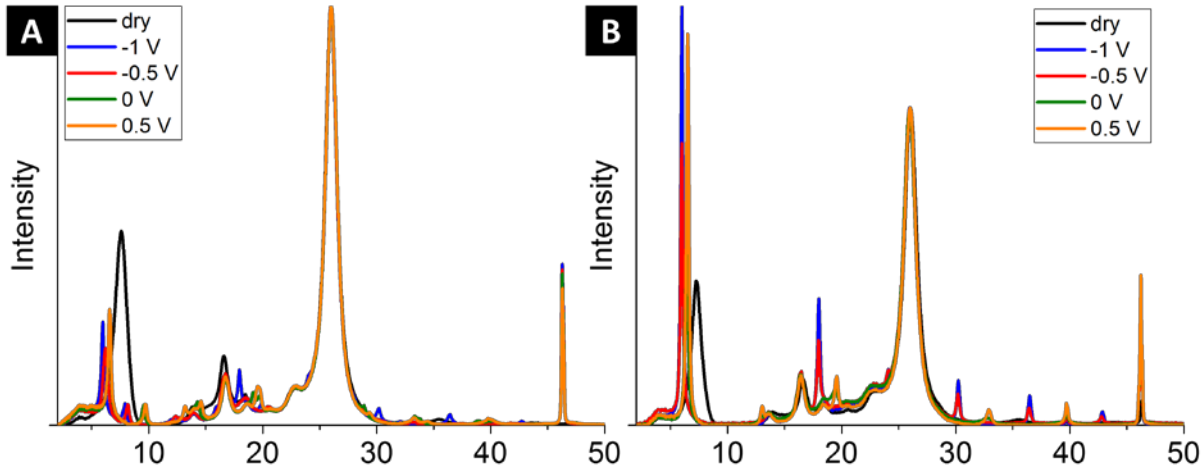

Figure S1: Full XRD pattern normalized to the Hostaphan peak at 26 ° 2Θ with (A) EMIM-TFSI and (B) BMIM-BF_4.

Supporting information on MAX phase and MXenes

Members of the MXene family are early transition metal carbides or carbonitrides, produced by etching ternary carbides (MAX phases), with M being an early transition metal, A - a group 13-15 metal, and X is carbon or/and nitrogen.[8] The transition from MAX to MXene is accomplished by selective etching of A-site atoms, for example by treatment in hydrofluoric acid (HF) or mixed solutions of lithium fluoride in hydrogen chloride (LiF in HCl).[1, 9] Depending on the degree of exfoliation, the obtained material exhibits a nano lamellar or flake-like morphology, which is ideally suited for the fabrication of binder-free electrodes (MXene paper) with very high intrinsic electrical conductivity.[3, 10] Just like graphene, MXene flakes may also undergo restacking and the interlayer spacing (along the *c*-axis) may be reduced after loss of water or other solvent. Yet, restacking may be mitigated by use of spacing agents like carbon nanotubes or carbon onions.[11-12]

Supporting information on cycling performance

The longtime CV measurement was conducted at 1 mV/s in BMIM-BF_4. The initial voltage window of -1.5 V to +0.8 V vs. carbon needed to be changed to -1.7 V to +0.7 V vs. carbon due to the onset of degradation at the upper vertex potential (**Fig. S2**) after the first few cycles. The initially vastly smeared anodic and cathodic peaks get sharpened to clear peaks at -0.3 V vs. carbon (anodic) and +0.2 V to +0.3 V vs. carbon (cathodic) after some cycles. The narrow peaks lead to a more pronounced change in strain at this potentials, meaning the (de-)insertion of $BMIM^+$ is more clearly traceable. Yet, the total values of strain decrease from 6 % to 4.5 % after 120 cycles.

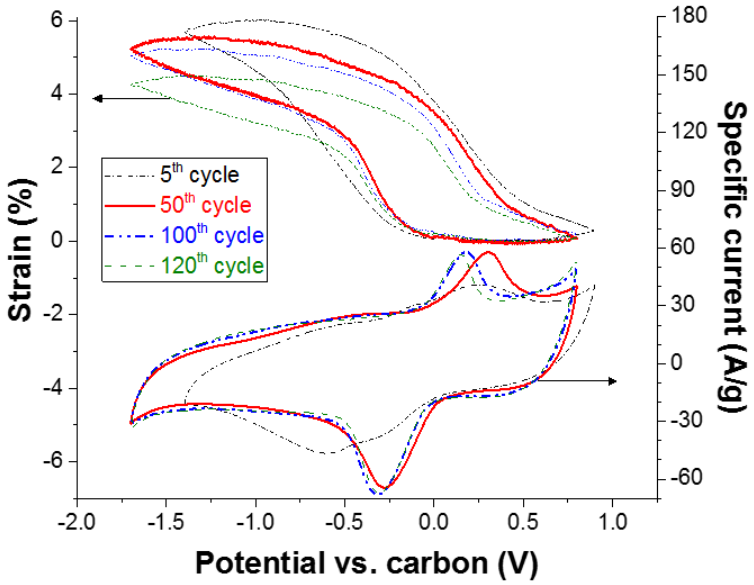

Figure S2: Longtime CV measurement with in situ dilatometry at 1 mV/s sweep rate. The expansion/contraction is normalized to the minimum equilibrium thickness.

Supporting references

1. Naguib, M.; Kurtoglu, M.; Presser, V.; Lu, J.; Niu, J.; Heon, M.; Hultman, L.; Gogotsi, Y.; Barsoum, M. W., Two-Dimensional Nanocrystals Produced by Exfoliation of Ti_3AlC_2. *Adv. Mater.* **2011,** *23* (37), 4248-4253.
2. Lipatov, A.; Alhabeb, M.; Lukatskaya, M. R.; Boson, A.; Gogotsi, Y.; Sinitskii, A., Effect of Synthesis on Quality, Electronic Properties and Environmental Stability of Individual Monolayer Ti3C2 MXene Flakes. *Advanced Electronic Materials* **2016**.
3. Shahzad, F.; Alhabeb, M.; Hatter, C. B.; Anasori, B.; Man Hong, S.; Koo, C. M.; Gogotsi, Y., Electromagnetic Interference Shielding with 2D Transition Metal Carbides (MXenes). *Science* **2016,** *353* (6304), 1137-40.
4. Largeot, C.; Portet, C.; Chmiola, J.; Taberna, P. L.; Gogotsi, Y.; Simon, P., Relation Between the Ion Size and Pore Size for an Electric Double-Layer Capacitor. *J. Am. Chem. Soc.* **2008,** *130* (9), 2730-2731.
5. Resende Prado, C. E.; Gomide Freitas, L. C., Molecular Dynamics Simulation of the Room-Temperature Ionic Liquid 1-Butyl-3-Methylimidazolium Tetrafluoroborate. *J. Mol. Struct.: THEOCHEM* **2007,** *847* (1-3), 93-100.
6. Nishida, T.; Tashiro, Y.; Yamamoto, M., Physical and Electrochemical Properties of 1-Alkyl-3-Methylimidazolium Tetrafluoroborate for Electrolyte. *J. Fluorine Chem.* **2003,** *120* (2), 135-141.
7. Buzzeo, M. C.; Evans, R. G.; Compton, R. G., Non-Haloaluminate Room-Temperature Ionic Liquids in Electrochemistry - A Review. *ChemPhysChem* **2004,** *5* (8), 1106-1120.
8. Dall'Agnese, Y.; Lukatskaya, M. R.; Cook, K. M.; Taberna, P.-L.; Gogotsi, Y.; Simon, P., High Capacitance of Surface-Modified 2D Titanium Carbide in Acidic Electrolyte. *Electrochem. Commun.* **2014,** *48*, 118-122.
9. Ghidiu, M.; Lukatskaya, M. R.; Zhao, M. Q.; Gogotsi, Y.; Barsoum, M. W., Conductive Two-Dimensional Titanium Carbide 'Clay' with High Volumetric Capacitance. *Nature* **2014,** *516* (7529), 78-81.
10. Naguib, M.; Mashtalir, O.; Carle, J.; Presser, V.; Lu, J.; Hultman, L.; Gogotsi, Y.; Barsoum, M. W., Two-Dimensional Transition Metal Carbides. *ACS Nano* **2012,** *6* (2), 1322-1331.
11. Dall'Agnese, Y.; Rozier, P.; Taberna, P.-L.; Gogotsi, Y.; Simon, P., Capacitance of Two-Dimensional Titanium Carbide (MXene) and MXene/Carbon Nanotube Composites in Organic Electrolytes. *J. Power Sources* **2016,** *306*, 510-515.
12. Zhao, M. Q.; Ren, C. E.; Ling, Z.; Lukatskaya, M. R.; Zhang, C.; Van Aken, K. L.; Barsoum, M. W.; Gogotsi, Y., Flexible MXene/Carbon Nanotube Composite Paper with High Volumetric Capacitance. *Adv. Mater.* **2015,** *27* (2), 339-345.